Transport Phenomena in Complex Two and Three-Phase Flow Systems

A Dissertation
Presented to
The Academic Faculty

by

Muhammad Khalid Akbar

In Partial Fulfillment
of the Requirements for the Degree

Doctor of Philosophy in Mechanical Engineering

Georgia Institute of Technology
November, 2004

Transport Phenomena in Complex Two and Three-Phase Flow Systems

Approved by:

Prof. S. Mostafa Ghiaasiaan (Chair), ME

Prof. Yogendra Joshi, ME

Prof. Cyrus Aidun, ME, IPST

Prof. Jeff Hsieh, ChE

Prof. Tom McDonough, IPST

Dr. Seppo Karrila, Eli Lilly

November 11, 2004

DEDICATION

This dissertation is dedicated to my parents and family, and to the people who dedicate their lives to seek for the truth.

ACKNOWLEDGEMENT

First I thank Allah for granting me the opportunity to come to Georgia Tech, and pursue my PhD in a wonderful environment of research in engineering and technology. It has been a great mercy of Him to have a very right combination of everything.

I could not be thankful enough for having had Professor S. Mostafa Ghiaasiaan as my advisor. His sound knowledge in science and technology, wisdom, and insightful suggestions were the key factors that always helped me to be on the right track in my study and research. His happy greetings and compassionate behavior to everybody, and soft speaking nature have set a brilliant example of a wonderful human being to me. He is a perfect example of the best elements in the academia. By the way, a very special thanks to Professor Ghiaasiaan for taking good care of my 'extra special' write-ups with great patience.

I would like to thank Dr Seppo Karrila for always being very helpful in every occasion that I needed his help. It was a great experience to work with Dr Seppo. He was my co-advisor before he left IPST, and his guidance with respect to those parts of my thesis that deal with pulp suspensions was invaluable. I also thank Professor Tomas McDonough for helping me out in dealing with many pulp-related issues.

Thanks to Professors William Wepfer, Yogendra Joshi, and Shabbir Ahmed (School of Industrial and System Engineering) for having helped me in a variety of academic and career issues. I would also like to thank Professors Cyrus Aidun and Jeff Hsieh for serving on my PhD thesis committee. It is a great honor to have such renowned professionals in my PhD Committee.

I am thankful to IPST and the US Department of Energy (DOE) for partially funding my research. Many individuals in IPST helped me out with my experiments over there, including Chris Nelson, Mike Buchanan, Kathleen Poll, Charles Courchene, and Mark Urbin. Thanks are due to all of them. Thanks to my colleagues Travis Laker, Shiela Rezak, Tao Xie, Clint Chedester, Jinhua Yan, and Jeff Cha. We helped each other at different occasions during our time together.

At last, but not the least, I thank my family, my little daughter in particular, for practicing patience, and freeing me from other obvious duties to fully dedicate my time to study and research. Their silent works and cheerful faces always have been inspirational to me.

TABLE OF CONTENTS

LIST OF FIGURES

LIST OF TABLES

NOMENCLATURE

a	Particle radius (m) (Ch. 6)
a_1, a_2, a_3	Coefficients in Eq. (7.4) (Ch. 7)
a_i''	Average effective interfacial surface area concentration (m^2/m^3) (Ch. 4)
$\overline{a}$	Particle median radius at inlet (m) (Ch. 6)
A	Hill's vortex strength ($m^{-1}\ s^{-1}$) (Ch. 5)
	Absorbed species (Ch. 5)
	Constant in Eq. (6.20) (Ch. 6)
	Parameter in Eq. (7.10) (Ch. 7)
	Flow area (m^2) (Ch. 9)
A_F	Frontal area (Ch. 10)
A_p	Total solid particle surface area concentration (m^{-1}) (Ch. 5)
A_i''	Normalized average interfacial area concentration ($= a_i'' \sqrt{\sigma/(g\Delta\rho)}$) (Ch. 4)
B	Solid (reactant) species (Ch. 5)
B	Parameter defined in Eq. (7.11) (Ch. 7)
c_p	Specific heat of gas ($J/kg\text{-}K$) (Ch. 6)
C	Cunningham correction factor (Ch. 7)
	Concentration ($kmol/m^3$ or mol/lit) (Ch. 4)
	Reaction product species; concentration $(kmol/m^3)$ (Ch. 5)
	Dimensionless coefficient (Ch. 9)
C_2	Constant in Eq. (6.6) (Ch. 6)
C_D	Drag coefficient (Chs. 5, 10)

C_p	Specific heat (Ch. 10)
C_T	Thermophoretic coefficient (Ch. 6)
d_p	Solid particle diameter (m) (Chs. 5,7)
D	Column diameter (m) (Ch. 4)
	Slurry droplet diameter (m) (Ch. 5)
	Diffusivity (m^2/s) (Ch. 5)
	Tube diameter (m) (Ch. 6)
	Aerosol diffusion coefficient (m^2/s) (Ch. 7)
	Diameter (m) (Ch. 9)
D_B	Brownian diffusion coefficient (m^2/s) (Ch. 6)
D_B'	Parameter defined in Eq. (6.22) (Ch. 6)
D_L	Diffusivity of reacting component in the liquid phase (m^2/s) (Ch. 4)
DF	Decontamination factor (Ch. 7)
e	Spectral emissive power function $(W/m^2\text{-}\mu m)$ (Ch. 6)
Eo	Eotvos number (Ch. 7)
f	Friction coefficient (kg/s) (Ch. 7)
f_c	Cunningham slip correction factor (Ch. 6)
F	Force (N) (Ch. 7)
g	Gravitational acceleration (m/s^2) (Chs. 4,7,9)
G	Random vector component (Ch. 7)
h	Dimensionless coordinate scale factor (Ch. 5)
h_L	Liquid level height (m) (Ch. 9)
H	Test section height (m) (Ch. 4)

	Height of channel cross-section (m) (Ch. 9)
He_{CO_2}	Henry's coefficient for CO_2 – water (Pa) (Ch. 4)
i	Mesh index for ξ coordinate (Ch. 5)
i_λ	Spectral radiation intensity (W/m^2-μm-sr) (Ch. 6)
j	Mesh index for ζ coordinate (Ch. 5)
j	Superficial velocity (m/s) (Ch. 9)
k	Gas thermal conductivity (W/m-K); Spectral absorption coefficient (m^{-1}) (Ch. 6)
k_2	Second order rate constant of CO_2 and NaOH reaction ($m^3/kmol$-s) (Ch. 4)
	Second-order reaction constant ($m^3 / kmol\ s$) (Ch. 5)
k_{2A}	Second-order reaction constant for species A ($m^3 / kg\ s$) (Ch. 5)
k_{2B}	Second-order reaction constant for species B ($m^3 / kg\ s$) (Ch. 5)
k_L	Liquid-side mass transfer coefficient (kg/m^2-s) (Ch. 4)
k_B	Boltzmann's constant (J/K) (Ch. 6)
k_p	Soot particle thermal conductivity (W/m-K) (Ch. 6)
Kn	Knudsen number (Ch. 6)
K_s	Mass transfer coefficient between solid particles and liquid (m / s) (Ch. 5)
l	Mean free path of the gas molecules (m) (Ch. 6)
L	Tube length (m) (Ch. 6)
$\dot{m}$"	Mass flux (Ch. 10)
M	Molar mass ($kg/Kmol$) (Chs. 4,5,6,7,10)
	Morton number (Ch. 7)

N_A	Avogadro's number (6.02257×10^{23} mol^{-1}) (Ch. 6)
N_P	Particle number density in the slurry (m^{-3}) (Ch. 5)
N''_{i,CO_2}	Interfacial molar flux of CO_2 (kmole/m^2-s) (Ch. 4)
P	Pressure (Pa) (Chs. 4,10)
Pe	Peclet number (Ch. 5)
Pr	Prandtl number ($=\mu c_p / k$) (Ch. 6)
q''	Heat flux (Ch. 10)
q_r''	Radiative heat flux (W/m^2) (Ch. 6)
r	Radial coordinate (m) (Chs. 5,6)
r_1, r_2	Principle radii of curvature (Ch. 10)
r_{co}	Radius of bubble's dry base (Ch. 10)
R	Universal gas constant (J $kmol^{-1}$ K^{-1}) (Ch. 4)
	Droplet radius (m) (Ch. 5)
	Radius (m) (Ch. 9)
	Microtube radius (Ch. 10)
$\mathcal{R}$	Universal gas constant (J/kmol K) (Ch. 7)
$\overline{R}$	Universal gas constant (Ch. 10)
R_B	Equivalent spherical bubble radius (m) (Ch. 7)
Re	Reynolds number (Chs. 4,10)
	Reynolds number ($=u_m D / \nu$) (Ch. 6)
	Bubble Reynolds number (Ch. 7)
Re_G	Droplet Reynolds number (Ch. 5)

s	Distance along particle path (m) (Ch. 5)
S	Perimeter (m) (Ch. 9)
Sh	Sherwood number (Ch. 5)
t	Time (s) (Chs. 5,7)
T	Temperature (K) (Chs. 4,6,7,10)
	Tangential unit vector
$\Delta T = T_0 - T_{we}$	Tube inlet-outlet wall temperature difference (K) (Ch. 6)
u	Liquid velocity $(\mathrm{m/s})$ (Ch. 5)
	Velocity (Ch. 10)
u, U	Velocity magnitude and vector (m/s) (Ch. 7)
u_e	Surface velocity at droplet equator (Ch. 5)
$u_{e,m}$	Maximum surface velocity at droplet equator (Ch. 5)
u_m	Gas mean velocity (m/s) (Ch. 6)
u_r	Reference velocity ($= \frac{2}{3} u_e$) (Ch. 5)
u_∞	Droplet's terminal velocity (m/s) (Ch. 5)
u^+	Dimensionless velocity = u / u^* (Ch. 10)
u^*	Friction velocity = $\sqrt{\tau_w / \rho_L}$ (Ch. 10)
U	Dimensionless liquid velocity (Ch. 5)
	Velocity (m/s) (Ch. 9)
U_{GS}	Gas superficial velocity (m/s) (Ch. 4)
U_{LS}	Liquid superficial velocity (m/s) (Ch. 4)
U_r	Liquid velocity used for drag force calculation (Ch. 10)

$\vec{v}$	Gas velocity *(m/s)* (Ch. 6)
$\vec{v}_T$	Particle velocity due to thermophoresis (*m/s*) (Ch. 6)
V	Volume (m^3) (Ch. 7)
w	Volume fraction of solid particles (Ch. 5)
w_a	Transmission loss fraction (Ch. 6)
x	Mass fraction (Ch. 5)
	Axial position (*m*) (Ch. 6)
x, y, z	Cartesian coordinates (m) (Ch. 7)
x, X	Dimensional and dimensionless horizontal coordinates (Ch. 10)
X	Mole fraction (Ch. 4)
	Normalized mass fraction (Ch. 5)
y, Y	Dimensional and dimensionless vertical coordinates (Ch. 10)
y_n	Parameter in Reichardt's eddy diffusivity model (Ch. 10)
Y	Mole fraction (Ch. 5)
z	Axial coordinate (m) (Ch. 4)
	Coefficient in the chemical reaction (Ch. 5)
Z	Parameter defined as dY/dX (Ch. 10)

Greek characters

α	Void fraction (Ch. 9)
β	Dimensionless parameter defined in Eq. (5.21) (Ch. 5)
β_g	Geometric standard deviation (Ch. 6)

δ	Thickness of the diffusion layer (m) (Ch. 5)
	Annulus width (R_o - R_i) (m) (Ch. 9)
Δ	Algebraic difference (Ch. 4)
Δ	Parameter defined in Eq. (5.28) (Ch. 5)
ε	Fraction of particles removed (Ch. 7)
	Eddy diffusivity (Ch. 10)
ϕ_j	Soot volume fraction for particles size group j (Ch. 6)
Φ	Total soot volume fraction (Ch. 6)
Γ	Dimensionless parameter defined in Eq. (5.20) (Ch. 5)
η	Consistency; or mass fraction of oven dried fiber in pulp-water mixture w/w (%) (Ch. 4)
	Dimensionless radial coordinate (Ch. 5)
κ	Boltzmann's constant (J/K) (Ch. 7)
	Planck mean absorption coefficient (Ch. 6)
	Karman's constant (Ch. 10)
λ	Wavelength (μm) (Ch. 6)
	Thickness of the reaction layer (m) (Ch. 5)
	Mean free path of molecules (m) (Ch. 7)
μ	Dynamic viscosity ($kg/m\text{-}s$) (Chs. 5,6,7,10)
ν	Kinematic viscosity (m^2/s) (Chs. 5,6,7,10)
θ	Tangential coordinator in polar spherical coordinates (R) (Ch. 5)
θ_o	Contact angle (Ch. 10)
ρ	Density (kg/m^3) (Chs. 4,5,7,9)

	Gas density (kg/m^3) (Ch. 6)
σ	Parametric for inlet radial distribution of Φ (Ch. 6)
σ	Surface tension (N/m) (Chs. 4,7,10)
	Standard deviation (Ch. 4)
τ	Dimensionless time (Ch. 7)
	Shear stress (N/m^2) (Ch. 9,10)
ω	Solid angle (sr) (Ch. 6)
Ω_A, Ω_B	Dimensionless parameters defined in Eqs. (5.18) and (5.19) (Ch. 5)
ξ	Parameter defined in Eq. (4.14) (Ch. 4)
	Parameter defined in Eq. (5.23) (Ch. 5)
	Parameter defined as $\left(\frac{h_L}{\delta}\right)\left(\frac{D_i}{D_o}\right)$ (Ch. 9)
ψ_L	Stokes stream function (m^3/s) (Ch. 5)
ζ	Variable defined in Eq. (5.24) (Ch. 5)

Subscripts

0	Tube inlet (Ch. 6)
a	Critical wavelength for transmittance (Ch. 6)
A	Absorbed species (Ch. 5)
b	Black body (Ch. 6)
B	Reactive species (Ch. 5)
	Bubble, Brownian (Ch. 7)
	Bubble (Ch. 10)

CO_2	Carbon Dioxide (Ch. 4)
D	Point D in Figure 1 (Ch. 10)
ex	Exit (Ch. 4)
f	Saturated liquid (Ch. 10)
g	Saturated water vapor (Ch. 4)
G	Gas (Chs. 4,7,9)
i	Gas-liquid interphase (Ch. 5)
	Incident (Ch. 6)
	Inertial (Ch. 7)
	Flow channel inner surface (Ch. 9)
	Bubble-liquid interphase (Ch. 10)
I	Gas-liquid interface (Ch. 9)
in	Inlet (Ch. 4)
j	Size group average (Ch. 6)
	Summation index (Ch. 7)
l	Droplet lower hemisphere (Ch. 5)
L	Liquid (Chs. 4,5,7,9,10)
max	Maximum (Ch. 6)
min	Minimum (Ch. 6)
mm	Mass mean (Ch. 6)
M	Point M in Figure 1 (Ch. 10)
N_2	Nitrogen (Ch. 4)
o	Flow channel outer surface (Ch. 9)

OH	Alkali (Ch. 4)
p (or *P*)	Particle (Chs. 5,6,7)
s	Saturated with respect to dissolved species B (Ch. 5)
sat (or *Sat*)	Saturation (Chs. 4,10)
T	Thermophoresis (Ch. 6)
u	Liquid-side interface (Ch. 4)
	Droplet upper hemisphere (Ch. 5)
w (or *W*)	Water (Ch. 4)
	Wall (Ch. 6,9,10)
x, *y*, *z*	Vector components in the *x*, *y*, and *z* directions (Ch. 7)
λ	Spectral (Ch. 6)
+	Size group limit (Ch. 6)

Superscript

n	Iteration index (Ch. 6)
$\bar{}$	Average (Ch. 4)
	Channel cross-section average (Ch. 6)
*	Dimensionless (Chs. 5,6,9,10)
′	Disturbed by interfacial wave (Ch. 9)
+	In wall units; non-dimensional using u^* (Ch. 10)

SUMMARY

Two-and three phase flows involving combinations of gas, liquid and solid particles occur in numerous natural and industrial systems, and currently are often among the most complex and least understood processes. The objective of this research was to investigate a number of multiphase flow processes. We were particularly interested in multiphase processes that involved solid particulates. As a result of this investigation, the following concluding remarks can be made. To this end, the following investigations were performed.

1. The interfacial surface area concentration in a short vertical column subject to the through flow of a solid-liquid-gas slurry made by mixing aqueous fibrous paper pulp with a nitrogen-carbon dioxide gas mixture was measured in the study. The gas absorption technique was applied, using CO_2 as the transferred species and sodium hydroxide as the alkaline agent in water. The flow regimes in the experiments were visually identified, and the test section void fraction was measured using a Gamma-ray densitometer. The test section was a 1.83 m-long column with 5.08 cm inner diameter. The ranges of experimental parameters were as follows: liquid-pulp superficial velocity 15 ~ 94 cm/s; average gas-superficial velocity 17 ~ 54.5 cm/s; pulp consistency in the water/pulp mixture 0.0 ~ 2.18%; and average mole fraction of carbon dioxide in the gas mixture 0.19 ~ 0.95. A total of 37 data points were obtained, each representing the average of 3 to 9 tests that confirmed reasonable repeatability. Statistical analysis of the experimental data indicates strong dependence of interfacial area on average gas superficial velocity and void fraction; and a relatively weak dependence on pulp consistency and liquid superficial velocity.

The effect of pulp consistency on the interfacial area concentration in the test section was particularly interesting. The test section average interfacial surface area concentration decreased with increasing consistency up to a consistency of 1.6%, but increased significantly when consistency was further increased to 2.18%. The experimental data were empirically correlated.

2. The absorption of a gaseous species by a slurry droplet containing reactive and sparingly soluble micro particles was numerically simulated. The problem studied is relevant to spray flue gas desulfurization systems, and the objective of this study was to elucidate the effect of the reactive solid particles on the parameters that determine the mass transfer processes. Spherical droplets with internal circulation similar to Hill's vortex flow were considered. Quasi-steady conservation equations representing the absorbed and dissolved reactant species and equations representing the dissolution of particles were numerically solved using the droplet internal circulation streamline as a coordinate. Second-order and instantaneous chemical reactions were both addressed. The results show that the reactant micro particles enhance the absorption rate by increasing the gradient of the absorbed species beneath the droplet surface. The relative effect of solid particles depends strongly on the droplet internal circulation, and diminishes as stronger recirculation occurs. Parametric calculations were performed, and were utilized to assess the adequacy of the widely-used film theory, and to examine the effect of particle size variation on the absorption rate. A transient model was also developed that utilizes the aforementioned quasi-steady droplet mass transfer and reaction models and calculates the time variation of the average solid particle size in the droplet.

Parametric calculations were presented that confirm the importance of particle size and its variation as a result of dissolution. Transient parametric calculations show a declining total absorption rate with time as a result of the shrinkage of the average particle size. The results are everywhere sensitive to droplet internal circulation, however. Partial suppression of droplet internal circulation leads to significant reduction in absorption rate, even with a high concentration of particles. The calculation results thus demonstrate that several parameters should be considered for optimal design of a slurry spray scrubber.

3. The transport of soot particles suspended in laminar hot gas, flowing in a tube, was numerically modeled and parametrically studied. The objective was to assess the coupled effects of radiation heat transfer and thermophoresis on the transport of monodisperse, as well as polydisperse soot particles. The wall material was assumed to be transparent to radiation for wavelengths shorter than a threshold wavelength at high temperatures, an essential property of high temperature-resistive materials. The results indicated that, as a consequence of strongly coupled thermal radiation transport and thermophoresis, a radially-nonuniform temperature profile develops as the distance from the tube inlet is increased, leading to the development of a sharp, non-uniform radial soot concentration profiles. The particles tend to accumulate at the vicinity of the point of inflection of the radial temperature profiles. The pace of the development of the non-uniform radial temperature and soot concentration profiles is sensitive to several parameters. Higher average soot concentration, and higher tube wall temperature both promote the development of sharp radial profiles. The development of temperature and concentration profiles is also sensitive to

particle size distribution. In comparison with model predictions obtained with the more realistic log-normally-distributed particles, and for the range of parameters covered in our simulations, the assumption of monodisperse particles leads to significant over prediction of the overall effect of thermophoresis, and of the pace of development of non-uniformity in the radial distributions of soot concentration and gas temperature.

4. The transport and removal of particles suspended in gaseous bubbles rising in a stagnant pool were modeled based on a hybrid Eulerian – Monte Carlo method. The bubble hydrodynamics were treated in Eulerian frame, using the Volume-of-Fluid (VOF) technique for modeling the motion of the gas-liquid interphase. Equations of motion were numerically solved for a large number of particles in Lagrangian frame, accounting for sedimentation, Brownian, convection, and inertial effects. Particles impacting the bubble surface were assumed to be removed from the bubble. Parametric calculation results were performed for 14.1 and 65.5 mm^3 bubble (equivalent to spheres with 3 and 5 mm diameters). These parametric calculations indicate that such bubbles are non-spherical, undergo shape change, and support strong and complex internal circulation patterns, all of which influence the pace of removal of particles. The particle removal rates are generally different than the model predictions based on assumed spherical bubbles with Hills vortex-type internal circulation. Model predictions are also compared with available experimental data.

5. There is an important resemblance between two-phase flow in microchannels and in common large channels at microgravity. In both system types the surface tension,

inertia, and the viscosity are important, while buoyancy is suppressed. Consequently, two-phase flow regime maps that have previously been developed for microgravity, or at least their underlying methodology, can be useful for microchannels. A simple Weber number-based flow regime map was thus developed for two-phase flow in microchannels. The available experimental data dealing with gas-liquid two-phase flow regimes in near-circular microchannels were carefully reviewed, and utilized for the validation of the proposed flow regime map. The following observations were made:

a. For near-circular channels with $D_H \leq 1$ *mm* channel size range (where D_H is the channel hydraulic diameter), the available data for near-circular microchannels and air-water like fluid pairs, are in reasonable agreement. For these conditions, the simple Weber number-based flow regime map that divides the entire map into four zones (surface tension-dominated, annular, froth, and transition) could be devised.

b. For $D_H > 1$ *mm*, the aforementioned flow regime map is in fair agreement with available data, with the exception of the boundaries of the froth (dispersed) flow regime zone.

6. The stability of gas-liquid stratified flow regime in horizontal annular channels was investigated. Based on the available air-water experimental data, a simple criterion for the prediction of conditions that lead to flow regime transition out of the stratified wavy flow pattern was proposed. The proposed method is an extension of the instability criterion of Taitel and Dukler (*AIChE* J. 22 (1976) 47-55) for gas-liquid flow in near-horizontal pipes.

7. Bubble nucleation and growth in microsystems, and in microchannels supporting subcooled nucleate boiling, occur within liquids with extremely large temperature gradients. Non-uniform bubble-liquid interfacial temperatures may occur, leading to important thermocapillary effects. An analytical investigation was performed as an attempt to demonstrate the potential impact of the thermocapillary effects on heterogeneously-generated micro-bubbles. Quasi-steady bubbles occupying heated microtubes were first modeled. It was shown that the temperature of the liquid-vapor interphase in these bubbles can be non-uniform. This temperature non-uniformity increases with increasing the heat transfer rate, and depends on the microtube size. A method for the prediction of liquid-vapor interphase geometry resulting from non-uniform bubble surface temperature was developed. It was shown that the aforementioned bubbles can be distorted from spherical geometry rather significantly. Quasi-steady bubbles attached to a heated microchannel surface supporting subcooled nucleate boiling were also addressed. The bubble-liquid interfacial temperature distribution was estimated based on assuming equal evaporation and condensation mass fluxes at the bubble base and top, and using the simple gas kinetic theory methods. The results showed that the thermocapillary effect tends to slightly distort and elongate the bubbles in the direction perpendicular to the heated surface, and leads to a thermocapillary force that resists bubble detachment. The geometric distortion of the bubble leads to an increase in drag force in comparison with a chopped-spherical bubble with equal volume.

CHAPTER 1: INTRODUCTION

1.1 Introductory Remarks

In the physical science, the term transport phenomena refers to the various mechanisms by which material properties can move from one place to another. The three common mechanisms for heat, for example, are diffusion, convection, and radiation. The transport of various properties can be of interest in different branches of engineering science. In this thesis we are primarily interested in the transport of three properties: heat transfer; which refers to the transport of thermal energy; mass transfer, which refers to physical processes that involve the preferential motion of species in a mixture caused by diffusive and convective mixing of atoms and molecules in systems comprised of gases, liquids and solids; and particle transport, which refers to the preferential motion of microscopic particles suspended in gases and liquids.

Transport processes are often characterized by the simultaneous presence of multiple dependent variables, multiple length scales, multiple phases, body forces, free boundaries, thin interfaces, and strong nonlinearities. They may also involve additional physical mechanisms, such as turbulence, combustion, chemical reaction, phase change, capillarity, and electromagnetic effects. A comprehensive theory that can accommodate the conservation and transport equations and their closure relations is not available. Semi-theoretical and empirical models, furthermore, often rely heavily on closure relations that are based experimental data. A thorough knowledge of the physical and chemical mechanism of the transport processes involved in the different industrial and engineering applications is simply overwhelming, however, and correlations obtained with model

experiments are often used. The experimentation thus often lacks the geometric, hydrodynamic, and physicochemical similarities with the real processes, and hence a fine conclusion becomes hard to draw. On the other hand, the physicochemical mechanism of transport processes cannot be treated simply as modules that can be added or deleted in the course of computation since they are all intrinsically coupled. In addition, it is still very difficult to completely resolve these mechanisms using the presently available (super) computing capability. Despite these difficulties, major progress has been made recently, primarily due to the advances in computing power and numerical simulation techniques. By coupling physical modeling with recent advances in computer hardware, numerical solution algorithms and grid generation schemes, many fluid flow and interfacial transport problems with physical as well as geometrical complexities can now be modeled and solved with details that can be considered satisfactory, at least from an engineer's point of view.

The goal of this research project was to obtain insight into several important and hitherto poorly understood transport processes, either by experimentation or state-of-the-art computation. To this end, several processes, all of which involve the diffusive and convective mass and transport phenomena in multiphase flow media, were investigated. The phenomena studied were as follows. In the first part of this investigation, the gas-liquid interfacial surface area concentrations in a short vertical column subject to a three-phase gas-liquid-pulp slurry, which greatly impacts both mass transfer and chemical reactions that are important in certain stages of paper production (e.g., in case of bleaching), were measured and correlated experimentally. In the second part, the absorption mechanism of gaseous species by a slurry droplet containing reactive and sparingly-soluble micro-particles (a problem that is of great interest for the well-known flu gas desulfurization) was studied in

detail. In the third part, the transport of soot particles in a laminar hot gas flow, caused by the thermophoresis phenomenon, and its impact on the radiative heat transfer in the carrier gas were investigated. In the fourth part, the transport and retention of aerosol particles in a rising bubble in a pool of liquid (a problem of great interest with respect to the transport and release of radioactive species following certain nuclear reactor incidents) was studied using a novel CFD-assisted numerical simulation method. In the fifth part, the distortion of micro-bubbles forming in microchannels cause by the thermocapillary forces that result from a nonuniform vapor-liquid interphase temperature were studied numerically. In the sixth part, a gas-liquid two-phase flow regime map was developed for microchannels (channels with hydraulic diameters of the order of 1 mm), using an important similarity between two-phase flow in microchannels on one hand and two-phase flow in large channels under microgravity conditions on the other. Finally, in the seventh part, a stability criterion for the stratified flow regime in annular channels was developed.

In the remaining sections of this chapter, the above processes, and the rationale and goals of these investigations, are briefly described.

1.2 Interfacial Surface Area Measurement in Three-Phase Gas-Liquid-Fiber Slurry Flow

The importance of gas-liquid-fiber slurry three-phase flows in various branches of chemical, petrochemical, and process industries is well recognized. Relatively little is understood about the basic hydrodynamics and transport phenomena in gas-liquid-fiber slurry three phase flow systems, however, despite its crucial role in several important

branches of industry, for example in paper production. The scarcity of published investigations dealing with three-phase fibrous slurries is primarily a result of the complexity of these systems. The main cause of the complexity of pulp slurry hydrodynamics is flocculation (entanglement of fiber groups to conformations that possess mechanical strength) that leads to the formation of three-dimensional networks (flocs) that resist shear, blocks the passage of bubbles through the networks, and complicates the mixture hydrodynamics. Understanding the role and effect of pulp fibers on the hydrodynamics of fiber-liquid-gas three-phase slurries is evidently crucial for the development of practical methods that would lead to the optimization of bleaching devices.

Gas-liquid fiber slurry three-phase flow occurs in a number of stages of paper production and recycling, including delignification and bleaching. Bleaching is achieved by dissolving an oxidizing agent such as chlorine, oxygen or ozone in an aqueous fiber suspension. The oxidizing agent is typically introduced into the mixture as fine bubbles. It must dissolve in water, be transported to the suspended pulps, and diffuse towards the fiber-liquid interface, before it can chemically react with lignin. The relatively low solubility of oxygen and ozone in water can cause poor efficiency in oxygen and ozone-based bleaching devices, and the performance of these devices can be improved by increasing the gas-liquid interfacial area. In this study, interfacial surface area was experimentally measured in a gas-liquid-fiber slurry flow in a short vertical column.

1.3 Absorption of Gaseous Species in Slurry Droplet Containing Reactive and Sparingly Soluble Microparticles

This numerical study addresses an absorption and transport process in a liquid droplet involving an instantaneous or second-order chemical reactions. The problem is relevant to the spray flue gas desulfurization (FGD) process. Flue gas desulfurization systems can be classified into six main categories: wet scrubbers; spray dry scrubbers; absorbent injection processes; dry scrubbers; regenerable processes; and combined SO_2/NOx removal processes. Wet scrubbers, in which nauseous components of flue gases (e.g., SO_2) are absorbed by a slurry containing sparingly-soluble micro particles (e.g., limestone particles) that chemically react with the absorbed gaseous species, are widely used. Wet scrubbers are followed by spray dry scrubbers, and absorbent injection systems in the FGD world market. Regenerable and combined SO_2/NOx processes have a small share.

The scrubbing reaction is often simplified and represented as an instantaneous or a second order chemical reaction between the absorbed gaseous species *A* (e.g., SO_2) and the dissolved, sparingly soluble species *B* (e.g., limestone):

$$A + zB \rightarrow Products \qquad (1.1)$$

It has been experimentally demonstrated that the absorption of species *A*, often gaseous, by the droplets can be enhanced by mixing fine solid particles of species *B* in the liquid, and such enhancement can be due to physical absorption into the particles, or under conditions where particles are reactive or catalytic. The exact mechanisms and processes involved in the enhancement have been a subject argument and conjecture, however. The specific rates of reaction in gas-slurry systems are strongly influenced by the particle sizes

and related characteristics of the slurry material. The dissolved particles are typically small enough to interact with the diffusing gaseous solute near the gas-slurry interface. Such an interaction is known to enhance the flux of the gaseous species being absorbed; however, particles are also likely to dissolve and this dissolution occurs near the interface as well as in the bulk slurry. The dissolution of particles leads to their shrinkage, and these size changes, in turn, further affect the absorption rates. Thus, the size and concentration of the dissolved particles, the droplet size and internal circulation, among other things, are likely to strongly influence the pace of the chemical reaction between the particle and the absorbed gaseous species.

This numerical study explores some of the most fundamental aspects of the above mentioned phenomena.

1.4 Thermophoresis Effect on the Transport of Soot Particles in Laminar Flow

Soot particles or smoke are the inevitable consequence of incomplete combustion of fossil fuel and other organic materials. Soot is wherever hydrocarbons are burned. The extent of soot formation is in fact an indication of the intensity of the loss of usable energy. Besides the loss of usable energy, extensive production of soot can cause many other problems as well. Deposits of soot vitiate the thermal and mechanical properties of an internal combustion engine. Emission of soot particles is a major source of atmospheric pollution that poses a significant health hazard to the public. The exhaust gas of diesel engines contains fine soot particles, for example, that are suspected to be cancer causing.

Although the black soot clouds of the diesel engines in the 1980s are gone from many of the large industrial cities, the remaining fine and invisible particles are a severe toxicological problem. These fine particles are believed to cause asthma and cardiac infarctions.

From a thermodynamic point of view, as mentioned earlier, the generation of soot particles is an indication of inefficient combustion, and hence a loss of useful energy. The energy loss is not only due to the unburned fuel, but also the fact that the soot particles emit large amounts of radiation heat, acting as a heat sink inside hydrocarbon flames. This type of heat loss that is caused by the suspended solid particles in fact results in design problems in many combustors. The presence of soot particles also changes the radiation properties of hydrocarbon flames and flue gases, further influencing the overall energy characteristics of combustion systems.

The transport of soot particles in combustion flue gases is a complicated process. In flue gas flow through a conduit, heat loss occurs from the flue gas by emission from the soot particles, while energy can be gained from the conduit wall by radiation absorption and conduction. Large temperature gradients may develop, leading to thermophoresis of soot particles, which in turn leads to a non-uniform soot concentration distribution, and Brownian diffusion in the particle field. Thermophoresis motion due to high temperature gradients may lead to particle velocities comparable to convective velocities.

This numerical study was conducted to illustrate the aforementioned effect of thermophoresis in log-normally distributed soot particles suspended in laminar hot gasses flowing in a duct.

1.5 Aerosol Transport in Rising Gas Bubbles

Transport of particles in bubbles rising in liquid is common in industrial, environmental, and sanitary processes. The transport and retention of radioactive aerosol during the wet scrubbing process in the suppression pools of boiling water reactors (BWRs); the transport of aerosols formed due to the partial evaporation of liquid metal fast breeder reactors (LMFBRs) during core disruptive accidents, in sodium vapor bubbles; and the scavenging of particles and bacteria to the surface of polluted pools by bubbles are excellent examples of particle transport in rising bubbles. In LMFBR core disruptive accidents, for example, important aerosol transport phenomena occur in a number of processes, including during the time the bubble is rising in the pool. In the BWR suppression pools, significant aerosol removal takes place as particle-carrying gas is injected into the suppression pool through a submerged vent and forms bubble swarms; during the bubble rise period; and during the arrival and rupture of bubble at the pool surface. During hypothetical LMFBR core disruptive accidents, the formation of an aerosol-containing bubble is likely to be preceded by a rapid and oscillatory expansion of a buoyant gaseous jet; and chemical reactions between the evaporating pool and the gas may generate particles.

The transport and removal of such particles during the bubble rise phase of the latter processes are the concern of this study.

1.6 Gas-Liquid Two-Phase Flow Regimes in Microchannels

The growing need for less expensive and smaller instruments has motivated a worldwide trend towards the use of microchannels in fluidic, thermal, nuclear and space

applications. Some industrial applications of microchannels include fuel cells, phase and particle separators, compact heat exchangers (with enhanced surfaces), thermal management systems, bioreactors, cooling systems for MEMS scale and lab-on-chips, and heat exchangers for advanced space components. Two-phase flow occurs in many microchannel applications. Technologies involved in these applications often exhibit a morphology of complex flow paths, multiple channels, and manifolds. Despite great advantages offered by microchannels, there is a substantial lack of detailed information about their thermal-hydraulic performance.

Two-phase flow characteristics of microchannels are known to be significantly different from the characteristics of larger channels. As a result, the existing vast literature associated with the phenomenology of change-of-phase heat transfer and two-phase flow hydrodynamic processes generally do not apply to microchannels. The surface tension is predominant in microchannels and significantly reduces the slip velocity, and renders the flow characteristics independent of channel orientation with respect to gravity. Furthermore, the microchannel diameters are about equal to or smaller than the Laplace length scale, and as a result, unlike larger channels, the hydrodynamic interfacial processes that are governed by Taylor instability do not apply to microchannel.

There is an important resemblance between two-phase flow in microchannels and in common large channels at microgravity. In both system types the surface tension, inertia, and the viscosity are important, while buoyancy is suppressed. Consequently, two-phase flow regime maps that have previously been developed for microgravity, or at least their underlying methodology, can be useful for microchannels. In this study, a simple two-phase flow regime map based on the aforementioned similarity between two-phase flow in

microchannels and commonly-applied large channels in microgravity is proposed, and its validity is demonstrated by comparison with experimental data.

1.7 Stratified Flow Transition for Near-Horizontal Flow Annular Passages

Flow regime transition out of stratified flow is important for near-horizontal flow passages. When adiabatic transport of fluids is of interest, stratified flow is preferred, and regime transition to slug or plug flow pattern is to be avoided due to the latter regimes' higher pressure drop and intermittency. Furthermore, in near-horizontal heated flow passages that rely on boiling, flow stratification can lead to early critical heat flux and is undesirable. The stability of stratified flow has therefore been studied by many researchers. Little has been done for flow in horizontal, annular channels.

In the present study a semi-empirical criterion is developed for the transition out of the stratified flow based stability considerations, and is shown to agree with the available experimental data.

1.8 Distortion of Micro-bubbles due to Thermocapillary in Microchannels

Heterogeneous bubble ebullition details in microchannels may be different from those in large systems, due to the occurrence of very large temperature and velocity gradients, and very small bubbles in the former. The relative magnitudes of various forces

that act on these microbubbles can be significantly different than those in large systems. The thermocapillary force, in particular, can be significant and appears to play a crucial role at least in the onset of nucleate boiling (ONB) and hydrodynamically-controlled onset of significant void (OSV) processes in microchannels. The current ONB and OSV models and correlation, as well as models and correlations dealing with other bubble ebullition processes in boiling, generally do not consider the thermocapillary-induced bubble shape distortion.

The present study theoretically investigates the distortion of micro-bubbles due to the thermocapillary effect in heated microchannels.

CHAPTER 2: OBJECTIVE AND OUTLINE

2.1 Objectives

The objectives of this thesis are as follows:

1. An experimental investigation into the effect of pulp fibers on the average interfacial surface area concentration in a short vertical column subject to co-current upward flows of gas-aqueous pulp slurry mixtures is performed. To our knowledge, no other similar study has been reported in the open literature.

2. The gas absorption process in a spherical, non-oscillating slurry droplet that contains reactive and sparingly soluble microparticles and undergoes internal circulation is numerically simulated. The objective of the study was to elucidate the details of the mass transfer processes, and examine the mechanism by which the solid reactant particles may influence these processes. The effect of various parameters, including the characteristics of the reactive micro particles, on the droplet rate of absorption is also investigated in this study.

3. The transport of soot particles suspended in a laminar hot gas, flowing in a tube, is numerically modeled and parametrically studied. The objective is to assess the coupled effects of radiation heat transfer and thermophoresis on the transport of monodisperse, as well as polydisperse soot particles.

4. A CFD-based hybrid Eulerian-Monte Carlo model for the transport and retention of aerosol in rising bubbles is developed and its performance is demonstrated. The developed model accounts for the combined effects of a

multitude of particle transport mechanisms, and does not include any arbitrary assumption regarding the shape or internal circulation of the bubble.

5. A simple Weber number-based two-phase flow regime map for microchannels is proposed and demonstrated, based on similarity between microchannels and large channels under microgravity conditions.

6. Based on the available air-water experimental data, a simple criterion for the prediction of conditions that lead to flow regime transition out of the stratified wavy flow pattern in horizontal annular channels is proposed.

7. The potential effect of non-uniform bubble-liquid interface temperature distribution on the shape of microbubbles forming heterogeneously in microtubes is analytically examined. For bubbles forming during subcooled boiling in microchannels, furthermore, it is shown that due to the large temperature gradients in the liquid, the thermocapillary effect can distort the bubble, lead to a thermocapillary force that resists the departure of the bubbles, and modify the hydrodynamic forces that act on the bubble.

2.2 Outline of the thesis

Chapter 3 presents a review of the past literature related to the topics that deal with the aforementioned objectives. Chapter 4 describes the experimental setup, procedures, results and discussion, and conclusions for the interfacial surface area measurement of gas-liquid-fiber slurry flow. Chapter 5 presents mathematical modeling, solution technique, results and discussions, and conclusions for the absorption of gaseous species by micro-

particles in slurry droplet. Chapter 6 is dedicated for the formulations, numerical solution method, results and discussion, and conclusions regarding the thermophoresis effect on soot particles in laminar flow.

The investigation dealing with aerosol transport in rising gas bubbles is described in Chapter 7. The development of a two-phase flow regime map for microchannels based on an analogy with large channel under microgravity is discussed in Chapter 8. Chapter 9 presents the model that was developed for stratified flow transition in near-horizontal flow passages. Chapter 10 presents the temperature non-uniformity analysis and its effect on the distortion of micro-bubbles due to thermocapillary effect in microchannels. Chapter 11 presents the conclusions and recommendations for future research.

Experimental data for interfacial surface area measurement discussed in Chapter 4 are presented in Appendix A. Some mathematical details related to Chapter 6 are provided in Appendix B. The User Defined Functions used in Fluent for the hydrodynamic simulation of the rising bubble discussed in Chapter 7 are presented in Appendix C. Likewise, some mathematical relations related to Chapter 9 are displayed in Appendix D. Appendix E contains the bibliography.

CHAPTER 3: REVIEW OF PAST LITERATURE

3.1 Interfacial Surface Area Measurement in Three-Phase Fiber Slurry Flow

3.1.1 Introductory Remarks

Oxidizing treatment of three phase slurries by oxygen and ozone gases is relatively common in environmental and waste management applications, and is gaining widespread use in paper bleaching. Bleaching is a process in paper making in which residual lignin (an amorphous and highly polymerized substance) is oxidized and removed from cellulose fibers. Bleaching has been done in the past using chlorine as the oxidizing agent. Oxygen and ozone-based bleaching are replacing chlorine-based methods due to environmental considerations, however. The low solubility of oxygen and ozone in water, the tendency of fibers to form three-dimensional networks and flocs, and the tendency of ozone to cause carbohydrate degradation in addition to delignification, render the bleaching process extremely complicated. The objective of the study reported in the next chapter is to measure the interfacial surface area, which directly influence the mass transfer and chemical kinetics associated with bleaching of low consistency (LC) aqueous pulp suspensions. Low, medium, and high consistencies of pulp suspensions have fiber mass percentages less than 8%, between 8 to 16%, and above 16% of the total aqueous mixture, respectively (Smook, 1990).

3.1.2 Hydrodynamics

Except at very low consistencies, pulp suspensions tend to form continuous fiber networks (flocs), which have are three-dimensional structures that have strength resulting from the interaction among fibers. To produce flow in a pulp suspension, sufficient stress must be applied to break up the fiber networks as well and the flocs. The initiation of motion in a pulp suspension first occurs at the weakest zones, i.e., between the flocs. When the applied shear is increased, the relative motion between the flocs increases and flocs are finally ruptured. More shear causes intense movement and eventually turbulent flow occurs. Hence, under shear stress, the pulp suspension starts behaving like lumps of solid in a liquid but eventually flows like a liquid as the magnitude of shear is increased. This behavior makes pulp suspension a unique 'fluid'. However, energy is dissipated during the flow and continuous supply of the energy is necessary to maintain the flow.

Good mixing is necessary for chemical treatment of pulp, including bleaching. Even when a pulp suspension is in apparent rapid motion, effective mixing may not occur in it. The scale of nonuniformity of a mixing process can be defined in many ways. One useful way is the distance of relative motion required to even out the concentration variations (Bennington, 1996). Based on this method, three scales of mixing can be defined (Figure 3.1):

Macroscale: Macroscale or large-scale bulk movement is necessary to even out the nonuniformities related to macroscale variations. In a typical pipe flow, macroscale variation may range from 10 mm up to the pipe diameter. Uniformity at macro scale may be achieved by bulk motion.

Fiber scale: Nonuniformity present to the scale of fiber size. The approximate distance of movement required ranges from 0.05 to 10 mm. Uniformity could be achieved by laminar and turbulent shear.

Microscale: Nonuniformity approaches the molecular scale in this type of mixing. The approximate distances of nonuniformity are typically less than 0.05 mm. Diffusion aided by small-scale fluid motion may help establishing uniformity at the microscale level. Evidently fiber scale uniformity is needed for effective bleaching.

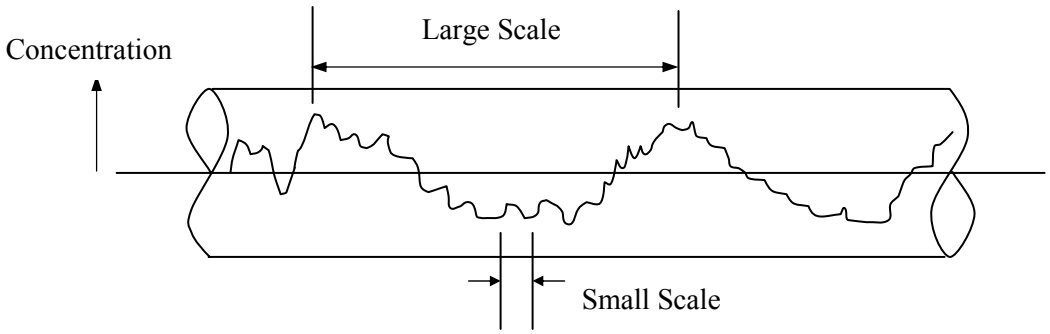

Figure 3.1: Macroscale and fiber scale variations of concentrations.

3.1.3 Bleaching Mechanism and Mass Transfer Issues

When gas containing a reactive species is introduced into a pulp suspension, the reactive species in the gas must diffuse from the bulk gas to the gas-liquid interface, transfer from the gas phase to the liquid phase, diffuse from the interface to bulk liquid, diffuse from the bulk liquid to the fiber surface, diffuse through the fiber pores and matrix to the reaction site, and finally react with the lignin and other non-cellulosic materials. All these steps occur in series and the slowest step controls the overall performance. The steps are shown

graphically in Figure 3.2 (Chaudhari et al, 1980). Once the reaction has actually occurred, the movement of the lignin product from the interior to the exterior of the fiber and into the bulk liquid phase is also important to avoid blocking the movement of the fresh bleaching agents to the reaction site.

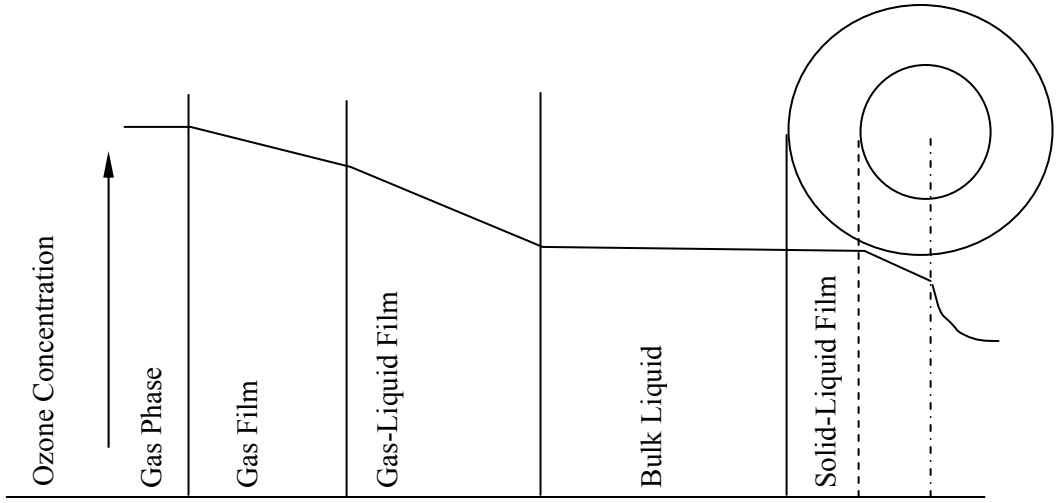

Figure 3.2: Resistances to mass transfer for the three-phase medium consistency ozonation system

In general, a homogeneous, fast and complete process of bleaching is expected to achieve good paper quality. In a well-mixed bleach system, fine gas bubbles are uniformly dispersed in the pulp-water suspension, leading to a large gas-liquid interfacial surface area. Such mixing ensures uniform and fast overall reaction in the system. In a poorly mixed system, on the other hand, the non-uniform gas dispersion may lead to a reduced interfacial surface area and therefore slow and inefficient chemical process, as well as nonuniform reaction with lignin.

In a low consistency system, the bleaching agent dissolves in the liquid phase quickly, since there is sufficient water in the pulp suspension. If the initial dispersion of the

gas into the pulp suspension is poor, the bubbles that do not initially dissolve in the liquid phase may coalesce into larger bubbles. As the bubble size increases, the mass transfer rate of the gas into the liquid decreases due to the reduction of the interfacial surface area. Conventional Static or Continuous Stirred Tank type mixers give fairly good bulk or large scale mixing. However, high shear mixers result in good local or small scale mixing, enhancing more homogeneous reaction as well as increasing the interfacial surface area. Although diffusivity of the gas in the liquid phase is typically relatively high, total diffusion and reaction rate are low in low consistency systems. This is probably because of the higher diffusion distance through the liquid to the fiber wall and lower concentration of the bleaching agent in the bulk liquid.

As the consistency increases, the reaction proceeds at a faster rate, but because the diffusion rate is relatively slow through the solid pulp, a good mixing, both macroscale and microscale, is necessary to get a homogeneous and thorough reaction (Paterson and Kerekes, 1985). For such systems, the amount of gas blown through the pulp suspensions is typically much higher compared to the solubility capacity of the available free water. Free water is defined as the water in the system that is not contained in either lumen or in the fiber wall. At medium consistency (8~16% fiber), a conventional mixing technique usually results in poor mixing. In cases where the bulk mixing is considered good, the local bleaching agent concentration may vary as high as 40% (Paterson and Kerekes, 1986). This scenario is even worse in the high consistency (above 16% fiber) systems.

3.1.4 Interfacial Surface Area in Two-Phase Systems Modeling

Currently two fundamentally different formulations of the macroscopic field equations for two-phase flow systems are applied for modeling gas-liquid systems: the mixture model, and the two-fluid model. Mixture model is formulated by considering the motion of the two-phase mixture as a whole in terms of the mixture continuity, momentum, and energy equations. The relative motion between the phases may be taken into account by a closure equation. A number of different models for this closure relation are used, for example: homogeneous flow, slip flow, and drift-flux model (Zuber and Findlay, 1965; Chawla and Ishii, 1980).

The two-fluid model (Ishii, 1975; Chawla and Ishii, 1980) considers each phase separately in terms of two sets of conservation equations. This model is evidently superior to the mixture model. Since the macroscopic field of one phase is not independent of that of the other phase, the interfacial interaction between the two phases must be accounted for. The weakest link in the two-fluid model formulation is the closure relations for the interfacial interaction terms (Ishii and Mishima, 1984). Therefore, the knowledge of the phase interactions at the interface, for example, determination of the interfacial area, friction, heat, and mass transfer, is indispensable (Kataoka et al., 1986).

Many approaches, including optical, ultrasonic, multiple probes, photoelectric capillary system, and chemical methods etc, have been used in the past to determine the interfacial surface area (Akita and Yoshida, 1974; Al Taweel et al., 1984; Banerjee and Lahey, 1981; Serizawa et al., 1975; Greaves and Kobbacy, 1984; Danckwerts and Sharma, 1966, to name a few). However, among the most popular approaches, the chemical method is based on the determination of the absorption rate of a substance in the gas phase that

disappears by an irreversible reaction in the liquid phase. The reacting gas, such as carbon dioxide mixed with another inert gas (e.g. nitrogen) reacts with a caustic solution, for example, of sodium hydroxide. If the reaction is a fast, irreversible, first or second order, the average interfacial area concentration can be measured by using the reaction rate and applying the surface renewal theory of Danckwerts (1955).

Chemical absorption techniques have been applied by many investigators in the past. Several correlations were proposed (Banerjee, 1979a-b; Jepsen, 1970; Kasturi, 1973; Shilimkan, 1975; Tomida et al., 1978) for gas-liquid two-phase flow without any suspension. The value of interfacial surface area depends on the flow regime. The interfacial surface area data obtained for various liquid and gas flow rate combinations display a maximum and a minimum with increasing gas flow rate, although different locations of maxima and minima were reported by different authors (Shilimkan, 1975; Dejesus, 1989; Watson et al., 1979). While the minimum interfacial area occurs at the developing churn flow region, the region of largest interfacial area occurs over the fully developed churn and annular flow regimes at high liquid velocities (Dejesus, 1989). Within their gas and liquid flow rates, Watson et al. (1979) found that the region of largest interfacial area occurred over the froth slug and froth flow regimes.

All the past interfacial area measurement studies discussed above are for common gas and liquid flows. In the study described in the forthcoming Chapter 4, we performed an experimental investigation into the effect of pulp fibers on the average interfacial surface area concentration in a short vertical column subject to co-current upward flows of gas-aqueous pulp slurry mixtures. Although there have been many studies on interfacial area determination in two-phase flow, to our knowledge, no other similar study has been reported

in the open literature. It is, however, well recognized that hydrodynamics change significantly even when a small amount of fiber is added into a pure gas-liquid flow.

3.2 Gas Absorption and Transport in Slurry Droplets Containing Reactive and Sparingly Dissolving Micro Particles

3.2.1 Introductory Remarks

Wet scrubbers are the most widely used FGD technology for SO_2 control throughout the world. Calcium-, sodium- and ammonium-based absorbents have been used in a slurry mixture, which is injected into a specially designed vessel to react with the SO_2 in the flue gas. The preferred absorbent in operating wet scrubbers is limestone followed by lime. These are favored because of their availability and relative low cost. The overall chemical reaction, which occurs with a limestone or lime absorbent, can be expressed in a simple form as:

$$SO_2 + CaCO_3 = CaSO_3 + CO_2 \qquad (3.1)$$

In practice, air in the flue gas causes some oxidation and the final reaction product is a wet mixture of calcium sulfate and calcium sulfite (sludge). A forced oxidation step, in situ or ex situ (in the scrubber or in a separate reaction chamber) involving the injection of air produces the saleable by-product gypsum, by the following reaction:

$$SO_2 + CaCO_3 + 1/2O_2 + 2H_2O = CaSO_4.2H_2O + CO_2 \qquad (3.2)$$

Waste water treatment is required in wet scrubbing systems.

A variety of scrubber designs is available including:

- Spray tower design where pump pressure and spray nozzles atomize the scrubbing liquid into the reaction chamber providing large particle surface area for efficient mass transfer;
- Plate tower design where the gas is dispersed into bubbles, which also provides large absorbent surface area;
- Impingement scrubber design where a vertical chamber incorporates perforated plates with openings that are partially covered by target plates. The plates are flooded with the absorbent slurry and the flue gas is accelerated upwards through the perforations. The flue gas and absorbent liquid make contact around the target plate, creating a turbulent frothing zone in order to provide the desired reaction contact;
- Packed tower design where the flue gas flows upwards through a packing material counter-current to the absorbent which is introduced at the top of the packing through a distributor;
- Fluidized packed tower design or turbulent contact absorber, which is similar to the packed tower, except that the packing is fluidized. The turbulence created keeps the packing material clean and improves the mass transfer between the flue gas and the slurry liquid.

3.2.2 Mass Transfer

In a spray tower, the presence of the sparingly soluble limestone particles is believed to enhance the absorption rate of sulfur dioxide. Most of the published studies dealing with

the basic FGD processes have addressed gas absorption in bubbling slurry reactors, however (Uchida et al., 1975; Lancia et al., 1994). Furthermore, virtually all relevant models are based on the Higbie's penetration theory (Ramachandran and Sharma, 1969; Uchida et al., 1975; Mehra, 1996) or Whitman's film theory (Muginstein et al. 2001). In these models, due to the low diffusivity of the absorbed species and the fast chemical reaction, the chemical reaction is believed to take place within a thin liquid film beneath the gas-liquid interface (the reaction layer). The enhancement of the absorption process by the reactant micro particles, it has been argued (Uchida et al., 1975; Uchida et al., 1981), can be achieved when these particles are much smaller in diameter than the thickness of the aforementioned reaction film, and occurs because the dissolution of the particles distorts the concentration profiles of the reacting species. Using the Higbie's penetration theory, Mehra (1996) has shown that the reactant particles in the reaction film can undergo significant dissolution and shrinkage, and neglecting this particle shrinkage can lead to the over prediction of the gas absorption rate.

3.2.3 Hydrodynamics- Internal Droplet Motion

Droplet internal recirculation and oscillation are known to strongly augment the transport processes at the surface and inside droplets (Calderbank and Korchinski, 1956; Sirignano, 1999; Ghiaasiaan and Eghbali, 1994). Muginstein et al. (2001) applied the Whitman film theory to a slurry droplet undergoing recirculation. A uniform film thickness, and a constant (tangential) liquid velocity equal to the droplet surface velocity at the droplet's equator as predicted by the Hadamart-Rybczynski solution (Levich, 1962), and

invariant particle diameter, were assumed. Their parametric calculations confirmed that the reactant particles greatly enhance the absorption rate.

Recently, the author and coworkers (Akbar et al., 2003) numerically simulated the gas absorption process in a spherical slurry droplet undergoing internal circulation similar to Hill's vortex flow. Using the orthogonal coordinates proposed by Kronig and Brink (1950), in which the internal circulation streamlines define one of the coordinates, they numerically solved the quasi-steady mass species conservation equations of the absorbed and reactant species (species A and B in Eqn. (1.1)), as well as equations representing the dissolution and shrinkage of reactant particles. The numerical simulations addressed the droplet surface phenomena over a single droplet circulation period. The micro particles were thus shown to modify the concentration profiles of both the absorbed and reactant species near the droplet surface. The extent of this concentration profile modification was found to be very sensitive to the vortex strength associated with the droplet circulation, however. The reactant particles appeared to have little effect on the concentration profiles when internal droplet recirculation was strong, but resulted in relatively significant enhancement of the concentration gradient of the absorbed species when droplet internal circulation was assumed to be partially suppressed.

3.3 Thermophoresis Effect on Soot Particles in Laminar Flow

The significance of thermophoresis transport of soot is well recognized, and has been demonstrated by several investigators. Cipolla and Morse (1987) investigated the effect of thermophoresis in a radiation absorbing aerosol in a hot gas flow. They studied both steady

and unsteady flows, and showed that thermophoresis initiated by temperature gradients could significantly alter the spatial distribution of the aerosol particles. They, however, neglected the emitting properties of the particles and the natural convection effects. Shaw et al. (1988) showed that ordinary diffusion and thermophoresis could both out balance the convective transport of soot particles in droplet combustion. Yoa et al. (1990) investigated the effect of radiation on the thermophoretic motion of highly absorbing and emitting particles in a laminar two-phase flow in a tube. They used an Eulerian uncoupled two-fluid model that included the effect of radiation in the energy conservation equation. Thermophoresis was found to be a dominant mechanism for particle diffusion for low stokes numbers in a non-isothermal fluid field. The particle diffusion velocity and particles concentration were found to change significantly when radiation effect was accounted for.

Kittelson et al. (1990) conducted an experimental and theoretical study of soot deposition on in-cylinder surfaces in diesel engines. They concluded that thermophoresis was the principal mechanism responsible for particle deposition. Suhre and Foster (1992) reached a similar conclusion based on their study of in-cylinder soot deposition rates in direct-injection diesel engines. Kennedy et al. (1991) performed experiments using an axisymmetric laminar jet or non-premixed flame, and a two-dimensional laminar ethylene diffusion flame. They accordingly proposed a model for soot formation in diffusion flames. Their model was based on the solution of the conservative equations in the boundary-layer form. Their calculations showed that local cooling caused by radiation had a significant impact on soot formation.

Vedha-Nayagam and Mackowski (1992) performed a theoretical study of the transport of soot particles in a high-temperature laminar gas flow in a tube. Their theoretical

model accounted for the coupled effects of thermophoresis and particle contribution to radiation heat transfer. Their model predictions showed that, as a result of thermophoresis and radiation heat transfer, the particles moved towards the tube centerline, eventually forming a narrow, particle-rich cylindrical zone along the tube centerline. The rate of compression of particle distribution towards the centerline strongly depended on the tube wall heat loss and radiative cooling of the particles. Vedha-Nayagam and Mackowski (1992) made several assumptions that could limit the applicability of their model, however. Among these assumptions were constant and uniform wall temperature, constant coefficients for particle Brownian diffusion and thermophoresis, and constant gas properties.

More recent studies dealing with soot particle transport include (Ben-dor et al., 2000; Tandon et al., 2003). Ben-dor et al. (2000) modeled the thermophoretic and diffusophoretic motion of burning soot particles in a multi-component gaseous mixture. Their results confirmed the importance of the thermophoretic effect on submicron soot particles, and the occurrence of a size-segregated soot shell structure. Tandon et al. (2003) modeled the transport of soot particles in gas streams, and identified thermophoresis as the dominant mechanism for particle deposition on adjoining surfaces.

3.4 Aerosol Transport in Rising Gas Bubbles

Transport of particles in bubbles is common in wet scrubbing processes, and in the phenomenology of certain accident scenarios for boiling water reactors (BWRs) and liquid metal fast breeder reactors (LMFBRs), (Owczarski et al. 1985; Wassel et al. 1985; Jonas and Schültz 1988; Ghiaasiaan et al. 1993; Calvo et al. 1991; Miyahara and Sagawa 1996; and

Herranz et al. 1997). Rigorous modeling of particle removal in rising bubbles is difficult, however, due to the complicated bubble hydrodynamics and the coupling among a multitude of mechanisms that contribute to particle motion. The mechanisms that are present in most applications include Brownian, inertial, and sedimentation (Fuchs, 1964); other mechanisms that are important in the aforementioned applications include convection (resulting from bubble size/shape variation), thermophoresis, and diffusophoresis. A simple method for calculation of the total aerosol removal rate in spherical bubbles, proposed by Fuchs (1964), assumes that aerosol fluxes resulting from various individual mechanisms can be added together in order to find the total aerosol flux. This method has been applied extensively in the past (Heinscheid and Schültz, 1984; Wassel et al., 1985; Ghiaasiaan et al., 1993; Pich and Schültz, 1991).

Rising bubbles are expected to undergo internal circulation, which strongly enhances diffusion and inertial particle motion (Fuchs, 1964). When diffusion is the sole transport mechanism for a continuum field and the bubble internal circulation is similar to Hill's vortex flow, a mathematical solution proposed by Kronig and Brink (1950) can be applied. Ghiaasiaan and Yao (1995, 1997) extended the method of Kronig and Brink, and solved the continuum-based (Eulerian) aerosol transport equations in a coordinate system that included the bubble internal circulation streamlines in order to model the transport of particles in spherical and non-oscillating bubbles due to the combined effects of Brownian, diffusive, and inertial mechanisms. More recently, Laker and Ghiaasiaan (2003) used a hybrid Eulerian—Monte-Carlo technique for the simulation of particle motion in spherical, non-oscillating bubbles.

Small bubbles and droplets can vibrate when their Reynolds number (defined based on properties of the continuous phase) is $Re > 200 \sim 600$ (Clift et al., 1978). The general form of the natural frequency of volume and sphere oscillations for spherical bubbles can be found in (Miller and Scriven, 1968; Shima, 1970) and (Lamb, 1932), respectively. Non-linear oscillations of bubbles and droplets have been modeled (Prosperetti, 1980; Tsamopoulos and Brown, 1983; Feng, 1992), using the domain perturbation technique of Joseph (1973). Shape oscillations of spherical bubbles can strongly impact their internal circulation, thereby enhancing the bubble internal transport processes. A similar trend is well-known in droplets. In fact, for droplets, shape oscillations can enhance the internal heat and mass transfer rates by an order of magnitude or more (Calderbank and Korchinski, 1956; Handlos and Baron, 1957; Johnson and Hamielec, 1960; Olander, 1966; Boyadzhiev et al., 1969; Brunson and Welleck, 1970). Most of the past studies deal with heat and mass transfer in droplets, and therefore address diffusion and convection only. More recent studies that have addressed the mass transfer outside bubbles also indicate that bubble oscillations can enhance the rate of such transfer processes quite significantly (Montes et al., 1999, 2002).

Only small bubbles remain spherical, or undergo simple oscillations, however. Large bubbles are typically non-spherical and undergo complex, three-dimensional shape change as they move (Clift et al., 1978). The complex shape change and often curvilinear motion of rising bubbles can lead to complex internal circulation patterns, further complicating the transport phenomena in the bubble interior. As noted earlier, however, most of the past studies dealing with aerosol transport in bubbles are based on simple bubble internal circulation models.

In this study, which is presented in Chapter 7, we performed a hybrid Eulerian – Monte Carlo treatment of particle transport in rising gas bubbles. The bubble hydrodynamics were treated by a Volume-Of-Fluid (VOF)-based method, thereby avoiding any assumption regarding the shape of the bubble, and the strength or configuration of its internal circulation patterns. Equations of motion of a large number of initially randomly-distributed particles were solved in Lagrangian frame in the bubble, as the bubble rose in a quiescent liquid pool. The objectives of this study were to demonstrate the feasibility of such hybrid simulations; compare the predictions of the hybrid model with a similar model where perfectly spherical bubbles were assumed; and attempt to compare the simulation results with experimental data. The comparison with perfect sphere results will be an indication of the effects of bubble shape deformation from spherical geometry on its internal particle transport process.

3.5 Two-Phase Flow Regime Map in Microchannels

Gas-liquid two-phase flow patterns in small channels have been investigated rather extensively in the past (Suo and Griffth, 1964; Barnea et al, 1983; Damianides and Westwater, 1988; Barajas and Panton, 1993; Fukano and Kariyasaki, 1993; Mishima et al., 1995, 1996; Triplett et al, 1999; Coleman and Garimella, 1999; Yang and Shieh, 2001; Zhao and Bi, 2001). In microchannels with near-circular cross-sections, when the hydraulic diameter is smaller than some threshold (approximately $D_H \leq 1\ mm$ with air and water like fluids, with D_H representing the hydraulic diameter) the buoyancy effect is suppressed by surface tension. With the exception of stratified flow, which does not occur due to suppression of buoyancy, however, other major flow patterns that are common in large

channels occur in microchannels as well, although certain flow pattern details may be different from those in larger channels (Suo and Griffith, 1964; Damianides and Westwater, 1988; Triplett et al., 1999; Coleman and Garimella, 1999; Yang and Shieh, 2001; Zhao and Bi, 2001). The widely used two-phase flow regime maps and semi-analytical regime transition models, furthermore, overall appear to do rather poorly when compared with microchannel data (Triplett at al., 1999; Ghiaasiaan and Abdel-Khalik, 2001).

3.6 Stratified Flow Transition for Near-Horizontal Annular Flow Passages

Stratified flow is the regime of choice for the operation of many pipelines, and the significance of the range of occurrence of stratified floe has already been explained in Section 1.6. The past investigations dealing with the stability of stratified flow have primarily dealt with rectangular or circular channels, however. Some experimental data are available for two-phase flow regimes in horizontal annuli (Osamusali and Chang, 1988; Ekberg et al. 1999), however. The oldest and simplest theory, the inviscid Kelvin-Helmholtz instability (Lamb, 1945; Milne-Thompson, 1960), considers long wavelength, small amplitude disturbances for deep and flat gas and liquid layers, and systematically over predicts the gas velocity for the onset of instability. Improvements to the Kelvin-Helmholtz theory have been proposed by several authors. A good review of some of these methods can be found in Mata et al. (2002)].

Based on the argument that gas velocity for the onset of slugging must be similar to the liquid velocity that would bring slug-flow bubbles to rest (Benjamin, 1968), Wallis and

Dobson (1973) semi-empirically derived the following criterion for the onset of slugging, using air-water data in rectangular channels,

$$j_G^* = 0.5\,\alpha^{\frac{3}{2}} \tag{3.3}$$

where

$$j_G^* = j_G\,\rho_G^{\frac{1}{2}}\left[g\,H\left(\rho_L - \rho_G\right)\right]^{-\frac{1}{2}} \tag{3.4}$$

Kordyban and Ranov (1970) considers instability caused by inviscid, finite-amplitude waves. Mishima and Ishii (1980) further elaborated the inviscid finite-amplitude waves by arguing that the disturbances that correspond to the instability threshold are associated with the fastest-growing wavelength. Shortcomings of the latter theories have been pointed out, among others, by Lin and Hanratty (1986).

Among the most widely used models for the instability of stratified flow in near-horizontal channels, is the model of Taitel and Dukler (1976). This model is an extension of the Kelvin-Helmholtz analysis to finite solitary waves in closed flow passages, where unstable wave growth is assumed to be due to the prevalence of gas pressure drop caused by Bernoulli effect over the weight of the raised liquid. Although the model only weakly accounts for the liquid viscous effects and disregards the gas viscous effect on wave growth (Lin and Hanratty, 1986; Barnea and Taitel, 1993), it is known to predict the air-water data in rectangular and circular channels with reasonable accuracy. Furthermore, the model is quite general, and can in principle be applied to channels with arbitrary geometry.

Horizontal heated annuli have been included in the design of the Accelerator Production of Tritium (APT) systems. They also can represent a simple simulation of horizontal rod bundles shrouded in cylindrical envelopes. In what follows, using the

experimental data of Osamusali and Chang (1988) and Ekberg et al. (1999), the applicability of the method of Taitel and Dukler (1976) to stratified flow in horizontal annular passages will be examined. It will be shown that, with a simple empirically-obtained constant, the method predicts the regime transition out of the stratified-wavy flow pattern with satisfactory accuracy. When applied to the stratified smooth-to-slug/plug regime transition, the method of Taitel and Dukler requires a constant that varies linearly with parameter ξ.

3.7 Distortion of Microbubbles due to Thermocapillary in Microchannels

As mentioned earlier in Section 1.6, heterogeneous bubble ebullition details during boiling in microchannels may be different from those in large systems, due to the occurrence of very large temperature and velocity gradients, and very small bubbles in the former. Thermocapillary-induced bubble shape distortions, which are likely in microchannels, are often not considered at all in commonly-applied models that deal with nucleate boiling phenomena.

The bubble ebullition phenomena in microchannels under high flow conditions are not well understood. Some experimental studies dealing with saturated flow boiling in microchannels also have shown the absence of visible bubbles under conditions where fully-developed saturated boiling should occur (Peng and Wang, 1993 and 1994). Attempts at explaining the apparent bubble extinction include a hypothesized threshold evaporation space (Peng et al., 1994), and a model based on molecular cluster dynamics (Peng et al., 2000). Heterogeneous bubble ebullition processes are of course stochastic, and bubbles are

likely to be deformed due to various effects. Assumed stochastically-averaged spherical or chopped-spherical bubbles, nevertheless, are central to the models for ONB (Bergles and Rohsenow, 1964; Sato and Matsumura, 1963; Davis and Anderson, 1966; Han and Griffith, 1965; Yin and Abedlmessih, 1974; Sudo et al., 1986; Marsh and Mudawar, 1989), OSV (Levy , 1967; Staub, 1968; Rogers et al., 1987), and many of the semi-empirical numerical models dealing with bubble growth and departure in nucleate boiling (Unal, 1976; Lee and Nydahl, 1989; Robin and Snyder, 1970; Zeng et al., 1993, 1993). Uniform bubble temperature and thermodynamic equilibrium at the liquid-vapor interface justify a spherical bubble geometry. However, spherical bubbles have also been assumed in numerical models that have examined the effect of the thermocapillary forces, which arise due to the non-uniform bubble surface temperature, on the liquid flow field around bubbles generated heterogeneously on a surface submerged in a quiescent liquid pool (Kao and Kenning, 1972; Gaddis, 1972; Straub et al., 1994; Marek and Straub, 2001). Perfect spherical geometry is also assumed in models that deal with the liquid-vapor interphase in microtubes (Yuan et al., 1999; Jiang and Carey, 2001; Hao and Prosperetti, 2000). Non-uniform vapor-liquid interphase temperatures may occur in heated microtubes, however. The assumption of uniform bubble surface temperature, furthermore, may not be adequate for subcooled nucleate boiling where evaporation and condensation can simultaneously occur over different parts of the bubble surface (Lee and Nydahl, 1989; Abdelmassih et al., 1972).

CHAPTER 4: INTERFACIAL SURFACE AREA MEASUREMENT

A brief background discussion regarding this topic was given in Section 1.2, and the relevant literature was reviewed briefly in Section 3.1.

4.1 Experimental Apparatus

A schematic of the test loop is shown in Figure 4.1. The main components of the loop are a feed tank and a receiving tank, a circulation pump, one variable speed static Lightning mixer in each tank, and a test section. The purpose of the mixers is to keep the liquid-fiber slurry as well-mixed as possible by not allowing the pulp fibers to settle down at the bottom of the tanks. The test section is a 1.83 m long transparent acrylic vertical bubble column with an inner diameter of 5.08 cm. The gas mixture is injected at the bottom of the test section. Two pressure gauges are attached to the test section at the depicted locations, and their readings are taken during the tests. A conical constriction at the top of the test section channels the gas-water-fiber mixture from the column into a 8 cm diameter pipe. The latter pipe is constructed as a "T" section with one end open to atmosphere to facilitate gas escape, while the other end allows the mixture to enter the receiving tank. The receiving and feed tanks are interconnected and are both open to atmosphere in order to provide time for entrained gas to leave the system. The water/fiber mixture is circulated continuously during tests by a Diskflow pump, which was tested to operate at up to 11% consistency without plugging. The pulp flow rates are monitored with a Krohne IFC080 Smart magnetic flow meter and encompass a range of 0 to 2 lit/s.

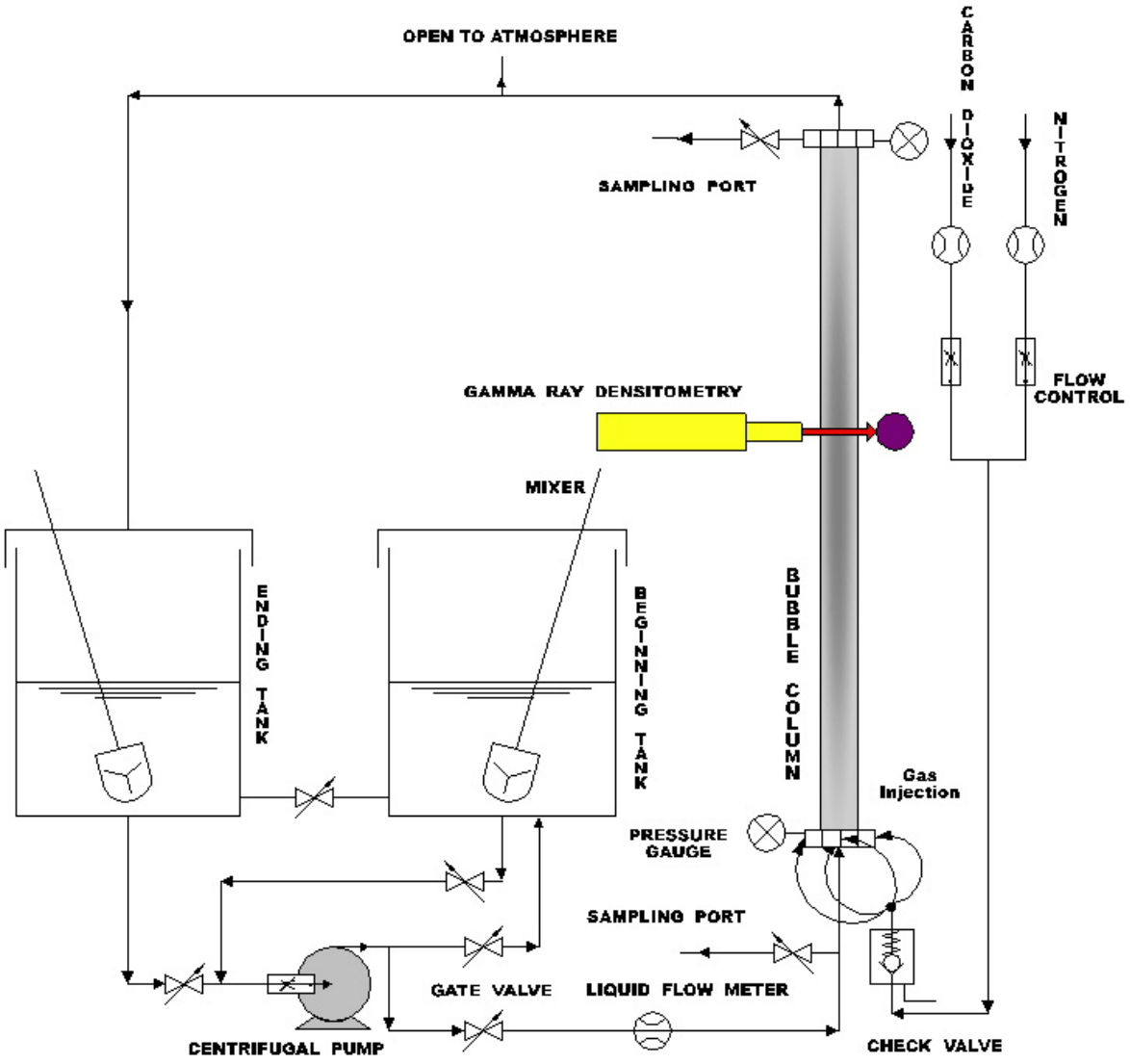

Figure 4.1: The test loop

Research grade CO_2 and N_2 gases are supplied from capsules at desired flow rates measured by two Top Trak flow meters, and mixed in a single tube before injection into the test section. The flow meter used for N_2 has a flow rate range of 0 ~ 40 SLPM (Standard Liter Per Minute), while the second one used for CO_2 has a range of 0 ~ 50 SLPM; and both

are calibrated against nitrogen gas. The flow meter used for CO_2 thus needed a flow rate correction factor of 0.74 (a value provided by the manufacturer).

The gas mixture was injected from the mixing tube into the test section via four identical tubes that had inner diameters of 6.3 mm each, and were connected to the column, perpendicular to the test section inner wall, at the lower end of the column. The tubes were installed at 90° intervals around the column periphery.

The column is mounted on a standby pipe frame, with a guided carriage affixed to the pipe frame and designed to travel along the length of the test section. A Gamma-ray densitometer equipped with a 45 mCi Americium-241 source and an Ortec Model 276 detector is housed on the carriage. The source and detector provide for the passage of a beam of Gamma rays approximately 5 mm in diameter, through the test section. The source and detector can be moved manually in vertical and lateral directions, and can be used for the measurement of chord-average void fractions at various parts of the test section (see Lindsay et al. 1995, for further details).

Two sampling ports are provided in the test loop, one in the piping about 35 cm upstream from the test section inlet, the other one at the exit of the test section. These sampling ports are connected to 12.7 mm inner diameter stainless steel collector pipes equipped with quick stop valves.

It should be noted that industrial paper making systems in which gas-liquid-pulp three-phase flow takes place are typically much larger than our test section. The geometric configurations of the industrial systems, furthermore, preclude fully developed flow conditions. The unavailability of general scaling laws for multiphase flows renders the precise experimental simulation of prototypical systems very difficult. This experimental

study is thus meant to shed light on the hydrodynamics and interfacial transport issues associated with the multiphase flows of interest rather than directly simulating prototypical systems.

4.2 Experimental Procedures

Appropriate amounts of fully bleached Kraft (FBK) softwood pulp and de-ionized (DI) water were added into the tanks. The pulp was dispersed by hand as much as possible before putting into the tanks. The mixer and circulating pump were then kept on for an hour or more to ensure effective mixing. Continuously flowing paper pulp suspensions can trap and maintain small bubbles well after through put gas has been terminated. In their experiments, Lindsay et al. (1995) found that the residual void fraction in continuously circulating paper pulp slurries is small, however, typically only up to 2%. Residual void fraction also can happen in pure water (without any pulp) due to continuous circulation into the system. For such cases the residual void fraction is even less than that of the pulp slurry cases. Therefore, attempt was not taken to eliminate the possible residual entrapped air from the paper pulp slurry before tests were conducted. Sodium hydroxide was added to the mixture as mixing was underway. Sufficient caustic was added to obtain a pH value in the 13.16 to 13.9 range. High concentration of NaOH was needed in order to ensure a fast first-order, chemical reaction with CO_2. The pulp appeared to absorb much of the caustic, and we typically had to mix 28mL of 50% (w/w) aqueous NaOH per liter of the mixture to obtain the aforementioned pH values. Following the adjustment of mixture pH and its effective mixing, the desired gas and liquid flow rates were established. The circulating pump was kept running for several more minutes to have a well mixed caustic solution.

Almost all solution was then transferred to the beginning tank, and the inter-tank valves were closed. The pump, gas flow valves, and the valve leading to the bubble column all were then turned on, and all flow rates for the run were set at their desired values. At this point, one mass transfer batch run would be conducted, whereby samples were simultaneously extracted from the two sampling ports. One or more replications of the case were also performed. Following the completion of sample extractions, Gamma-Ray Densitometry was performed along the diameter of the column at two vertical positions: 50 cm up from the bottom and 50 cm down from the top. An average value of these two measured void fractions was used in the analysis. The samples taken from the batch run were titrated within 5 to 10 hrs of the experiment. Ranges of the flow rates and other parameters, all representing the test column inlet, are as follows: pulp consistency = 0.0 ~ 2.18 %; caustic molarity (based on the titration) = 0.146 ~ 0.772 mol/lit, liquid superficial velocity = 15 ~ 94 cm/s; average gas superficial velocity = 17 ~ 54.5 cm/s; average CO_2 mole fraction in the gas mixture = 0.19 ~ 0.95. Standard titration procedure was followed for determining the concentrations of OH, CO_3, and HCO_3 in samples, using METTLER DL 70 ES titrator with electrode model 'METTLER TOLEDO DG 111 – Sc'. The titrator was calibrated daily before the first titration of the day. The collected samples from the experiment were filtrated by glass fiber filter papers to remove the interferences of the pulp fibers. Sub-samples for titration were drawn from the filtered sample solution by either volumetric (using a pipette) or gravimetric (using a scale) method. Each of the sub-samples was approximately 20 cm^3 or 20 g.

The viscosity of the pulp slurries was not directly measured in this study. Pulp consistency did not exceed 2% in our experiments. The frictional loss for a pulp consistency

below 2% is approximately equal to that of water (Heald, 1988), implying that at such low consistencies pulp stocks have a viscosity close to water. The viscosity for a 2% NaOH solution at 25°C is about 1×10^{-3} N-s/m^2, and the latter is a good estimate for the viscosity of the pulp slurries in our experiments.

4.3 Data Analysis

Sources of uncertainty in the experiments included the usual instrument and measurement precision errors; possible presence of entrained micro-bubbles in the samples; the change in chemical make-up of the liquid during sampling; and the possibility of backflow near the sampling ports. The Gamma-ray densitometer void fraction measurements also included the uncertainty associated with the random nature of Gamma-ray counts. In addition, the data scattering common in multiphase flow experiments of this type must be considered. In view of these issues, experimental runs representing individual cases in the test matrix to be presented later were repeated 3 to 9 times. For any individual entry in the test matrix, a set of repetition runs were accepted only if the measured results showed good reproducibility. Lack of good reproducibility, which was observed in a few cases, was assumed to indicate error in measurement procedures. The data that lacked reproducibility would therefore be discarded, and fresh sets of experiments would be performed instead. The effects of various experimental uncertainties were included in the data analysis, although for most cases the cumulative effect of experimental uncertainties was smaller than the data scatter.

The effective average column interfacial area concentration, a_i'', is calculated for each run assuming: (1) quasi-steady state, one-dimensional flow; (2) liquid side-controlled mass transfer; (3) pseudo first–order chemical reaction between absorbed CO_2 and dissolved $NaOH$ in water; and (4) negligible effect of absorption / desorption of species other than CO_2 on the modeled mass transfer process. Assumption 1 is a simplifying idealization and given that time –averaged measurements are of interest, is reasonable. Assumption 3 is widely accepted (Nijsing et. al. 1959, Kasturi and Stepanek 1974). All other assumptions are also reasonable.

The liquid and gas-side species conservation equations can then be written as:

Conservation of alkaline species in liquid:

$$\frac{\rho_L U_{LS}}{M_L}\frac{d}{dz}X_{OH,L} = -2\,a_i''\,N''_{i,CO_2} \tag{4.1}$$

Conservation of CO_2 species in the gas phase:

$$\frac{d}{dz}\left(\frac{\rho_G U_{GS}}{M_G}X_{CO_2,G}\right) = -a_i''\,N''_{i,CO_2} \tag{4.2}$$

Overall mass conservation for the gas phase:

$$\frac{d}{dz}\left(\frac{\rho_G U_{GS}}{M_G}\right) = -a_i''N''_{i,CO_2} \tag{4.3}$$

where

$$C_{OH} = \left[OH^-\right] = C_L X_{OH,L} \tag{4.4}$$

$$C_L = \rho_L / M_L \tag{4.5}$$

The molar flux of CO_2 at the interface, in accordance with Danckwerts' surface renewal theory (Danckwerts 1955), is represented by

$$N''_{i,CO_2} = C_{CO_2,u}\sqrt{D_L k_2 C_{OH}} \tag{4.6}$$

where

$$X_{CO_2,u} = \frac{X_{CO_2,G}\,P}{He_{CO_2}} \tag{4.7}$$

$$C_{CO_2,u} \approx C_w X_{CO_2,u} \tag{4.8}$$

$$M_G = \left(X_{CO_2,G} M_{CO_2}\right) + \left(1 - X_{CO_2,G} - X_g\right) M_{N_2} + \left(X_g\, M_w\right) \tag{4.9}$$

$$X_g = \frac{P_{Sat}}{P} \tag{4.10}$$

where, P is total local pressure, and is estimated from

$$P = P_{in} - \frac{P_{in} - P_{ex}}{H} z \tag{4.11}$$

where H is the height of the test section. Also, assuming ideal gas:

$$\rho_G = \rho_g + \frac{\left(P - P_{Sat}\right)}{RT_L / M_G} \tag{4.12}$$

The rate constant k_2, for the irreversible reaction between CO_2 and $NaOH$, was estimated from (Danckwerts, 1970):

$$log_{10}\, k_2 = 13.635 - \tfrac{2895}{T} \tag{4.13}$$

For each experimental case, the ordinary differential equations (4.1 to 4.3) were numerically integrated starting from the test section inlet ($z = 0$), to the exit ($z = H$). The

numerical calculations were repeated, and a_i'' was iteratively changed until the estimated $X_{OH,\,L}$ at exit matched the experimentally measured value.

4.4 Results and Discussion

4.4.1 Test Matrix and Data

The parameters that could potentially influence a_i'' in a run include the liquid superficial velocity $U_{LS;}$ the average NaOH concentration, $\overline{C}_{OH}$; the average superficial gas velocity, $\overline{U}_{GS}$; the average mole fraction of CO_2 in the gas, $\overline{X}_{CO_2,G}$; and the column average void fraction (gas holdup). Parameters $\overline{X}_{CO_2,G}$ and $\overline{U}_{GS}$ can be calculated by performing an overall species mass balance on the test section based on sampling results. Since the extent of total rate of CO_2 absorption in each test case is not known a priori, however, the test matrix was designed based on the inlet values of all parameters. Parameters C_{OH} and $X_{CO_2,G}$ of course should not directly influence a_i''. Parameter C_{OH} was included among the important parameters for the test matrix design for testing the validity of Danckwerts' theory for our experiments. Furthermore, parameter $X_{CO_2,G}$ was included since its value varies between the test section inlet and outlet, leading to a reduction in U_{GS} along the test section, and therefore a reduction in a_i''.

The test matrix was determined using a rotatable, uniform-precision, central-composite method. This method, described in detail in Neter et. al. (1996), allows for an optimum design of a test matrix with a minimal number of tests that can provide for the estimation of all the important parametric dependencies. With 5 controllable variables

(factors) at five levels, 34 runs were needed for this design. However, as mentioned earlier, to verify repeatability of these 34 tests, each was repeated 3 to 9 times. A total of 37 runs including 3 additional random runs are tabulated in Appendix A.

4.4.2 Parametric Dependencies

The parametric effects of various factors on the average effective interfacial surface area concentration are discussed in this section. These parametric effects are deduced from the statistical analysis of the data, using the main factor effects (as described in Neter et al., 1996, for example). All parameters are presented in dimensionless form for convenience. Figure 4.2, plotted using the commercial software Minitab (Minitab, Inc., 2000), shows the effects of the main variables on the dimensionless interfacial area concentration, A_i''. The plots depicted in Figure 4.2 are basically components of the matrix plot generated by the aforementioned software. A matrix plot is a two-dimensional matrix of individual plots that provide the two-variable relationships among a number of variables all at once. The parametric dependence of A_i'' on any factor depends on the average trend of the depicted data points. Random scatter of the data points around an approximately horizontal mean, as noted for example, for the case of alkali, indicates that A_i'' is insensitive to the concentration of alkali. This trend is consistent with the assumed validity of the surface renewal theory. The data scatter also shows a weak dependence of A_i'' on the liquid superficial velocity (the latter represented by $Re_L = U_{LS} D / \nu_L$). A_i'' depends strongly on the void fraction and gas superficial velocity (represented by $\overline{Re}_G = \overline{U}_{GS} D / \overline{\nu}_G$, with $\overline{U}_{GS}$ and $\overline{\nu}_G$ defined as mean gas superficial velocity and gas mixture viscosity in the test

section). Gas mixture properties were calculated using the rules described in Edwards et al. (1979). The positive overall slope of the distributions of data points for the aforementioned factors, furthermore, indicates that A_i'' is an increasing function of both parameters, a trend that is well expected. The distribution of the data showing the effect of the mean mole fraction of CO_2 in the gas mixture $\left(\overline{X}_{CO_2}\right)$ suggests that A_i'' would decrease with increasing $\overline{X}_{CO_2}$ in the experiments. However, this apparent dependence of A_i'' on $\overline{X}_{CO_2}$ is primarily due to the fact that a significant fraction of the injected CO_2 is absorbed in the test section, and this can lead to a sizable reduction in mean gas superficial velocity and therefore a reduction in a_i''.

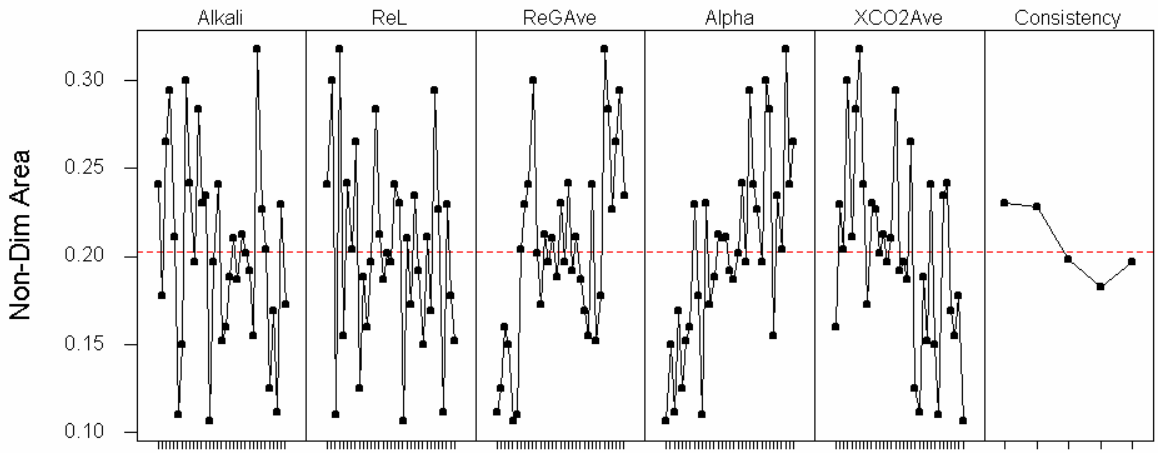

Figure 4.2: Main factor effects plots showing the effects of predictor variables on the response variable A_i''.

An important parametric effect is caused by fiber consistency. There is little scatter in the consistency plot of Figure 4.2 because we had good control over consistency. Evidently, A_i'' tends to decrease as consistency is increased up to a consistency of about 1.6%. The effect of fibers and fiber consistency on the column hydrodynamic processes,

and in particular on the interfacial area concentration is complicated, and has several attributes. The fibers modify turbulence, influence bubble coalescence and bubble rise velocity, and modify the overall flow patterns in the column. With respect to bubble coalescence, for example, fibers enhance coalescence as long as bubbles move faster than the pulp networks, while the opposite may occur when the velocity of bubbles is in fact lower than the velocity of the liquid-pulp mixture (Lindsay et al., 1995). Increased coalescence among bubbles in the lower part of the bubble column (where bubble coalescence leads to churn/slug flow regime in the remainder of the column), on the average, with increasing consistency for $\eta \leq 1.6\ \%$, is likely to lead to the decreasing trend of A_i'' with increasing η in the latter range. At higher consistencies the flocs are likely to be large and sturdy, and therefore capable of entrapping and maintaining some of the smaller bubbles, thereby leading to the apparent increasing A_i'' with η. The effect of fiber consistency on the intricate flow pattern characteristics also obviously influences the interfacial area concentration. The complexity of the fiber consistency on all hydrodynamic and transport processes must be emphasized. Rewatkar and Bennington (2000) had used commercial laboratory-scale pulp mixer to measure the volumetric mass-transfer coefficient $(k_L a_i'')$. It is interesting to note that, although their system is totally different from that of the present study, they also found that volumetric mass transfer coefficient depends positively on the void fraction and negatively on the fiber consistency.

Table 4.1 shows the statistical correlation among different variables and A_i''. These correlation levels were calculated using the aforementioned Minitab (Minitab, Inc., 2000) statistical software. A positive correlation number between two variables implies a mutual positive effect between them (i.e., increasing either one would increase the other parameter),

and vice versa. The levels of correlation between A_i'' and each of the depicted factors are of course consistent with the trends displayed in Figure 4.2. The correlations between pairs of other parameters also depict some important internal associations. For example, the large and positive correlation between the gas flow rate (represented by $\overline{Re}_G$) and the void fraction indicates that they are correlated, as expected. As expected, there is also a strong effect of fiber consistency on void fraction. The effect of $\overline{X}_{CO_2,G}$, and its cause, have been discussed earlier. Other pair correlations are all small, as expected.

Table 4.1: Correlations among the main variables and the interfacial surface area

	$C_{OH,in}$	Re_L	$\overline{Re}_G$	α	$\overline{X}_{CO_2,G}$	η
Re_L	0.031					
$\overline{Re}_G$	-0.125	0.099				
α	-0.099	-0.574	0.658			
$\overline{X}_{CO_2,G}$	-0.107	0.042	-0.016	-0.299		
η	-0.023	0.006	0.053	0.229	0.045	
A_i''	-0.245	-0.216	0.723	0.716	-0.403	-0.288

4.4.3 Empirical correlations of the Data

For convenience of the correlation development, the effect of pulp consistency is represented by the parameter

$$\xi = 10 - \eta \tag{4.14}$$

where η is the pulp consistency, in weight percent of dry pulp in water. Attempt was made to develop empirical correlations of the forms:

$$A_i'' = c_1 \, \alpha^{c_2} \, Re_L^{c_3} \, \xi^{c_4} \tag{4.15}$$

$$A_i'' = b_1 \, \overline{Re}_G^{\,b_2} \, Re_L^{\,b_3} \, \xi^{\,b_4} \tag{4.16}$$

These correlations can be useful for estimating the relative effect of various important factors on a column's average interfacial surface area concentration, although the correlations may not be directly applicable to columns with significantly different geometric characteristics. As discussed earlier, there was a strong association between α and $\overline{Re}_G$; therefore only one of these two parameters was explicitly maintained in each expression. The results for Eqn. (4.15) were:

$c_1 = 1.378 \times 10^{-4}$

$c_2 = 1.26$

$c_3 = 0.311$

$c_4 = 2.62$

The standard deviation and the coefficient of determination for this fit are 0.1153 and 0.93, respectively. The predictions of Eqn. (4.15) are compared with the experimental results in Figure 4.3.

For Eqn. (4.16), the best fit was obtained with:

$b_1 = 1.448 \times 10^{-4}$

$b_2 = 0.763$

$b_3 = -0.186$

$b_4 = 1.57$

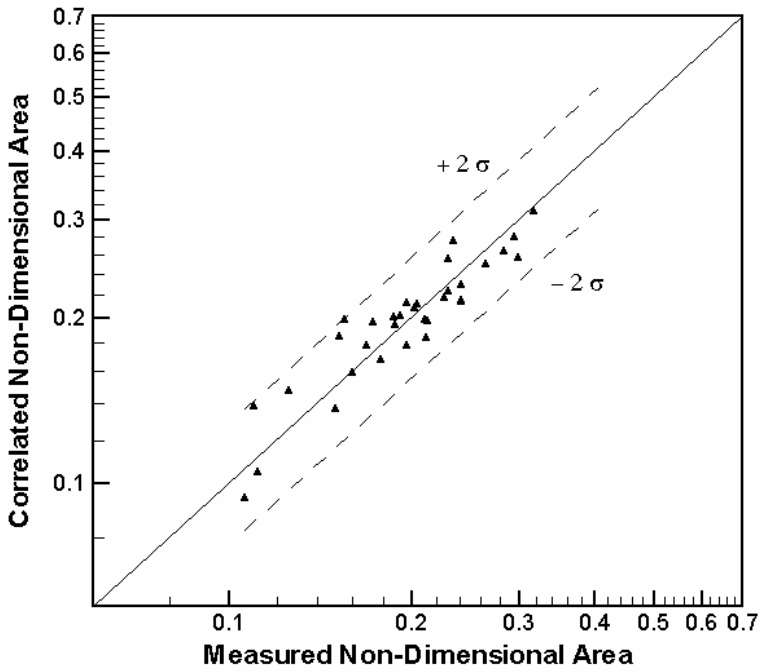

Figure 4.3: Comparison of the interfacial surface area concentration values obtained from the experimental and the correlation (Eqn. 4.15).

The standard deviation and the coefficient of determination for this fit are 0.1562 and 0.85, respectively. It should be pointed out that the apparent conflict between Eqns (4.15) and (4.16) with respect to the sign of the power of Re_L is due to the relatively strong correlation between α and Re_L (see Table 4.1). Equation (4.15) includes α^{c_2} on its right side, and this modifies its explicit dependence on Re_L. The true correlation between A_i'' and Re_L is negative, as noted in Table 4.1 and Figure 4.2. The predictions of the latter expression are compared with the experimental results in Figure 4.4. Equation (4.15) is evidently a better correlation, although Eqn. (4.16) is easier to apply.

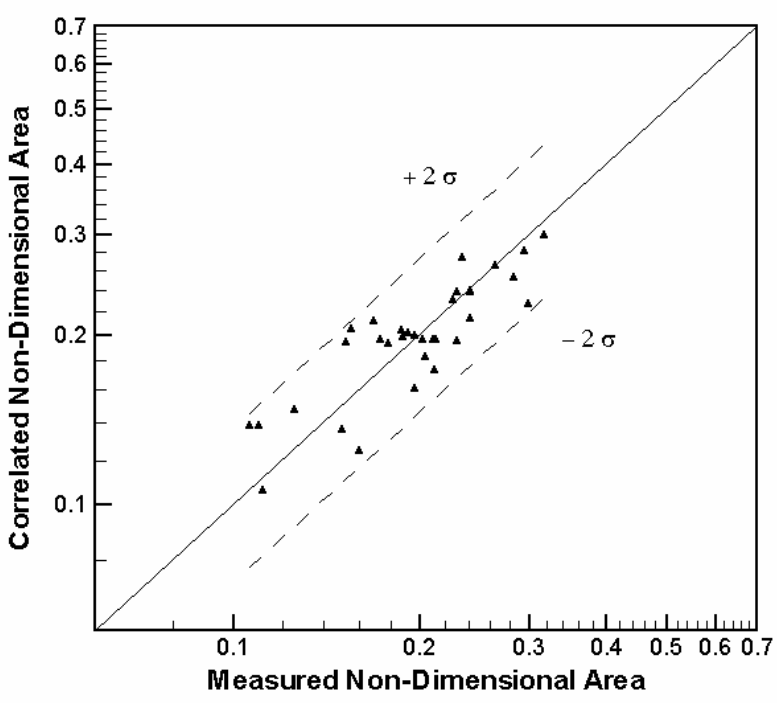

Figure 4.4: Comparison of the interfacial surface area concentration values obtained from the experimental and the correlation (Eqn. 4.16).

4.5 Concluding Remarks

In this study we reported on an investigation into the effects of various parameters on the effective, average interfacial surface area concentration in a short vertical column subject to a through-flow of a paper pulp-water-gas three-phase mixture. The experiments were performed in a 1.83 m-long column that was 5.08 cm in inner diameter. The average interfacial area concentration was quantified using the gas absorption technique, with CO_2 as the transferred species, and sodium hydroxide as the reacting agent in the liquid. The test matrix was designed using the central-composite, uniform precision rotatable design method with 5 factors, each represented at 5 levels. A total of 37 test cases, each repeated 3 to 9 times, were performed, the tabulated experimental data were presented, and their statistical

characteristics were analyzed, whereby important parametric dependencies were identified. The results confirmed that pulp affects all major hydrodynamic processes, including the interfacial surface area. The experimental data were then empirically correlated.

CHAPTER 5: ABSORPTION OF GASEOUS SPECIES BY MICRO-PARTICLES IN SLURRY DROPLET

A brief background discussion regarding this topic was given in Section 1.3, and the relevant literature was reviewed briefly in Section 3.2.

5.1 Physical System and Assumptions

As mentioned in Chapter 3, although the chemistry of FGD is complicated (Brogren and Karlsson, 1997; Pasiuk-Bronikowska and Rudzinski 1991), it is often simplified by an instantaneous or second-order chemical reaction between the absorbed gas A and the dissolved, sparingly soluble reactive species B. Figure 5.1 is a schematic of a modeled droplet. Slurry droplets are typically about 1 mm in diameter, and contain limestone particles typically a few μm in diameter. For such droplets undergoing free fall in flue gas, $\mathrm{Re}_G \approx 300 \sim 400$. Droplets with sufficiently strong surface tension remain approximately spherical and non-oscillating within the latter range (Clift et al., 1978). For spherical droplets with creep flow ($\mathrm{Re}_G < 1$) the droplet internal circulation follows the well-known Hadamart-Rybczinski solution (Hadamard, 1911; Levich, 1962). At higher Re_G values, as long as the droplet remains spherical and the internal circulation motion is assumed inviscid (Batchelor, 1956), the following equation for Stokes' stream function approximately applies to the droplet's inviscid core (Batchelor, 1956; Harper and Moore, 1968):

$$\psi_L = \frac{1}{2} A\, r^2 (R^2 - r^2) \sin^2 \theta \tag{5.1}$$

Equation (5.1) is identical to the Hadamard-Rybczynski, if A is found from:

$$A = \frac{u_\infty}{2R^2\left(\mu_L / \mu_G + 1\right)} \tag{5.2}$$

For $\mathrm{Re}_G >> 1$, and in the absence of surface active contaminants, however (Harper and Moore, 1968):

$$A = 1.5 u_\infty R^{-2} \tag{5.3}$$

The droplet internal circulation configuration is qualitatively depicted in Figure 5.1. The species concentration profiles depicted represent infinitely fast reaction kinetics, and define the reaction and diffusion layers (Uchida et al., 1975; Uchida et al., 1981). Absorption of species A takes place at the surface of the droplet, while chemical reaction between A and B occurs in the liquid phase. Species A and B evidently have to diffuse in opposite directions, and for an infinitely fast reaction the two species can not coexist anywhere. A thin reaction layer, and a wider diffusion layer thus form, starting near the leading pole of the droplet, and develop along the droplet surface. The closed streamlines move through the droplet internal wake after passing the vicinity of the droplet rear pole. For the diffusion of a single species without chemical reaction, based on dimensional analysis, an estimate of the diameter of the droplet internal wake is $R\,Pe^{-1/4}$ (Brignell 1975). Mixing can be expected in the droplet interior wake and fresh liquid would emerge at the vicinity of the droplet leading pole. The droplet internal recirculation can thus lead to a quasi-steady state process whereby the liquid in the droplets near-surface streamlines undergo a cycle during each circulation period. For an infinitely fast reactions complete depletion of dissolved species B should occur in the reaction layer. The small solid particles of species B are expected to enhance the absorption process by their slow dissolution, if they are small compared with the thickness of the reaction layer, λ.

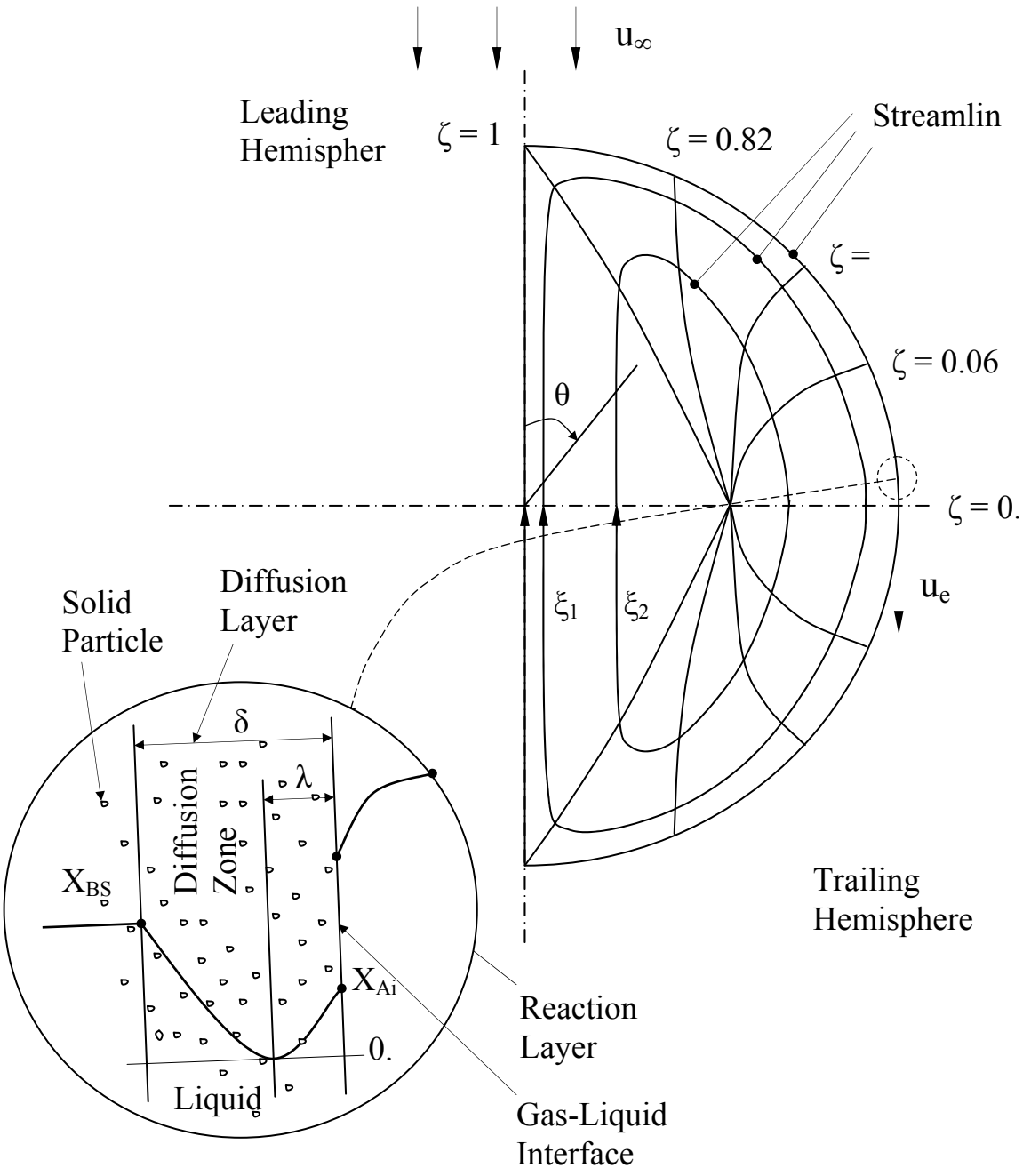

Figure 5.1: Schematic of the modeled system.

The following assumptions are made in accordance with the above discussion:

1. The slurry droplet is spherical and non-oscillating; with an internal circulation similar to Hill's vortex flow.

2. Each solid particle in the droplet slurry moves along the streamline of, and with the same velocity as, it's surrounding liquid.
3. The gas-side mass transfer resistance associated with the transfer of species A to the droplet is negligible in comparison with the liquid-side resistance.
4. The droplet interior is saturated with respect to dissolved species B.
5. The chemical reaction between A and B is either infinitely fast, or is second order.
6. The mass transfer process is quasi-steady.
7. The solid particles are spherical, and are made of pure species B.

Justification for assumption 1 has been provided in the aforementioned discussion. Assumption 2 is appropriate in view of the small size of the particles and the typically short droplet recirculation period that renders Brownian dispersion of particles negligible. Assumptions 3-5 are also all reasonable. The 6th assumption is also reasonable since the droplet recirculation period is of the order D/u_e, and is therefore much shorter than the order of magnitude of the characteristic time associated with a significant change in the slurry droplet's make-up. The last assumption is a simplifying idealization.

5.2 Mathematical Model

The mass conservation equation for species A and B, both sparingly can be written as:

$$\rho_L \vec{u}.\nabla x_A = \rho_L \nabla.(\mathsf{D}_A \nabla x_A) - k_{2A}\rho_L^2 x_A x_B \qquad (5.4)$$

$$\rho_L \vec{u}.\nabla x_B = \rho_L \nabla.(\mathsf{D}_B x_B) - k_{2B}\rho_L^2 x_A x_B + N_p \pi {d_p}^2 \rho_L K_s (x_{BS} - x_B) \tag{5.5}$$

where, due to the low solubility of either species in the liquid:

$$k_{2A} = k_2 / M_B \tag{5.6}$$

$$k_{2B} = k_2 / M_A \tag{5.7}$$

The micro particles undergo slow dissolution according to:

$$\rho_P \vec{u}.\nabla d_P = -2\,\rho_L K_s (x_{BS} - x_B) \tag{5.8}$$

The boundary conditions are as follows. At the droplet surfaces $(\nabla x_B).\vec{N} = 0$ and $x_A = x_{A,i}$; where $x_{A,i}$ represents the solubility of species A in the liquid corresponding to the system temperature and the partial pressure of A in the surrounding gas, and $\vec{N}$ represents a unit normal vector; $x_A = 0$ and $x_B = x_{BS}$ at the leading pole on the droplet surface; and $x_B = x_{BS}$ deep inside the droplet. Due to the very small size of particles, molecular diffusion is the primary mechanism for mass transfer between the solid particles and the liquid, therefore:

$$Sh_p = K_s d_p / D_B = 2 \tag{5.9}$$

The above equations can be normalized assuming that $\mathbf{D_A}$ and $\mathbf{D_B}$ are constants, using $u_r = \frac{2}{3}u_e$ as reference velocity, d_{p_o} as the reference particle diameter, and R as the reference length scale everywhere else, to get:

$$\vec{U}.\nabla^* X_A = 2Pe_A^{-1}\,\nabla^{*2} X_A - \Omega_A X_A X_B \tag{5.10}$$

$$\vec{U}.\nabla^* X_B = 2Pe_B^{-1}\,\nabla^{*2} X_B - \Omega_B X_A X_B + \Gamma(1 - X_B) \tag{5.11}$$

$$\vec{U}.\nabla^* d_p^* = -\beta(1 - X_B) \tag{5.12}$$

where:

$$X_A = x_A / x_{Ai} \tag{5.13}$$

$$X_B = x_B / x_{BS} \tag{5.14}$$

$$d_p^* = d_p / d_{p_o} \tag{5.15}$$

$$Pe_A = 2u_r R / \mathsf{D}_A \tag{5.16}$$

$$Pe_B = 2u_r R / \mathsf{D}_B \tag{5.17}$$

$$\Omega_A = \frac{\rho_L R\, k_2}{u_r M_B} x_{BS} \tag{5.18}$$

$$\Omega_B = \frac{\rho_L R\, k_2}{u_r M_A} x_{Ai} \tag{5.19}$$

$$\Gamma = \pi N_p R\, d_p^2 K_s / u_r \tag{5.20}$$

$$\beta = 2\rho_L\ R\ K_s x_{BS} / \left(\rho_p u_r d_{p_o}\right) \tag{5.21}$$

Surface-active contaminants can significantly reduce the droplet internal recirculation (Clift et al., 1978; Levich, 1962; Chang and Chung, 1985). In the absence of surface-active contaminants, however, the droplet surface velocity at its equator is related to the droplet's terminal velocity according to (see Eq. (5.3)):

$$u_e = u_{e,m} = \tfrac{2}{3} u_\infty \tag{5.22}$$

The aforementioned dimensionless equations are now cast in the (ξ,ζ,ϕ) coordinates, where $\xi = const$ represents a closed internal circulation streamline, and (Kronig and Brink, 1950; Ghiaasiaan and Eghbali, 1994):

$$\xi = 4\eta^2\left(1-\eta^2\right)\sin^2\theta \tag{5.23}$$

$$\zeta = \frac{\eta^4\cos^4\theta}{2\eta^2-1} \tag{5.24}$$

$$h_\xi = 8\eta\sin\theta\sqrt{\Delta} \tag{5.25}$$

$$h_\zeta = \frac{\left(2\eta^2-1\right)^2}{4\eta^3\cos^3\theta\sqrt{\Delta}} \tag{5.26}$$

$$h_\phi = \eta\sin\theta \tag{5.27}$$

$$\Delta = \left(1-\eta^2\right)^2\cos^2\theta + \left(2\eta^2-1\right)^2\sin^2\theta \tag{5.28}$$

$$\eta = r/R \tag{5.29}$$

It can also be shown that (Kronig and Brink, 1950):

$$\left(1-\eta^2\right)^2\left(2\eta^2-1\right)\zeta - \left[\eta^2\left(1-\eta^2\right) - \frac{1}{4}\xi\right]^2 = 0 \tag{5.30}$$

In writing the species conservation equations, symmetry with respect to ϕ is assumed. The species conservation equations can then be represented as:

$$U\frac{(\xi,\zeta)}{h_\zeta}\frac{\partial X_A}{\partial\zeta} = \left(\frac{1}{h_\xi h_\zeta h_\phi}\right)\frac{2}{Pe_A}\left[\frac{\partial}{\partial\xi}\left(\frac{h_\zeta h_\phi}{h_\xi}\frac{\partial X_A}{\partial\xi}\right) + \frac{\partial}{\partial\zeta}\left(\frac{h_\xi h_\phi}{h_\zeta}\frac{\partial X_A}{\partial\zeta}\right)\right] - \Omega_A X_A X_B \tag{5.31}$$

$$U\frac{(\xi,\zeta)}{h_\zeta}\frac{\partial X_B}{\partial \zeta}=\left(\frac{1}{h_\xi h_\zeta h_\phi}\right)\frac{2}{Pe_B}\left[\frac{\partial}{\partial \xi}\left(\frac{h_\zeta h_\phi}{h_\xi}\frac{\partial X_B}{\partial \xi}\right)+\frac{\partial}{\partial \zeta}\left(\frac{h_\xi h_\phi}{h_\zeta}\frac{\partial X_B}{\partial \zeta}\right)\right] \qquad (5.32)$$
$$-\Omega_B X_A X_B+\Gamma\left(1-X_B\right)$$

The particle mass conservation equation, furthermore, gives:

$$\frac{U(\xi,\zeta)}{h_\zeta}\frac{d\,d_p^*}{d\zeta}=-\beta\left(1-X_B\right) \qquad (5.33)$$

The dimensionless fluid velocity resulting from Eqs. (5.1) and (5.3) is (Clift et al., 1978):

$$U(\eta,\theta)=\frac{3}{2}\left\{\left(1-\eta^2\right)^2\cos^2\theta+\left(1-2\eta^2\right)^2\sin^2\theta\right\}^{\frac{1}{2}} \qquad (5.34)$$

The boundary conditions for Eqs. (5.31-5.33) are as follows: At $\zeta=1$, in the leading hemisphere (see Figure 5.1): $dp^*=1$, $X_A = 0$, and $X_B = 1$. At $\xi=0$, representing the droplet surface: $X_A = 1$, $\partial X_B/\partial\xi=0$. Deep inside the droplet, represented by $1\geq\xi\geq 0$: $X_A = 0$, and $X_B = 1$. Finally, at $\zeta=1$ in the trailing hemisphere, $\partial X_A/\partial\zeta=\partial X_B/\partial\zeta=0$ is assumed.

5.3 Numerical Solution Method

Equation (5.31-5.33) were numerically solved, using the finite-difference technique, in the pseudo-rectangle defined by $0\leq\xi\leq\xi_{\max}$, $0\leq\zeta\leq\zeta_{o,u}$ and $0\geq\zeta\leq\zeta_{o,l}$, where $\zeta_{o,u}=\left|\zeta_{o,l}\right|=0.95$ were assumed. The latter assumed values correspond to $1.6^\circ\leq\theta\leq 178.4^\circ$ on the droplet surface. Based on scoping calculations, $\xi_{\max}=0.5$ was used, and parametric calculations all indicated that the latter value for $\xi_{\max}$ was quite adequate. The computational domain is depicted in Figure (5.2). A non-uniform mesh size distribution was

used, and based on extensive convergence tests, the number of mesh points were 1000 for ξ and 1600 for ζ in all parametric calculations. Calculations showed that increasing the mesh numbers beyond the aforementioned values caused negligibly small changes in the results. An outline of the nodalization scheme and the numerical solution method is described next.

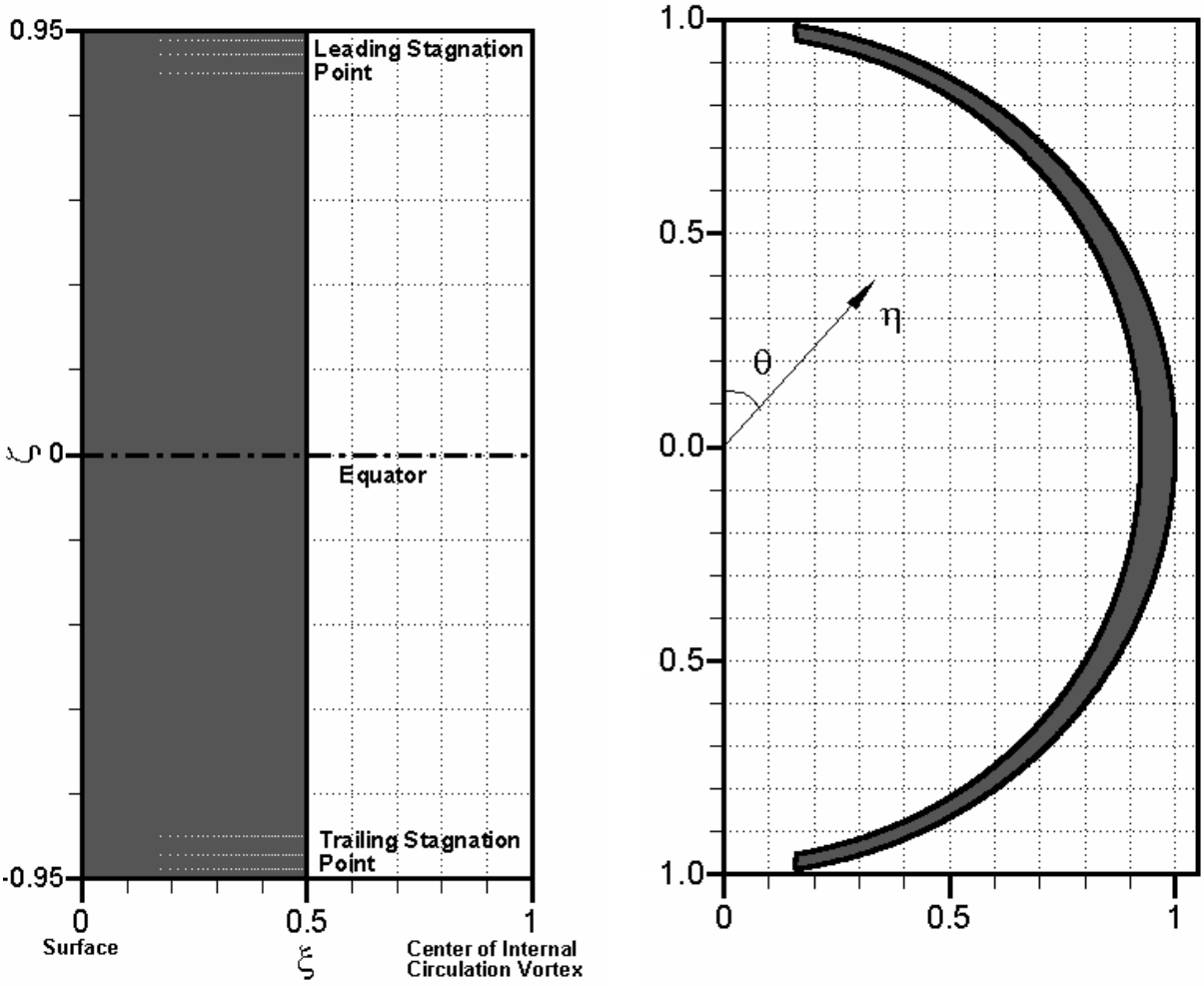

(a) (b)

Figure 5.2: Computation domain. a) transformed (in ξ, ζ) shape; b) actual shape.

5.4 Nodalization and Numerical Solution Technique

The computational domain was divided into different segments based the concentration profiles, and different mesh sizes were used in each segment. Along the ξ-

direction, two thin strips were defined near the droplet surface (typically defined according to $0. \le \xi < 0.04167$ and $0.04167 \le \xi < 0.1$, respectively), followed by a third region represented by $0.1 \le \xi < \xi_{max}$. Structured meshes were generated with uniform and very fine grids in the two strips near the droplet surface. Typically 450 nodes were used in the first (outermost) layer, and 470 nodes were used for the second layer. In the third thick region, where concentration gradients are small, non-uniform and gradually increasing grids toward the droplet interior were generated. Similarly, in the ζ-direction, the northern hemisphere was divided into three zones, with thinnest zone residing near the equator. Non-uniform in (ξ, ζ), but roughly uniform meshes in (η, θ) coordinate system, were generated in each of these regions, such that the equatorial region had the finest grids. The trailing hemisphere was the mirror image of the leading one. The zones were typically defined as follows. The first zone covered $0.95 = \zeta_{0,1} \le \zeta < 0.095$ and had 133 grids. The second zone covered $0.095 \le \zeta < 5.0 \times 10^{-6}$ and had 333 nodes. The third zone covered $5.0 \times 10^{-6} \le \zeta < 0_+$ and included 334 nodes. The singularity associated with the equator ($\zeta = 0$) was avoided by putting the first node point nearest to the equator at a very small distance from the equator (equal to 0.01 times the distance between the next two consecutive nodes). Very good numerical convergence was obtained by using a total of 1000 grids in the ξ direction, and 1600 grids (northern and southern hemispheres collectively) in the ζ direction.

The central-differencing technique was used, and the discretized equations were solved iteratively, using the Line Gauss-Seidel (LGS) method. For a structured grid, the coefficient matrix of the finite-difference equations is banded and special line-by-line iterative techniques such as LGS can be applied. LGS method involves solving the equations representing all the nodes on a sweep line simultaneously. The nodes on ξ=constant lines

represented the sweep line for us. The finite-difference equations for each sweep line formed a tri-diagonal matrix, and were solved via a standard Tri-Diagonal Matrix Algorithm (TDMA) solver. In the numerical solution, starting from the leading edge of the solution domain, and marching along ζ, the equations in the sweep direction (ξ) were simultaneously solved for each ζ=constant grid line, using values from the previous sweep for the downwind nodes, and values from the previous iteration for the upwind nodes, until the trailing edge of the solution domain was reached. The solution over the entire solution domain would then be repeated, and continued until convergence was achieved. The criterion for numerical convergence was a maximum change of 5×10^{-7} in the calculated concentrations. For the default case, convergence was achieved with 236 iterations, although for slower recirculation droplets it took more than 1000 iterations.

5.5 Absorption Rate and Transient Analysis

The total absorption rate for species A can be found from:

$$m_A^* = \frac{m_A}{x_{Ai}\rho_L D_{A,L}} = 2\pi \int_{\zeta_{o,u}}^{\zeta_{o,l}} \left(\frac{h_\zeta h_\phi}{h_\xi} \frac{\partial X_A}{\partial \xi} \right)_{\xi=0} d\zeta \tag{5.35}$$

where $\zeta_{o,u}$ and $\zeta_{o,l}$ represent the extreme values of ζ at upper and lower hemispheres of the droplet, representing the leading and trailing poles.

The size characteristics of solid particles in the slurry droplet vary with time, affecting the reaction process rate (Mehra, 1996). A rigorous transient analysis would therefore need to consider the temporal variation of the particle size distribution by solving the particle population balance equation, coupled with the droplet internal circulation. Such

an analysis is difficult, however, and only a simplified model is proposed here based on the following additional assumptions:

1. The particles are well mixed in the droplet core, and can be represented by an effective average diameter that varies with time.
2. The characteristic droplet recirculation period, u_∞ / R, is much shorter than the characteristic time associated with a significant change in the average solid particle size in the droplet.

It can then be shown that:

$$\frac{d}{dt} d_p^3 = -\frac{36\, z\, M_B}{\pi^2 \rho_p N_p D^3 M_A} m_A \tag{5.36}$$

where m_A is the total absorption rate for species *A*, as predicted by the quasi-steady model described earlier.

Equation (5.36) is numerically integrated using Euler's method, over time steps that are larger than the droplet characteristic recirculation period.

The performance of gas absorbers is often presented in terms of an enhancement factor, ϕ_A, defined as the ratio of the absorption rate of the absorbed species (species *A* in our case), and the absorption rate when chemical reaction are absent (Bird et al., 2002). The influence of the solid particles on the reaction rate, furthermore, can be better understood in terms of ϕ_R, the ratio between enhancement factors, with and without particles.

5.6 Results and Discussion

5.6.1 Properties and Default Parameters

For parametric calculations the standard thermophysical and transport property values for $CO_2 - Ca(OH)_2$, proposed and used by Mehra (1996), were applied. Accordingly, for all (default) parametric calculations $C_{Ai} = 3 \times 10^{-2} kmol/m^3$ and $C_{BS} = 9 \times 10^{-2} kmol/m^3$ were assumed, leading to $X_{Ai} = 1.32 \times 10^{-3}$ and $X_{BS} = 4.44 \times 10^{-3}$. Other default parameters were: $D_{A,L} = D_{B,L} = 2 \times 10^{-9} m^2/s$; $k_2 = 1 \times 10^8 m^3/kmol - s$; and $\rho_p = 1.5 \times 10^3 kg/m^3$. For the liquid, water properties at 300 K were used. The terminal velocity of the spray droplet was calculated using the correlation of Lapple (Clift et al., 1978) for drag coefficient:

$$u_\infty = \left[\frac{4D(\rho_L - \rho_G)g}{3C_D \rho_G} \right]^{\frac{1}{2}} \tag{5.37}$$

$$C_D = \frac{24}{\mathrm{Re}_G} \left[1 + 0.125 \, \mathrm{Re}_G^{0.72} \right] \tag{5.38}$$

where $\mathrm{Re_G} = \mathrm{u_\infty D}/\nu_\mathrm{G}$. Instantaneous (infinitely fast) reactions are simulated by using $k_2 = 10^{13}$ *m³/kmol-s.*

5.6.2 Mass Transfer Enhancement Mechanism

The results depicted in this section are meant to elucidate the mechanisms responsible for the enhancement of gas absorption in slurry droplet by the reactant micro particles.

For a contaminant-free droplet unimpeded internal circulation would lead to Eq. (5.22). Significantly reduced droplet internal circulation may be expected in FGD systems, however, and will be considered in the forthcoming parametric calculations. The effect of the solid reactant particles, furthermore, will be addressed by parametrically varying w, the initial volume fraction of particles in the slurry droplet.

Concentration profiles for a droplet 1 mm in diameter, in free fall in gas, and with internal circulation ten times slower than that for a surface active-contaminant free droplet ($u_e = \frac{1}{10} u_{e,m}$), are displayed in Figure 5.3, where a second-order chemical reaction has been assumed. The depicted concentration profiles in represent the radial variations of the normalized mass fractions of species A and B at azimuthal angles θ = 45°, 90°, 135°, and 178.4° , respectively (see Figure 5.1). These figures also show the effect of the volume fraction of the solid particles (w) on the concentration profiles. The solid particles were assumed to be 2 μm in diameter initially, and uniformly distributed in the liquid. The development of the reaction layer (defined as the zone where $X_A > 0$), and the diffusion layer (defined as the zone where $X_B < 1$) along the droplet surface, and the influence of the reactant solid particles on them, can be readily noticed. Due to the finite reaction rate, the two reacting species coexist virtually in the entire reaction layer thickness. The development of the reaction and diffusion layers is complicated due to the recirculation velocity. In the droplet leading hemisphere, down to the droplet equator, these layers both grow in thickness as a result of the diffusion process, and more importantly due to the favorable circulation velocity effect which tends to expand the streamlines (Figures 5.3(a,b)). An opposite trend is observed in the droplet southern hemisphere, however (Figures 5.3(c,d)). These opposing circulation velocity effects are due to the fact that the

lateral distance between specific circulation streamline pairs increases as the equator is approached, and the opposite occurs when the fluid moves away from the equator in the trailing hemisphere.

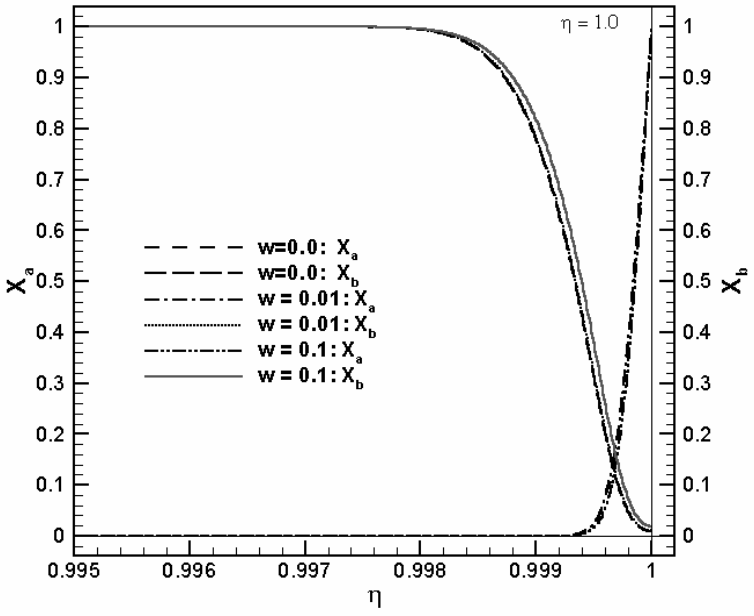

(a)

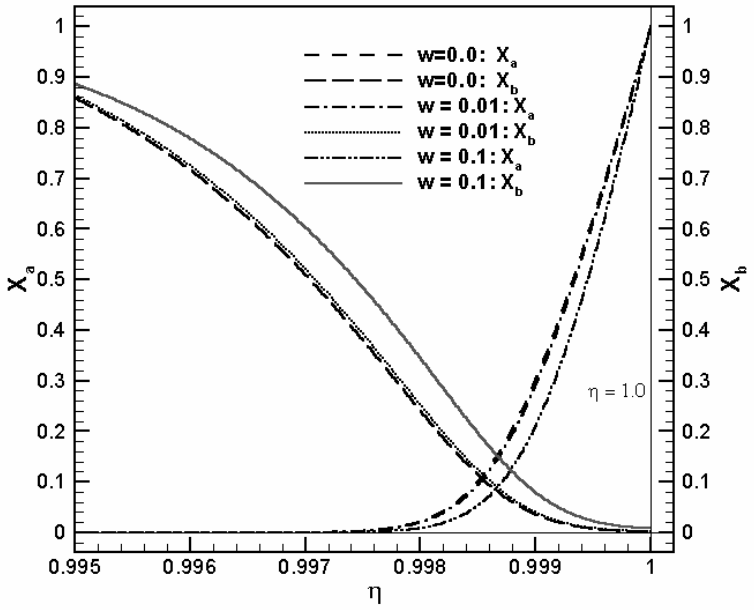

(b)

Figure 5.3: Effect of solid particles on concentration profiles for the second-order reaction, with droplet recirculation ten times slower than that for an unimpeded recirculation: a) 45º, b) 90º, c) 135º, and d) 178.4º.

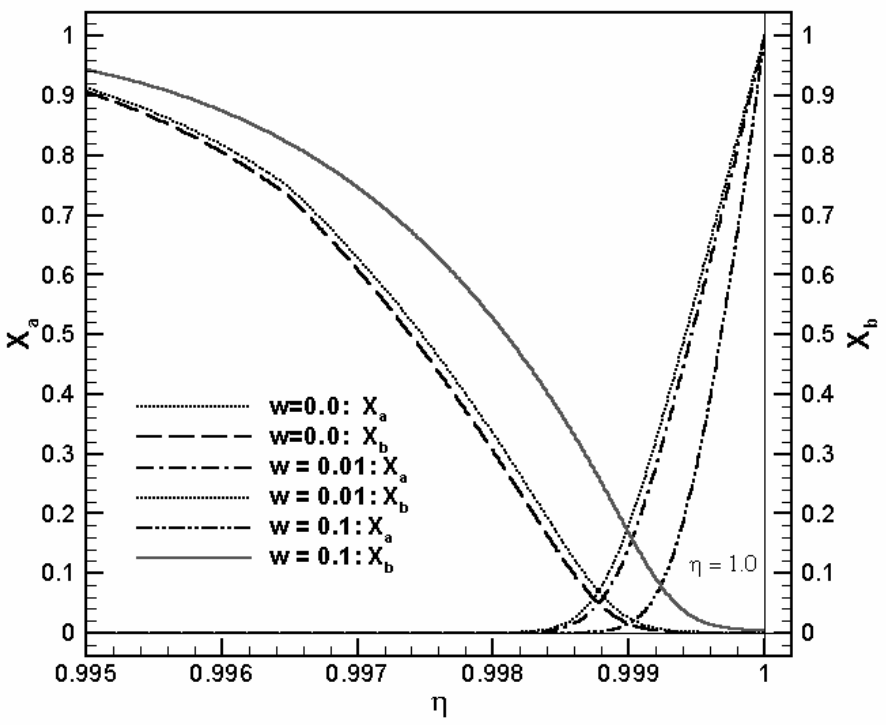

(c)

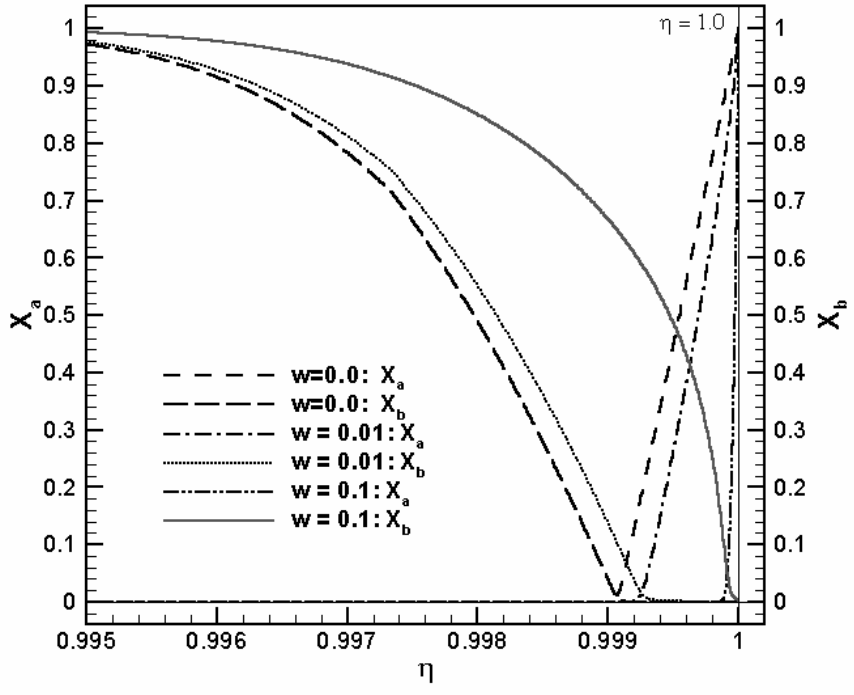

(d)

Figure 5.3: Effect of solid particles on concentration profiles for the second-order reaction, with droplet recirculation ten times slower than that for an unimpeded recirculation: a) 45º, b) 90º, c) 135º, and d) 178.4º. (Continued.)

The influence of particles is easily discernible in Figures 5.3(a-d). The presence of solid particles evidently does not cause a significant qualitative effect in the shapes of the concentration profiles. The particles, however, tend to reduce the thickness of both reaction and diffusion layers, leading to a steeper concentration gradient species A, and hence an enhanced absorption rate. This effect of the particles on the species A concentration gradient grows in strength along the streamlines, and is particularly significant near the droplet trailing pole.

Concentration profiles, and the effect of the solid particle volume fraction on them, are depicted in Figures 5.4(a-d) for an instantaneous chemical reaction ($k_2 = \infty$). The instantaneous chemical reaction renders the profiles qualitatively different than those depicted in Figures 5.3(a-d). With $k_2 \to \infty$, the concentrations of both species vanish at the edge of the reaction layer, as expected; the reaction layer is everywhere significantly thinner than the reaction layer with finite k_2; and hence significantly higher concentration gradients of species A occur everywhere. The influence of the solid particles on the concentration profiles and the reaction layer is similar to those described for Figures 5.3(a-d), however, and higher volume fractions of the solid particle lead to thinner reaction layer, and higher species A concentration beneath the droplet surface.

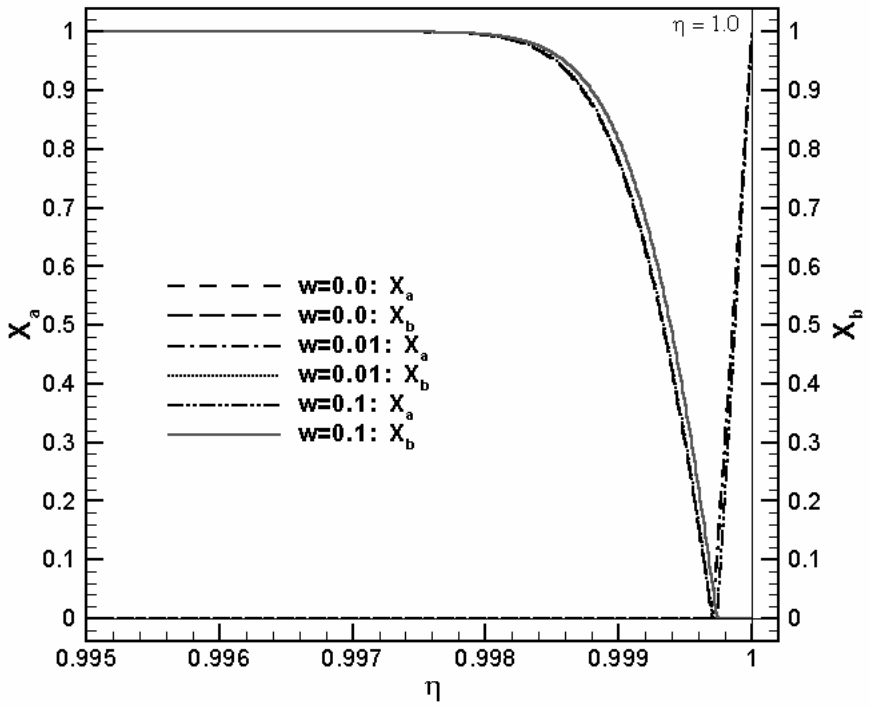

(a)

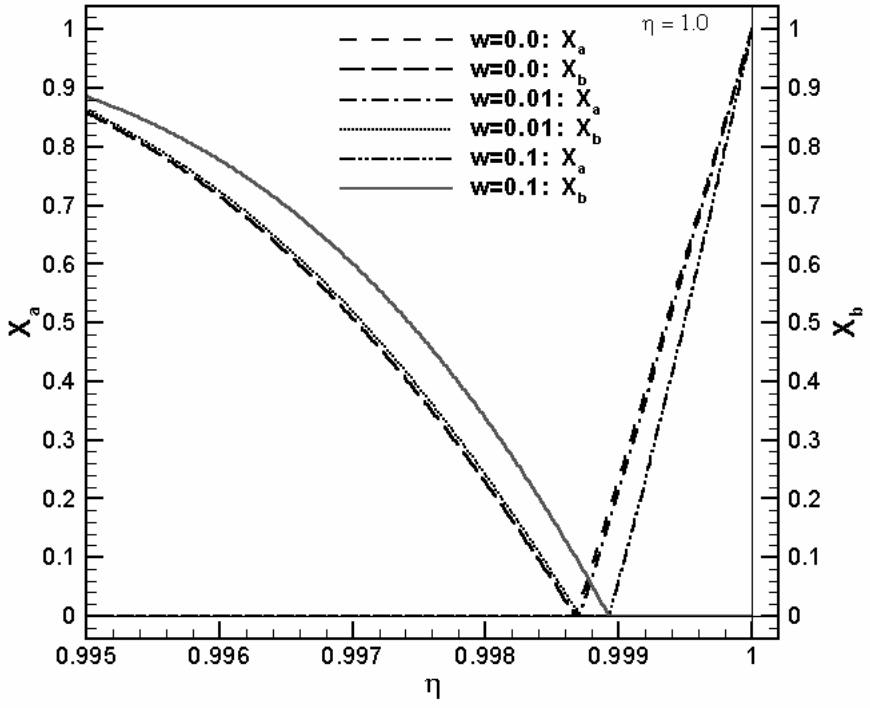

(b)

Figure 5.4: Effect of solid particles on concentration profiles for an instantaneous reaction, with droplet recirculation ten times slower than that for an unimpeded recirculation: a) 45º, b) 90º, c) 135º, and d) 178.4º.

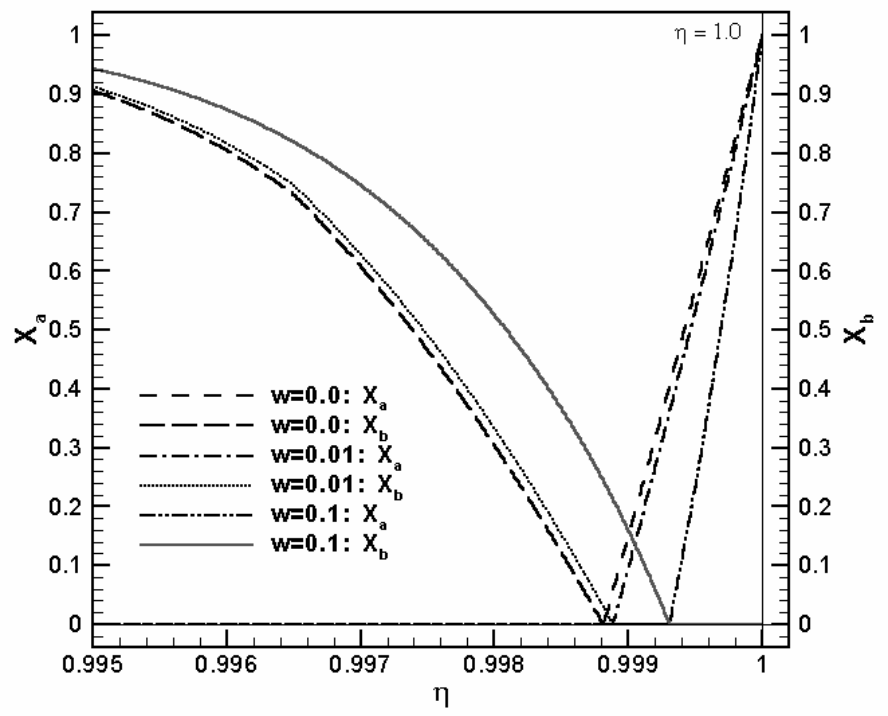

(c)

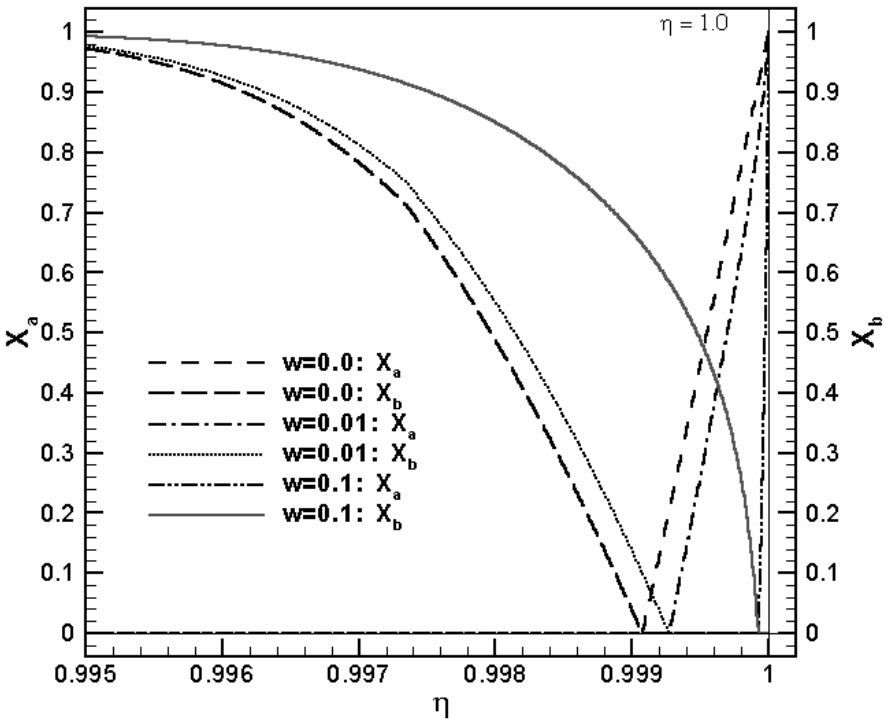

(d)

Figure 5.4: Effect of solid particles on concentration profiles for an instantaneous reaction, with droplet recirculation ten times slower than that for an unimpeded recirculation: a) 45º, b) 90º, c) 135º, and d) 178.4º. (Continued.)

The enhancing influence of particles on the absorption rate depends on the duration of the exposure time of the liquid surface to the gas. A shorter exposure duration would lead to smaller enhancement effect of the solid particles, and for extremely short exposure times the effect of solid particles will be negligible (Bjerle et al., 1972). Smaller effects of solid particles on the concentration profiles should thus be expected as stronger droplet internal circulations are considered. Figures 5.5 and 5.6 are similar to Figures 5.3 and 5.4, respectively, with the difference that the droplet internal circulation in the simulations represented by Figures 5.5 and 5.6 is assumed to be unimpeded, whereby $u_e = u_{e,m} = \frac{3}{2} u_\infty$. Curves representing w = 0.01 are not displayed in the latter figures since they are virtually indistinguishable from the curves representing w = 0.1. The concentration profiles are of course everywhere steeper in these figures than their counterparts representing lower droplet recirculation, evidently as a result of shorter exposure times in the former. The effect of the reactant solid particles on the concentration profiles and the reaction layer thickness, although qualitatively similar to those discussed earlier (i.e., thinner reaction layers and steeper transferred species concentration profiles due to solid particles), are small, indicating that relatively insignificant absorption enhancement can be achieved by adding solid particles to droplets with fast, unimpeded internal circulation.

The dissolution of particles evidently leads to their shrinkage. Mehra (1996) has showed that, for a droplet with no internal circulation, the solid particle size change is important. Typical model-predicted particle size variations are depicted in Figure 5.7, where the variations of d_p / d_{p_o} along the streamlines are shown, with d_{p_o} representing the particle average diameter as it emerges to the droplet surface near its leading pole. These results

indicate trends consistent with the concentration profiles discussed earlier. The variations in particle diameter in a single recirculation period are evidently very small, however.

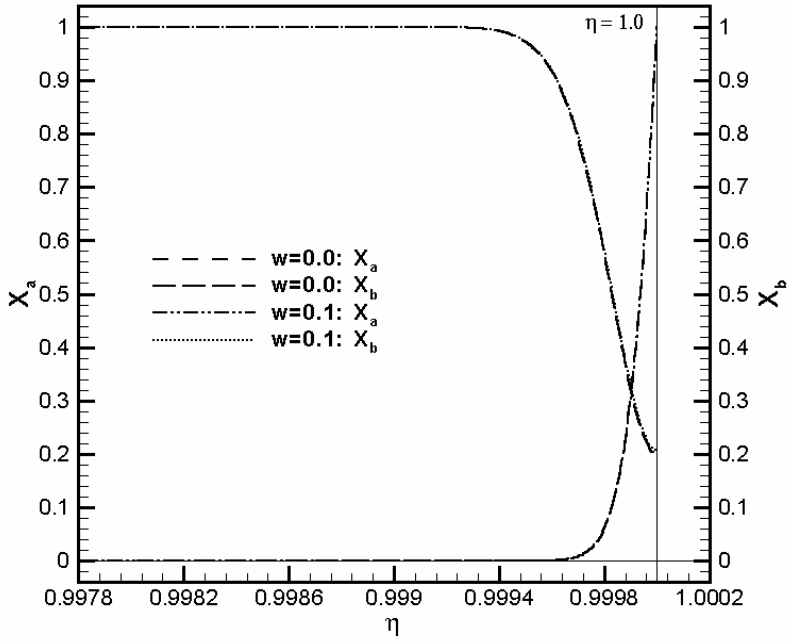

(a)

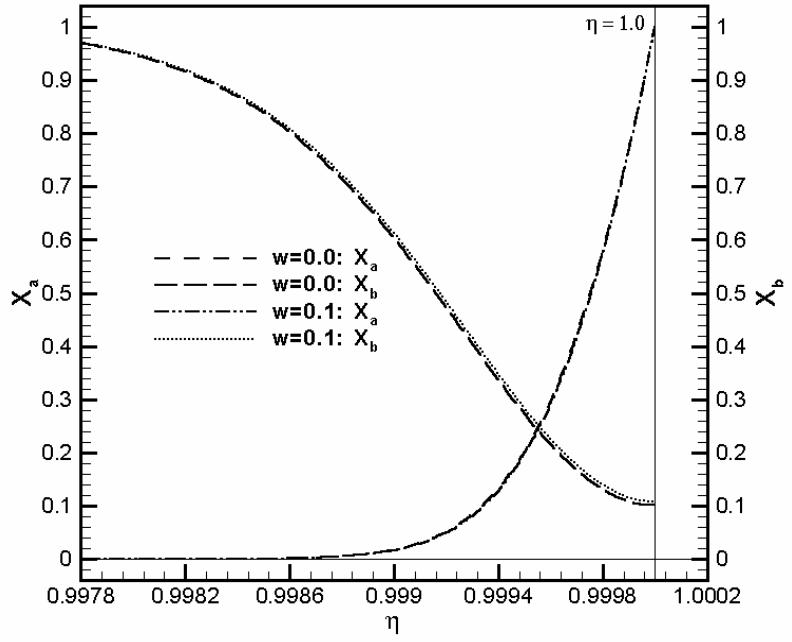

(b)

Figure 5.5: Effect of solid particles on concentration profiles for the second-order reaction, with unimpeded droplet recirculation: a) 45º, b) 90º, c) 135º, and d) 178.4º.

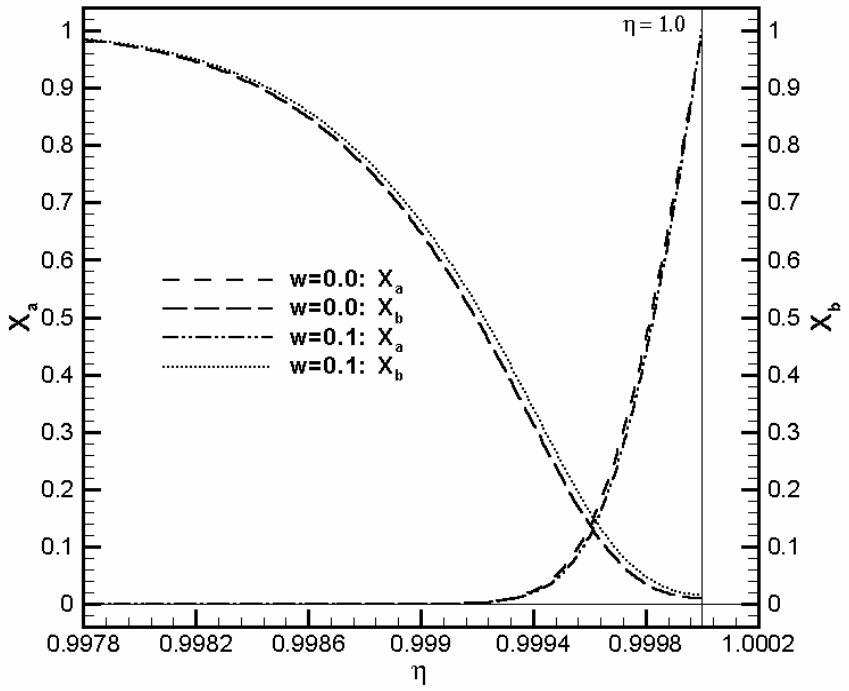

(c)

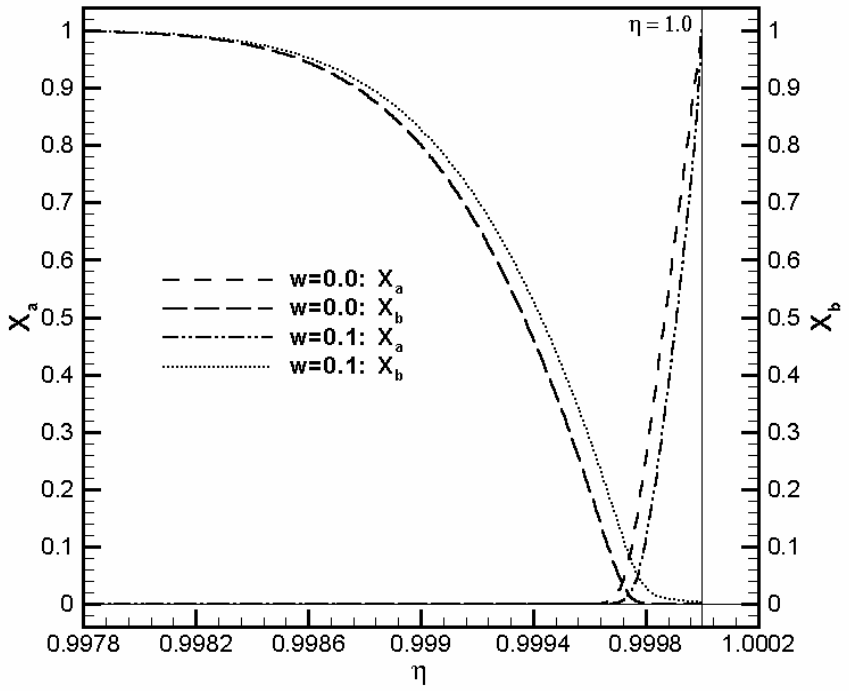

(d)

Figure 5.5: Effect of solid particles on concentration profiles for the second-order reaction, with unimpeded droplet recirculation: a) 45º, b) 90º, c) 135º, and d) 178.4º. (Continued.)

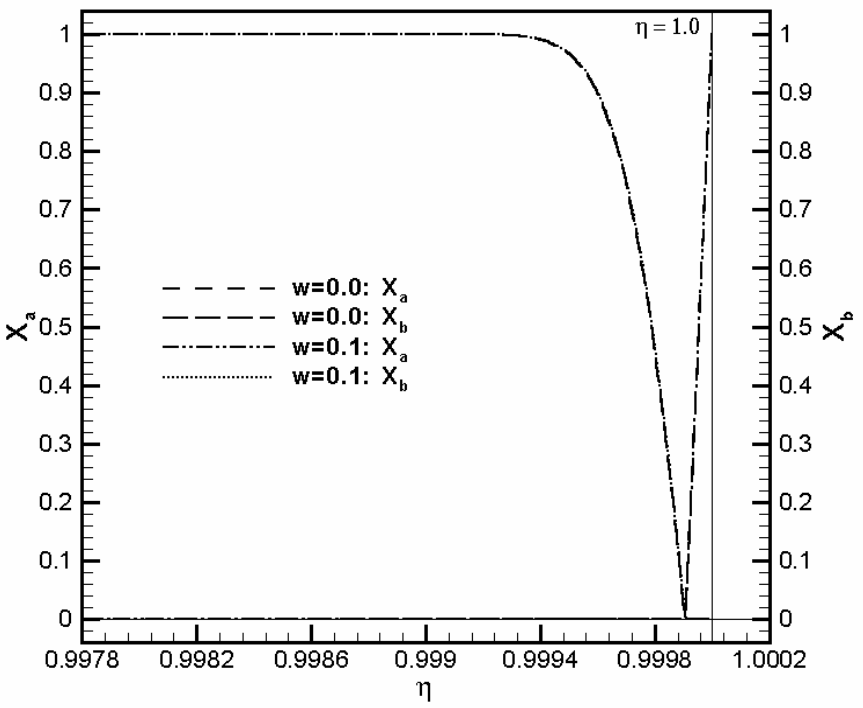

(a)

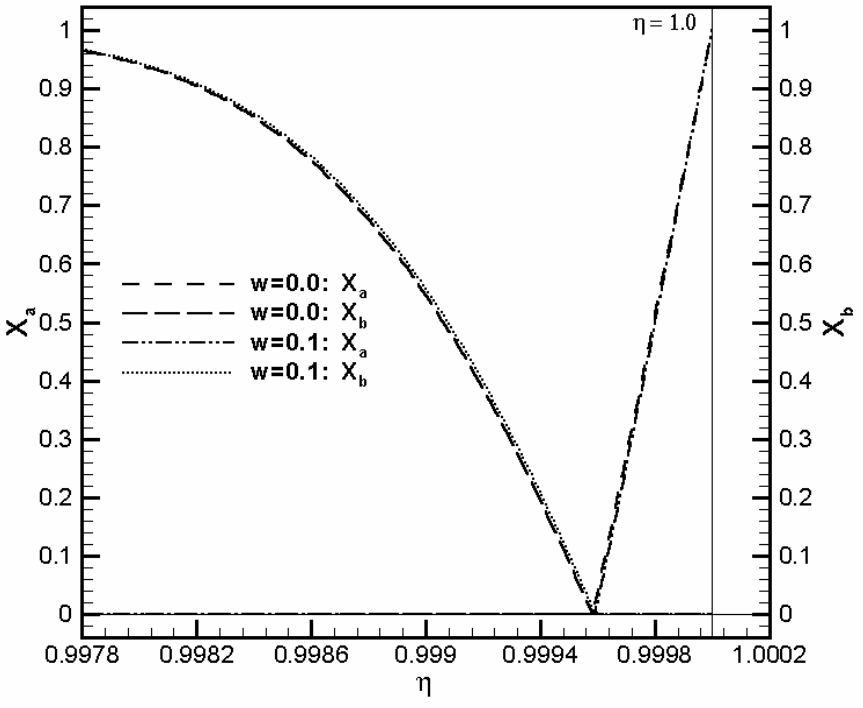

(b)

Figure 5.6: Effect of solid particles on concentration profiles for an instantaneous reaction with unimpeded droplet recirculation: a) 45º, b) 90º, c) 135º, and d) 178.4º.

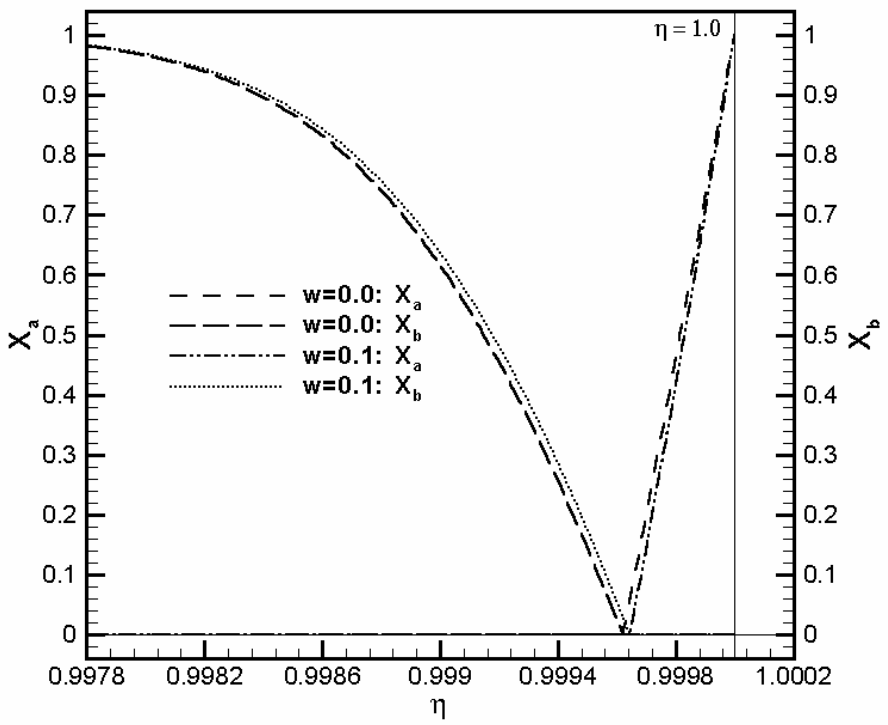

(c)

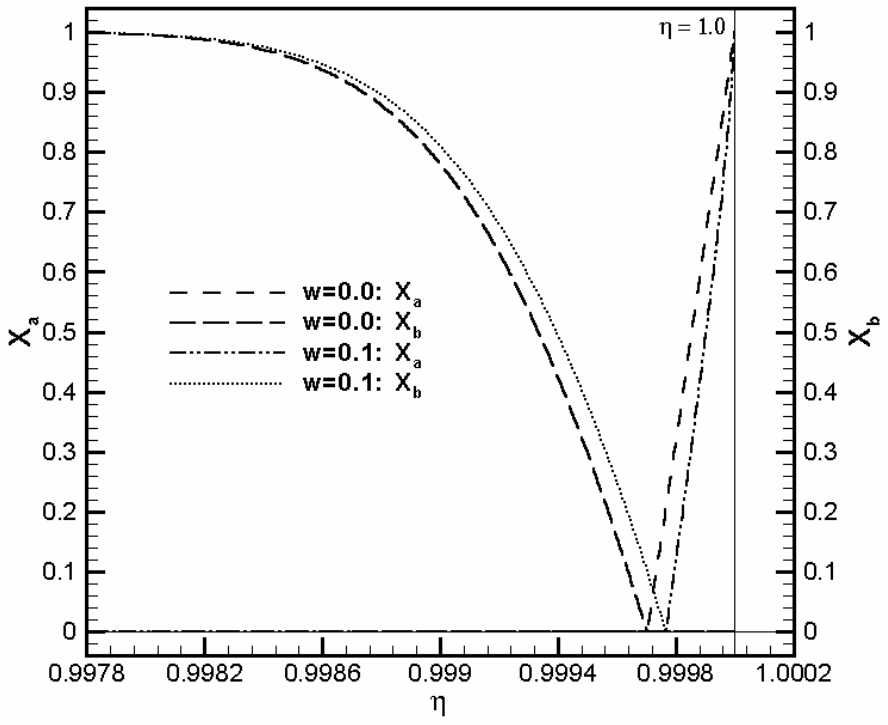

(d)

Figure 5.6: Effect of solid particles on concentration profiles for an instantaneous reaction with unimpeded droplet recirculation: a) 45º, b) 90º, c) 135º, and d) 178.4º. (Continued.)

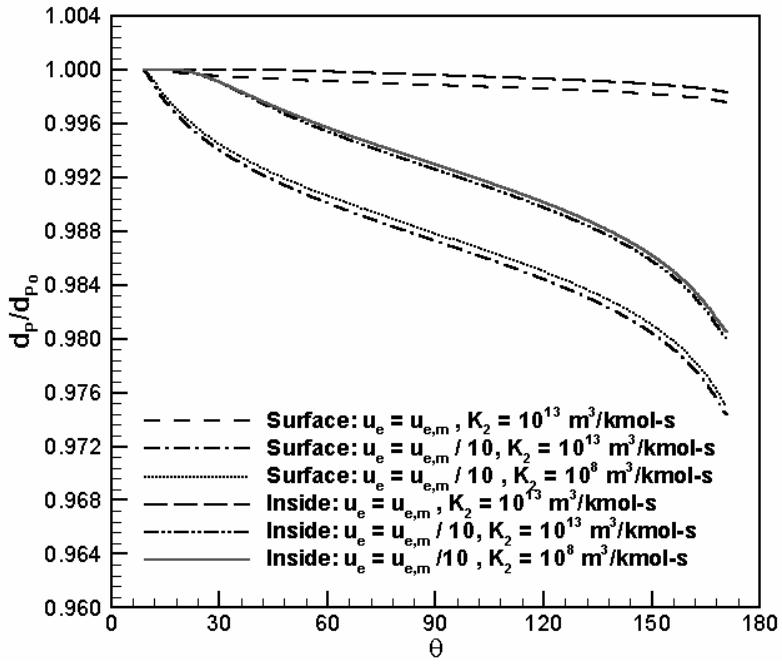

Figure 5.7: Some calculated solid particle size variations over a single droplet recirculation. The curves designated as inside represent the streamline with $\xi = 2.69\times10^{-3}$.

Using the numerical models described in this study, extensive parametric calculations have been performed that examine the effect of various parameters, as well as particle size variations, on droplet absorption rates.

5.6.3 Parametric Effects

Some calculation results showing the effects of various parameters on the absorption process are described in this section.

Typical concentration profiles, calculated for a slurry droplet 1 mm in diameter, in free fall in gas, and with internal circulation four times slower than that for a droplet with unimpeded internal circulation (f_u = 0.25) are shown in Figure 5.8. The concentration profiles correspond to the equator of the simulated droplet, and depict the effects of the

volume fraction of the solid particles, and the reaction rate constant (second-order vs. instantaneous reaction kinetics). The solid particles emerging from the droplet core neat the droplet's frontal pole were assumed to be 2 μm in diameter in these simulations. These and other parametrically calculated concentration profiles (Akbar et al., 2003) confirm that the solid particles tend to reduce the thickness of the reaction layer (where $X_A > 0$) and the concentration layer (where $X_B < 1$), leading to a steeper concentration gradient for species A (Uchida et al., 1975, 1981). The extent of the effect of particles, however, depends on various parameters, most importantly the internal circulation period and the reaction kinetics, as discussed below. The calculated variations of λ/R (or λ^*) and δ/R (or δ^*) along the droplet surface are displayed in Figures 5.9, 5.10 and 5.11, where λ, the thickness of the reaction layer, is defined as the zone where $X_A \geq 0.001$; and δ, the thickness of the diffusion layer, represents the zone where $X_B \leq 0.999$. These figures show that the development of both the reaction and diffusion layers is complicated due to the droplet internal circulation. The development of the two layers starts near the leading pole, and the two layers grow in thickness up to the equator. This growth is due to the combined effects of diffusion and the favorable internal circulation velocity, which tends to expand the streamlines (see Figure 5.2). An opposite trend occurs in the droplet trailing hemisphere, however, where, as the trailing pole is approached, the streamlines tend to contract.

Figure 5.9 shows the influence of reaction kinetics and droplet internal circulation on the development of the reaction layer, while Figure 5.10 shows similar effects for the diffusion layer. Calculated results for no chemical reaction (i.e., simple diffusion of species A into the droplet) are also shown in Figure 5.9(a) for comparison. The diffusion layer thickness, and hence the mass transfer resistance, are evidently very sensitive to both. Faster

internal circulation (i.e., larger f_u) implies shorter liquid exposure to gas at droplet's surface during each recirculation period, hence thinner reaction and diffusion layers. Furthermore, faster reaction kinetics evidently leads to a faster consumption of species *A*, leading to a thinner layer.

The effects of the solid particle volume fraction, *w*, on the reaction and diffusion layer thickness are depicted in Figures 5.11 and 5.12, respectively. Parametric calculation results are shown for assumed $f_u = 0.25$ only, for brevity. The predicted relative influence of the particles evidently depends strongly on the reaction kinetics.

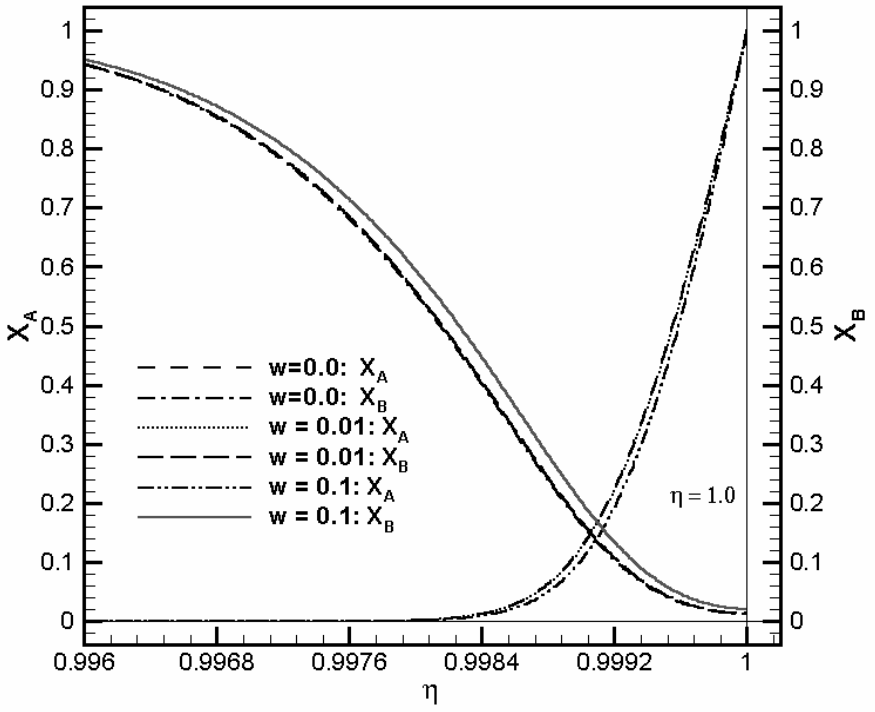

(a)

Figure 5.8: Effect of solid particles on concentration profiles at the equator of a droplet (R = 0.5 mm, d_p = 2 μm, f_u = 0.25): a) second-order kinetics; b) instantaneous reaction.

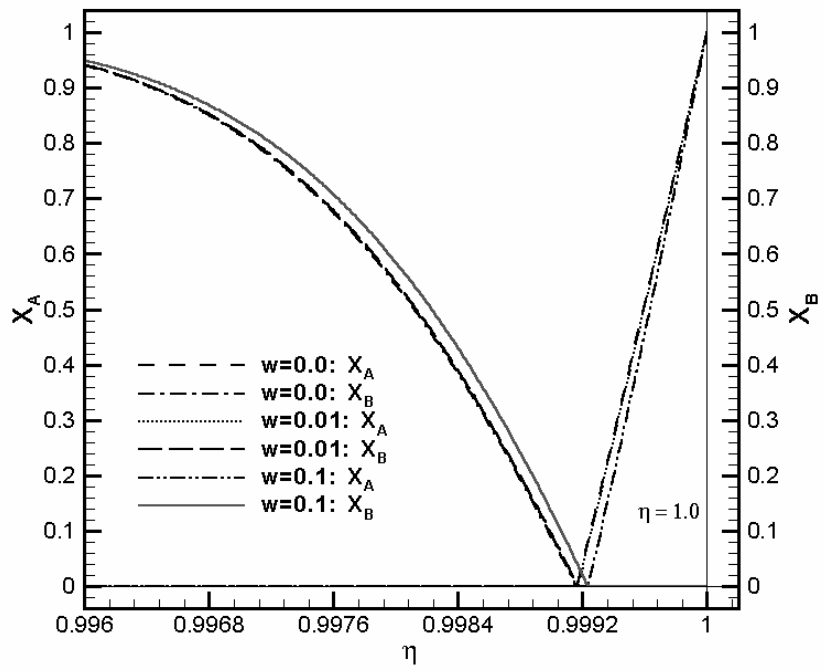

(b)

Figure 5.8: Effect of solid particles on concentration profiles at the equator of a droplet (R = 0.5 mm, d_p = 2 μm, f_u = 0.25): a) second-order kinetics; b) instantaneous reaction. (Continued.)

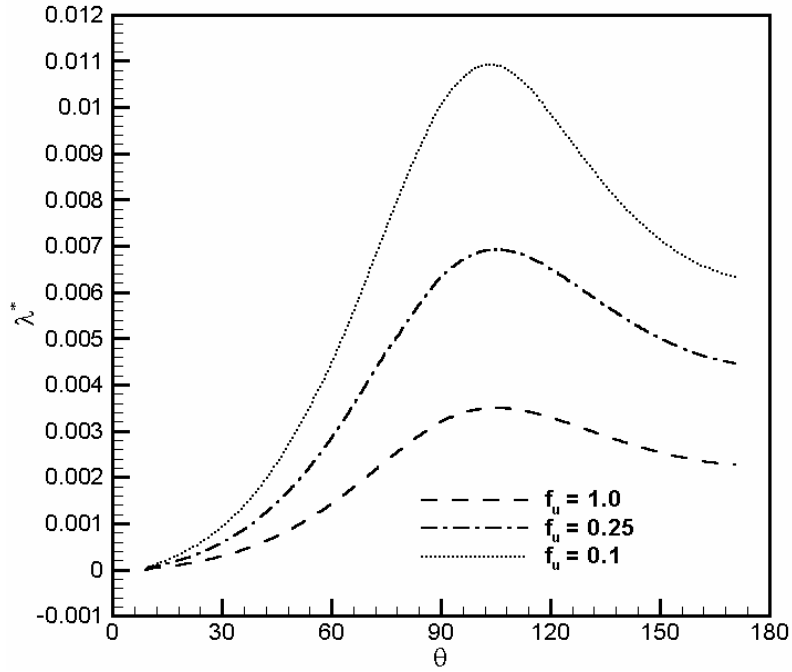

(a)

Figure 5.9: Effects of droplet internal circulation and reaction kinetics on the reaction layer thickness (R = 0.5 mm, d_p = 2 μm): a) no reaction; b) second-order reaction; c) instantaneous reaction.

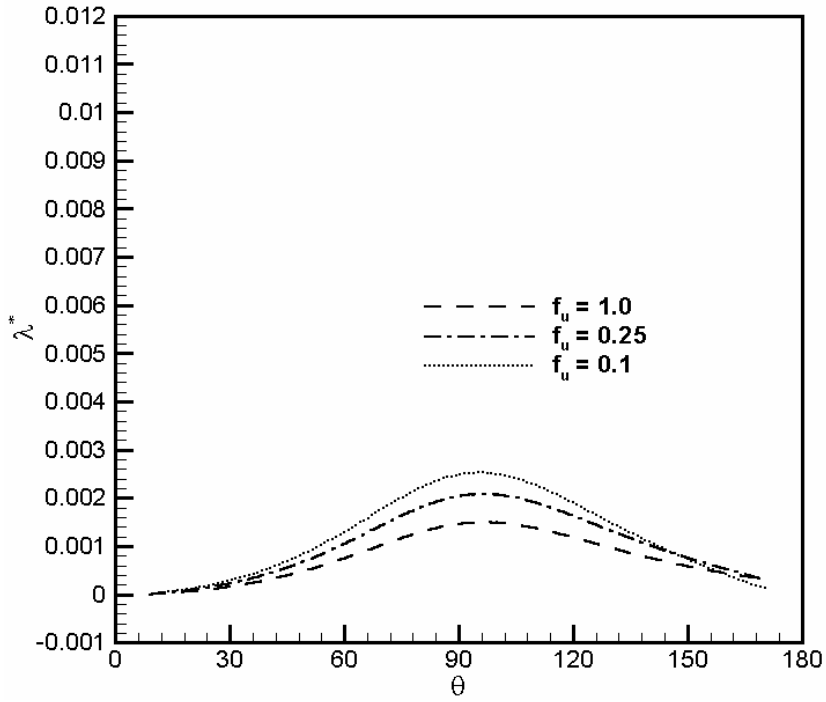

(b)

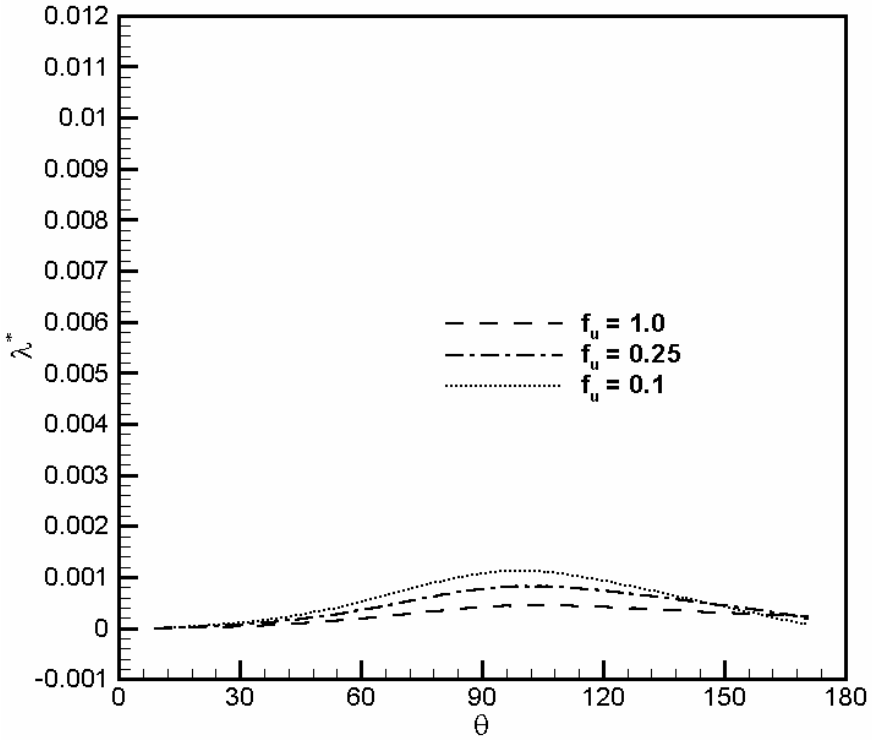

(c)

Figure 5.9: Effects of droplet internal circulation and reaction kinetics on the reaction layer thickness (R = 0.5 mm, d_p = 2 μm): a) no reaction; b) second-order reaction; c) instantaneous reaction. (Continued.)

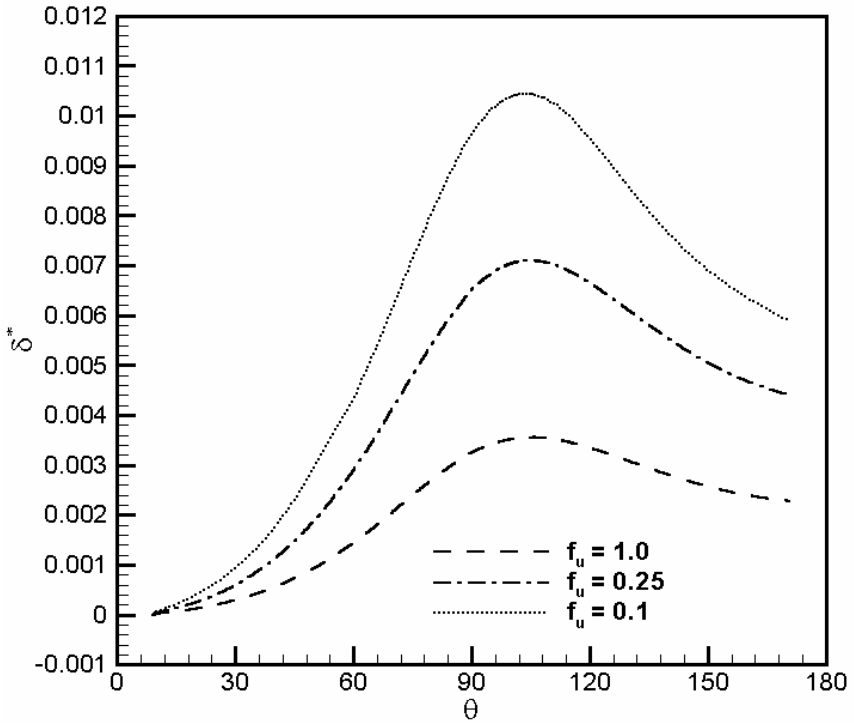

(a)

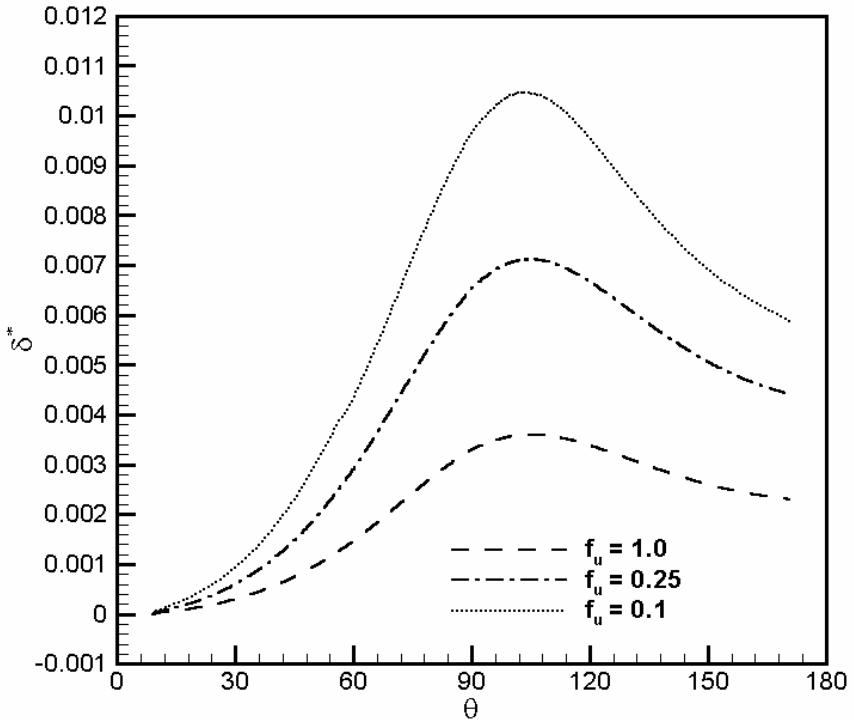

(b)

Figure 5.10: Effects of droplet internal circulation and reaction kinetics on the diffusion layer thickness (R = 0.5 mm, d_p = 2 μm): a) second-order reaction; b) instantaneous reaction.

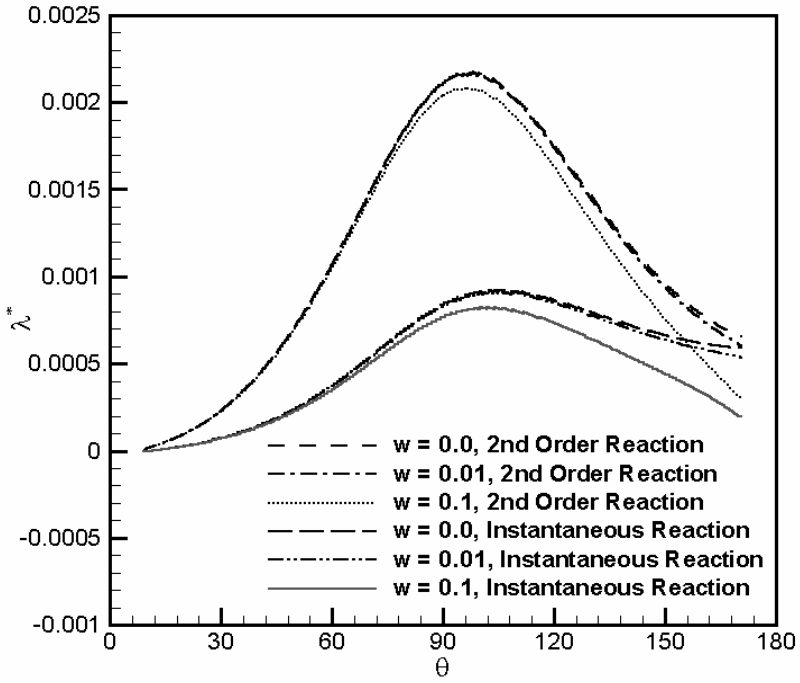

Figure 5.11: Effect of solid particle total volume fraction on the reaction layer thickness (R = 0.5 mm, d_p = 2 μm, f_u = 0.25).

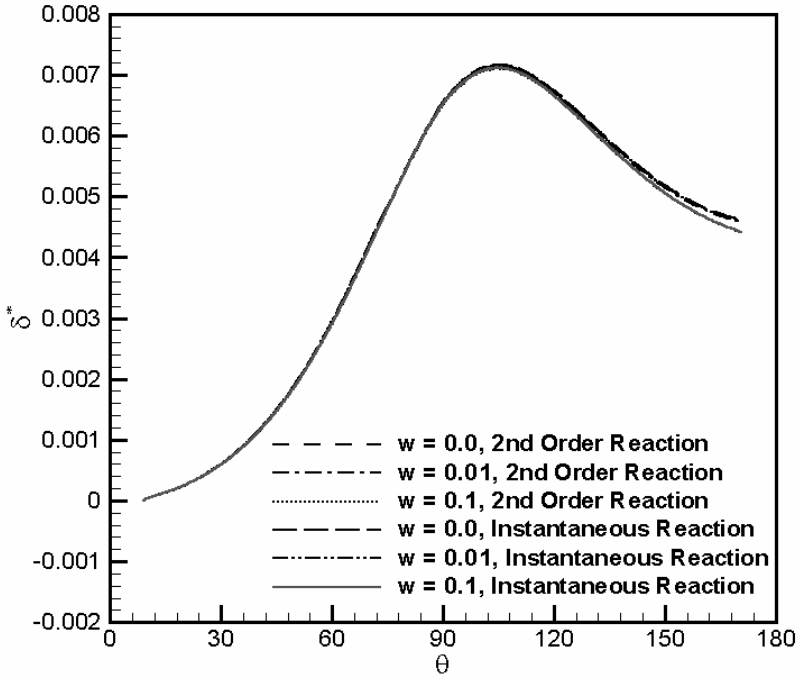

Figure 5.12: Effect of solid particle total volume fraction on the diffusion layer thickness (R = 0.5 mm, d_p = 2 μm, f_u = 0.25).

5.6.4 Absorption Rates and Transient Analyses

As noted in Section 5.5, the quasi-steady droplet mass transfer and reaction models described in Section 5.2 were utilized for the development of a transient model that accounts for the effect of time variation of average solid particle diameter on the droplet absorption rates. Some illustrative parametric results showing the absorption rates, and illustrative results obtained with the transient model are described in this section.

A summary of parametric calculations is provided in Table 5.1, where the dependence of dimensionless total mass absorption rate, m_A^*, on several parameters is depicted. Included among the calculated results is the enhancement factor, ϕ_R. The total dimensionless absorption rate, as predicted by the model of Ramachandran and Sharma (1969) is also provided in the table for comparison. According to the model of Ramachandran and Sharma (1969), for the reaction of Eq. (1.1), assuming an instantaneous reaction, and very fine solid particles.

$$m_A^* = \left(\frac{2\pi D M_A}{x_{Ai} D_{A,L} M_L z} \right) Y_{BS} \sqrt{D_{B,L} K_s A_p} \coth\left(\sqrt{\frac{K_s A_p}{D_{B,L}}} \delta \right) \tag{5.39}$$

where $\delta = 2\times10^{-5}$ m, and $A_p = N_p \pi d_p^2$ represents the total particle surface area concentration. Ramachandran and Sharma (1969) also proposed a model for instantaneous reaction with finite solid particle diameter, and developed an approximate model for a second-order reaction. These latter models require knowing λ or k_L, however, which were quantified rather arbitrarily. Therefore, they will not be used for comparison here. Significantly higher absorption rates are predicted by the present model in comparison with Ramachandran and Sharma (1969), evidently as a result of droplet internal circulation; the predictions of the two

models approach only when strong suppression of internal circulation (f_u <<1) is assumed in the present model.

Table 5.1: Summary of Some Parametric Calculations

R (mm)	f_u	k_2 (m^3/kmol-s)	d_p (μm)	w	m_A^*	m_A^* [1]	ϕ_R
0.50	1.00	1×10^8	5.00	0.10	28069.00	2754.01	1.00429
0.50	1.00	1×10^8	10.00	0.10	27979.00	1411.44	1.00107
0.50	1.00	1×10^8	10.00	0.01	27952.00	725.77	1.00011
1.00	1.00	1×10^8	5.00	0.10	52614.00	5508.03	1.00483
0.50	1.00	0	2.00	0.10	9772.00	6882.88	1.00041
0.50	1.00	1×10^8	2.00	0.10	28698.00	6882.88	1.02680
0.50	1.00	1×10^{13}	2.00	0.10	30329.00	6882.88	1.03501
0.50	0.25	0	2.00	0.10	4891.00	6882.88	1.00000
0.50	0.25	1×10^8	2.00	0.10	16442.00	6882.88	1.12794
0.50	0.25	1×10^{13}	2.00	0.10	16719.00	6882.88	1.13944
0.50	0.10	0	2.00	0.10	3097.00	6882.88	1.00000
0.50	0.10	1×10^8	2.00	0.10	12284.00	6882.88	1.32371
0.50	0.10	1×10^{13}	2.00	0.10	12431.00	6882.88	1.33796
0.50	1.00	0	2.00	0.01	9768.00	2180.83	1.00000
0.50	1.00	1×10^8	2.00	0.01	28024.00	2180.83	1.00268
0.50	1.00	1×10^{13}	2.00	0.01	29407.00	2180.83	1.00355
0.50	0.25	0	2.00	0.01	4891.00	2180.83	1.00000
0.50	0.25	1×10^8	2.00	0.01	14770.00	2180.83	1.01324
0.50	0.25	1×10^{13}	2.00	0.01	14881.00	2180.83	1.01418
0.50	0.10	0	2.00	0.01	3097.00	2180.83	1.00000
0.50	0.10	1×10^8	2.00	0.01	9598.00	2180.83	1.03427
0.50	0.10	1×10^{13}	2.00	0.01	9620.00	2180.83	1.03541

[1] According to Ramachandran and Sharma (1969).

These parametric calculations indicate that, as intuition would suggest, the total absorption rate monotonically increases with increasing the droplet internal recirculation, increasing total particle volume fraction w, decreasing particle diameter (at the same total particle mass concentration), d_p, and increasing the reaction kinetic speed (represented by k_2). Furthermore, although the droplet total absorption rate increases when droplet diameter is increased, doubling the droplet diameter only results in an approximate doubling of m_A^* and an approximate four-fold increase in m_A; the absorption rate per unit mass of slurry increases as droplet size is decreased. Among these, f_u has the most dramatic effect on m_A^*. The calculated values of m_A^* are also significantly larger than the predictions of the model of Ramachandran and Sharma (1969), primarily due to the effect of droplet internal circulation. The predictions of the two models approach each other as lower f_u values are used.

The calculated enhancement factor ratios, ϕ_R, are also observed to depend strongly on the aforementioned parameters, most notably on f_u. These ϕ_R values are in general smaller than enhancement factor ratios measured in bubbling slurry reactors where $1.1 \le \phi_R \le 2.4$ are typical (Sada et al., 1977), evidently due to much larger gas-liquid interfacial surface exposure times (surface renewal times) in the latter systems.

The present model thus suggests that large enhancement factor ratios can be expected only when droplet internal circulation is significantly suppressed. It also shows that m_A^* monotonically increases with increasing w, however, once again the results are highly sensitive to w only when internal circulation is significantly suppressed. It must be emphasized, however, that these results do not necessarily imply the redundancy of solid particles, or even the adequacy of using very low solid particle volumetric concentrations.

These model calculations are based on the assumption of saturated droplet interior with respect to dissolved reactant species, which is realistic only when dissolving solid particles are present. With strong internal droplet circulation, therefore, the influence of particles is indirect, by ensuring that their dissolution would maintain the droplet bulk saturated with dissolved reactant.

Some parametric transient calculation results are displayed in Figures 5.13, and 5.14, where variations of total droplet absorption rate and mean particle diameter with time are shown for a droplet 0.5 mm in diameter, with f_u=1.0 and 0.1, respectively. The dimensionless time in these figures is defined as $\tau = t\, u_\infty / D$. These results clearly indicate that significant particle shrinkage can occur, and they show a declining absorption rate with time as the particles shrink, in consistence with previous arguments (Mehra, 1996). The mass absorption rate is evidently much higher with f_u=1, indicating the importance of internal circulation on droplet mass transfer. With f_u=1, as discussed earlier, mass absorption is fast primarily due to short exposure time of liquid at droplet surface in each circulation period, and consequently the predicted absorption rate decreases with time only slightly. In other words, the shrinkage of particle size with time has a small effect on the absorption rate. When droplet internal circulation is strongly suppressed, as with the assumption of f_u=*0.1,* on the other hand, the mean size of the particles (with their number density fixed) influences the total absorption rate, and consequently the absorption rate declines with time rather sharply as a result of the declining particle diameters. (This decline can equivalently be attributed to the decline of *w* with time.) Figures 5.13 and 5.14 also show that the reaction kinetics has a larger impact when internal circulation is strong. With f_u=*1* (Figure 5.13), where the direct impact of particles on mass absorption is relatively

small due to the very short surface renewal time, the speed of reaction kinetics becomes important as expected. In contrast, with f_u=0.1, the relatively low droplet recirculation implies longer surface renewal times, more direct influence of particles on the near-surface mass transfer processes, and relatively small difference between results with instantaneous and second-order reactions.

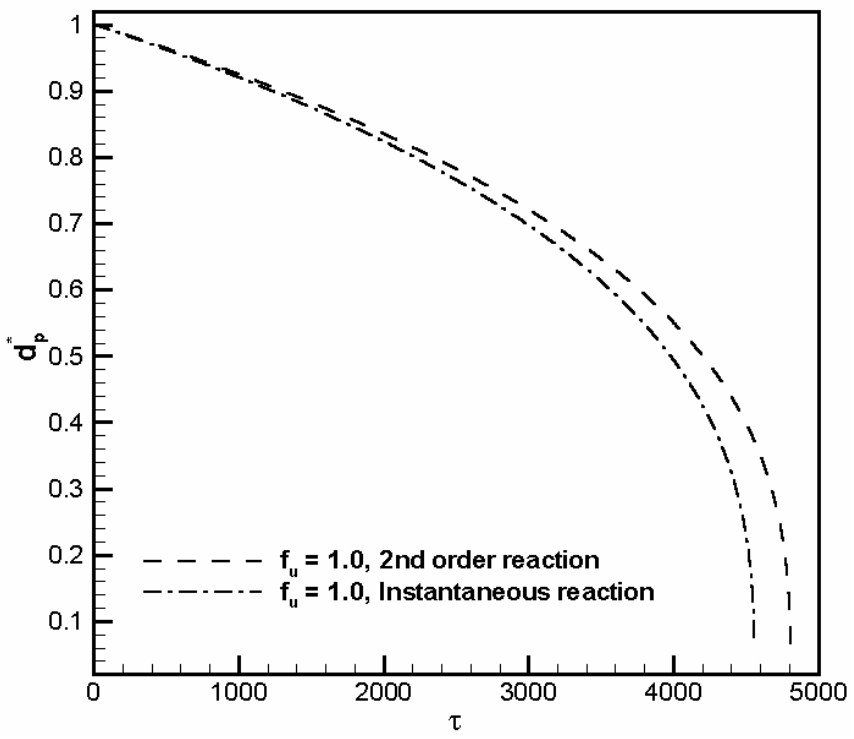

(a)

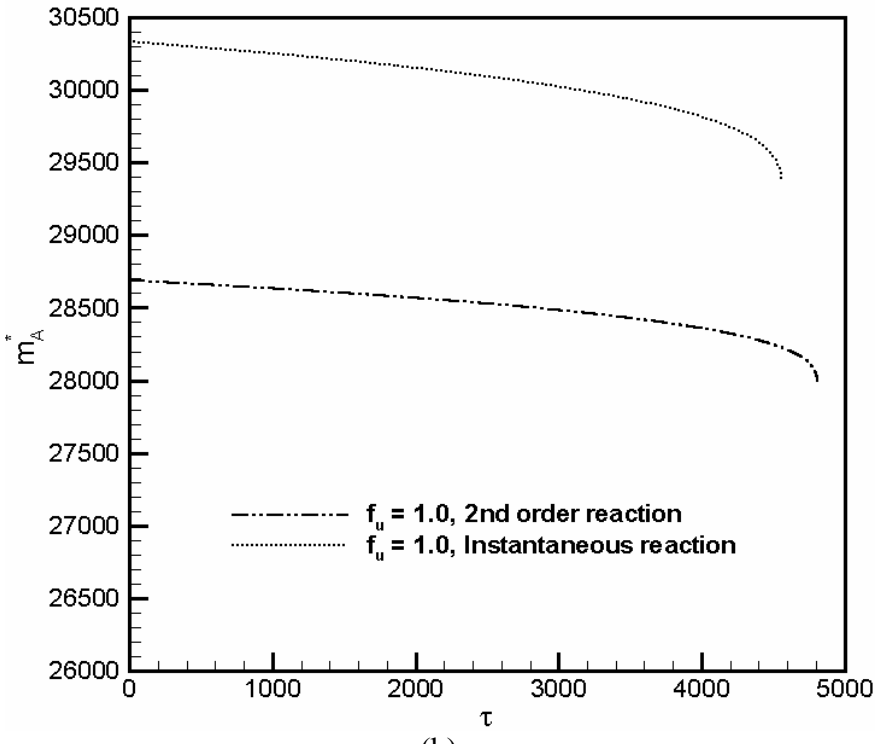

(b)

Figure 5.13: Variations of totals absorption rates and mean reactive particle diameter with time (R = 0.5 mm, d_{po} = 2 μm; f_u=1, w=0.1): a) total absorption rate; b) mean particle diameter.

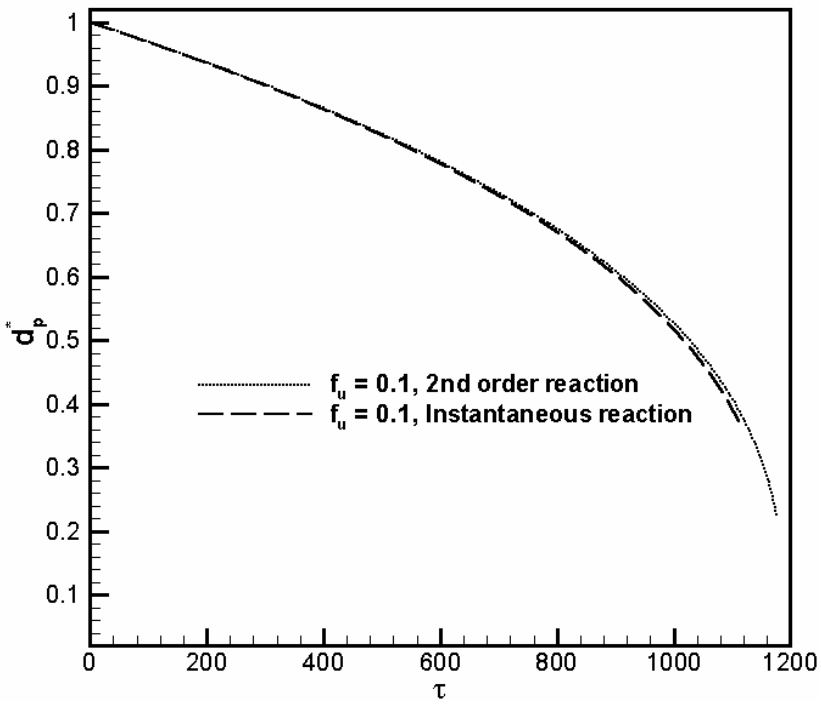

(a)

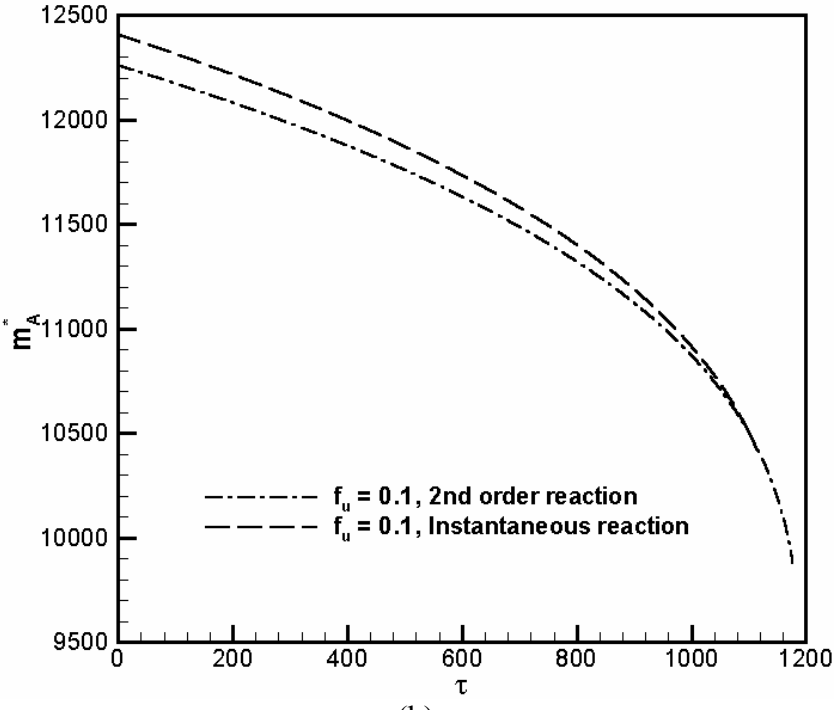

(b)

Figure 5.14: Variations of totals absorption rates and mean reactive particle diameter with time (R = 0.5 mm, d_{po} = 2 μm; f_u=0.1, w=0.1): a) total absorption rate; b) mean particle diameter.

5.7 Concluding Remarks

A numerical study aimed at the elucidation of the effect of sparingly soluble reactant micro particles on the absorption of a gaseous species by a slurry droplet undergoing internal circulation was reported here. The problem studied is relevant to the spray flue gas desulfurization (FGD) systems. Quasi-steady conservation equations governing mass conservation of the absorbed and reactant species, and equations governing the shrinkage of solid particles due to their partial dissolution, were numerically solved using the coordinate system of Kronig and Brink (1950). Calculations were performed for a droplet with unimpeded internal circulation, and a droplet for which the internal recirculation was ten times slower. The droplet recirculation was assumed to be similar to Hill's vortex flow, and the chemical reaction is assumed to be either instantaneous or of second order. Conservation equation representing the reactive gas species and particle dissolution were numerically solved based on the finite-difference technique, using droplet recirculation streamlines as a coordinate.

The simulation results indicated that a reaction layer (where the absorbed species A is present, namely $X_A > 0$) and a diffusion layer (where the reactant species concentration is affected by the absorption process at droplet surface, namely $X_B < 1$) are formed and developed along the droplet surface. The reactant solid particles enhance the absorption rate by reducing the thickness of the reaction layer and increasing the concentration gradient of the transferred species beneath the droplet surface. Stronger droplet internal circulation reduces the effect of particles due to shorter droplet surface exposure time, however.

Parametric calculations were performed, and are utilized to assess the adequacy of the film theory, and to examine the effect of particle size variation on the absorption rate. These calculations confirmed that particles cause a reduction in the thickness of the reaction layer near the droplet surface, thereby enhancing the absorption rate. A transient model was also developed that utilizes the aforementioned quasi-steady droplet mass transfer and reaction models and calculates the time variation of the average solid particle size in the droplet. Transient parametric calculations were presented that show a rapid shrinkage of average particle size with time in slurry droplets, and a declining total absorption rate with time as a result of the shrinkage of the average particle size. The results were everywhere sensitive to droplet internal circulation, however. With slow circulation, the particles' direct influence over the mass transfer process near the droplet surface is relatively significant. When a full and unimpeded droplet internal circulation is assumed, the predicted absorption rates are very high as a result of short droplet surface renewal times, and the particles primarily influence the absorption rate indirectly by maintaining the droplet interior saturated with dissolved reactant. Partial suppression of droplet internal circulation thus leads to significant reduction of absorption rate, even with a high concentration of particles. The calculation results thus demonstrate that a multitude of parameters should be considered for optimal design of a slurry spray scrubber.

CHAPTER 6: THERMOPHORESIS EFFECT ON SOOT PARTICLES IN LAMINAR FLOW

A brief background discussion regarding this topic was given in Section 1.4, and the relevant literature was reviewed briefly in Section 3.3.

6.1 Assumptions

Figure 6.1 is a schematic of the modeled system. A quasi-steady process is assumed. At inlet, a mixture of flue gas with properties similar to air, mixed with soot particles, with a uniform temperature T_0, is assumed. The radial concentration profile of soot particles at inlet is assumed to be non-uniform, and comply with the distribution assumed in (Vedha-Nayagam and Mackowski, 1992). The tube wall is assumed to be semi-transparent.

The gas flow field is assumed to be hydrodynamically fully developed, and the effect of particles on the gas momentum conservation is neglected. This assumption is reasonable as long as the particle loading is low (Yoa et al., 1990; Lee and Humphrey, 1986). The energy and soot transport equations are assumed to be coupled, however. The flow system is assumed to be non-reacting, and the thermophysical properties of the gas are assumed to be unaffected by particles. Soot particles are assumed to be spherical, and locally at thermodynamic equilibrium with their surrounding gas. Soot particles are reasonably spherical in shape as long as coagulation is not severe (Puri, 1993).

6.2 Mathematical Model

The quasi-steady state gas phase energy equation can be expressed as:

$$\rho c_p \vec{v}.\nabla T = k\nabla^2 T - \nabla.q_r'' \tag{6.1}$$

where, q_r'' represents the net radiation heat flux caused by emission and absorption by the soot particles. Soot particles absorb part of the radiation coming from the tube wall, and the remainder of radiation from the wall is lost due to the transparent nature of the wall material at low wavelengths. The radiation heat source term for a translucent medium is (Siegel and. Howell, 2002):

$$-\nabla.q_r'' = -4\int_0^\infty k_\lambda e_{b\lambda}(T)\, d\lambda + \int_0^\infty k_\lambda \left[\int_0^{4\pi} i_\lambda(\lambda, \omega_i) d\omega_i\right] d\lambda \tag{6.2}$$

where $e_{b\lambda}(T) = \pi\, i_{b\lambda}(T)$. We assume zero reflectivity for the wall material for all wavelengths. For wavelengths larger than an absorption cut-off wavelength, λ_a, furthermore, the wall is assumed to be opaque, whereby $i_\lambda(\lambda, \omega_i) = i_{b\lambda}(T_w)$. For shorter wavelengths, however, the wall is assumed to be fully transparent. Therefore, no particle irradiation occurs from the wall for $\lambda < \lambda_a$. Equation (6.2) can be cast as:

$$-\nabla.q_r'' = -4\int_0^\infty k_\lambda e_{b\lambda}(T) d\lambda + 4\left(\int_0^\infty k_\lambda e_{b\lambda}(T_w) d\lambda - \int_0^{\lambda_a} k_\lambda e_{b\lambda}(T_w)\, d\lambda\right) \tag{6.3}$$

The first term on the right hand side of the above equation represents the volumetric emission from the soot particles, the second term represents the total volumetric absorbable energy emitted by the wall, and the third term represents part of the wall emission that is

transmitted out of the system. For carbon soot, the spectral absorption coefficient, k_λ, can be approximated according to (Kennedy et al., 1991):

$$k_\lambda = \frac{7\Phi}{\lambda} \tag{6.4}$$

Equation (6.3) can be integrated to obtain, in SI unit system (see the Appendix B):

$$-\nabla.q_r'' = -4.23\times10^{-4}\,\Phi\,T^5\left[\left(\frac{T}{T_w}\right)^5 - 1 + w_a\right] \tag{6.5}$$

where w_a, the transmission loss fractions is given as,

$$w_a = e^{-\frac{C_2}{\lambda_a T_w}}\frac{4.02\times10^{-2}}{(\lambda_a T_w)^4}\begin{bmatrix} {C_2}^4 + 4{C_2}^3(\lambda_a T_w) + 12{C_2}^2(\lambda_a T_w)^2 \\ + 24C_2(\lambda_a T_w)^3 + 24(\lambda_a T_w)^4 \end{bmatrix} \tag{6.6}$$

where $C_2 = 14387.69\,\mu\text{m.K}$. (Note that, in Eq. (6.6), T_w is in K and λ_a should be in μm.) The value of w_a depends on the magnitude of $\lambda_a T_w$, and varies between *0* to *1*.

For particles with non-uniform size distribution, a number of size groups are defined, as will be described in the next section. Particle transport is assumed to occur due to convection, diffusion and thermophoresis only. Photophoresis is thus neglected. The quasi-steady state particle transport equation, for particles of size groups *j* (represented by the group volume-average radius a_j, and the size group volume fraction ϕ_j), can be expressed in terms of particle volume fraction as:

$$\vec{v}.\nabla\phi_j = \nabla.\left(D_{B,j}\nabla\phi_j - \phi_j\,\vec{v}_{T,j}\right) \tag{6.7}$$

The Brownian diffusion coefficient is found from Einstein's expression (Friedlander 2000), whereby for spherical particles with radius a_j:

$$D_{B,j} = \frac{k_B T f_{c,j}}{6\pi\mu a_j} \tag{6.8}$$

where $f_{c,j}$ is Cunningham slip correction factor for size group j, expressed as (Reist, 1993):

$$f_{c,j} = 1 + Kn_j \left[1.257 + 0.4 e^{-\frac{1.1}{Kn_j}} \right] \tag{6.9}$$

$$Kn_j = \frac{l}{a_j} \tag{6.10}$$

The mean free path of the gas molecules, l, can be calculated from (Friedlander, 2000):

$$l = \nu \left[\frac{\pi M}{2 k_B N_A T} \right]^{\frac{1}{2}} \tag{6.11}$$

The particle thermophoresis velocity, $\vec{v}_{T,j}$, is obtained from the semi-empirical expression of Talbot et al. (1980):

$$\vec{v}_{T,j} = -\frac{C_{T,j}\nu}{T} \nabla T \tag{6.12}$$

where,

$$C_{T,j} = \frac{2.34\left(k/k_p + 2.18 Kn_j\right) f_{c,j}}{\left(1 + 3.42 Kn_j\right)\left(1 + 2k/k_p + 4.36 Kn_j\right)} \tag{6.13}$$

6.3 Particle Size Distribution

Monodisperse and spherical particles have often been assumed in models dealing with soot thermophoresis (Vedha-Nayagam and Mackowski, 1992; Yoa et al., 1990; Kennedy et al., 1991). Soot particles generated in flames have a non-uniform size distribution however, conforming to log-normal and bimodal distributions (Maricq et al., 2003; Zhao et al., 2003; Kiss et al., 1999). A log-normal size distribution is assumed here for the soot particles, whereby the probability density function for particles is represented as:

$$f(a) = \frac{1}{a\left(\ln\beta_g\right)\sqrt{2\pi}} \exp\left[-\frac{\left(\ln a - \ln\bar{a}\right)^2}{2\left(\ln\beta_g\right)^2}\right] \tag{6.14}$$

The particles are assumed to cover a range of $\bar{a} \pm n\beta_g$ with n=3, and $\beta_g = 2.4$. For simplicity of the analysis, this size range is divided into 20 size groups, each represented by a group volume-average radius. The size groups are defined according to:

$$\ln a_j^+ - \ln a_{j-1}^+ = \frac{\ln a_{\max} - \ln a_{\min}}{N} \tag{6.15}$$

where a_{j-1}^+ and a_j^+ represent lower and upper limits of the particle size range in size group j. The mass mean radius of the particles at inlet can be found from (Raabe, 1971):

$$a_{mm} = \left[\int_0^\infty a^3 f(a) da\right]^{1/3} = \exp\left[\ln\bar{a} + 1.5\left(\ln\beta_g\right)^2\right] \tag{6.16}$$

The volume fraction of particles of size group j at inlet, at radial coordinate r, is found from,

$$\phi_j(0,r) = \Phi_0(r)\frac{a_j^3}{a_{mm}^3}\int_{a_{j-1}^+}^{a_j^+} f(a) da \tag{6.17}$$

where a_j, the volume-average radius of particles in size group j is defined as:

$$a_j = \left\{ \int_{a_{j-1}^+}^{a_j^+} a^3 f(a) da \Big/ \int_{a_{j-1}^+}^{a_j^+} f(a) da \right\}^{1/3} \tag{6.18}$$

6.4 Normalized Transport Equations

The aforementioned transport equations, Eqs. (6.1) and (6.7), are normalized using dimensionless parameters defined as:

$$r^* = \frac{2r}{D};\ x^* = \frac{2x\,k_0}{D^2 u_m \rho_0\, C_{p,0}} = \frac{2x}{D\,\mathrm{Re}_{D,0}\,\mathrm{Pr}_0};\ T^* = \frac{T}{T_0};\ \phi_j^* = \frac{\phi_j}{\overline{\Phi}_0} \tag{6.19}$$

where $\overline{\Phi}_0$ and u_m are total average inlet concentration and the gas mean velocity, respectively. The resulting normalized conservation equations are:

$$\left(1 - r^{*2}\right)\frac{\partial T^*}{\partial x^*} = \frac{1}{r^*}\frac{\partial}{\partial r^*}\left(r^* \frac{\partial T^*}{\partial r^*}\right) - \frac{A T_0^{\,4} D^2 \Phi^* \overline{\Phi}_0}{4k}\left[T^{*5} - T_w^{\,*5}\left(1 - w_a\right)\right] \tag{6.20}$$

$$\left(1 - r^{*2}\right)\frac{\partial \phi_j^*}{\partial x^*} = \frac{\rho C_p D_{B,j}{}' T_0}{k}\frac{1}{r^*}\frac{\partial}{\partial r^*}\left(T^* r^* \frac{\partial \phi_j^*}{\partial r^*}\right) + \frac{C_T C_p \mu}{k}\frac{1}{r^*}\frac{\partial}{\partial r^*}\left(r^* \phi_j^* \frac{1}{T^*}\frac{\partial T^*}{\partial r^*}\right) \tag{6.21}$$

where $A = 4.23 \times 10^{-4}\, W/m^3 K^5$, and for particles with radius a_j:

$$D_{B,j}{}' = \frac{k_B f_{c,j}}{6\pi\,\mu\, a_j} \tag{6.22}$$

Note that Eq. (6.21) has been derived using Eqs. (6.12) and (6.13), and assuming that the axial component of $\vec{v}_T$ is negligible in comparison with the gas axial velocity. The boundary conditions are for the above equations:

$$T^*\left(0,r^*\right)=1;\ \left.\frac{\partial T^*}{\partial r^*}\right|_{r^*=0}=0;\ \left.\frac{\partial T^*}{\partial r^*}\right|_{L^*}=0;\ T^*\left(x^*,1\right)=1 \tag{6.23}$$

$$\phi_j^*\left(0,r^*\right)=\frac{\phi_j(0,r)}{\overline{\Phi}_0};\ \left.\frac{\partial \phi_j^*}{\partial x^*}\right|_{L^*}=0;\ \left.\frac{\partial \phi_j^*}{\partial r^*}\right|_{r^*=0}=0;\ \phi_j^*\left(x^*,1\right)=0 \tag{6.24}$$

where, using the inlet particle concentration distribution according to (Vedha-Nayagam and Mackowski, 1992), $\frac{\phi_j(0,r)}{\overline{\Phi}_0}=\frac{\phi_j(0,r)}{\Phi_0(r)}\frac{\Phi_0(r)}{\overline{\Phi}_0}=\left[\frac{a_j^3}{a_{mm}^3}\int_{a_{j-1}^+}^{a_j^+}f(a)da\right]\cdot\frac{2e^{\left(-r^{*2}/\sigma\right)}}{\sigma\left(\sigma\left(e^{\frac{-1}{\sigma}}-1\right)+1\right)}$. This distribution is depicted in Figure 6.1 for $\sigma=0.45$.

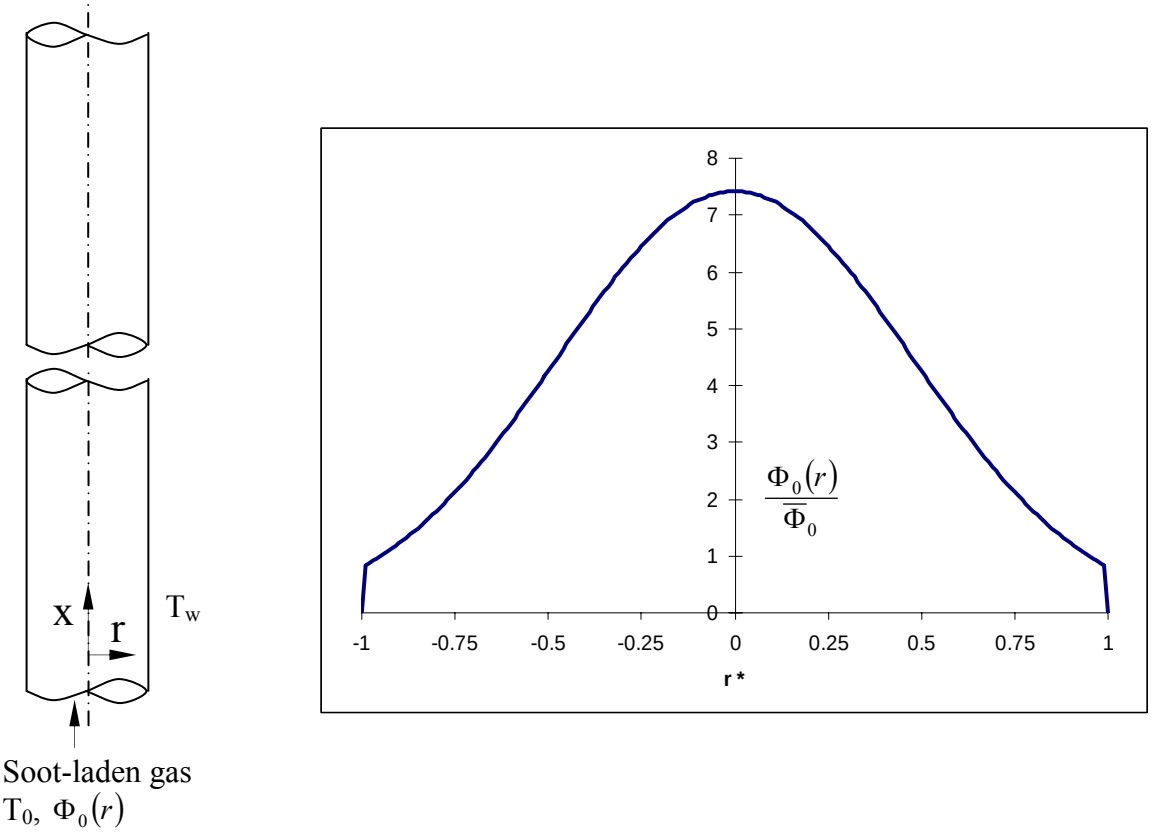

(a) (b)

Figure 6.1: Schematic of the modeled system; (a) the physical system, (b) concentration of soot particles at inlet.

6.5 Numerical Solution Method

A second order upwind implicit finite-difference method was used for the numerical solution of the energy and soot concentration equations (Eqs. (6.20) and (6.21)). To simplify the finite difference solutions, the fifth order temperature term in Eq. (6.20) was linearized as,

$$\Phi^*\left[T^{*5} - T_w^{*5}\left(1 - w_a\right)\right] = \Phi^{*n}\left[\left(T^{*n}\right)^4 T^{*n+1} - \left(T_w^{*n+1}\right)^5 + \left(T_w^{*n+1}\right)^5 w_a\right] \tag{6.25}$$

where, *n* and *n+1* represent old and new iterations, respectively. As will be shown later, soot particles tend to move towards the tube center due to thermophoresis, and their concentration gradually increases near the centerline. The peak soot concentration can thus reach excessively high values, leading to numerical difficulties and unrealistic results. Excessively high particle concentrations would be inconsistent with some of the basic assumptions discussed earlier, furthermore. To avoid these difficulties, the total length of the simulated pipe, L, was kept relatively small and constant throughout each simulation. A non-dimensional tube length of 2.0 was used for all cases with inlet temperature up to 1200 K, while a dimensionless length of 1.1 was used for the cases with an inlet temperature of 1400 K or an initial average soot concentration of 5×10^{-6}. Uniform axial and radial meshes were used. Convergence was assumed when deviation of any ϕ^* and T^* in every node throughout the simulation system from one iteration to the next was within 5×10^{-5}. Numerical oscillations occurred during most iterations; however, the oscillations would die out as convergence was approached. The number of iterations needed for convergence was typically 40 to 180.

6.6 Results and Discussion

For all the simulated cases in this study the factor σ of soot concentration distribution at inlet was assumed to be 0.45. The wall temperature was assumed to be uniform and equal to the inlet gas temperature ($T_{w0} = T_0$). Other default parameter values, unless otherwise specified, were: $\lambda_a = 3\ \mu m$; $\bar{a} = 0.05\ \mu m$; $D = 1\ cm$; and $u_m = 10\ cm/s$. The carrier gas was assumed to be ideal and have the properties of air. The thermal conductivity of carbon soot material was assumed to be $k_p = 0.26\ W/m\text{-}K$ (Incropera and Dewitt, 2000). The thermophysical properties of air, including k and Pr, were assumed to depend on temperature, and were interpolated from the properties tables of (Incropera and Dewitt, 2000).

An extensive numerical experimentation was conducted to check the grid independency of the results. For most of the parametric runs grid independence could be achieved with 400 and 800 nodes in radial and axial directions, respectively, and doubling and tripling the grid numbers did not have any significant effect on the results. To ensure grid-independence, however, a fine mesh of 800 radial and 1600 axial nodes was used for all cases.

Figure 6.2 (a - d) depict the variations of soot particle concentration profiles along the simulated tube for four soot size groups. In the simulations leading to these results $\overline{\Phi}_0 = 10^{-6}$ and $T_w = T_0 = 1200\ K$ were assumed. The particle concentration profiles are depicted in the figures at 4 different axial positions. As noted before, thermophoresis causes the soot particles to move towards the centerline, a trend that would be opposed by Brownian diffusion. The axial variation of the particle concentration profiles evidently

depends on the relative significance of thermophoresis and diffusion. For all the size groups thermophoresis prevails, leading to the sharpening of the particle concentration profiles. An essentially particle-free gas layer develops close to the wall due to the large temperature gradient and the resulting strong thermophoresis, the thickness of which grows along the tube. The formation of an essentially particle-free layer near a hot surface due to thermophoresis is of course a well-known phenomenon (Friedlander, 2000; Talbot et al., 1980), recognized several decades ago (Watson, 1936). Direct experimental measurement of particle thermophoretic diffusivities in high-temperature combustion products has been reported by Gomez and Rosner (1993). Extremely small particles can leak through the particle-free layer due to Brownian diffusion. Friedlander et al. (1988) have shown that for slightly heated surfaces thermophoresis can effectively protect the surface against particle deposition for particles with diameters of a few hundred angstroms or larger. Smaller particles can diffuse and reach the surface, however. The smallest particles addressed by our size groups are too large to diffuse through the particle-free layer, however.

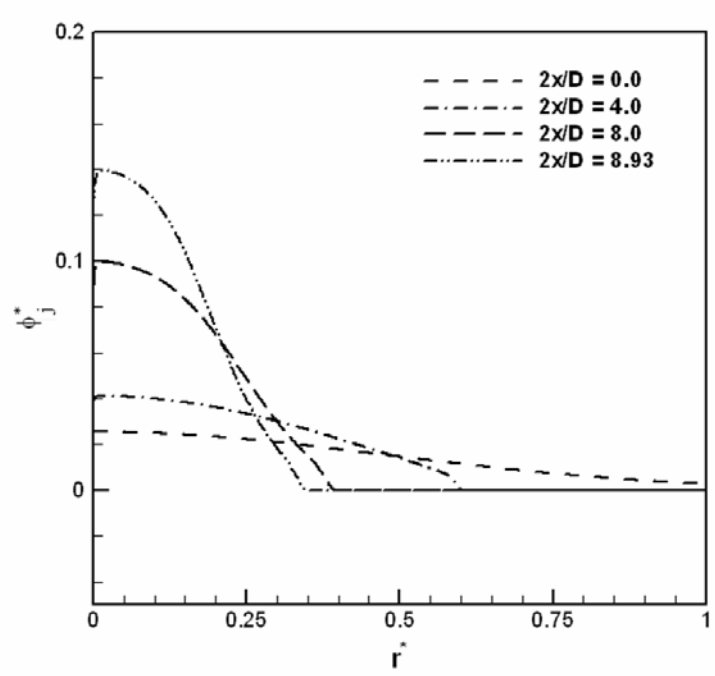

(a)

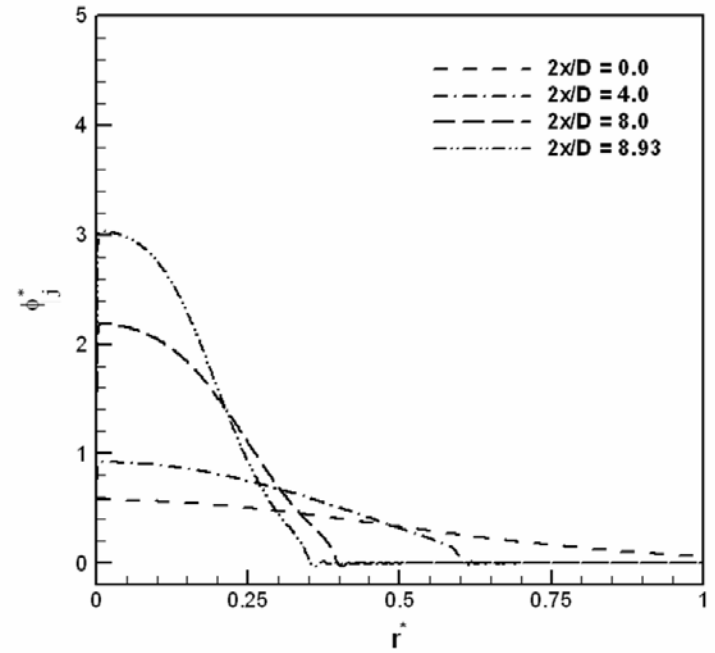

(b)

Figure 6.2: Soot particle concentration profiles at different tube lengths for selected different size groups (out of 20 total groups) - (a) size group *j =10* (radius = 8.26×10^{-2} μm), (b) size group *j = 13* (radius = 2.99×10^{-1} μm), (c) size group *j = 16* (radius = 1.08 μm), (d) size group *j = 19* (radius = 3.92 μm). (Median radius is 0.05 μm).

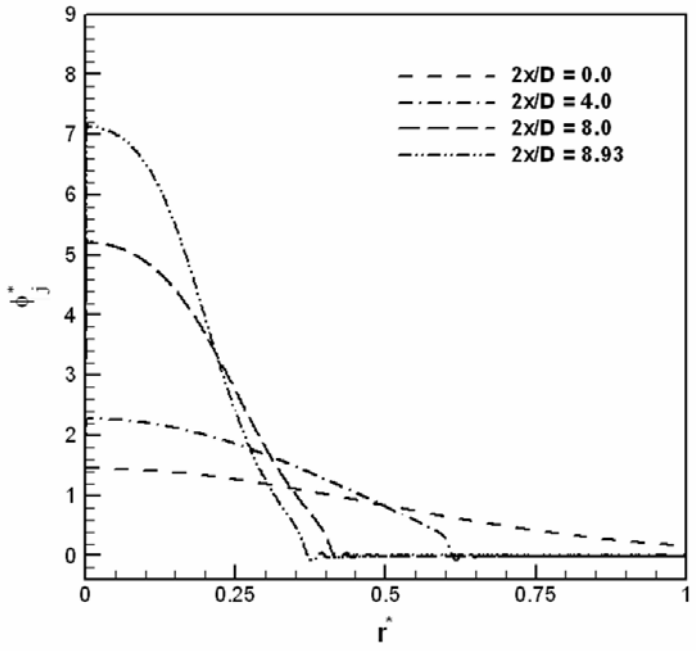

(c)

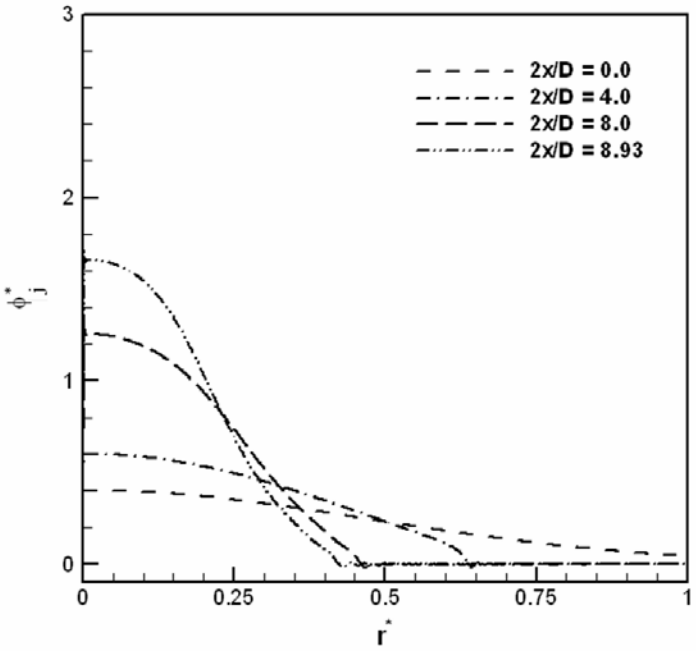

(d)

Figure 6.2: Soot particle concentration profiles at different tube lengths for selected different size groups (out of 20 total groups) - (a) size group j *=10* (radius = 8.26×10^{-2} μm), (b) size group j *= 13* (radius = 2.99×10^{-1} μm), (c) size group j *= 16* (radius = 1.08 μm), (d) size group j *= 19* (radius = 3.92 μm). (Median radius is 0.05 μm). (Continued.)

The evolution of the gas radial temperature profiles corresponding to the simulation leading to Figures 6.2(a – d), is depicted in Figure 6.3. The radiative energy transport by soot particles and their thermophysical motion are coupled, and lead to the development of a non-uniform radial temperature profile in the carrier gas. The gas temperature profile evolves along the tube, and displays a sharp temperature drop towards the centerline everywhere along the tube. Calculated profiles obtained with the aforementioned log-normal soot size distribution, and profiles obtained assuming uniform sized-particles with a = 0.05 μm radius, are also compared in Figure 6.3. The predicted temperature profiles are evidently different, indicating that the assumption of uniform-size soot particles can impact the simulated results. The effect of particle size distribution (log-normal vs. uniform) on the evolution of soot total concentration profiles, obtained from the same simulation, is displayed in Figure 6.4. The assumption of uniform particle size distribution leads to a major over prediction of the sharpening of the soot concentration profile.

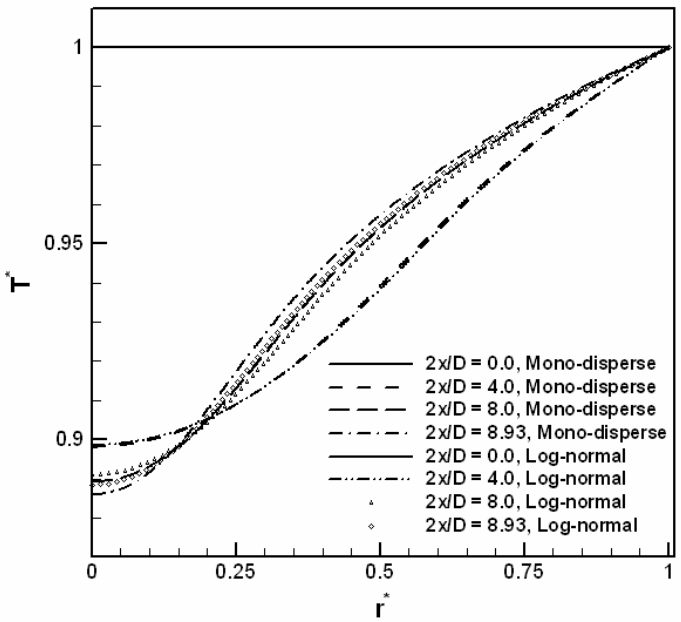

Figure 6.3: Evolution of the radial gas temperature profiles. (Simulation conditions are similar to Figure 6.2.)

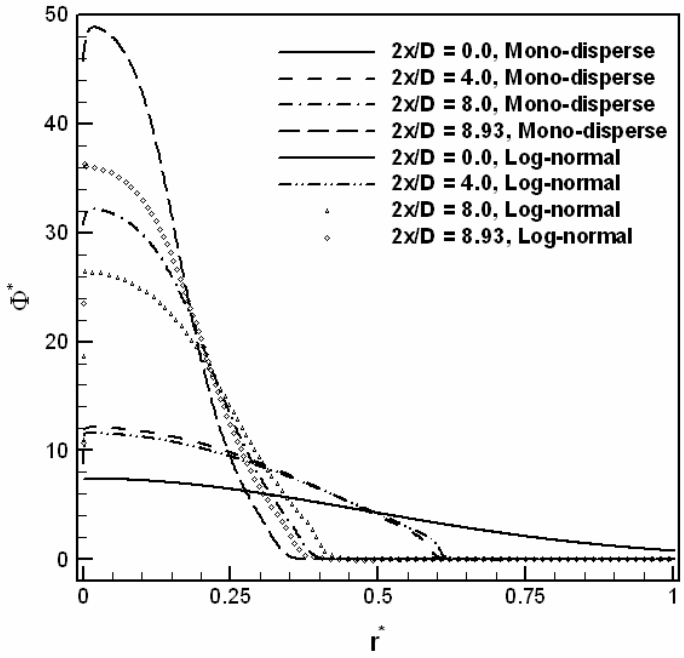

Figure 6.4: Effect of particle size distribution at inlet on total soot particle concentration profiles. (Simulation conditions are similar to Figure 6.3)

The thermophoresis effect is a strong function of tube wall temperature, as depicted in Figures 6.5(a, b), where simulation results displaying the radial profiles of total soot particle concentrations are presented for T_w = *1000 K* and *1400 K*, respectively. The compression of the soot concentration profiles is of course stronger for the higher wall temperature. The effect is significantly more when monodisperse particles are assumed, further confirming the inadequacy of monodisperse idealization in simulations.

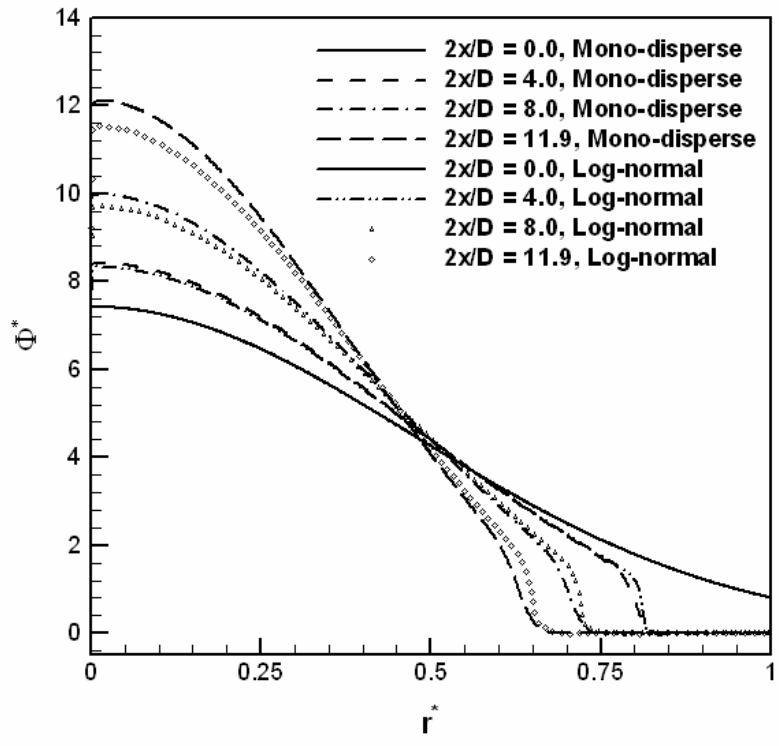

(a)

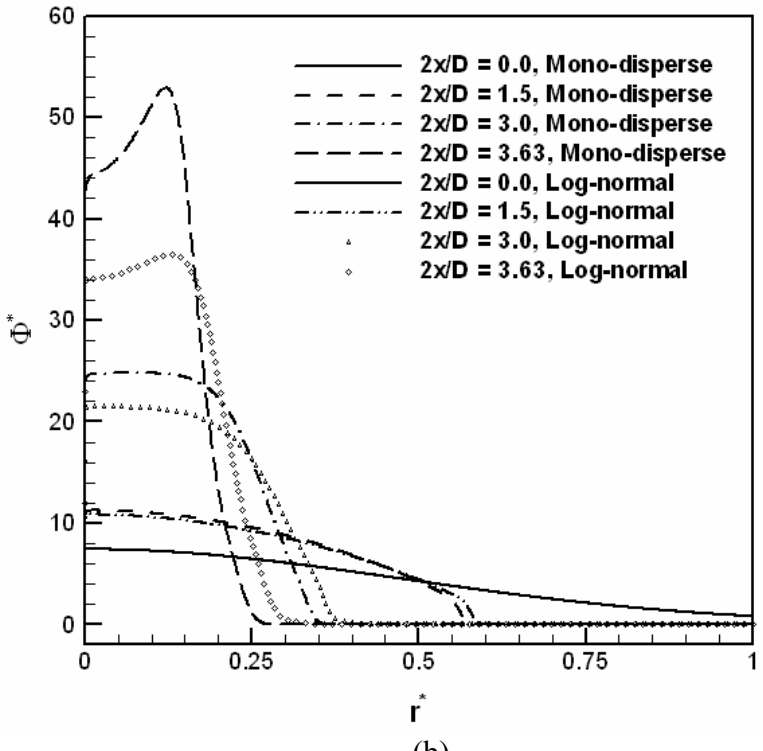

(b)

Figure 6.5: Wall temperature effect on the soot concentration profiles: a) T_w = 1000 K; b) T_w = 1400 K.

The soot concentration profile compression also depends on the initial concentration of soot in the carrier gas. The reason is that, as noted in Eq. (6.20), with increasing $\overline{\Phi}_0$, the contribution of the radiative term to the mixture energy is increased. The dependence of concentration profiles on initial soot concentration is displayed in Figures 6.6(a – c) for assumed monodisperse particles, and in Figures 6.7 (a – c) for log-normally distributed particles. These simulations are based on all default parameters, except the initial average total soot concentration.

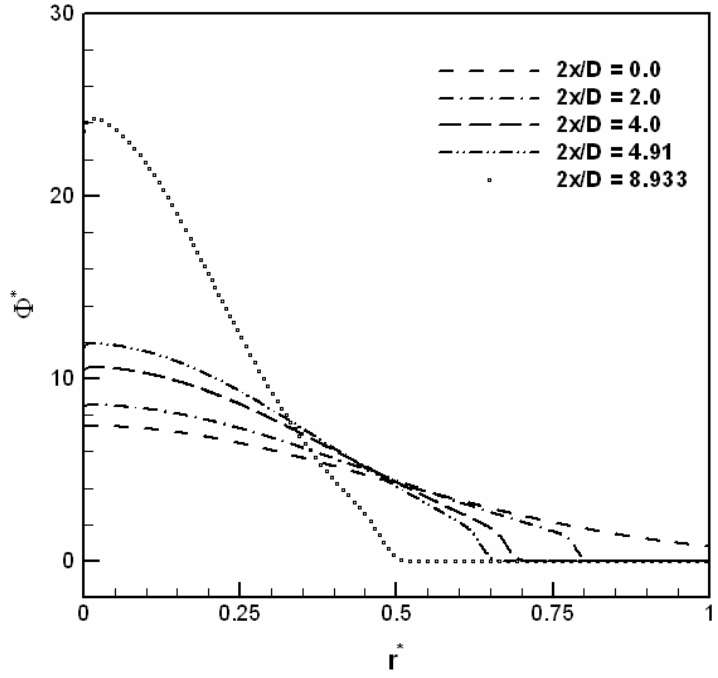

(a)

Figure 6.6: Initial particle concentration effect on the concentration profile for monodisperse size distribution: (a) $\overline{\Phi}_0 = 0.5\times10^{-6}$, (b) $\overline{\Phi}_0 = 5\times10^{-6}$ (c) evolution of concentration for $\overline{\Phi}_0 = 5\times10^{-6}$.

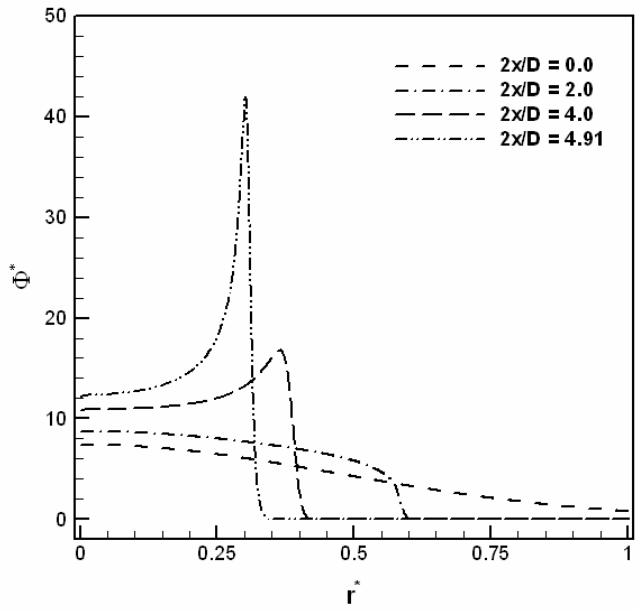

(b)

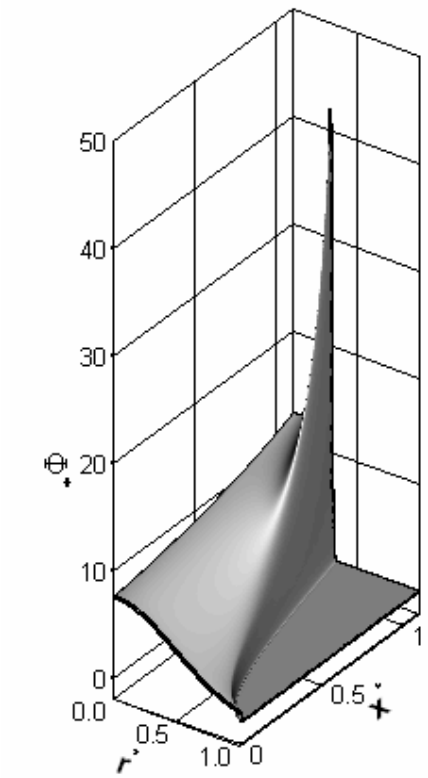

(c)

Figure 6.6: Initial particle concentration effect on the concentration profile for monodisperse size distribution: (a) $\overline{\Phi}_0 = 0.5\times10^{-6}$, (b) $\overline{\Phi}_0 = 5\times10^{-6}$ (c) evolution of concentration for $\overline{\Phi}_0 = 5\times10^{-6}$. (Continued.)

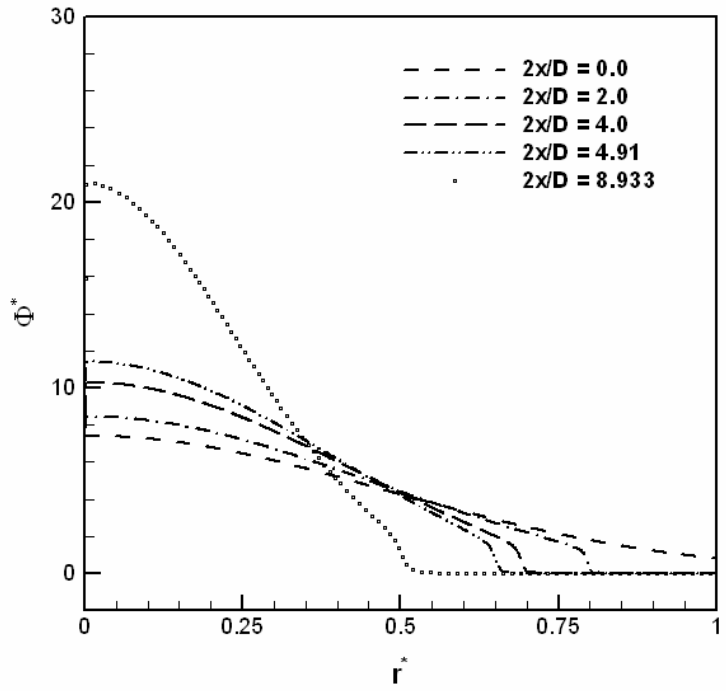

(a)

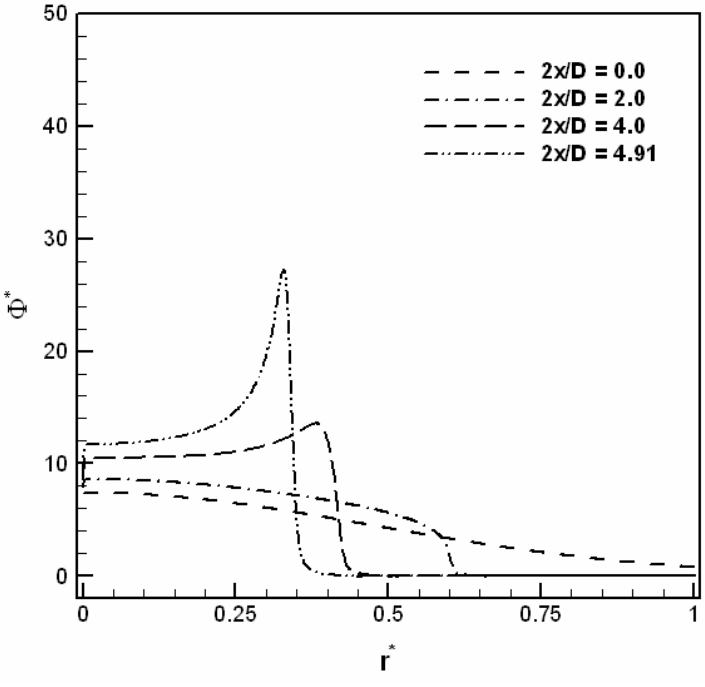

(b)

Figure 6.7: Initial particle concentration effect on the concentration profile for lognormal size distribution: (a) $\overline{\Phi}_0 = 0.5\times10^{-6}$, (b) $\overline{\Phi}_0 = 5\times10^{-6}$ (c) evolution of concentration for $\overline{\Phi}_0 = 5\times10^{-6}$.

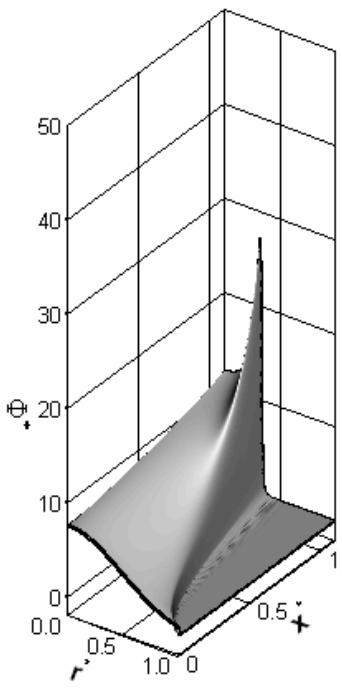

(c)

Figure 6.7: Initial particle concentration effect on the concentration profile for lognormal size distribution: (a) $\overline{\Phi}_0 = 0.5\times10^{-6}$, (b) $\overline{\Phi}_0 = 5\times10^{-6}$ (c) evolution of concentration for $\overline{\Phi}_0 = 5\times10^{-6}$. (Coninuted.)

The peak soot concentrations in the radial concentration profiles occur at the point of inflections of the radial temperature profiles. The calculated radial temperature profiles corresponding to the concentration profiles of Figure 6.7 (b) are depicted in Figure 6.8. The concentration and temperature profiles are closely interdependent due to the sensitivity of thermophoresis on the temperature gradient in the gas. The soot concentration peak occurs because, for particles located at larger radial coordinates than the radial coordinate of the temperature point of inflection (where $\partial^2 T/\partial r^2 > 0$), the radially-inward thermophoretic velocity become larger as *r* is reduced (see Eq. (6.12)). The opposite trend occurs at smaller radial coordinates than the radial coordinates of the point of inflection (where $\partial^2 T/\partial r^2 < 0$), where the radially-inward thermophoretic velocity in fact diminishes as *r* is reduced. We

emphasize, however, that the relative effects of thermophoresis and Brownian diffusion on particle transport of course depend on the particle size. In the particle size range of interest here, both mechanisms gain significance as particle size is reduced. In the free molecular regime, the thermophoretic diffusivity is insensitive to particle size, and can be proportional to the kinematic viscosity of the carrier gas (Waldmann and Schmitt, 1966).

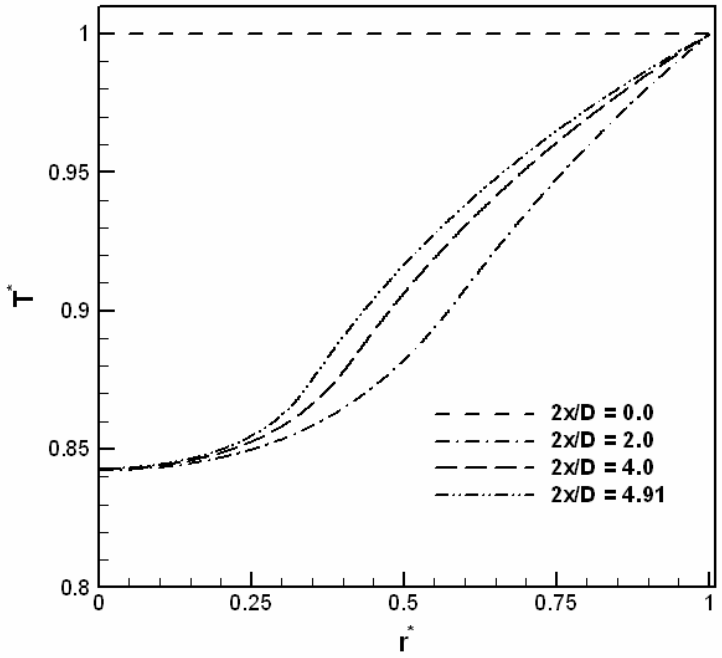

Figure 6.8: Radial temperature profiles corresponding to the concentration profiles in Figure 6.7 (b).

In the analysis presented in this study, the effect of photophoresis was not considered. It is noted, however, that photophoresis can be significant for small absorbing particles in high radiative transfer combustion environments (Mackowski, 1989; Castillo et al., 1990). Castillo et al (1990) have shown that for micron-sized absorbing particles, photophoretic diffusivity can be as large as 10% of the thermophoretic diffusivity.

The practical implications of the radially non-uniform concentration profiles are evidently significant with respect to the sampling, qualification, and clean-up of soot in systems relevant to this study. Validation of the developed models against experimental data was not possible due to the unavailability of such data, however. The need for such experimental data is therefore emphasized.

6.7 Concluding Remarks

The transport of carbon soot in a laminar hot gas, flowing in a tube, was numerically investigated in this study. The carrier fluid was assumed to be an ideal gas with properties similar to air, and the tube wall material was assumed to be transparent to radiation for wavelength shorter than a certain threshold. The carrier gas flow was assumed to be steady and fully-developed, and the energy conservation and soot particle transport equations, which are coupled due to the participation of particles in radiation heat transfer, were numerically solved using an implicit, upwind, second-order finite-difference technique. Monodisperse, as well as polydisperse soot particles were simulated. Polydispersity was addressed by assuming a log-normal particle size distribution and dividing the particles into 20 size groups.

The results showed that radially non-uniform soot concentration and gas temperature profiles develop as a result of the coupling between thermal radiation and soot thermophoresis. The soot particle radial concentration profile peaks at the radial coordinate that corresponds to the point of inflection of the corresponding radial temperature profile. The evolution of radial soot concentration and gas temperature profiles depends on several

parameters, however. Sharper soot concentration profiles are obtained as a result of higher tube wall temperature and higher initial average soot particles. The size distribution of soot particles also had a significant effect on the model predictions, indicating that the assumption of monodisperse soot particles may lead to the over prediction of the effect of thermophoresis.

CHAPTER 7: AEROSOL TRANSPORT IN RISING GAS BUBBLES

A brief background discussion regarding this topic was given in Section 1.5, and the relevant literature was reviewed briefly in Section 3.4.

7.1 Bubble Hydrodynamic Model

The hydrodynamics of the rising bubble was modeled by using the Volume-of-Fluid (VOF) approach of the commercial CFD Code Fluent (Fluent Inc., 2003, Chapter 22.2). To model the bubble and its surrounding liquid, a cylindrical domain with about 121,000 hexahedral shaped cells was created with the GAMBIT mesh generation software (GAMBIT, 2003). The height and diameter of the cylinder were 5.33 and 4 times larger than the bubble's equivalent spherical diameters of 3 mm and 5 mm, respectively. The largest and smallest volumes of the cells in m^3 were of the order of 10^{-11} and 10^{-12}, respectively. Figures 7.1 (a) and (b) show the computational mesh as seen on a vertical plane passing through the axis, and on a horizontal cross-section of the cylindrical computational domain, respectively.

The bubble was initially placed at the center of the cylindrical domain by using the region adaptation option of Fluent. To do that, a spherical patch or domain was selected at the middle of the cylinder with void fraction of 1. The rest of the cylindrical domain was specified as water, i.e., with a void fraction of zero. Figure 7.2 depicts the bubble inside the computational domain at the initiation of a simulation. The initial rise velocity for the bubble was zero. The boundaries of the cylindrical domain, namely the outer, top, and

bottom surfaces of the cylinder, all were specified as hydrostatic pressure boundary conditions. The top and bottom surfaces were of course flat.

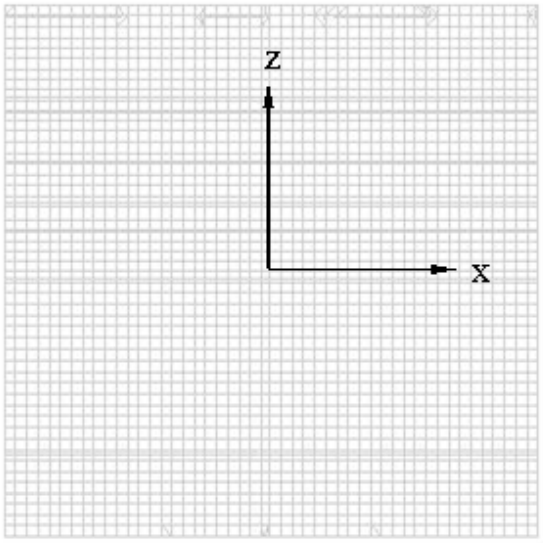

(a)

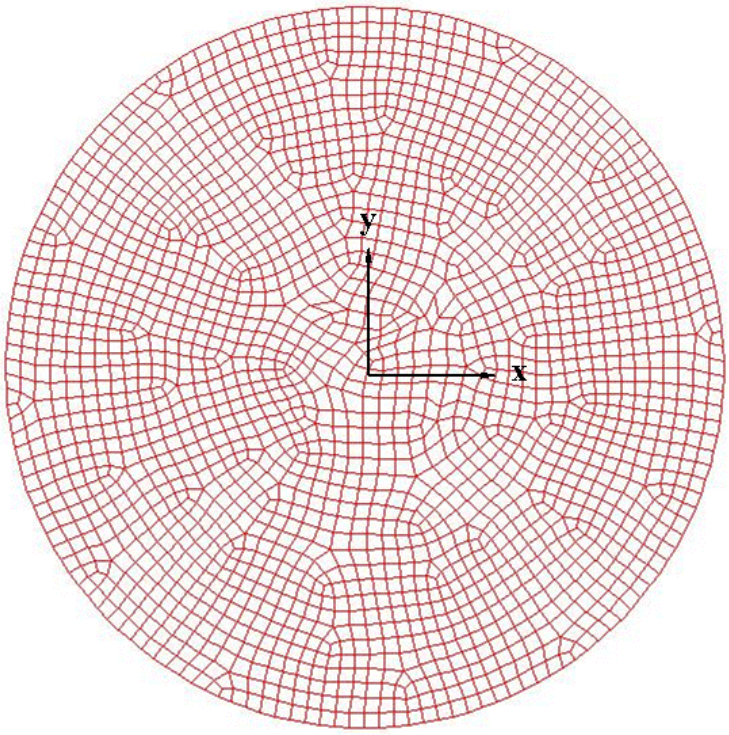

(b)

Figure 7.1: Nodalization scheme in the cylindrical computational domain. (a) vertical plane passing through the axis (b) horizontal cross-section.

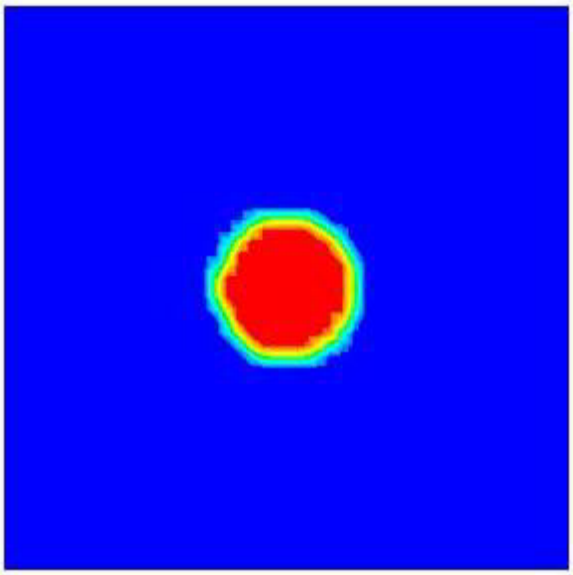

Figure 7.2: Bubble, initially placed at the center of the computational domain.

A dynamic mesh scheme (Fluent Inc., 2003, Chapter 9.6) was used, in order to keep the cylindrical computational domain moving vertically upward (along the z axis in Figure 7.1) at approximately the same velocity as the rising bubble. For this purpose, the cylindrical domain was moved upwards after each time step by a distance corresponding to the average rise of the bubble, i.e., the average upward distance covered in a time step by all the gas-occupied nodes. By using the aforementioned dynamic mesh, the computational domain was kept small without allowing the bubble to leave the domain. 'Layering' dynamic mesh, and 'Rigid body' dynamic zones were used in the simulation. In prismatic (hexahedral and/or wedge-shaped) mesh zones, dynamic layering can be used to add or remove layers of cells adjacent to a moving boundary. Rigid body zones have a rigid-body motion. Detail of the dynamic mesh approach can be found in (Fluent Inc., 2003). A User Defined Function (UDF) was developed (Appendix C) and used to calculate the

displacements of the top and bottom flat boundaries of the computational domain, based on the distance that the bubble had moved in the previous time step. The bubble (or, equivalently, the cylinder) rise distance in each time step was thus calculated from:

$$z_{rise} = \frac{\Delta t}{n} \sum_{j=1,n} u_{z,j} \tag{7.1}$$

where Δt is the time step, n is the number of cells inside the bubble, and u_z is the vertically upward velocity of a gas-occupied node.

Since there was one-way coupling between the particles and the gas, the bubble hydrodynamics were not affected by the particles and could therefore be simulated first. The bubble hydrodynamic data generated during a hydrodynamic simulation were then stored, and were subsequently used in particle transport computations. A file generating UDF (Appendix C) was developed and used in order to record the bubble node positions and velocities in data files after each time step. The shape of the bubble of course did not remain spherical once the simulation had started. The VOF technique captures the location of the phase interphase in a relatively coarse manner by solving a differential time-dependent equation representing the liquid-occupied volume fraction of cells. The interphase is smeared typically over about two mesh points. Figure 7.3 depicts a typical case. In this study, the part of the computational domain with void fractions higher than 0.5 was considered to be the bubble.

The hydrodynamic simulations were performed using $\Delta t = 2 \times 10^{-5}$ s as the time step. The scaled residual tolerances for mass and momentum conservation were 10^{-4} and 10^{-3}, respectively. A typical bubble rise simulation was performed for 60000 time steps

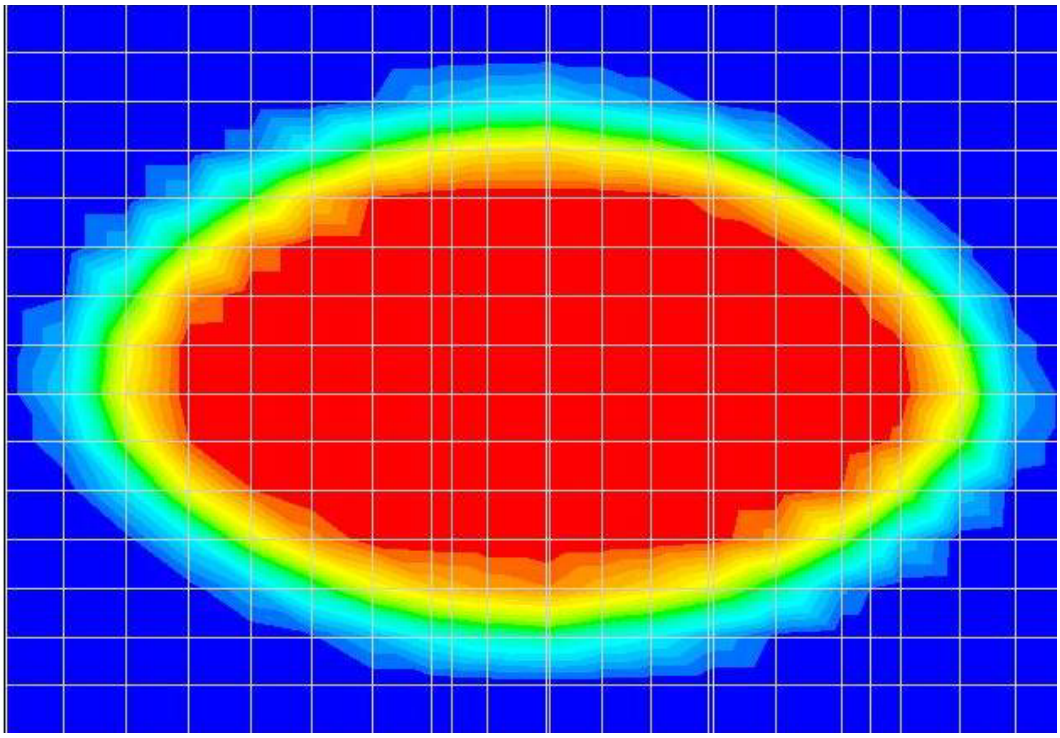

Figure 7.3: Typical smearing of the bubble-liquid interface.

7.2 Particle Motion

For particle volume fractions smaller than 10^{-2} it can be assumed that particles do not interact unless they approach to within a grazing distance (Wen, 1996). Significant coagulation, furthermore, is possible over relatively long residence times. Since particle volume fractions of interest to this study are considerably lower, and in light of the short bubble residence times of interest, coagulation of particles is neglected.

The simplified particle Lagrangian equation of motion is often applied in the simulation of particle-laden flows, and is modified for the inclusion of Brownian dispersion and other forces (Ounis et al., 1991; Chen and McLaughlin, 1995; Thakurta et al., 1998;

Elghobashi and Truesdell, 1992). Accordingly, the particle equation of motion is represented here as:

$$\rho_P V_P \frac{d\vec{U}_P}{dt} = -f\left(\vec{U}_P - \vec{U}_G\right) + \left(\rho_P - \rho_G\right) V_P \vec{g} + \vec{F}_B \tag{7.2}$$

where

$$f = \frac{6\pi\mu_G d_P}{C} \tag{7.3}$$

The Cunningham correction factor is found from (Friedlander, 2000; Reist, 1993):

$$C = 1 + \frac{2\lambda_G}{d_P}\left[a_1 + a_2 \exp\left(-a_3 \frac{d_P}{2\lambda_G}\right)\right] \tag{7.4}$$

$$\lambda_G = \nu_G \left(\frac{\pi M_G}{2\mathcal{R} T_G}\right)^{\frac{1}{2}} \tag{7.5}$$

where $a_1 = 1.252$, $a_2 = 0.399$, and $a_3 = 1.10$ (Reist, 1993). The Brownian dispersion effect in represented by the inclusion of the random Brownian force term $\vec{F}_B$, whose Cartesian components are found from (Ounis et al., 1991; Chen and McLaughlin, 1995; Thakurta et al., 1998):

$$F_{B,i} = G_i \left(\frac{6\pi\mu d_P \kappa T_G}{\Delta t}\right)^{\frac{1}{2}} \tag{7.6}$$

where Δt is the time step in the numerical particle motion calculations, and G_i (i = 1, 2, 3) are three independent Gaussian random numbers (for the three coordinates) with zero means and unit variances. In Eq. (7.2), $\overrightarrow{U_G}$ represents the component of gas velocity at the

particle's location. The position of a particle should also be updated by integrating the following equation:

$$\frac{dx_j}{dt} = u_{P,j} \tag{7.7}$$

The ordinary differential equation set represented by Eqs. (7.2) and (7.7) were explicitly integrated over each time step according to:

$$u_{P,i}^{(t+\Delta t)} = \left(u_{g,i} + B/f\right)^{(t)} + \left[u_{P,i} - \left(u_{g,i} + B/f\right)\right]^{(t)} e^{-\frac{f}{A}\Delta t} \tag{7.8}$$

$$x_i^{(t+\Delta t)} = x_i^{(t)} + \left(u_{g,i} + B/f\right)\Delta t + \frac{A}{f}\left[u_{p,i} - \left(u_{g,i} + B/f\right)\right]^{(t)} \left(1 - e^{-\frac{f}{A}\Delta t}\right) \tag{7.9}$$

where:

$$A = \rho_P V_P \tag{7.10}$$

$$B = \left(\rho_P - \rho_G\right) V_P g_i + F_{B,i} \tag{7.11}$$

The time step for the integration was identical to the time step in the hydrodynamic simulation ($\Delta t = 2 \times 10^{-5}$ s).

Both particle and gas velocities are required in Eqs. (7.8) and (7.9). For all particle positions, the corresponding local gas velocities were calculated by interpolated among the velocity data provided by Fluent. Numerical Algorithms Group (NAG) interpolation routines E01TGF and E01THF (NAG, 2002) were used to interpolate the gas velocities. The first routine generates a three-dimensional interpolant to a set of scattered data points, using a modified Shepherd method. The second routine evaluates the three-dimensional interpolating function generated by E01TGF and its first partial derivatives. A particle is

assumed to be outside the bubble if the first routine needs an extrapolation for that particle position coordinates. Such a particle is assumed to have struck the bubble surface, and is therefore removed from the field. Numerical simulations are initiated by randomly distributing 7,000 uniform-sized particles throughout the spherical bubble that is initially located at the center of the computational domain. The aforementioned procedure is repeated over consecutive time steps until only a limited number of particles (typically 100) remains inside the bubble. The computation time needed for the particle transport depends on the particle size, and is longer for smaller particles. On a Personal Computer with 3 GHz processor typically 12 to 60 hrs of computation time were needed.

7.3 Results and Discussion

7.3.1 Bubble Hydrodynamics

The VOF-based Fluent simulation, as described earlier, addresses the rise of initially spherical bubbles, released with a zero initial velocity, in quiescent water. Simulation results for nitrogen (N_2) bubbles with initial volumes of 14.1 and 65.5 mm^3 (equivalent to the volumes of spheres with R_B = 1.5 mm and 2.5 mm, respectively) are briefly presented and discussed here.

Typical calculated bubble cross-sections on the yz plane (at x = 0) (See Figure 7.1 for the definition of the coordinate system) are displayed in Figures 7.4 and 7.5 for bubbles with R_B = 1.5 mm and 2.5 mm, respectively. The apparent large variations in the size of the cross-sectional area are due to the lateral (zigzag) motion of bubbles as they rise in the liquid pool. The lateral bubble motion causes the bubble to go back and forth with respect to the

$x = 0$ plane. Shape oscillations are also visible for both bubble sizes, and the deformation from spherical geometry is more significant for the larger bubble (Figure 7.5), as expected. Bubbles freely rising in infinitely large liquid pools can exist in several different shape regimes. A shape regime map can be constructed in terms of three dimensionless parameters Eotvos number, defined as $Eo = 4g(\rho_L - \rho_G)R_B{}^2/\sigma$; Morton number, defined as $M = g\mu_L{}^2(\rho_L - \rho_G)/\rho_L{}^2\sigma^3$, and the bubble Reynolds number (Clift et al., 1978). Based on the shape regime map of Clift et al. (1978), both bubbles simulated in this study occur in the ellipsoid and wobbling regime, and their behavior as predicted by the simulations is consistent with the known behavior of bubbles in the ellipsoidal and wobbling regimes.

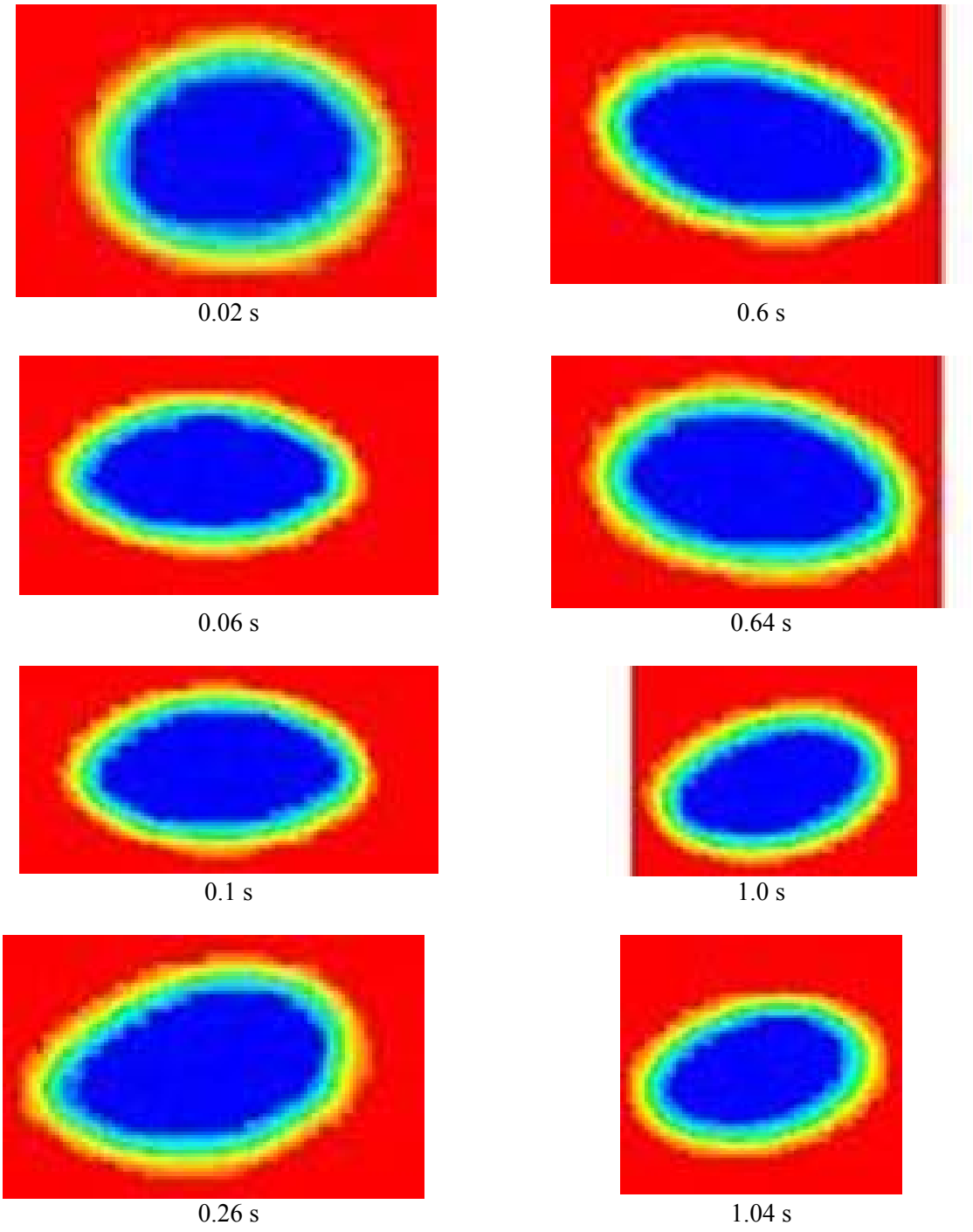

Figure 7.4: Variation of bubble cross-section on the yz plane (at x = 0) with time for R_B = 1.5 mm.

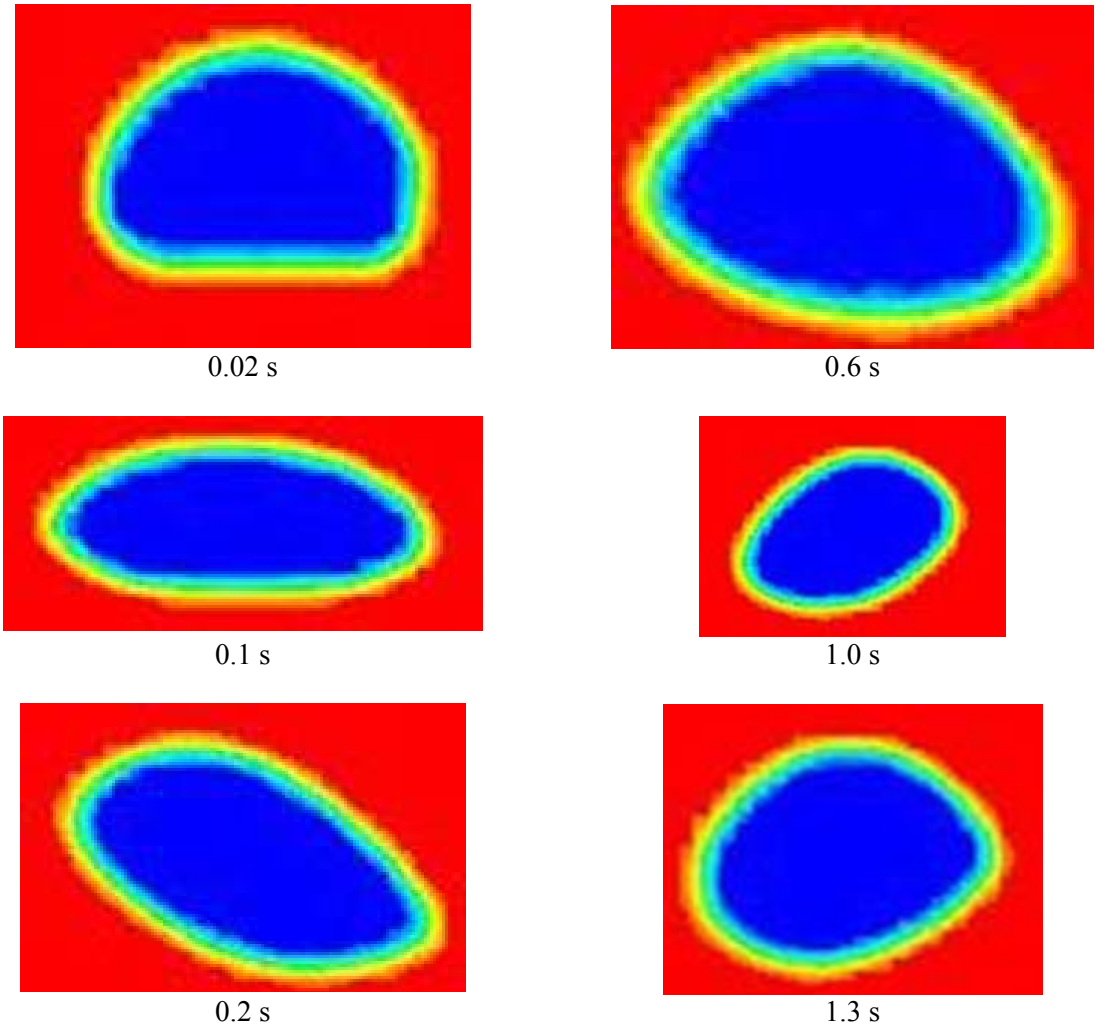

Figure 7.5: Variation of bubble cross-section on the yz plane (at x = 0) with time for R_B = 2.5 mm.

The lateral motion of bubbles during their rise is depicted in Figure 7.6, where the temporal variations of the x and y coordinates of the bubble centers are displayed. The familiar curvilinear motion of the deformed bubbles is notable, and is significantly more pronounced for the larger bubble. The rise distances of the two bubbles as a function of time are also displayed in Figure 7.7, and are compared with the predictions of the empirical correlation of Peebles and Garber (1953). The simulation results are in good agreement with the correlation of Peebles and Garber for the smaller bubble, while for the larger bubble the

rise velocity is over predicted by the simulation. Figure 7.6 shows that the path of the larger bubble is curvilinear with a zigzag motion that occurs at a high frequency, but minor amplitude. However, the zigzag motion of the smaller bubble is far more significant than the larger bubble with respect to the amplitude. The lateral zigzag motion of the smaller bubble has a considerably smaller frequency, furthermore.

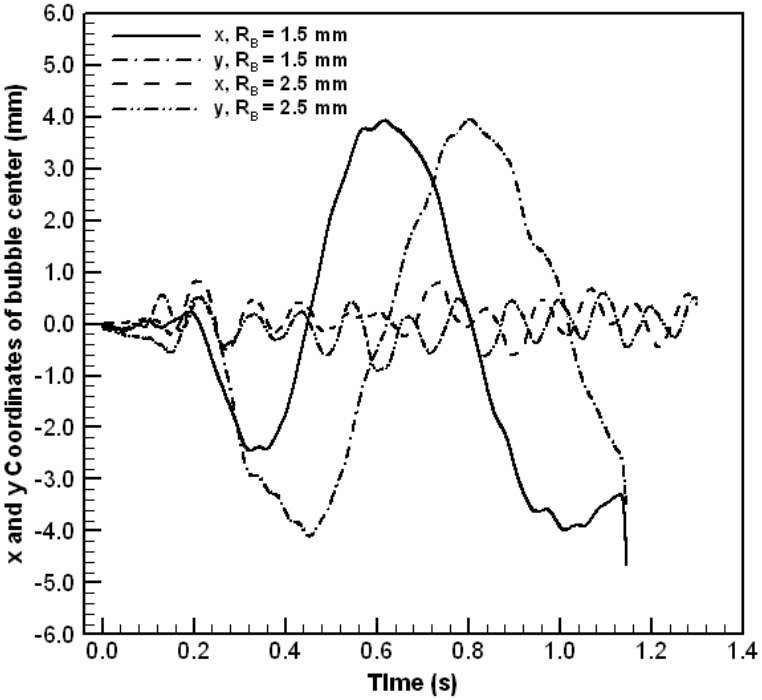

Figure 7.6: Temporal variation of x and y coordinates of the bubble centers.

Typical snapshots of the predicted bubble internal flow fields are depicted in Figures 7.8 and 7.9, where gas velocity vectors are projected on the vertical yz plane (at x=0). Complex recirculation patterns can be observed. For the smaller bubble, the bubble motion is nearly rectilinear and the lateral bubble movements are relatively minor (Figure 7.6). For this bubble, the internal recirculation pattern is similar to the well-known Hill's vortex flow at times when the bubble is nearly spherical. The internal recirculation thus results in two

vortices in the bubble, as in Fig 7.8(a). Clear internal recirculation pattern and twin vortices can be seen in Figure 7.8(b) as well, even though the bubble is highly deformed. Deviations from axi-symmetry caused by bubble deformation and curvilinear bubble motion lead to complicated three-dimensional recirculation patterns for the larger bubble, as observed in Figures 7.9(a, b).

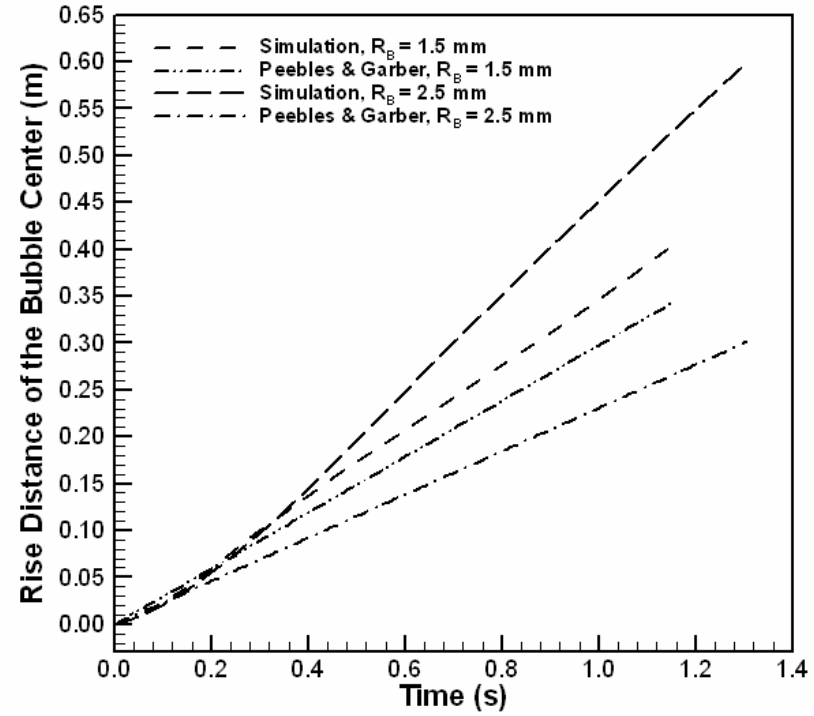

Figure 7.7: The rise distance of bubble centers.

The simulation results discussed above show that the bubble hydrodynamic phenomena predicted by the CFD simulations are reasonably accurate, and agree with the known behavior of bubbles when near-spherical bubble geometry and nearly rectilinear bubble rise occur. Strong internal circulation also occurs when the bubble is highly deformed, and under circumstances when a bubble is highly deformed from spherical

geometry and moves in a strongly curvilinear path, the bubble internal circulation pattern can be three-dimensional and very complex.

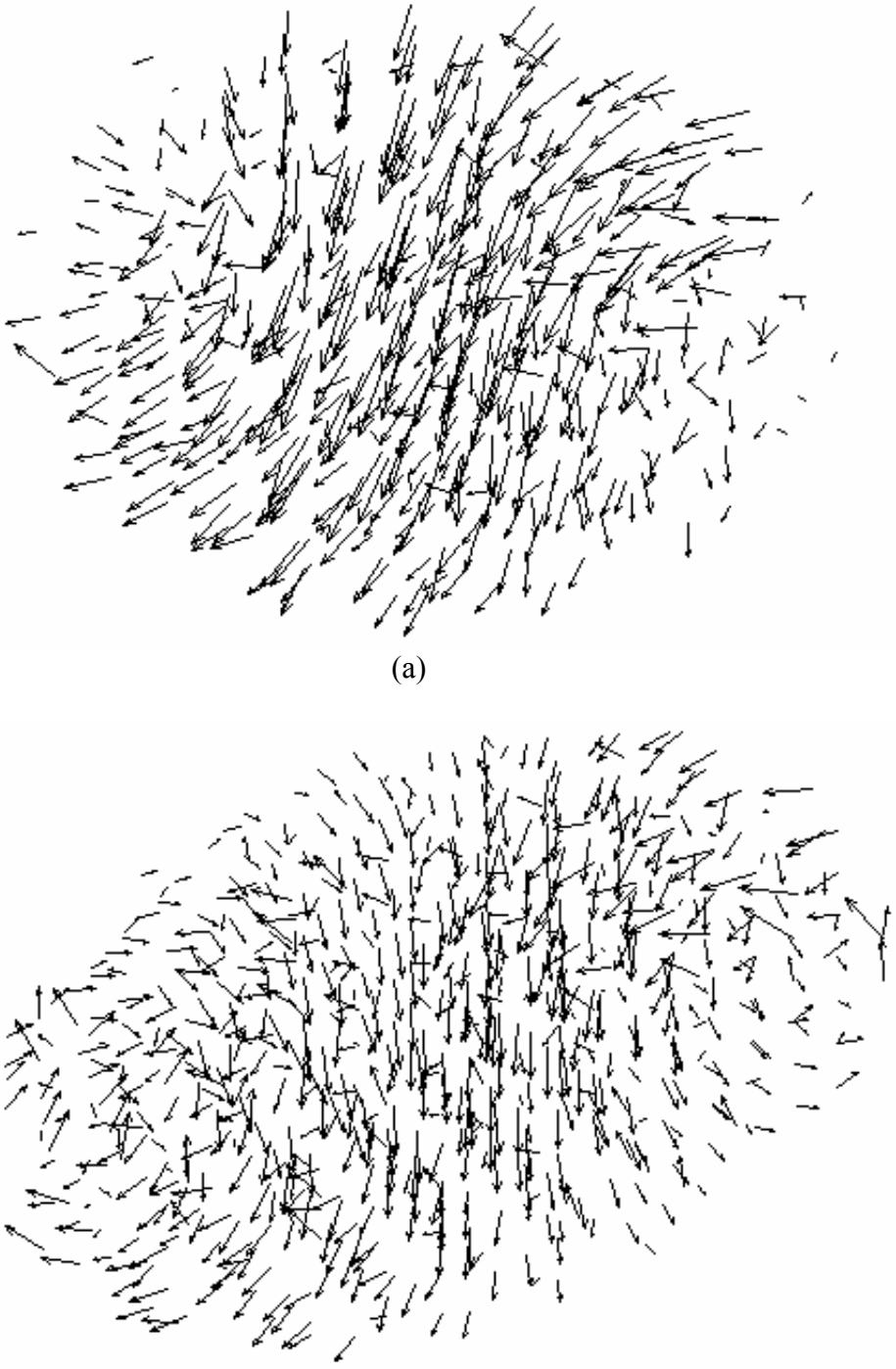

(a)

(b)

Figure 7.8: Gas velocity vector projected on the yz plane (at x = 0) for the bubble with R_B = 1.5 mm. (a) t = 0.025 s, (b) t = 0.5 s.

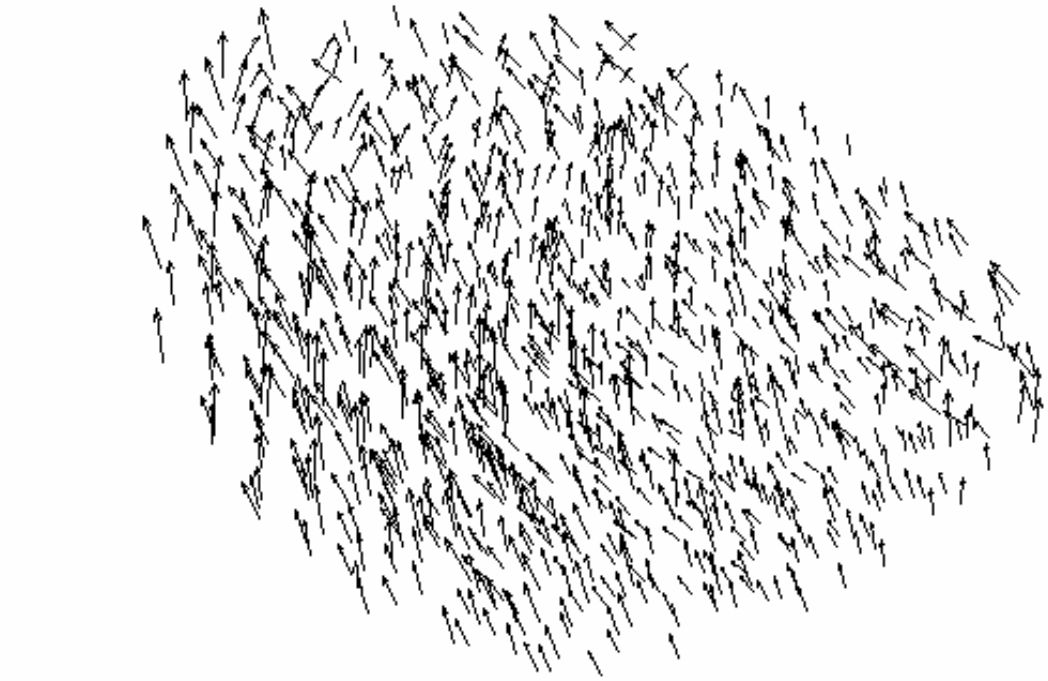

(a)

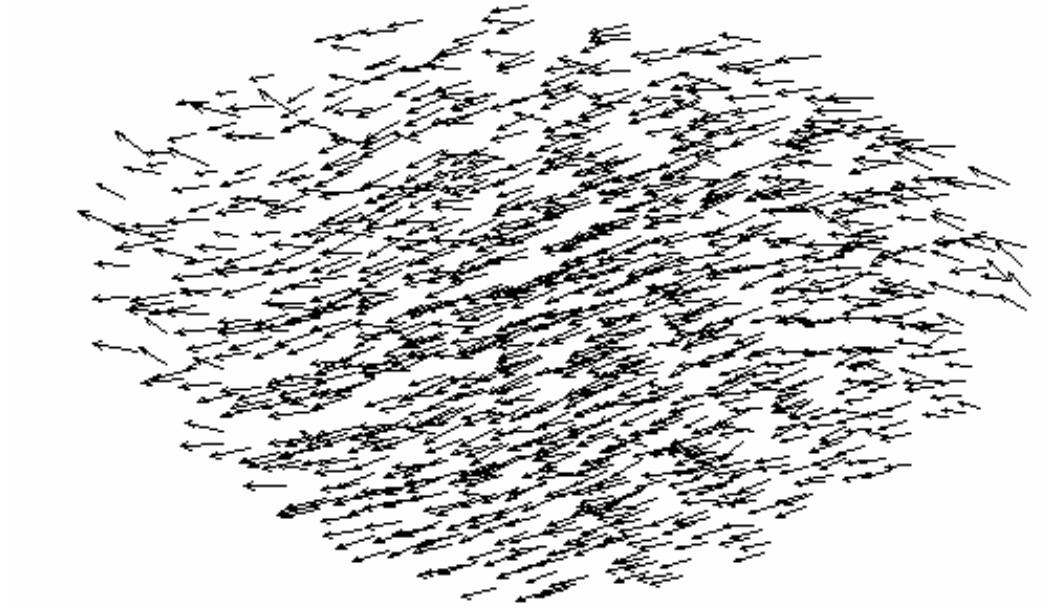

(b)

Figure 7.9: Gas velocity vector projected on the yz plane (at x = 0) for the bubble with R_B = 2.5 mm. (a) t = 0.22 s, (b) t = 0.5 s.

7.3.2 Aerosol Transport

7.3.2.1 Parametric Results

For parametric calculations the particle properties were chosen to be similar to the particles used in the experiments of Herranz et al. (1997), to be described later. The particles were thus assumed to be spherical, and made of Nickel. All the parametric results are based on assumed mono-dispersed particles.

Variations of the fraction of particles remaining in the bubble ($1 - \varepsilon$), as a function of dimensionless time, are depicted in Figures 7.10 and 7.11, for the aforementioned bubbles with R_B = 1.5 mm and 2.5 mm, respectively. The dimensionless time is defined as (Friedlander, 2000):

$$\tau = \frac{t\,\mathrm{D}}{R_B{}^2} \tag{7.12}$$

where D is the particle diffusivity and is found from the Stokes-Einstein expression (Friedlander, 2000):

$$\mathrm{D} = \frac{\kappa T_G}{f} \tag{7.13}$$

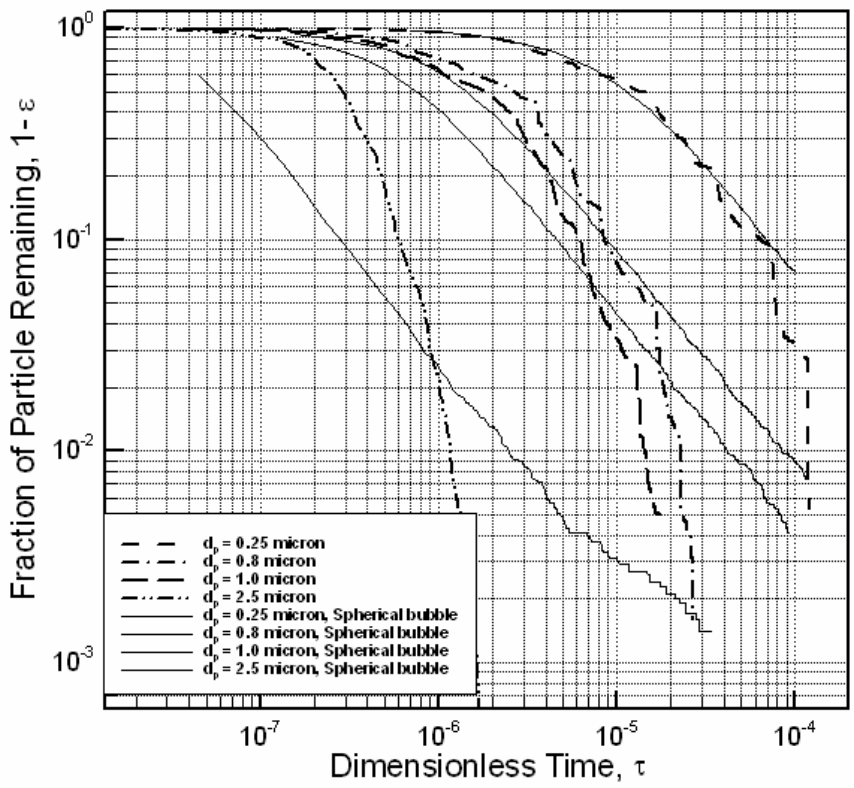

Figure 7.10: Particle removal in the bubble with R_B = 1.5 mm.

In Figures 7.10 and 7.11, for comparison, the model predictions for ideal and perfectly spherical bubbles, rising in a straight line with a constant velocity equal to the bubble terminal velocity predicted by the correlations of Peebles and Garber (1953), and supporting full internal circulation are also displayed. These ideal-case predictions, referred to in the figures as spherical bubble results, were calculated using the method described in detail in Laker and Ghiassiaan (2003).

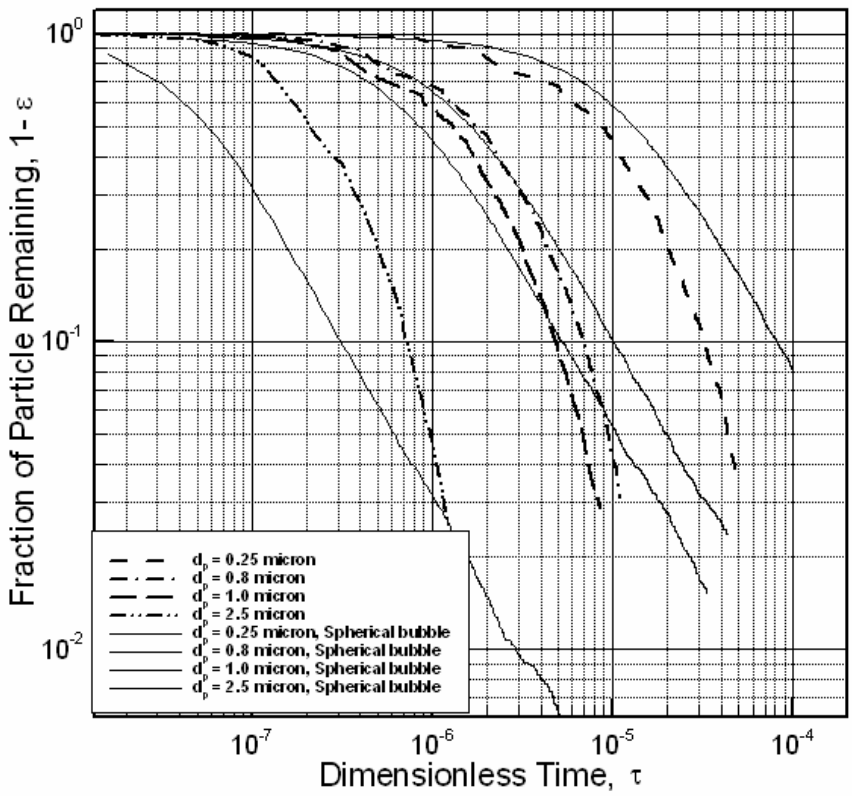

Figure 7.11: Particle removal in the bubble with R_B = 2.5 mm.

As noted in Figures 7.10 and 7.11, bubble deformation from spherical geometry modifies the particle removal rate, in particular for larger particles which are susceptible to inertia-induced removal and are therefore sensitive to the bubble internal circulation. The variation of 1-ε with dimensionless time is relatively smooth for the spherical bubbles, and becomes slight jagged for these bubbles only when the number of the surviving particles in the bubble becomes very small such that the effect of stochastic nature of the particle removal process becomes visible in the depicted curves. For the CFD-simulated bubbles, however, the particle removal curves indicate abrupt variations in particle removal rate caused by incessant bubble deformation and shape change. These shape change-induced particle removals are evidently particularly strong during the later stages of the simulations.

The impact of bubble shape variation with time is particularly significant for sub-μm particles (e.g., d_p = 0.25 μm in Figure 7.10(a)) because for these particles the overall removal rate is very small in the absence of bubble shape oscillations.

The above parametric results are evidently limited in scope. Nevertheless, they confirm the significance of bubble deformation and shape variation with time on particle removal.

7.3.2.2 Comparison with Experimental Data

Experimental data that can unambiguously provide the particle removal rates in a bubble, with known bubble and particle characteristics, are not available. Rigorous validation of models dealing with particle transport in bubbles is thus difficult.

An experimental study of pool scrubbing of simulated radioactive aerosols was performed by Herranz et al. (1997). In these experiments, the aerosol was injected through a horizontal submerged vent, and subsequently formed a rising bubble plume in a pool. Herranz et al. (1997) attempted to estimate the contribution of each of these phases to their measured overall particle removal (decontamination) factors.

Simulation results are compared with the results of Tests RCA1 and RCA2 of Herranz et al. (1997) in Figure 7.12. The decontamination factor is defined as:

$$DF = (1-\varepsilon)^{-1} \tag{7.14}$$

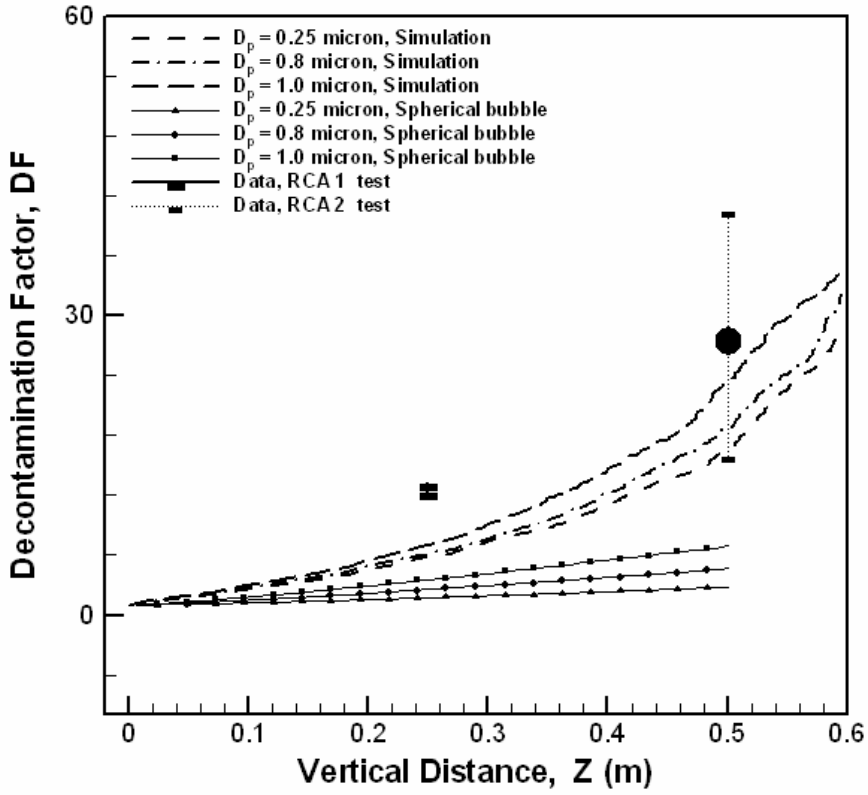

Figure 7.12: Comparison between the simulated results for R_B = 2.5 mm and the experimental results of Herranz et al. (1997).

In these tests, the bubble rise distances were 0.25 m and 0.5 m, respectively. The bubbles covered the relatively wide range of diameters 0.8 mm ~ 100 mm, although most of the bubbles had diameters in the 0.8~10 mm range. The particles were made of Nickel, and had a log-normal size distribution with a count median diameter of 0.8 μm and a geometric standard deviation of approximately 1.4. The parametric calculations depicted in Figure 7.12 were obtained for each displayed particle size in simulations that assumed mono-dispersed particles. An equivalent spherical bubble diameter of 5 mm was assumed, which is approximately the average experimental bubble size. The bubble hydrodynamics were identical to those described earlier and depicted in Figures 7.5, 7.6, and 7.9. Furthermore, given the fact that the simulations start with a stationary and spherical bubble with relatively

uniform entrained particle distribution, the experimental decontamination factors represent the total measured decontamination factors. Also shown in the figure are the predictions of the aforementioned model of Laker and Ghiaasiaan (2003) which assumes a perfectly spherical bubble moving on a vertical line and supporting ideal Hill's vortex flow-like internal circulation.

Figure 7.12 indicates reasonable agreement between the experiments and the simulation results, given the uncertainties about the experimental data. Model-predicted DF values for a perfectly spherical bubble are considerably lower, however. Simulation results with larger particles (not shown here for brevity) show that particles with diameters equal to a few μm or larger would be rapidly removed from the bubbles.

7.4 Concluding Remarks

A CFD-based model for the transport and retention of aerosol in rising bubbles was described and its performance was demonstrated. The bubble hydrodynamics were simulated using the Fluent commercial CFD package, and utilizing the Volume of Fluid (VOF) technique for capturing the bubble-liquid interphase. Equations of motion for a large number of particles (typically 7000) were then solved in Lagrangian frame, and particles that collided the bubble-liquid interphase were assumed to be removed from the bubble. Parametric results for bubbles with equivalent spherical diameter of 3 and 5 mm showed the occurrence of bubble deformation and shape change with time, and complex bubble internal circulation patterns. As a consequence of bubble deformation and complex internal circulation, particle removal rates were different than the particle removal rates predicted for

spherical bubbles with similar volumes. Comparison was made between the particle decontamination factors predicted by the simulations and the experimental data of Harranz et al., (1997), with reasonable agreement.

CHAPTER 8: TWO-PHASE FLOW REGIME MAP IN MICROCHANNELS

A brief background discussion regarding this topic was given in Section 1.5, and the relevant literature was reviewed briefly in Section 3.5.

8.1 Two-Phase Flow in Microchannels and in Microgravity

For adiabatic, steady-state, and developed gas-liquid two-phase flow in a smooth pipe, assuming immiscible and incompressible phases, the important variables are ρ_L, ρ_G, μ_L, μ_G, σ, D, g, θ, ϕ, U_{LS}, and U_{GS}, where subscripts L and G represent liquid and gas, respectively, ρ is density, μ is viscosity, σ represents the surface tension, D is the channel diameter, θ is the channel angle of inclination with respect to gravity force, ϕ is the contact angle, g is the gravitational acceleration, and U_{LS} and U_{GS} are the liquid and gas superficial velocities, respectively. Since there are three relevant fundamental dimensions (time, length and mass), eight independent dimensionless parameters can be defined. The independent dimensionless parameters can be chosen as: $\Delta\rho/\rho_L$ (where $\Delta\rho = \rho_L - \rho_G$), θ, ϕ, and

$$Eo = \frac{\Delta\rho\, g\, D_H^2}{\sigma} \tag{8.1}$$

$$We_{LS} = \frac{U_{LS}{}^2 D_H \rho_L}{\sigma} \tag{8.2}$$

$$We_{GS} = \frac{U_{GS}{}^2 D_H \rho_G}{\sigma} \tag{8.3}$$

$$\mathrm{Re}_{LS} = U_{LS} D_H / \nu_L \tag{8.4}$$

$$\mathrm{Re}_{GS} = U_{GS} D_H / \nu_G \tag{8.5}$$

where ν is the kinematic viscosity, and Eo, We, and Re stand for $Eötvös$, Weber and Reynolds numbers, respectively. Other relevant and widely-used dimensionless parameters include the Bond number, $Bo = D_H / \sqrt{\sigma/(g\,\Delta\rho)}$; Capillary number, $Ca = \mu_L U_{LS} / \sigma$; phase Froude numbers, $Fr_{GS} = U_{GS}^2 / (g\,D_H)$ and $Fr_{LS} = U_{LS}^2 / (g\,D_H)$; Ohnesorge number $\Gamma = \mu_L / (\sigma D_H\ \rho_L)^{\frac{1}{2}}$; and Suratman number $Su = \sigma \rho_L D_H / \mu_L^2$. These can all be derived by manipulating and/or combining the aforementioned dimensionless parameters.

In a class of microchannels of interest to a wide range of applications, $Eo < 1$; at least one of the Weber numbers is of the order of $1\sim10^2$; and $Re_{LS} \geq 1$; whereby the surface tension dominates buoyancy while inertia is important. Similar conditions, however, apply to the two-phase flow in microgravity as well, indicating that important similarities between two-phase flow processes in the two system categories should be expected.

Zhao and Rezkallah (1993), Rezkallah (1996), and more recently Lowe and Rezkallah (1999) developed two-phase flow transition models for microgravity channel flows based on phasic Weber numbers. Based on the argument that inertia and surface tension are the dominant forces in microgravity two-phase flow, Zhao and Rezkallah used the phasic Weber numbers $We_L = U_L{}^2 D \rho_L / \sigma$ and $We_G = U_G{}^2 D \rho_G / \sigma$ (where U_L and U_G are phase velocities) as the most appropriate dimensionless parameters for the correlation of the flow

regime transitions. Furthermore, they argued that the entire flow regime map can be divided into three zones: the surface tension dominated zone, including bubbly and slug regimes, where surface tension effect predominates inertia; the inertia-dominated zone, including annular flow regime, where inertia is significantly larger than the surface tension force; and the transition zone, where inertial and surface tension forces are comparable. In view of the difficulty associated with the calculation of phase velocities, however, they cast their regime transition models using We_{LS} and We_{GS}. Zhao and Rezkallah (1993) suggested $We_{GS} \approx 1$ as the upper bound for surface tension-dominated zone, and $We_{GS} \approx 20$ as the lower bound for the inertia-dominated zone. Revisions were subsequently made by Rezkallah (1996) and Lowe and Rezkallah (1999), whereby the $We_{GS} = \text{const}$ transition lines were replaced with transition lines approximately following $We_{GS} \propto We_{LS}^{0.25}$.

In microchannels operating within the aforementioned parameter range of interest, similar to the microgravity case, surface tension and inertial forces are likely to determine, or at least play significant roles with respect to the flow regimes and their transitions. The role of viscosity is likely to be more important in microchannels, however. Nevertheless, some useful similarities between the flow regime transitions in microchannels and channels operating under microgravity conditions should be expected.

8.2 Experimental Data

Table 8.1 is a summary of the available relevant experimental investigations utilized in this study. In some of these investigations two or more channel diameters were used. However, only experimental data representing near-circular channels for which

$D_H \lesssim 1.5\,mm$ are shown. In such channels, with air/water-like fluids, flow regimes are insensitive to the channel orientation when $D_H \lesssim 1.0\,mm$. This is in approximate agreement with the following criterion proposed by Suo and Griffith (1964) for negligible buoyancy effect: $Bo^{1/2} \lesssim 0.3$, or equivalently, $D_H \lesssim 0.3\lambda$ where $\lambda = \sqrt{\sigma/(g\,\Delta\rho)}$ represents the Laplace length scale. Significantly larger channels, as well as narrow rectangular or annular flow passages, lack the afore-mentioned distinct microchannel characteristics and will not be considered. Some experimental data dealing with air-water and steam-water flow in much smaller round channels ($D = 10 \sim 100\,\mu m$) have been performed by Serizawa and Feng (2001). These data show complicated flow patterns some of which are different than those common in channels in the 1-*mm* range. The major regimes included bubbly, slug (dominated by large gas plugs), liquid ring (a regime characterized by a contiguous gas core with a periodic structure that includes thick, ring-like, annular liquid films), liquid lump (a regime dominated by discrete liquid lumps), and liquid droplet flow (similar to the aforementioned froth flow regime). Other, more complicated flow regimes have also been observed by Serizawa and Feng. These data will not be addressed, since they evidently deal with a channel size range outside the range of interest here. Some important attributes of the experiments listed in Table 8.1 of particular interest here are briefly mentioned.

The data of Triplett et al. (1999) were obtained with air and water at near-atmospheric pressure and room temperature, in circular channels with 1.1 and 1.45 *mm* inner diameter test sections, and in microchannels with semi-triangular (equivalent triangular with one corner smoothed) cross-sections with 1.09 and 1.49 *mm* hydraulic diameters. Flow patterns and flow pattern maps were overall similar for the two channel cross-section geometries.

Table 8.1: Summary of experimental data used in the present study

Source	Test Section Characteristics	Fluids	Pressure and Temperature	Gas Superficial Velocity (m/s)	Liquid Superficial Velocity (m/s)	Observed Flow patterns
Damianides and Westwater (1988)	1.0 *mm* I. D. Horizontal glass tube	Air-Water	Atmospheric pressure and 20^0 C	0.715 ~ 55.3	0.0095 ~ 1.53	Dispersed-bubbly, Bubbly, Plug, Slug, Pseudo-slug, Dispersed-droplet, and Annular
Barajas and Panton (1993)	1.6 *mm* I. D. 34^0 Inclined horizontal	Air-Water	Room conditions (Atmospheric pressure and 25^0C)	0.1 ~ 100.0	0.003 ~ 2.0	Bubbly, Dispersed, Plug, Slug, Annular, Wavy; and Rivulet for partially non-wetting conditions
Mishima et al. (1995)	1.05 *mm* I. D. Vertical round tube	Air-Water	Room conditions	1.0 ~ 80.0	0.5 ~ 20.0	Slug and Annular
Coleman and Garimella (1999)	1.3 *mm* I. D. Horizontal round tube	Air-Water	Room conditions	1.0 ~ 100	0.1 ~ 10.0	Bubbly, Plug, Slug, Wavy-annular, Annular, and Dispersed
Triplett et al. (1999)	1.1 *mm* I. D. Horizontal round tube; Semi-triangular channel with D_H = 1.1 and 1.49 *mm*	Air-Water	Room conditions	0.04 ~ 100.0	0.04 ~ 8.0	Bubbly, Slug, Churn, Slug-annular, and Annular
Yang and Shieh (2001)	1.0 *mm* I. D. Horizontal round tube	Air-Water	Room conditions	0.21 ~ 75.0	0.014 ~ 1.34	Bubbly, Plug, Slug, Slug-annular, Annular, and Dispersed
Zhao and Bi (2001)	0.866 and 1.443 *mm* D_h Equilateral triangular vertical channel	Air-Water	Room conditions	0.1 ~ 100.0	0.1 ~ 10.0	Bubbly, Slug, Churn, Annular; and Capillary–bubbly in the smaller channel

Barajas and Panton (1993) were concerned with the effect of surface wettability on flow regimes in microchannels, and used air and water at room conditions, in microchannels made of different materials such that contact angles in the $34^0 \sim 106^0$ range were obtained. Overall, the flow regime transition lines were relatively insensitive to the contact angle when the contact angle was in the $\theta \leq 74^0$. With $\theta = 106^0$, however, the regime transition lines were significantly displaced. Furthermore, wavy and annular flow patterns were partly replaced with rivulets in tests with large contact angles. Their data representing $\theta = 34^0$ (which were similar to their data with $\theta = 74^0$) are used here.

Zhao and Bi (2001) used equilateral triangular-cross section channels with D_H = 0.87, 1.44 and 2.89 *mm*, and observed the occurrence of all major flow regimes. Their smallest test section supported, however, a novel capillary-bubbly flow pattern at very low liquid superficial velocities, characterized by a single train of ellipsoidal bubble. Mishima et al. (1995) used vertical test sections with D_H = 1.05 ~ 4.08 *mm*. With their smallest channel, they only identified slug and annular flow patterns, however.

8.3 Flow Regime Maps

In accordance with the above discussion, we divide the entire flow regime map into four regions.

a) The surface tension-dominated region, including bubbly, plug, and slug (where a flow pattern dominated by large and elongated bubbles is meant).

b) Inertia-dominated zone 1, including annular and wavy-annular regimes.

c) Inertia-dominated zone 2, including the dispersed flow regimes.

d) Transition zone.

As mentioned earlier, microgravity two-phase flow patterns have been divided into three groups: surface tension dominated; inertia dominated; and transition. Careful review of the microchannel data, however, indicates that the above-mentioned four flow regime zones can be easily defined.

Comparison among the microchannel two-phase flow regime data is complicated and due to the inconsistent terminology used by various authors for some flow patterns (Triplett et al., 1999; Ghiaasiaan and Abdel-Khalik, 2001). Thus, in the above division of flow patterns distinction is made between slug flow regime, when it is defined as the pattern dominated by elongated, large bubbles (e. g. in Damianides and Westwater, 1988); and the flow pattern that represents transition from plug to annular flow, and is characterized by large waves superimposed on an otherwise separated phases that intermittently block the channel (e. g., Yang and Shieh, 2001). Also, the flow pattern referred to as churn flow by Triplett et al. (1999) in fact included two different regimes according to most of the other investigators: churn flow characterized by unstable and aerated long bubbles similar to the pseudo-slug regime as defined by Suo and Griffith (1964) and frothy-slug defined by Zhao and Rezkallah (1993); and churn flow characterized by churning waves and froth. The latter flow pattern, furthermore, appears to have been identified as dispersed flow by some of the other investigators (Damianides and Westwater, 1988; Barajas and Panton, 1993; Coleman and Garimella, 1999; Yang and Shieh, 2001). In view of the apparent inconsistency regarding the latter flow pattern, it will be addressed as froth flow in the forthcoming

discussions. In the figures, however, "(dispersed)" will be included in reference to this flow regime.

Zhao and Bi (2001) identified a churn flow pattern based on pressure fluctuation characteristics which occupied a transition zone between slug and annular flow patterns. Comparison with the experimental data of Damianides and Westwater (1998), Triplett et al. (1999), and others, however, shows that Zhao and Bi's churn flow may be the same as the slug-annular regime of the latter investigators, and the wavy-annular regime of others.

Figures 8.1 and 8.2 displays the transition lines representing the boundaries among the aforementioned flow regime zones, in U_{LS} vs. U_{GS}, and We_{LS} vs. We_{GS} coordinates, respectively. Only the data that represent near-circular microchannels with $D_H \leq 1\ mm$ are depicted, and other data sets will be discussed shortly. With the exception of the data of Mishima et al. (1995) and Zhao and Bi (2001), all other data in the figures are in overall agreement. Mishima et al. (1995) only distinguished slug and annular regimes in tests with their smallest channel, apparently disregarding the flow patterns that represent transition between slug and annular flow regimes. The churn-slug transition line of Triplett et al. (1999) also is not shown since, as explained earlier, the churn flow region of Triplett et al. in fact included the dispersed flow and the flow pattern characterized by aerated long bubbles. The latter flow pattern is included in the transition zone here, however. The discrepancy among the data with respect to regime transition lines are at least partly a result of the uncertainty in visually distinguishing subtle regime variations, which is particularly difficult at low liquid flow rates. The data of Zhao and Bi (2001) will be discussed shortly. The overall good agreement among the displayed data with respect to the aforementioned major flow patterns supports the feasibility of an empirical flow regime map. Figures 8.1 and 8.2

show that flow regime transition lines can be easily defined using either coordinate system. Weber number coordinates, which are dimensionless and utilize the potential similarity with microgravity, may be more appropriate. It should, however, be emphasized that the transition zone in the flow regime maps covers a number of complex and subtle flow patterns, including the aerated-slug and pseudo-slug flows, and possibly others. Detailed characterization of these flow regimes and their transitions is difficult due to the scarcity of data.

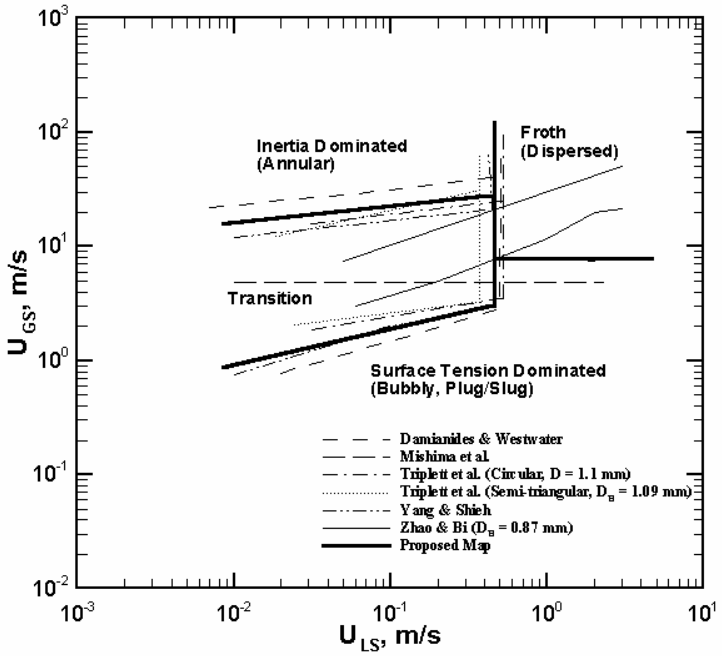

Figure 8.1: Flow regime transition lines for circular and near-circular channels with $D_H \leq 1\ mm$, using superficial velocities as coordinates.

The regime transition lines fitted to all relevant data for air-water flow in circular and near-circular microchannels with $D_H \lesssim 1.0\,mm$, and recommended for regime transition predictions, are also depicted in Figure 8.2, and can be represented by the following expressions:

- Surface tension dominated zone:
    - For $We_{LS} \leq 3.0$:

$$We_{GS} \leq 0.11\, We_{LS}^{0.315} \tag{8.6}$$

    - For $We_{LS} > 3$:

$$We_{GS} \leq 1.0 \tag{8.7}$$

- Annular flow zone (inertia dominated zone 1):

$$We_{GS} \geq 11.0\, We_{LS}^{0.14} \tag{8.8-a}$$

$$We_{LS} \leq 3.0 \tag{8.8-b}$$

- Dispersed flow zone (inertia dominated zone 2):

$$We_{LS} > 3.0 \tag{8.9-a}$$

$$We_{GS} > 1.0 \tag{8.9-b}$$

Two major influences with the aforementioned microgravity two-phase flow regime maps can be emphasized. First, the slopes of the regime transition lines between the surface tension-dominated and inertia-dominated zones and the transition zone are different from the approximate $We_{LS} \propto We_{GS}^{0.25}$ relation that applies to microgravity (Lowe and Rezkallah, 1999). More importantly, a frothy flow region can be easily defined and its borders correlated here. It represents conditions when the liquid and gas inertias are comparable, and may be attributable to the relative importance of liquid viscous effects in microchannels.

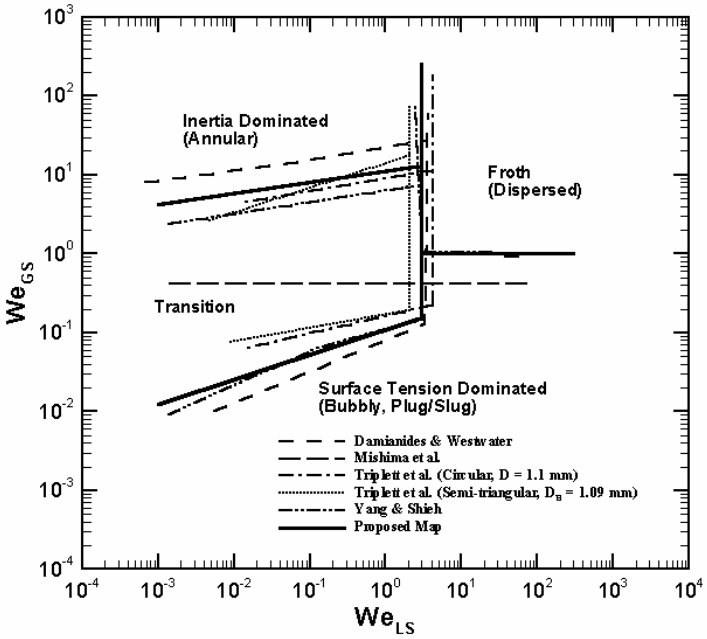

Figure 8.2: Flow regime transition lines for circular and near-circular channels with $D_H \leq 1\ mm$, using Weber numbers as coordinates.

8.4 Effects of Channel Hydraulic Diameter, Geometry, and Orientation

All the displayed data in Figure 8.1, as noted earlier, represent air-water flow in circular and near-circular (triangular with one corner smoothed) channels with $D_H \leq 1\ mm$. Therefore, the flow regime model proposed in the previous section should be applied to other geometric and flow conditions with caution. To better illustrate the potential weaknesses of the proposed method, the effects of channel size and cross-section geometry are now discussed. It is emphasized, however, that the range of interest is limited to $D_H \lesssim \lambda/2$.

The flow regime transition lines of Triplett et al. (1999) for their Semi-Triangular channel with $D_H = 1.49\ mm$, Barajas and Pantom (1993), and Coleman and Garimella (1999)

for their test sections with $D_H = 1.3\ mm$, are shown in Figures 8.3 and 8.4, and are compared with the average transition lines obtained with smaller test sections. Flow regimes are depicted in We_{LS} vs. We_{GS} conditions only, for brevity. The trends to be discussed are similar when U_{LS} and U_{GS} coordinates are used, however. Also depicted in the figures are the relevant regime transition lines of Zhao and Bi (2001) representing their data with $D_H = 1.44\ mm$. Figure 8.4 indicates that the mean regime transition line representing the transition zone-surface tension dominated zone regime change (Eq. (8.6)) is in good overall agreement with the data. Only fair agreement can also be noted with respect to the transition zone-annular zone boundary (Eq. (8.8)), however. The available data disagree with respect to the boundaries of the dispersed flow regime zone, furthermore, and no clear and consistent trend can be deduced from the data. Complications associated with the exact definition of this flow regime may cause the apparent disagreement. More experiments are evidently needed before the effect of channel size can be ascertained, and incorporated in the regime transition expressions if needed.

The effect of channel cross-section geometry can also be assessed by comparison among the data of Zhao and Bi (2001), Triplett et al. (for their semi-triangular channels), and the remainder of the data. The transition lines of Zhao and Bi (2001) for their smaller test section deviates from the remainder of the date in Figure 8.2, and suggests that the flow patterns in a triangular test section with sharp corners may in fact be different than the flow patterns in a circular channel with a diameter equal to its hydraulic diameter.

Most of the experimental studies dealing with two-phase flow in near-circular microchannels have used horizontal test sections, and insensitivity of flow regimes and their transition boundaries to channel orientation has been expected (Ghiaasiaan and Abdel-

Khalik, 2001). The data of Zhao and Bi (2001), however, appear to indicate the absence of froth (dispersed) flow in their vertically orientated test section, in disagreement with virtually all other data.

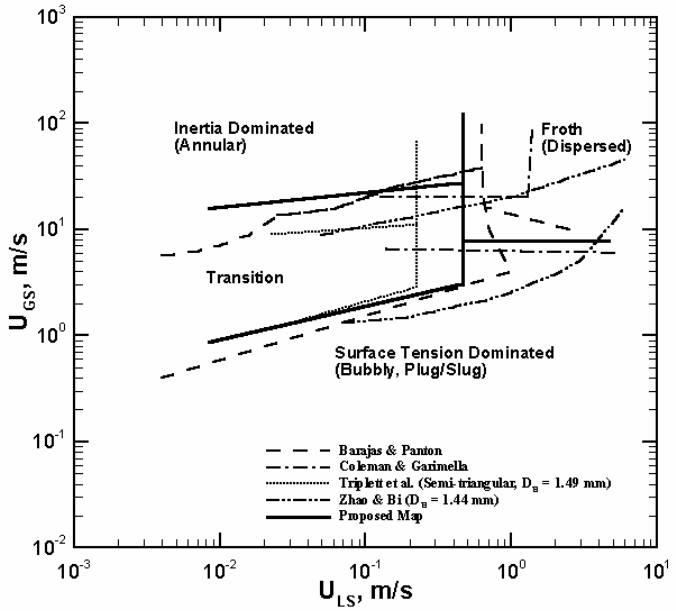

Figure 8.3: Flow regime transition lines for circular and near-circular channels with $D_H > 1\ mm$, using superficial velocities as coordinates.

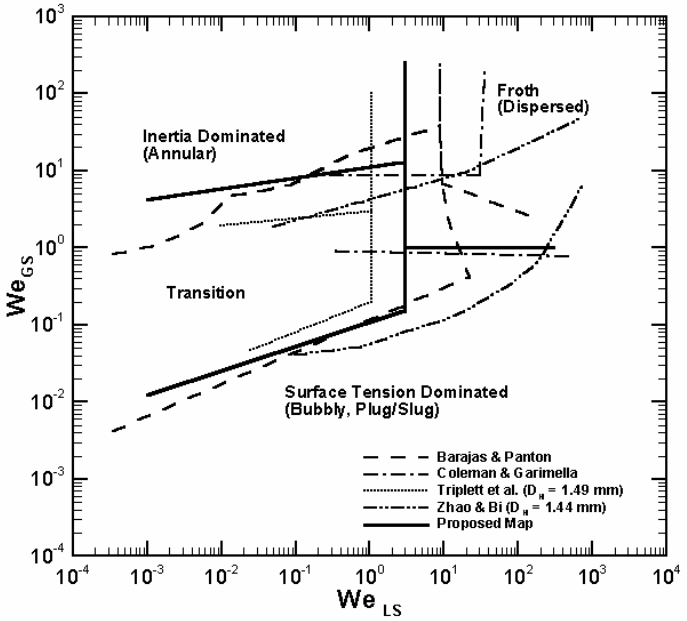

Figure 8.4: Flow regime transition lines for circular and near-circular channels with $D_H > 1\ mm$, using Weber numbers as coordinates.

8.5 Summary and Concluding Remarks

1. For $D_H \leq 1$ *mm* channel size range, the available data for near-circular microchannels and air-water like fluid pairs, are in reasonable agreement. For these conditions, a simple Weber number-based flow regime map that divides the entire map into four zones (surface tension-dominated, annular, froth, and transition) could be devised.

2. For $D_H > 1$ *mm*, the aforementioned flow regime map is in fair agreement with available data, with the exception of the boundaries of the froth (dispersed) flow regime zone.

3. The limited available data indicate that triangular channels with sharp corners may support somewhat different regimes and transition boundaries than near-circular channels.

4. Systematic experiments addressing the effects of channel cross-section size and geometric configuration are needed.

5. Virtually all available data represent air/water and air/water-like fluid pairs at room conditions. The potential effects of fluid properties are thus unknown, and systematic experimental studies using other fluids are needed.

CHAPTER 9: STRATIFIED FLOW TRANSITION FOR NEAR-HORIZONTAL FLOW PASSAGES

A brief background discussion regarding this topic was given in Section 1.6, and the relevant literature was reviewed briefly in Section 3.6.

9.1 Outline of the model

The criterion of Taitel and Dukler (1976) for the instability of stratified flow can be represented as:

$$U_G \geq C\left[\frac{(\rho_L - \rho_G)g}{\rho_G}\frac{A_G}{(dA_L/dh_L)}\right]^{\frac{1}{2}} \tag{9.1}$$

The coefficient $C \approx A'_G / A_G$ is difficult to predict theoretically. When C = 0.5 is assumed, the model is consistent with the expression of Wallis and Dobson (1973) (Eqn. (3.2)). For circular channels, Taitel and Dukler proposed:

$$C = 1 - h_L / D \tag{9.2}$$

with h_L predicted from the following equilibrium momentum balance on the gas and liquid phases:

$$\tau_{WG}\frac{S_G}{A_G} - \tau_{WL}\frac{S_L}{A_L} + \tau_I S_I\left(\frac{1}{A_L} + \frac{1}{A_G}\right) = 0 \tag{9.3}$$

The model of Taitel and Dukler (1976) has been shown to do well for some flow and geometric configurations other than horizontal pipes and rectangular channels as well, provided that the parameter C is appropriately adjusted. For example, for countercurrent

flow in pipes, C = 0.5 when the channel is horizontal, and C is quite sensitive to the channel gradient when the channel is inclined (Johnston (1985)). Krishna and Kowalski (1984) applied the model to air-water experimental data in a horizontal rod bundle by correlating C in terms of void fraction and the ratio between the interfacial and wetted surface areas.

Figure (9.1) is a schematic of a horizontal, annular channel subject to stratified flow. Equations (9.2) and (9.3) are applied to the displayed system in this study. Details of the analysis for the application of the model of Taitel and Dukler (1976) to the depicted horizontal annular channel can be found in the Appendix D.

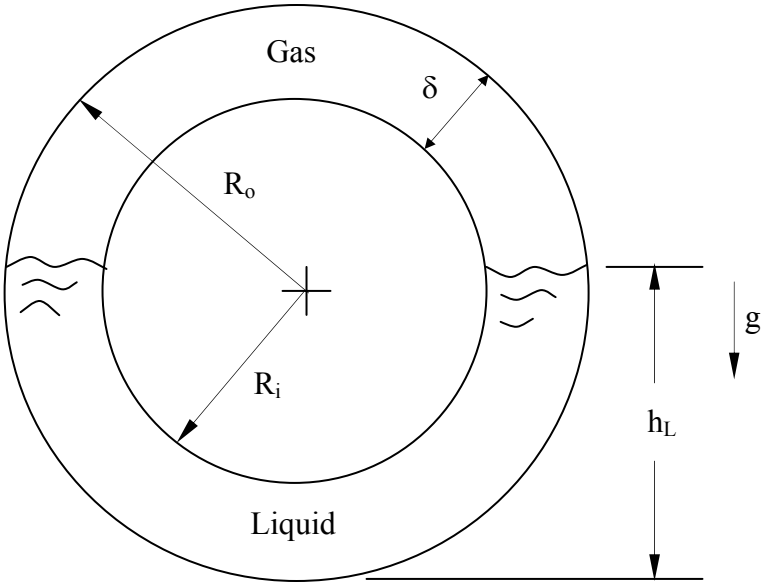

Figure 9.1: Schematic of an annular horizontal channel.

9.2 Experimental Data

The experimental data of Osamusali and Chang (1988) and Ekberg et al. (1999) are used in this study. Osamusali and Chang performed experiments using air and water in horizontal annuli with D_i = 5.08 cm. Three different outer channel diameters were used in their experiments, leading to D_i/D_o = 0.375, 0.5 and 0.625. They developed empirical flow

regime maps based on their experiments. Figure 9.2 displays the portion of their flow regimes map that is relevant to this study.

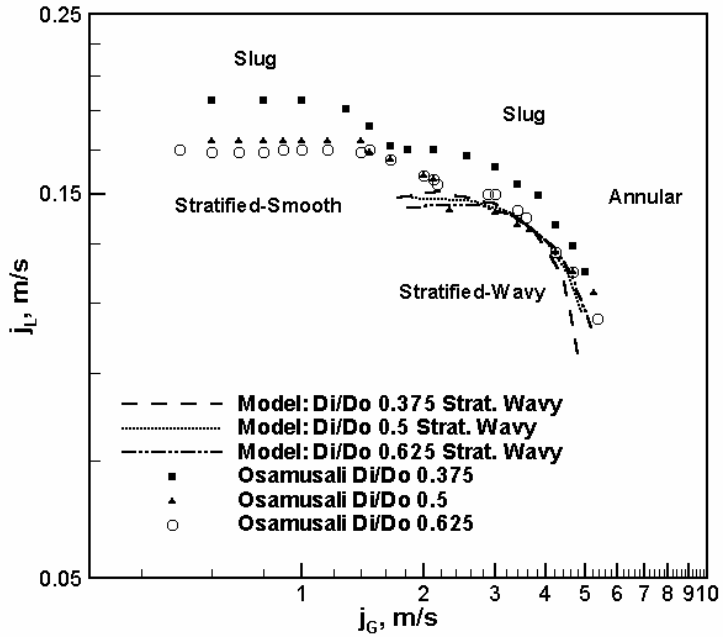

Figure 9.2: Stratified and wavy flow regime boundaries of Osamusali and Chang (1988).

Ekberg et al. (1999) performed air-water experiments using two thin horizontal annuli. Their test parameters covered the stratified flow range only for one of their test sections, for which D_i = 33.2 mm and D_o = 35.2 mm. Figure 9.3 displays the portion of their flow regime map that is of interest to this study.

9.3 Results and Discussion

Equations (9.1) and (9.3), along with the expressions outlined in the Appendix D, were applied to the aforementioned data of Osamusali and Chang (1988) and Ekberg et al. (1999), as described below.

For the data of Osamusali and Chang (1988), the flow rates for several points that defined their stratified-to-plug and wavy-to-slug regime transition lines, as depicted in Figure (9.2), were calculated. Using Eqn. (9.3), all equilibrium stratified flow parameters including h_L, were then calculated. Equation (9.1) with equal sign was then applied with C as the unknown, leading to the values for parameter C.

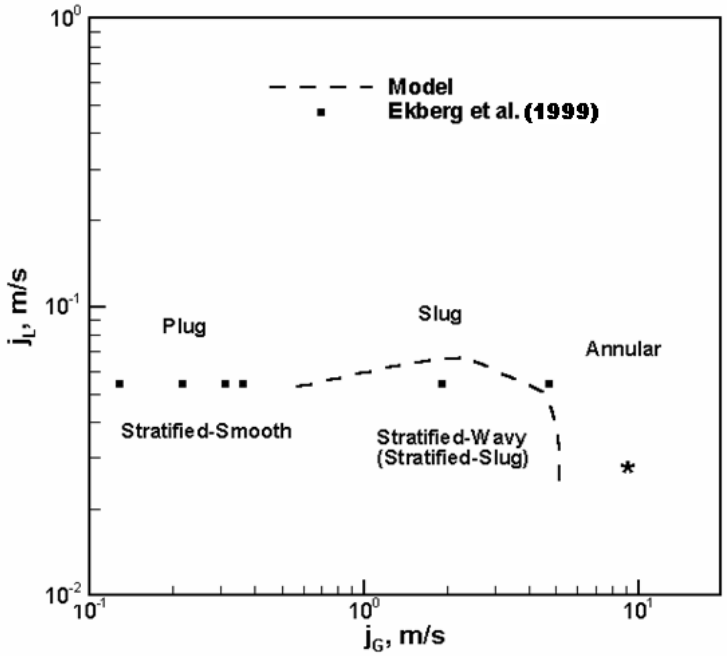

Figure 9.3: Stratified and wavy flow regime boundaries of Ekberg et al. (1999). (The data point designated by * represents transition to annular flow.)

The procedure for the analysis of the data of Ekberg et al. (1999) was similar, with the difference that calculations were performed for their discrete data points that defined the lower limits of plug and slug flow regimes in the Mandhane (j_L vs. j_G) coordinates.

The calculated values of parameter C for the three test sections of Osamusali and Chang (1988) are displayed in Figures 9.4, 9.5 and 9.6, using $\xi = (h_L/\delta)(D_i/D_o)$ as a coordinate. For these data, h_L/D_o predicted by the equilibrium stratified flow model covers

the range 0.3 ~ 0.86 (0.3 ~ 0.68 for transition out of stratified-wavy). A strong systematic dependence of C on flow regime is apparent, and three distinct zones can be evidently defined: the flow regime change out of stratified-wavy; regime change out of stratified-smooth; and a transition zone in-between. Furthermore, C = 0.45 approximately applies to the transition out of the stratified-wavy regime in all three figures. In the zone where regime change out of stratified-smooth occurs, furthermore, C appears to be a linear function of ξ. The straight lines, however, are different for the three figures and no conclusion can be drawn regarding the generality of this apparent linear dependence without more data.

The flow regime transition lines predicted using C = 0.45 for the regime change out of stratified-wavy are displayed in Figure 9.2 for the data of Osamusali and Chang (1988), confirming good agreement.

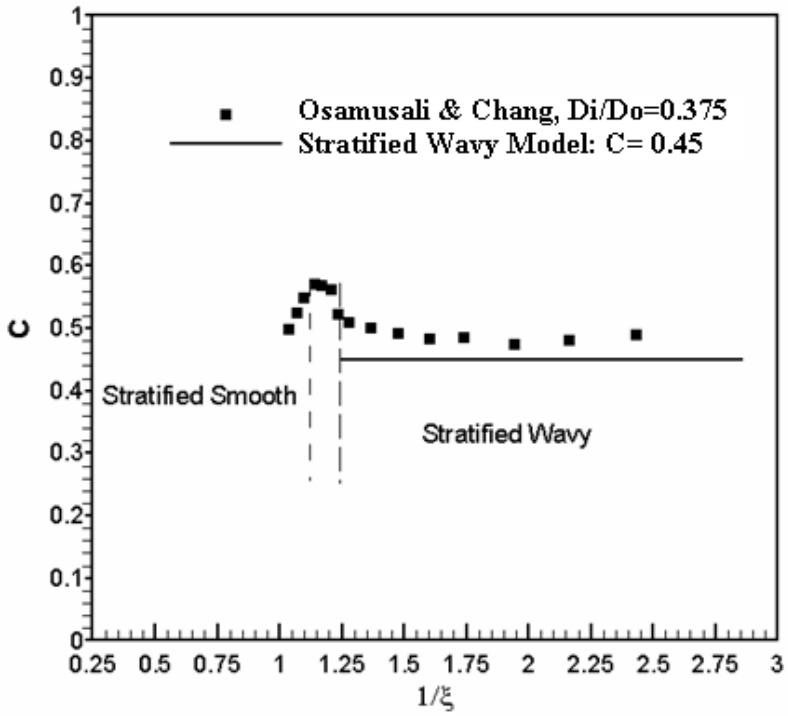

Figure 9.4: Coefficient C for the data of Osamusali and Chang (1988), with D_i/D_o = 0.375.

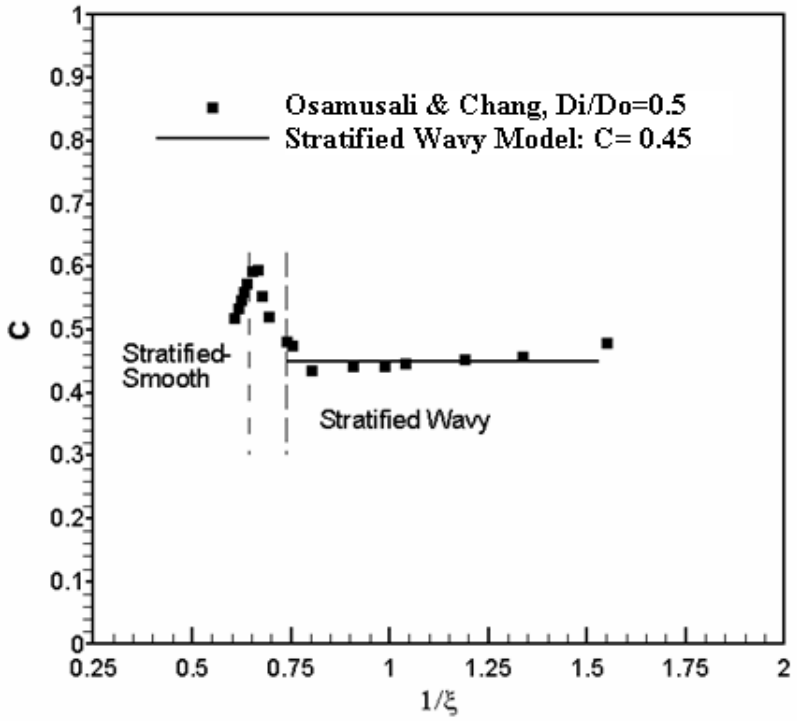

Figure 9.5: Coefficient C for the data of Osamusali and Chang (1988), with $D_i/D_o = 0.5$.

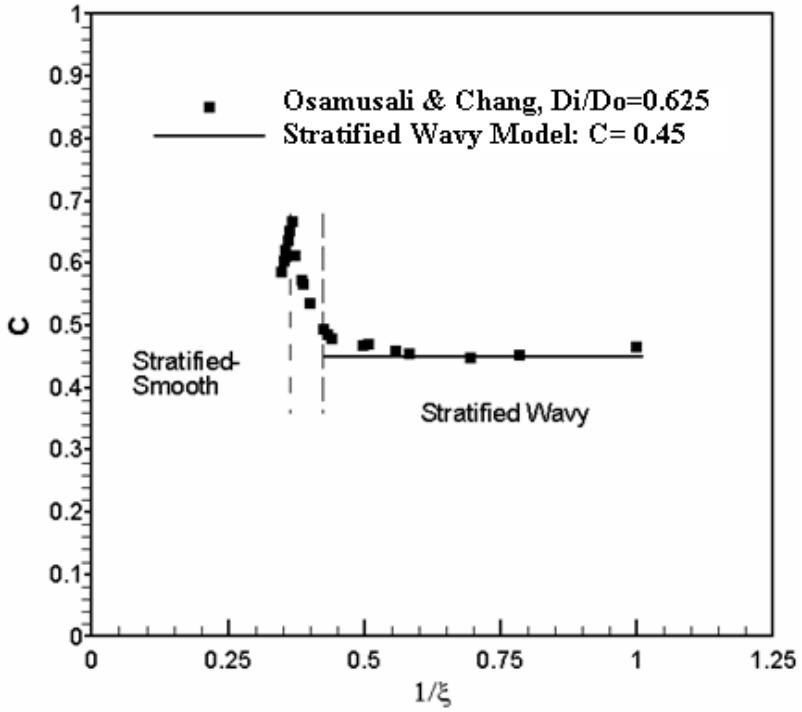

Figure 9.6: Coefficient C for the data of Osamusali and Chang (1988), with $D_i/D_o = 0.625$.

The applicability of C = 0.45 for regime transition from stratified-wavy to slug flow was also tested for the experiments of Ekberg et al. (1999). As mentioned earlier, only the available discrete data points that defined the upper bounds of stratified flow region in Figure (9.3) were used in the analysis, hence the apparent sparse and scattered data. The parameter h_L/D_o, as predicted by the equilibrium stratified model, covered the range 0.31 ~ 0.98 (0.31 ~ 0.9 for transition out of stratified-wavy regime) for these experiments. As noted in Figure (9.3), C = 0.45 appears to agree with the data that define the boundary of the stratified-wavy regime at least marginally.

According to the above calculations, based on the available experimental data, the criterion of Eqn. (9.1) with C = 0.45 can be recommended for predicting the conditions that lead to flow regime change out of the stratified-wavy in horizontal annuli subject to air/water-like gas and liquid mixtures.

9.4 Concluding Remarks

The stability of stratified gas-liquid two-phase flow in horizontal annuli subject to air-water two-phase flow was investigated in this study. The widely-used semi-analytical model of Taitel and Dukler (1976) was modified based on the air-water experimental data of Osamusali and Chang (1988) and Ekberg et al. (1999), leading to a simple method for the prediction of conditions that lead to flow regime transition out of stratified-wavy.

CHAPTER 10: DISTORTION OF MICROBUBBLES DUE TO THERMOCAPILLARY IN MICROCHANNELS

A brief background discussion regarding this topic was given in Section 1.8, and the relevant literature was reviewed briefly in Section 3.7.

10.1 Interfacial Temperature of a Stationary Bubble in a Heated Microtube

10.1.1 Modeled System

Figure 10.1 is the schematic of a microbubble cap, assumed to exist in quasi-steady state in the depicted heated microtube. An elongated microbubble in this configuration can act as an effective micro heat pipe. Such microbubbles are also heterogeneously generated and used as actuators in microsystems. For simplicity, the microtube surface is assumed to remain at a known uniform temperature, T_w. The bubble, furthermore, is assumed to contain pure vapor at a uniform temperature, T_B. The liquid phase (water) is at P_∞, while the pressure in the bubble, P_B, is uniform. When $T_w > T_B$, vigorous evaporation takes place at the interphase. As will be shown later, the interphase temperature, T_i, is non-uniform, causing the distortion of the interphase geometry. At this point, however, the interphase is assumed to remain a hemispherical cap. This assumption, it is emphasized, is used only to simplify the estimation of interphase temperature.

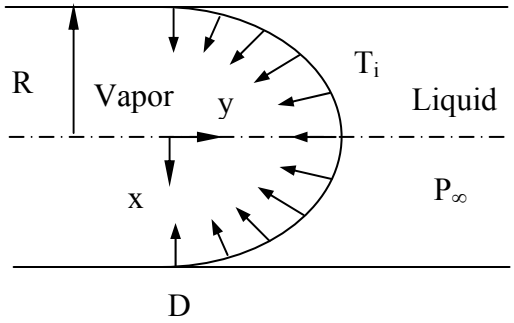

Figure 10.1: Modeled stationary bubble cap in a microtube.

Mechanical equilibrium at point D in Figure 10.1 requires that:

$$P_B = P_\infty + \frac{2\sigma_w}{R} \tag{10.1}$$

Since spherical cap is assumed, however, in these calculations σ_w was replaced with $\overline{\sigma}$, calculated at $\frac{1}{2}(T_B + T_W)$ temperature. The evaporation at interphase can be modeled using the simple kinetic theory (Kao and Kenning, 1972; Gaddis, 1972; Marek and Straub, 2001), assuming that the evaporation coefficient is equal to unity (Maa, 1967). Therefore, at any point on the liquid-vapor interphase:

$$q_i'' = \dot{m}_i'' \hat{h}_{fg} \tag{10.2}$$

$$\dot{m}_i'' = \sqrt{\frac{M}{2\pi \overline{R}}} \left[\frac{P_{sat}(T_i)}{\sqrt{T_i}} - \frac{P_B}{\sqrt{T_B}} \right] \tag{10.3}$$

$$T_B = T_{sat}(P_B) \tag{10.4}$$

10.1.2 Numerical Simulation Method

Heat transfer through the liquid phase is responsible for evaporation at the bubble-liquid interphase. This heat conduction was simulated using the finite-element ANSYS (2001) computer code. Axi-symmetric and two-dimensional, steady-state conduction was assumed. Nodalization was performed using the default grid generation package of ANSYS. Figure 10.2 depicts the grids used in a typical simulation. Approximately 1000 elements were used. Smaller cells were used in parts of the simulated system where steep temperature gradients are expected.

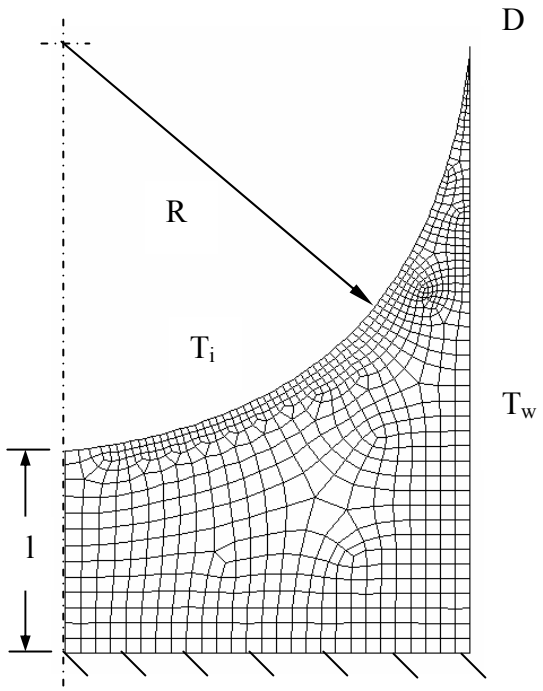

Figure 10.2: A typical nodalization scheme (R = 5 μm, l = 0.5 R).

The vapor-liquid interfacial temperature, T_i, is not known a priori, is expected to be non-uniform, and must be represented by Eqns. (10.3) and (10.4). To avoid tedious iterations, the following procedure was used, whereby the boundary condition at the

interphase was replaced with fictitious convection with non-uniform but known heat transfer coefficients. For each simulated case, knowing T_w, P_∞ and geometric parameters R and *l*, Eqns. (10.3) and (10.4) were numerically solved with T_i as a parameter, thereby deriving a table representing the function $q_i'' = f(T_i)$. Subsequently, a heat transfer coefficient, defined as $h(T_i) = q_i'' / (T_i - T_B)$, was curve-fitted to represent the aforementioned table. This fictitious heat transfer coefficient was then used to define the vapor-liquid interfacial boundary conditions in ANSYS calculations. This procedure was repeated for each simulation.

10.1.3 Calculation Results

Typical calculated temperature distributions are depicted in Figures 10.3 and 10.4. In both cases, T_w=145°C was assumed, representing about 20°C temperature difference between bubble and tube wall. A large temperature difference between the wall and bubble was used since bubble generation in microsystems is known to require large wall superheats. The non-uniformity of the interfacial temperature is evident in both figures. Indeed, for the case in Figure 10.3, T_i varies in the 124.46 to 145.0 °C range. For the case displayed in Figure 10.4, the range was 122.813 to 145.0 °C. These and other numerical calculations indicated that the interfacial temperature non-uniformity increases as R is reduced, and is relatively insensitive to *l* in the $0.2R < l < R$ range.

The strong non-uniform interfacial temperatures can evidently lead to significant thermocapillary effects due to the dependence of σ on T_i. Among these effects is the distortion of the bubble cap.

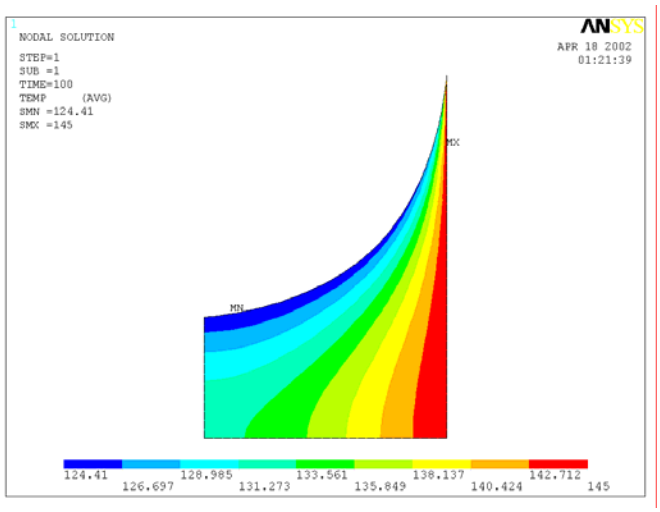

Figure 10.3: Temperature distribution for R = 5 μm, $T_w = 145\ ^0$ C, $P_\infty = 2$ bar.

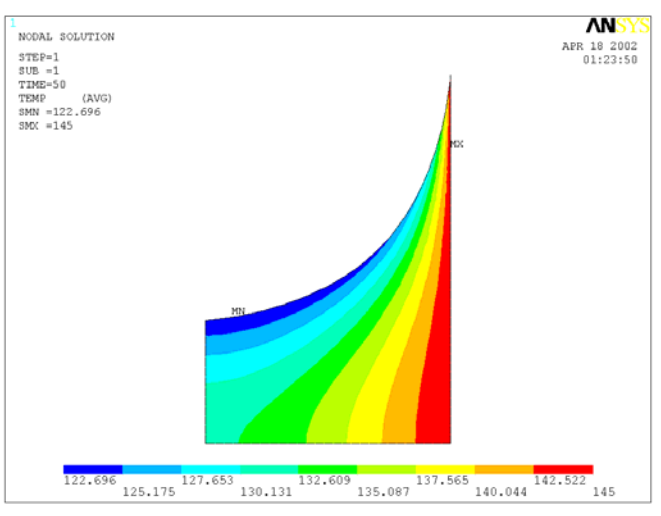

Figure 10.4: Temperature distribution for R = 20 μm, $T_w = 145\ ^0$ C, $P_\infty = 2$ bar

10.1.4 Bubble Shape

The thermocapillary effect on the shape of a heterogeneously generated bubble is now modeled. For generality, the case of a bubble that has formed on a circular-mouthed wall crevice in a subcooled liquid flow situation is modeled. The resulting model, however, can easily be applied to the bubble cap depicted in Figure 10.1, as will be shown later.

We consider a stochastically averaged bubble. The following assumptions are made (Chedester, 2002):

1. The bubble is axi-symmetric.
2. Hydrodynamic and inertial forces have a negligible effect on the bubble shape, and the bubble is at a quasi-steady state.
3. The bubble is surrounded by liquid in a thermal boundary layer with known, quasi-steady velocity distributions.
4. The bubble and the surrounding liquid represent a pure, single-component substance, without any impurity.
5. The pressure inside the bubble is uniform.

The rationale of the above mentioned assumptions are given in Chedester (2002).

A schematic of a bubble is depicted in Figure 10.5. The bubble is assumed to have a dry, circular footprint in accordance with Assumption 1 above, the radius of which is r_{co}. Mechanical equilibrium at any point on the bubble requires that

$$P_B - P_\infty = \sigma\left(\frac{1}{r_1} + \frac{1}{r_2}\right) \tag{10.5}$$

where r_1 and r_2 are the principle radii of curvature. At point D, assuming locally-spherical geometry, one can write:

$$r_1 = r_2 = \frac{r_{co}}{\sin\theta_o} \tag{10.6}$$

At any arbitrary point on the bubble surface, it can be shown that:

$$r_1 = \frac{\left(1 + y'^2\right)^{3/2}}{\left|y''\right|} \tag{10.7}$$

$$r_2 = \left|x\right|\left(1 + \frac{1}{y'^2}\right)^{1/2} \tag{10.8}$$

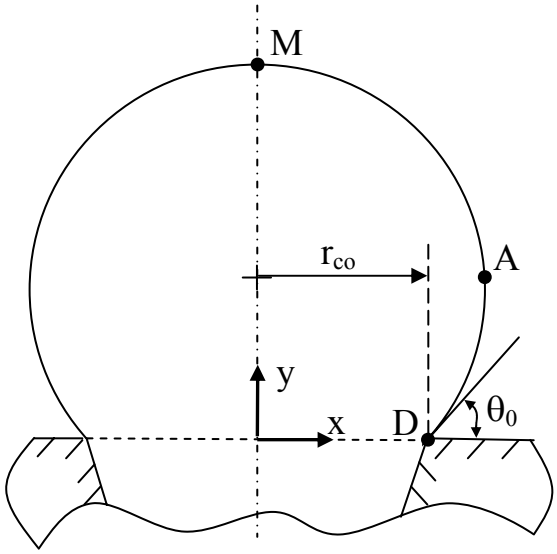

Figure 10.5: Schematic of heterogeneously generated bubble.

Substitution of Eqns. (10.7) and (10.8) in Eqn. (10.5) would provide the following differential equation, which determines the shape of the bubble.

$$\left|Y''\right| = \left(1 + Y'^2\right)^{3/2}\left[\frac{2\sigma_w}{\sigma} - \frac{1}{\left|X\right|\left(1 + 1/Y'^2\right)^{1/2}}\right] \tag{10.9}$$

where X and Y are non-dimensionalized coordinates corresponding to x and y, with $r_{co}/\sin\theta_o$ as the reference length scale. Equation (10.9) should be solved using the following boundary (initial) conditions. At $X = \sin\theta_o$, we have Y = 0; and:

$$\frac{dY}{dX} = \tan\theta_0 \tag{10.10}$$

10.1.5 Shape of Stationary Bubbles in a Heated Microtube

For the stationary vapor-bubble interfacial caps described previously and depicted in Figures 10.1 and 10.2, Eqns. (10.4-10.10) were numerically solved. For this purpose, coordinates x and y in Figure 10.5 were defined as those depicted in Figure 10.1; and $\theta_0 = \pi/2$ and r_{co} = R were assumed. Equation (10.9) was replaced with two coupled ordinary differential equations (ODEs) with Y and Z as dependent parameters, where Z = dY/dX. The ODEs were numerically integrated using the LSODA computer code (Petzold and Hindmarsh, 1997), which is based on a powerful and robust variable-order and variable-step numerical integration method suitable for stiff systems. The ODEs were integrated over the X > 0 and Y > 0 quarter plane. These calculations were initialed using dY/dX = -10^5 as the initial condition, representing point D in Figure 10.1. Numerical integration would continue until X = 0 was reached. In these calculations, the interphase temperatures were assumed to depend on x, and were borrowed for each simulated case from the corresponding ANSYS simulation described earlier.

Typical model calculation results are depicted in Figures 10.6 and 10.7, where the horizontal and vertical coordinates are x/R and y/R, respectively. The calculated profiles are compared with the spherical geometry. Significant distortions from sphere are evident. The interphase cap is stretched in the axial direction, due to higher surface tension near the axis of symmetry where the interfacial temperature is lower. As expected, parametric numerical calculations indicate that the distortion from spherical geometry is increased as the interfacial temperature non-uniformity is increased. The interphase temperature non-uniformity depends on the microtube size in two ways. Smaller tube radius implies stronger capillary effect, and hence higher distortion of the cap shape. On the other hand, smaller

tube radius implies lower conduction resistance in the liquid phase and therefore less severe temperature nonuniformity.

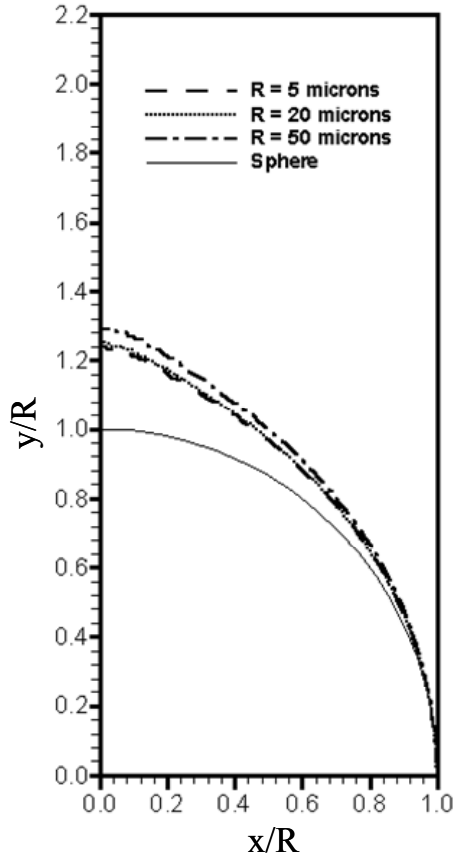

Figure 10.6: Profile of a stationary bubble cap in a heated microtube (P_∞ = 2 bar, l = 0.5 R, and $T_w = 145^0$ C)

The above analysis is of course idealized, and does not account for the momentum effect of the evaporation flux. The interphase temperature non-uniformity would also cause a thermocapillary-induced flow, which may augment heat transfer in the liquid, and may add complication to the interfacial geometry. Nevertheless, the analysis clearly indicates that assumed spherical interphase geometry in microbubbles could be unrealistic.

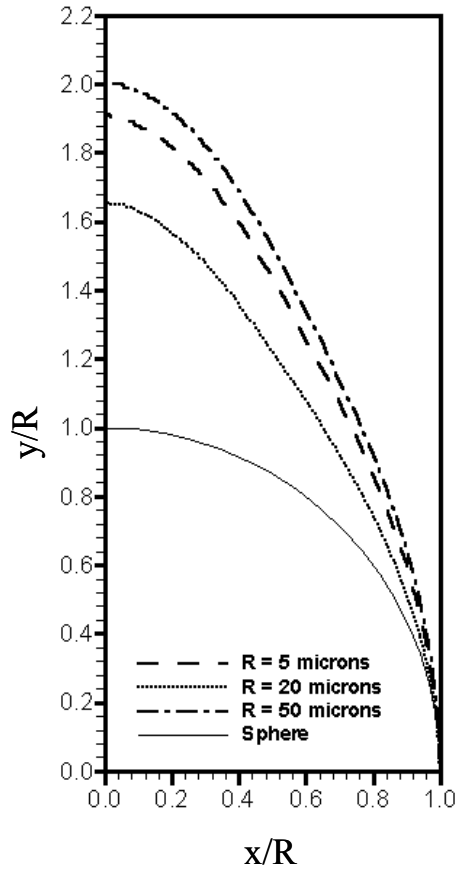

Figure 10.7: Profile of a stationary bubble cap in a heated microtube (P_∞ = 2 bar, l = 0.5 R, and $T_w = 190^0$ C)

10.2 Shape of Bubbles in a Forced-Flow Subcooled Boiling

Calculation of the bubble interphase temperature distribution is difficult for heterogeneously generated bubbles in forced-flow subcooled boiling due to the complicated liquid flow field. For our purpose, however, a simple estimation may be sufficient. During heterogeneous bubble growth a thin liquid film (microlayer) separates the bubble base from the heated surface, except for a dry centrally located area. Assuming that a similar phenomenology also applies to heterogeneous bubble growth in a microchannel, the liquid-vapor interphase temperature at point D (Figure 10.5) can be conservatively estimated by assuming a quasi-steady one-dimensional conduction through the liquid microlayer, and

representing the interfacial thermal resistance based on the simple kinetic theory. Assuming that the evaporation and condensation coefficients are both equal to unity (Maa, 1967), $T_{D,i}$, the interphase temperature at point D in Figure 10.5, can then be calculated using Eqns. (10.2) and (10.3), where T_i is replaced with $T_{D,i}$. The microlayer thickness is non-uniform, and is thickest at point D. The film thickness varies with time during the bubble lifetime (Abdelmassih et al., 1972). In view of the small scale of the microbubbles of interest, and given the uncertainty regarding the processes involved, the thermal resistance of the microlayer is neglected, and the local heat flux is estimated as:

$$q_i'' = q_w'' \tag{10.11}$$

The interphase temperature at the bubble's top (point M in Figure 10.5) can be estimated similarly, this time for condensation. The interphase temperatures at M and D evidently bracket the entire interfacial temperature distribution. For subcooled pool boiling, and assuming spherical bubble geometry, Marek and Straub (2001) have developed expressions for the interfacial temperature profile that well agree with the predictions of their detailed numerical calculations. Possible distortion from spherical geometry evidently may render the expressions inapplicable to our case. For simplicity, therefore, a linear profile, in terms of y, is assumed for the interphase temperature here.

The bubble pressure is obtained by applying the mechanical equilibrium to point D in Figure 10.5, whereby:

$$P_B - P_\infty = \frac{2\sigma_w \sin\theta_o}{r_{co}} \tag{10.12}$$

The thermocapillary force element acting on the liquid over an axi-symmetric surface element at *(x,*y), whose projection on the y-axis is *dy* long, can be shown to be:

$$dF_\sigma = 2\pi|x|\left(\frac{d\sigma}{dT}\right)\left(\frac{dT_s}{dy}\right)dy \tag{10.13}$$

Since the bubble is axi-symmetric, only the *y*-component of F_σ is finite. Accordingly, and after dividing through by *dx*, there results:

$$\frac{dF^*_{\sigma,Y}}{dX} = \frac{2\pi r_{co}}{\sigma_w \sin\theta_o}\left(-\frac{q''_w}{\mu_f c_{pf}}\right)\left(\frac{d\sigma}{dT}\right)\frac{|Y'|Y'}{\sqrt{1+Y'^2}}\frac{dT^+_s}{dy^+} \tag{10.14}$$

where, here and elsewhere, $\sigma_w\, r_{co} / sin\theta_o$ is used as the reference force. The thermocapillary force acting on the bubble will be equal to $F_{\sigma,y}$, but will be oriented in the negative *y* (downward in Figure 10.5) direction.

Several other forces, besides thermocapillary, act on a heterogeneously generated, bubble, and semi-empirical expressions have been derived for the prediction of these forces for macro system nucleate boiling (Zeng et al., 1993, 1993). For comparison, however, only the drag force is estimated here, since it is the main force assumed to lead to bubble detachment in subcooled boiling. The drag force is estimated according to

$$F^*_D = \frac{\rho_L u^{*2} r_{co} C_D u^{+2}_r}{2\sigma_w \sin\theta_o} \tag{10.15}$$

where u^+_r represents the dimensionless undisturbed, time-averaged liquid velocity at $y^+_{M/2}$, with y_M representing the bubble height (Figure 10.5). The drag coefficient is estimated using the correlations of Al-Hayes and Winterton (1981):

$$C_D = \frac{24}{\mathrm{Re}_B} \qquad \text{for} \qquad \mathrm{Re}_B < 20 \tag{10.16}$$

$$C_D = 1.22 \qquad \text{for} \qquad 20 < \mathrm{Re}_B < 400 \tag{10.17}$$

where

$$\mathrm{Re}_B = \frac{y_M u_r}{\nu_f} \tag{10.18}$$

The frontal area of the bubble is calculated from

$$\frac{dA_F^*}{dX} = 2|X|Y' \tag{10.19}$$

where $A_F^* = \dfrac{A_F}{\left(r_{co}/\sin\theta_o\right)^2}$.

The local undisturbed liquid velocity is obtained by noting that, for incompressible, fully-developed and constant-property flow in a circular tube (Ghiaasiaan and Laker, 2001):

$$\mathrm{Re} = \frac{\overline{U}D}{\nu_L} = 4\int_0^{R^+} u^+ dy^+ - \frac{4}{R^+}\int_0^{R^+} u^+ y^+ dy^+ \tag{10.20}$$

where $y^+ = yu^*/\nu_L$; $u^+ = u/u^*$; and

$$u^* = \sqrt{\tau_w/\rho_L} = \overline{U}\sqrt{f/8} = 2R^+\overline{U}/\mathrm{Re} \tag{10.21}$$

$$u^+ = \frac{1}{R^+}\int_{r^+}^{R^+} \frac{r^+ dr^+}{1+\varepsilon_M/\nu_L} \tag{10.22}$$

The above equations are used along with the eddy diffusivity model of Reichardt (1951):

$$\varepsilon_M / \nu_L = \kappa\left[y^+ - y_n^+ \tanh\left(y^+ / y_n^+\right)\right] \tag{10.23}$$

for $y^+ \le 50$, and

$$\varepsilon_M / \nu_L = \left(\kappa y^+ / 3\right)\left[0.5 + \left(r^+ / R^+\right)^2\right]\left(1 + r^+ / R^+\right) \tag{10.24}$$

for $y^+ > 50$, where $\kappa = 0.4$ and $y_n^+ = 11$.

10.2.1 Calculation Method

The parametric calculation results described in the next section were obtained as follows. For the assumed local microtube conditions, Eqns. (10.20-10.24) were first numerically solved, following the procedure detailed in (Ghiaasiaan and Laker, 2001). These numerical calculations were performed by using a total of 1800 radial nodes, with 1000 equal-sized nodes representing the $1 < r/R \le 0.85$ region of the tube cross-section, and another 800 equal-sized radial nodes for the remainder for the cross-section. The standard values of $\kappa = 0.4$ and $y_n^+ = 11$ were used for these calculations unless otherwise stated. Knowing the heat flux, $T_{D,i}$ was calculated from Eqns. (10.2,10.3,10.11). Then, Eqns. (10.9), (10.14), and (10.19) were numerically integrated over the $x > 0$ and $y > 0$ quarter plane. This was of course done by replacing Eqn. (10.9) with two coupled first-order ordinary differential equations (ODEs) with Y and Z as the dependent variables, where $Z = dY/dX$. The resulting four ODEs were numerically integrated using the LSODA package (Petzold and Hindmarsh, 1997). In each calculation, the ODEs were first integrated over the DA portion of the bubble surface in Figure 10.5, noting that $dY/dX > 0$, where for convenience the location of A was defined as the point where $dY/dX > 10^5$. The numerical

solution of the ODEs would then be re-initiated starting from point A, using $dY/dX = -10^5$ as an initial condition, and would continue until $X = 0$ was reached, bearing in mind that now $dY/dX < 0$.

10.2.2 Calculation Results and Discussion

The experiments of Vandervort et al. (1994) are used as the basis of parametric calculations here. These experiments addressed critical heat flux in a microchannel with D = 2.016 mm diameter in highly subcooled water. In the calculations, using the reported experimental conditions for a selected run, the location of the ONB point was first specified using the correlation of (Ghiaasiaan and Chedester, 2002). The local conditions at a point downstream from the ONB point, but significantly upstream from the CHF point, were then used for the parametric calculations. The selected local conditions were as follows: q" = 18800 kW/m^2; Re_L = 51380; $\overline{T}_L = 72.6^\circ C$; and P_L = 202 kPa. Several parametric calculations were performed. The bubble profiles for some of the parametric runs are displayed in Figures 10.8-10.12. Table 10.1 is a summary of assumed conditions for the parametric runs to be discussed below. Some important parameters related to the bubbles are summarized in Table 10.2.

Figures 10.8 and 10.9 depict the calculated quasi-steady profiles for bubbles forming on a crevice 4μm in radius. Figure 10.8 assumes $\theta_0 = 90^o$, and is meant to represent a hemispherical bubble consistent with the widely-used ONB models (Bergles and Rohsenow, 1964; Sato and Matsumura, 1963; Davis and Anderson, 1966). Figure 10.9, on the other hand, depicts a bubble with $\theta_0 = 50^o$, which has formed on a dry base 4μm in radius. In both

figures the horizontal and vertical coordinates are x/R_{B0} and y/R_{B0}, respectively, where R_{B0} is the radius of the spherical bubble that can be based on the assumed circular micro crevice with the given contact angle. The conservative estimation for the bubble interphase base and top temperatures, according to Eqns. 10.2 and 10.3 leads to a very small temperature variation for the bubble surface (see Table 10.2). Nevertheless, a small distortion from spherical geometry results, leading to a slight elongation of the bubble in the direction perpendicular to the heated surface. The dimensionless thermocapillary and drag forces are displayed in Table 10.2, along with the drag force on the same bubbles if they were perfectly chopped-spherical. The elongation of the bubble leads to a slight increase in the drag force, while the non-uniformity of its surface temperature produces a small thermocapillary force.

Table 10.1: Summary of calculation results for a bubble that is a hemisphere when it is not distorted ($\theta_0 = 90^0$, $r_{co} = 4$ μm)

Case	$\mathbf{P_\infty}$ kPa	F_σ^*	F_d^* Bubble	F_d^* Sphere	A_F^* Bubble	A_F^* Sphere	$\mathbf{T_M}$ ^{0}C	$\mathbf{T_D}$ ^{0}C
$T_d = T_{sat}(P_B) + \Delta t$ $T_{Top} = T_{sat}(P_B) - \Delta t$	202	-0.047	0.492	0.481	1.585	1.577	123.0	126.1
$T_d = T_{sat}(P_B) + 2\Delta t$ $T_{Top} = T_{sat}(P_B) - 2\Delta t$	202	-0.093	0.520	0.489	1.599	1.585	121.5	127.6
$T_d = T_{sat}(P_B) + 4\Delta t$ $T_{Top} = T_{sat}(P_B) - 4\Delta t$	202	-0.185	0.574	0.496	1.625	1.599	118.4	130.6

Here,
T_D = Temperature of the liquid at bubble bottom
T_{TM} = Temperature of the liquid at bubble top
$\Delta t = T_D - T_{sat}(P_B)$

The calculations leading to Figures 10.8 and 10.9 are likely to be conservative. The interfacial distribution is affected by the gas and liquid-side thermal resistances everywhere, and evaporation and condensation mass fluxes will be non-uniform. For demonstration

purposes, however, parametric calculations are now presented in which larger interfacial temperature variations are assumed.

Table 10.2: Summary of calculation results for a bubble that is a hemisphere when it is not distorted ($\theta_0 = 50^o$, $r_{co} = 4$ μm) *See Table 10.1 for definitions

Case	P_∞ kPa	F_σ^*	F_d^* Bubble	F_d^* Sphere	A_F^* Bubble	A_F^* Sphere	T_M ^{0}C	T_D ^{0}C
$T_d = T_{sat}(P_B) + \Delta t$ $T_{Top} = T_{sat}(P_B) - \Delta t$	202	-0.048	3.536	3.45	2.783	2.773	122.2	125.1
$T_d = T_{sat}(P_B) + 2\Delta t$ $T_{Top} = T_{sat}(P_B) - 2\Delta t$	202	-0.097	3.64	3.517	2.81	2.789	120.8	126.5
$T_d = T_{sat}(P_B) + 4\Delta t$ $T_{Top} = T_{sat}(P_B) - 4\Delta t$	202	-0.194	3.875	3.56	2.857	2.818	117.9	129.3

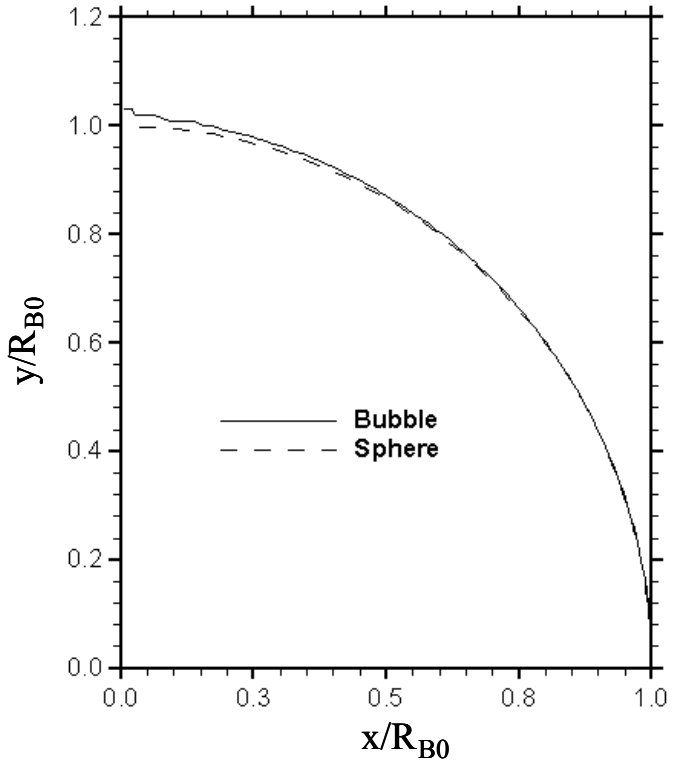

Figure 10.8: Profile of a bubble in subcooled boiling ($r_{co} = 4$ μm, $\theta_o = 90^o$)

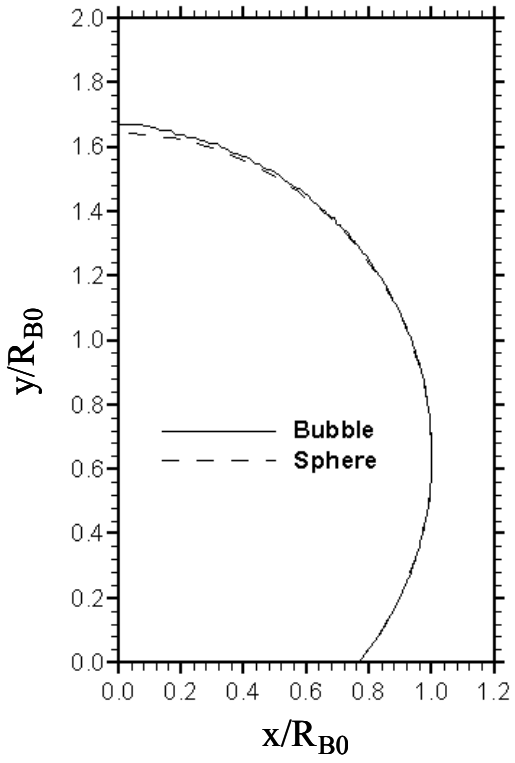

Figure 10.9: Profile of a bubble in subcooled boiling (r_{co} = 4 μm, θ_o = 50 ^{o})

Figures 10.10 and 10.11 are similar to Figure 10.9 with the modification that in Figure 10.10 the temperature differences predicted by Eqn. (10.3) have been doubled. Similarly, in Figure 10.11, the temperature difference predicted by Eqn. (10.3) has been multiplied by 4. The bubble elongation of course increases as a result of higher interfacial temperature non-uniformity. Distortion from spherical geometry is noticeable, and the elongation of bubbles leads to deviation in the drag force in comparison with spherical geometry. The thermocapillary force is also significant. The predicted elongation of bubbles, which can lead to pear-shaped bubbles at larger bubble surface temperature non-uniformities (or large surface tension variation), is consistent with the subcooled boiling experimental observations (Bibeau and Salcudean, 1994) where pear-shaped bubbles are common. Bubble geometric distortion and the thermocapillary force can be particularly

significant in fluids for which the surface tension is quite sensitive to temperature. The bubble shape is of course affected by a multitude of other hydrodynamic effects. The thermocapillary effect, however, may be a major contributor to bubble ebullition in heterogeneous boiling, and has been by and large disregarded in the past.

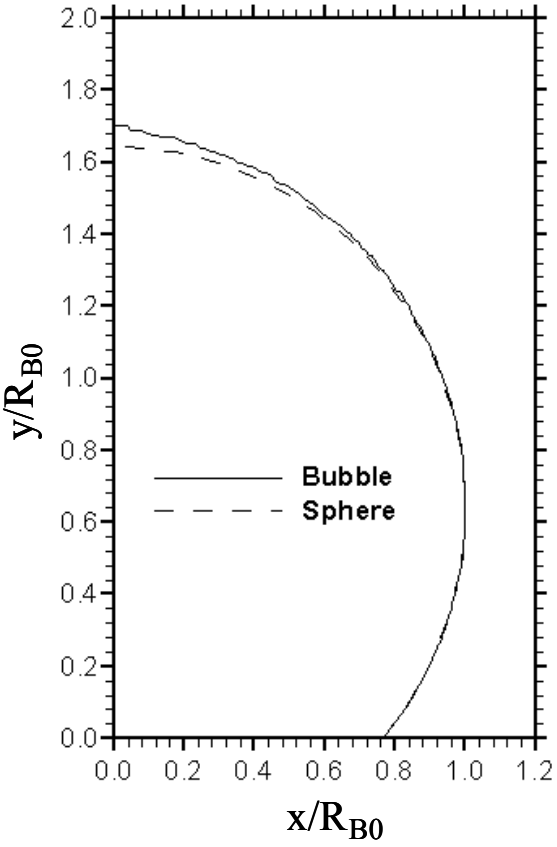

Figure 10.10: Profile of a bubble in subcooled boiling (r_{co} = 4 μm, θ_o = 50 ^{o}, see the results section)

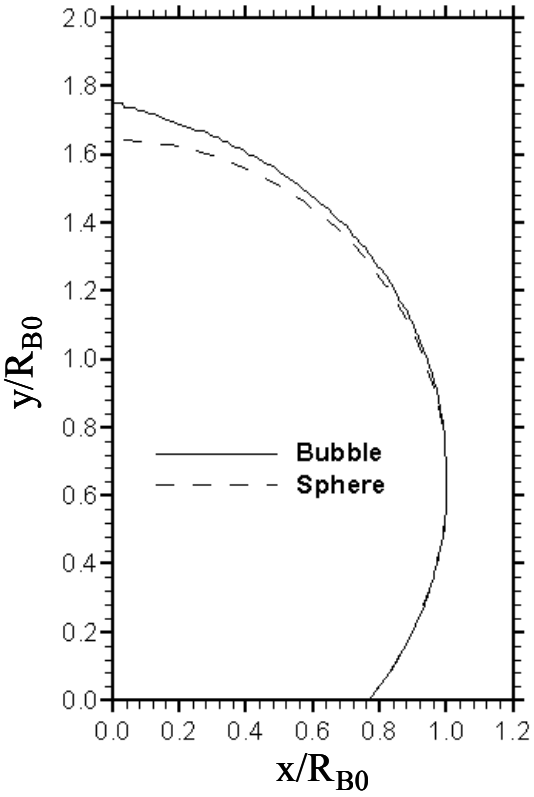

Figure 10.11: Profile of a bubble in subcooled boiling (r_{co} = 4 μm, θ_o = 50 °, see the results section)

10.3 Concluding Remarks

The potential impact of thermocapillary effects during heterogeneous bubble ebullition in microchannels was analytically studied. Quasi-steady bubble caps occupying the cross-section of a heated microtube, and quasi-steady microbubbles surrounded by a liquid thermal boundary layer in a microchannel were modeled, and a method for the prediction of the bubble profile knowing its surface temperature was developed. Parametric calculations were performed for stationary bubble caps, and for bubbles in subcooled nucleate boiling. It was shown that the thermocapillary effect leads the distortion of the interphase from spherical geometry. For bubbles in subcooled boiling, it leads to the

elongation of bubbles in the direction perpendicular to the heated surface, and results in a thermocapillary force that resists bubble departure. However, with water, these effects are significant in subcooled boiling only when large interfacial temperature non-uniformity occurs. In view of the potentially important role of the thermocapillary effects in bubble ebullition in micorsystems, more detailed investigations are strongly recommended.

CHAPTER 11: CONCLUSIONS, SUMMARY OF CONTRIBUTIONS, AND RECOMMENDATIONS

11.1 Conclusions

Two-and three phase flows involving combinations of gas, liquid and solid particles occur in numerous natural and industrial systems, and currently are often among the most complex and least understood processes. In two and three-phase flow processes where liquid-gas interphase occurs, the deformability of the interphase is in fact the main difficulty. When solid particles are involved, furthermore, the particle-fluid velocity differential is a key complicating factor. In situations where the solid particles themselves are deformable, and particularly when they can form flocs (as it occurs in flows involving pulp suspensions) the flow complexity is increased enormously. As a consequence of these complications, the filed of multiphase flow still relies heavily on empiricism. The objective of this research was to investigate a number of these multiphase flow processes. We were particularly interested in multiphase processes that involved solid particulates. As a result of this investigation, the following concluding remarks can be made.

1. An experimental investigation into the effects of various parameters on the effective, average interfacial surface area concentration in a short vertical column subject to a through-flow of a paper pulp-water-gas three-phase mixture was reported. Statistical characteristics were analyzed on the experimental data with a focus on the important parametric dependencies identification. The results confirmed that pulp affects all major hydrodynamic processes, including the interfacial surface area concentration. The experimental data were then empirically correlated.

2. A numerical study aimed at the elucidation of the effect of sparingly soluble reactant micro particles on the absorption of a gaseous species by a slurry droplet undergoing internal circulation was reported here. The reactant solid particles enhance the absorption rate by reducing the thickness of the reaction layer and increasing the concentration gradient of the transferred species beneath the droplet surface. Stronger droplet internal circulation reduces the effect of particles due to shorter droplet surface exposure time, however. Parametric calculations confirmed that particles cause a reduction in the thickness of the reaction layer near the droplet surface, thereby enhancing the absorption rate. Transient parametric calculations were presented that show a rapid shrinkage of average particle size with time in slurry droplets, and a declining total absorption rate with time as a result of the shrinkage of the average particle size.

3. The transport of carbon soot in a laminar hot gas, flowing in a tube, was numerically investigated. The carrier gas flow was assumed to be steady and fully-developed, and the energy conservation and soot particle transport equations, which are coupled due to the participation of particles in radiation heat transfer, were numerically solved using an implicit, upwind, second-order finite-difference technique. Monodisperse, as well as polydisperse soot particles were simulated. The results showed that radially non-uniform soot concentration and gas temperature profiles develop as a result of the coupling between thermal radiation and soot thermophoresis. Sharper soot concentration profiles are obtained as a result of higher tube wall temperature and higher initial average soot particles. The size distribution of soot particles also had a significant effect on the model predictions, indicating that the assumption of

monodisperse soot particles may lead to the over prediction of the effect of thermophoresis.

4. A CFD-based Eulerian-Lagrangian model for the transport and retention of aerosol in rising bubbles was described and its performance was demonstrated. Rising bubbles were found to deform and change shapes with time, in addition to complex bubble internal circulation patterns. As a consequence of bubble deformation and complex internal circulation, particle removal rates were different than the particle removal rates predicted for spherical bubbles with similar volumes. Comparison was made between the particle decontamination factors predicted by the simulations and available experimental data, with reasonable agreement.

5. A simple Weber number-based flow regime map for near-circular microchannels and air-water like fluid pairs that divides the entire map into four zones (surface tension-dominated, annular, froth, and transition) was devised. For microchannels the proposed map is in good agreement with the available experimental data. For diameters bigger than 1 mm, the aforementioned flow regime map is in fair agreement with available data, with the exception of the boundaries of the froth (dispersed) flow regime zone. The limited available data indicate that triangular channels with sharp corners may support somewhat different regimes and transition boundaries than near-circular channels.

6. The stability of stratified gas-liquid two-phase flow in horizontal annuli subject to air-water two-phase flow was investigated. The widely-used semi-analytical model of Taitel and Dukler was modified based on some air-water experimental data. A simple

method was developed for the prediction of conditions that lead to flow regime transition out of stratified-wavy.

7. The potential impact of thermocapillary effects during heterogeneous bubble ebullition in microchannels was analytically studied. Quasi-steady bubble caps occupying the cross-section of a heated microtube, and quasi-steady microbubbles surrounded by a liquid thermal boundary layer in a microchannel were modeled, and a method for the prediction of the bubble profile knowing its surface temperature was developed. Parametric calculations were performed for stationary bubble caps, and for bubbles in subcooled nucleate boiling. It was shown that the thermocapillary effect leads the distortion of the interphase from spherical geometry. For bubbles in subcooled boiling, it leads to the elongation of bubbles in the direction perpendicular to the heated surface, and results in a thermocapillary force that resists bubble departure. However, with water, these effects are significant in subcooled boiling only when large interfacial temperature non-uniformity occurs.

11.2 Summary of Contributions

The following is a summary of the original contributions of this dissertation.

1. The experimental measurement of interfacial surface area concentration a short vertical column subject to fiber-liquid-gas three-phase flow was novel. To the best of the author's knowledge, although much research has been reported for interfacial area in gas-liquid two-phase flows, virtually no investigation has been reported on three-phase pulp slurries in a short column with gas through-flow.

Thus, the information about the effects of various parameters on the surface area is valuable and useful.

2. The numerical study on gas absorption by droplets containing sparingly-soluble, reactive micro-particles elucidated beyond any un-ambiguity the real mechanism responsible for the enhancement of the gas absorption rate by the micro-particles. Researchers in the past had speculated about the mechanism, based on extremely simplified models. The present study also was based on a novel Eulerian-Lagrangian analysis not applied to problems of this type in the past. Our investigation also elucidated several important trends and parametric dependencies that are far from obvious.

3. In the study of soot particle transport the coupled effect of the radiation and thermophoresis was examined with detail and rigor far superior to the relevant earlier studies. The elucidation of the significant impact of particle size distribution on the thermophoretic particle transport was in particular was novel and shows that simplified models based on mono-disperse particles lead to unrealistic results.

4. The CFD-based Eulerian-Lagrangian model for the transport and retention of aerosol in bubbles was novel, and demonstrated the powerful methodology for the analysis of these important processes. Previous studies of particle transport in bubbles have all been based on idealized bubble characteristics. No CFD-based analyses have been reported in the past.

5. The simple Weber number-based two-phase flow regime map for near-circular microchannels and air-water like fluid pairs in microchannels was new. The idea

of using the similarity between flow regimes in large channels under microgravity, and micro-channels was innovative. The outcome of this investigation will provide a simple and useful predictive method for application in the design and analyses of microchannels.

6. In the study of the stability of stratified gas-liquid two-phase flow in horizontal annuli subject to two-phase flow, a simple method was developed for the prediction of conditions that lead to flow regime transition out of stratified-wavy. The analysis was novel, and led to the semi-empirical modification of a well-known theory for application to annular channels.

7. The potential impact of thermocapillary effect during heterogeneous bubble ebullition in microchannels was also analytically studied. The study was novel and focused attention on an important and hitherto mostly ignored effect. The past studies dealing with mocrobubbles have virtually all assumed uniform bubble surface temperature, and spherical bubble geometry. The present study has clearly shown that these assumptions can be incorrect in microscale, and can lead to inaccuracy in theoretical predictions dealing with the thermo-hydraulic processes in microsystems.

11.3 Recommendations

Based on this investigation, the following critical areas could be identified for future research.

1. The experimental study on interfacial surface area concentrations in gas-liquid-fiber flows was evidently limited in scope. Further investigations, addressing systems with through-flows, and systems with different scales, are recommended.

2. The study of sparingly soluble reactant micro particles on the absorption of a gaseous species by a slurry droplet confirms that a multitude of parameters should be considered for optimal design of a slurry spray scrubber. The model assumed a spherical and non-oscillating droplet, and considered a simple, overall chemical reaction, however. A more detailed chemical reaction model, accounting for possible droplet deformation, and an initially non-uniform size distribution of the reactant particles, may give lead to a more realistic model.

3. With respect to soot particle transport in hot fume gases, there is a lack of experimental data. Experimental investigations in hot gas flow with soot particles are therefore needed for the validation of theoretical model predictions such as those generated in this investigation. With respect to modeling, furthermore, the assumption of a uniform wall temperature is likely to be an over simplification. A more rigorous modeling that accounts for a decreasing wall temperature in the downstream direction is recommended.

4. Concerning particle transport in rising bubbles, there is the lack of unambiguous and directly relevant experimental data. Such experiments need to be well controlled, and should measure the rates of particle removal from single bubbles with known size, or swarms of uniformly-sized bubbles with a known size. With respect to modeling, it will be interesting to revisit the effects of bubble growth/shrinkage (as a

result of evaporation and condensation), and the effect other particle motion mechanisms (e.g., thermophoresis) on the aerosol removal rates.

5. With respect to two-phase flow hydrodynamics in microchannels, systematic experiments addressing the effects of channel cross-section size and geometric configuration are needed. Flow in channels with sharp corners are particularly important, since such channels are more likely to be used in practice than circular channels. Virtually all available data represent air/water and air/water-like fluid pairs at room conditions. The potential effects of fluid properties are thus unknown, and systematic experimental studies using other fluids are needed.

6. With respect to the stability of stratified flow in horizontal, annular channels, lack of sufficient experimental data base is evident. Indeed, because of shortage of experimental data, the conditions for the disruption of stratified-smooth regime could not be addressed in this study. Experimental investigations to better understand the transition out of stratified-smooth and stratified-wavy regimes in horizontal annuli are recommended.

7. Finally, in view of the potentially important role of the thermocapillary effects in bubble ebullition in micorsystems, more detailed studies, especially experimental investigations, are strongly recommended.

APPENDIX A

Table A1: Summary of experimental data for interfacial surface area concentration

Case	η (%)	Regime	$C_{OH^-,in}$ $\sigma_{C_{OH^-}}$ (mol/lit)	α σ_{α} (-)	$\overline{X}_{CO_2,G}$ $\sigma_{\overline{X}_{CO_2,G}}$ (-)	$\overline{U}_{GS}$ $\sigma_{\overline{U}_{GS}}$ (m/s)	U_{LS} $\sigma_{U_{LS}}$ (m/s)	a_i'' $\sigma_{a_i''}$ (m^2/m^3)
1	0.000	Churn	0.545	0.357	0.327	0.423	0.390	141.05
			1.1E-04	*2.7E-03*	*1.0E-02*	*1.2E-02*	*3.1E-02*	*7.14*
2	0.000	Churn	0.472	0.261	0.564	0.349	0.543	81.57
			3.1E-02	*8.7E-03*	*1.6E-02*	*2.0E-02*	*9.9E-03*	*3.35*
3	0.000	Churn	0.328	0.284	0.538	0.516	0.752	107.35
			1.2E-02	*3.6E-03*	*8.7E-03*	*1.1E-02*	*9.9E-03*	*0.92*
4	0.545	Bubbly-Churn	0.649	0.210	0.613	0.192	0.360	45.64
			1.5E-02	*1.5E-02*	*2.2E-02*	*2.5E-02*	*9.9E-03*	*1.85*
5	0.545	Slug	0.329	0.329	0.359	0.373	0.345	106.97
			6.6E-04	*5.5E-03*	*1.7E-02*	*1.5E-02*	*1.3E-02*	*2.19*
6	0.545	Slug	0.329	0.284	0.768	0.321	0.348	88.80
			1.1E-02	*3.6E-03*	*1.2E-02*	*1.3E-02*	*9.9E-03*	*8.70*
7	0.545	Slug	0.623	0.383	0.543	0.489	0.345	111.87
			1.3E-02	*2.6E-03*	*2.2E-02*	*1.1E-02*	*2.7E-02*	*5.80*
8	0.545	Churn	0.663	0.244	0.361	0.374	0.740	85.73
			1.0E-02	*4.5E-03*	*1.8E-01*	*1.4E-01*	*9.9E-03*	*1.02*
9	0.545	Bubbly	0.329	0.167	0.640	0.195	0.708	52.78
			6.1E-03	*7.2E-03*	*2.1E-02*	*1.0E-02*	*9.9E-03*	*8.51*
10	0.545	Churn	0.652	0.204	0.768	0.323	0.738	62.42
			1.1E-02	*5.4E-03*	*1.2E-02*	*1.0E-02*	*9.9E-03*	*5.88*
11	0.545	Slug	0.321	0.291	0.541	0.530	0.740	106.65
			1.2E-02	*3.5E-03*	*3.0E-01*	*4.7E-02*	*9.9E-03*	*2.77*
12	1.090	Churn-Slug	0.491	0.273	0.559	0.363	0.556	69.45
			2.0E-03	*3.8E-03*	*1.5E-02*	*1.5E-02*	*1.7E-02*	*1.34*
13	1.090	Churn-Slug	0.487	0.274	0.564	0.362	0.543	67.73
			8.0E-03	*6.6E-03*	*1.4E-02*	*2.7E-02*	*9.9E-03*	*5.97*
14	1.090	Churn-Slug	0.490	0.282	0.563	0.354	0.543	74.98
			3.7E-03	*3.7E-03*	*1.2E-02*	*1.7E-02*	*9.9E-03*	*2.18*
15	1.090	Churn-Slug	0.487	0.270	0.567	0.349	0.543	76.71
			8.4E-03	*7.8E-03*	*1.4E-01*	*9.3E-02*	*2.9E-01*	*5.47*
16	1.090	Churn-Slug	0.485	0.270	0.569	0.349	0.548	75.79
			5.8E-03	*7.3E-03*	*1.2E-02*	*1.0E-02*	*9.9E-03*	*7.07*
17	1.090	Churn-Slug	0.772	0.268	0.560	0.352	0.550	64.94
			2.0E-02	*1.8E-02*	*1.2E-02*	*1.3E-02*	*2.4E-02*	*7.19*
18	1.090	Bubbly	0.482	0.224	0.565	0.376	0.942	53.98
			1.5E-03	*5.2E-03*	*3.6E-02*	*1.1E-02*	*8.7E-02*	*3.54*

Table A1 (Continued)

Case	η (%)	Regime	$C_{OH^-,in}$ $\sigma_{C_{OH^-}}$ (mol/lit)	α σ_{α} (-)	$\overline{X}_{CO_2,G}$ $\sigma_{\overline{X}_{CO_2,G}}$ (-)	$\overline{U}_{GS}$ $\sigma_{\overline{U}_{GS}}$ (m/s)	U_{LS} $\sigma_{U_{LS}}$ (m/s)	a''_i $\sigma_{a''_i}$ (m^2/m^3)
19	1.090	Churn-Slug	0.471	0.340	0.396	0.536	0.543	102.92
			1.9E-03	*2.9E-03*	*1.1E-01*	*1.2E-01*	*9.9E-03*	*6.51*
20	1.090	Churn-Slug	0.484	0.268	0.580	0.347	0.530	68.17
			5.3E-03	*3.9E-03*	*1.7E-02*	*1.9E-02*	*1.5E-02*	*4.80*
21	1.090	Churn-Slug	0.146	0.305	0.565	0.378	0.543	86.10
			8.5E-03	*3.6E-03*	*1.2E-02*	*1.1E-02*	*9.9E-03*	*7.37*
22	1.090	Bubbly-Churn	0.483	0.228	0.264	0.222	0.539	57.31
			5.9E-03	*1.1E-02*	*2.0E-02*	*1.1E-02*	*9.9E-03*	*2.40*
23	1.090	Bubbly-Churn	0.475	0.151	0.974	0.168	0.544	39.13
			8.4E-03	*7.5E-03*	*3.6E-02*	*1.3E-01*	*1.3E-01*	*0.85*
24	1.090	Slug	0.478	0.396	0.563	0.342	0.153	86.56
			2.5E-02	*3.2E-02*	*2.0E-02*	*1.6E-02*	*2.0E-02*	*11.19*
25	1.090	Slug	0.474	0.351	0.685	0.501	0.551	85.72
			1.5E-02	*2.5E-02*	*8.3E-03*	*1.5E-02*	*9.9E-03*	*6.64*
26	1.090	Churn-Slug	0.476	0.286	0.563	0.358	0.543	71.90
			1.4E-02	*3.6E-03*	*1.2E-02*	*1.5E-02*	*9.9E-03*	*4.70*
27	1.635	Slug	0.622	0.345	0.768	0.332	0.347	55.88
			1.8E-02	*3.6E-03*	*1.3E-02*	*1.5E-02*	*9.9E-03*	*4.06*
28	1.635	Bubbly-Churn	0.655	0.173	0.610	0.195	0.743	43.12
			4.4E-03	*6.7E-03*	*2.1E-02*	*1.2E-02*	*9.9E-03*	*1.37*
29	1.635	Slug	0.313	0.413	0.539	0.526	0.354	94.03
			2.4E-02	*4.9E-03*	*1.7E-02*	*1.4E-02*	*9.9E-03*	*2.85*
30	1.635	Churn-Slug	0.325	0.271	0.360	0.393	0.726	75.38
			5.3E-03	*4.6E-03*	*2.2E-02*	*1.7E-02*	*9.9E-03*	*7.55*
31	1.635	Churn-Slug	0.304	0.251	0.770	0.356	0.743	63.97
			3.9E-03	*4.4E-03*	*1.5E-02*	*1.8E-02*	*9.9E-03*	*0.42*
32	1.635	Slug	0.638	0.308	0.540	0.523	0.741	81.49
			1.1E-02	*3.5E-03*	*8.9E-03*	*1.3E-02*	*1.3E-02*	*9.46*
33	1.635	Slug	0.641	0.361	0.358	0.373	0.354	75.77
			9.3E-03	*2.7E-03*	*1.3E-02*	*1.3E-02*	*3.6E-02*	*2.54*
34	1.635	Churn-Slug	0.326	0.260	0.621	0.211	0.345	39.18
			4.4E-03	*4.0E-03*	*2.0E-02*	*1.5E-02*	*9.9E-03*	*2.38*
35	2.181	Slug	0.327	0.422	0.322	0.443	0.405	120.73
			2.2E-03	*2.2E-03*	*1.0E-02*	*1.5E-02*	*3.1E-02*	*23.02*
36	2.181	Slug	0.463	0.327	0.562	0.358	0.543	74.03
			1.1E-02	*8.1E-03*	*1.2E-02*	*2.3E-02*	*1.7E-02*	*3.39*
37	2.181	Slug	0.338	0.339	0.534	0.537	0.740	94.65
			1.4E-02	*2.9E-03*	*8.3E-03*	*1.3E-02*	*3.1E-02*	*7.57*

APPENDIX B

The net radiation loss (W/m^3) by particles is given by the Eq. (6.3): where the emission, absorption (from wall) and transmission components are, respectively:

$$-\nabla.q_{em}'' = -4\int_0^\infty k_\lambda e_{b\lambda}(T)d\lambda \tag{A-1}$$

$$-\nabla.q_{ab}'' = 4\int_0^\infty k_\lambda e_{b\lambda}(T_w)d\lambda \tag{A-2}$$

$$-\nabla.q_{tr}'' = -4\int_0^{\lambda_a} k_\lambda e_{b\lambda}(T_w)d\lambda \tag{A-3}$$

From Eqs. (4) and (A-1):

$$-\nabla.q_{em}'' = -28\Phi T^5 \int_0^\infty \frac{1}{\lambda T}\frac{2\pi C_1}{\lambda^5 T^4\left[e^{\frac{C_2}{\lambda T}}-1\right]}d\lambda \tag{A-4}$$

using $\lambda = \dfrac{C_2}{zT}$; with boundary conditions $\lambda = 0,\ z = \infty;\quad \lambda = \infty,\ z = 0$ (Lawson, 1997):

$$\begin{aligned}-\nabla.q_{em}'' &= -28\Phi T^5\left(\frac{2\pi C_1}{C_2{}^5}\right)\int_0^\infty \frac{z^4}{e^z-1}dz \\ &= -\Phi T^5\left(\frac{56\pi C_1}{C_2{}^5}\right)\int_0^\infty z^4 e^{-z}\begin{pmatrix}1+e^{-z}+\\ e^{-2z}+.....\end{pmatrix}dz \\ &= -\Phi T^5\left(\frac{56\pi C_1}{C_2{}^5}\right)\sum_{n=1}^{\infty}\int_0^\infty z^4 e^{-nz}\,dz\end{aligned} \tag{A-5}$$

$$-\nabla.q_{em}'' = \Phi T^5\left(\frac{56\pi C_1}{C_2{}^5}\right)\times\sum_{n=1}^{\infty}\left\{\frac{e^{-nz}}{n}\left[z^4+\frac{4z^3}{n}+\frac{12z^2}{n^2}+\frac{24z}{n^3}+\frac{24}{n^4}\right]_0^\infty\right\} \tag{A-6}$$

Although expressed as the emission component, Eq. (A-6) is generic, and all three terms in Eqs. (A-1) through (A-3) can be obtained from this equation with appropriate integral limits. Here $C_1 = 0.5955 \times 10^8$ W-μm^4 m^{-2} sr^{-1}, and $C_2 = 14387.7$ μm K.

For the emission part, in the SI units, Eq. (A-1), numerical calculation leads to:

$$-\nabla.q_{em}'' = -4.23 \times 10^{-4} \Phi T^5 \tag{A-7}$$

Similarly the absorption component, Eq. (A-2) leads to:

$$-\nabla.q_{ab}'' = 4.23 \times 10^{-4} \Phi T_w^{\ 5} \tag{A-8}$$

For the last component, Eq. (A-4), the integration limits should be from $\frac{C_2}{\lambda_a T_w}$ to ∞. When only the first term in the series expansion (*n = 1*) is considered, one gets:

$$-\nabla.q_{tr}'' = -\frac{1.7 \times 10^{-5}}{(\lambda_a T_w)^4} e^{-(C_2/(\lambda_a T_w))} \Phi T_w^{\ 5} \times \left[\begin{array}{l} C_2^{\ 4} + 4C_2^{\ 3}(\lambda_a T_w) + 12C_2^{\ 2}(\lambda_a T_w)^2 + \\ 24C_2(\lambda_a T_w)^3 + 24(\lambda_a T_w)^4 \end{array} \right] \tag{A-9}$$

Adding the including terms associated with the second term in the series expansion (*n = 2*) with in the right hand side of Eq. (A-9) contributes only 5%, as long as $\lambda_a T_w = C_2$. Based on these observations all higher order terms were neglected.

APPENDIX C

UDF 1: For Recording Bubble Data in Output Files

```
#include "udf.h"
FILE *fout; /* Output file open */
double sumx0=0.; /* Initial x position of the bubble in the pool */
double sumy0=0.; /* Initial y position of the bubble in the pool */
double sumz0=0.8; /* Initial z position of the bubble in the pool */
double uvel; /* u Velocity, a global variable */
double vvel; /* v Velocity, a global variable */
double wvel; /* w Velocity, a global variable */

DEFINE_ON_DEMAND(first_iter_only)
{
  Domain *d=Get_Domain(1);
  Thread *t,*gt;
  cell_t c;
  double XC[3],VF,x[5000],y[5000],z[5000],
    u[5000],v[5000],w[5000]; /* Defining variables */
  double sumx = 0.0;
  double sumy = 0.0;
  double sumz = 0.0;
  int p = 0;  /* Number of cells in the bubble */
  int n = 0;
```

```
/* Bubble data for 25 time steps will stored in a single data file.  N_TIME is the current time
step number*/
  int curtim = (N_TIME - 1) / 25 + 1;
  char nam[] = "vx";   /* The file name will start with 'vx' */
  char buf[BUFSIZ];
  char temp[] = ".out";  /* The file name will end with '.out' */
  sprintf(buf, "%s %06d", nam, curtim); /* Coverting the time step number into a
character */
  strcat(buf, temp); /* Generating file name based on the time step number */
/* Assigning the file name. For example, 'vx 000001.out' is for the bubble date of first 25
time steps */
  fout = fopen(buf,"a");
  thread_loop_c(t,d)
    {
      gt=THREAD_SUB_THREAD(t,1);
     /* Loop over all cells */
      begin_c_loop(c,t)
          {
            C_CENTROID(XC,c,t);
            VF=C_VOF(c,gt); /* Getting volume factions of cells */
          /* If the water volume fraction is less than 0.5, the current cell is a part of the bubble
*/
            if (VF < 0.5)
```

```
        {
            /* Getting positions, and velocities of the bubble cells */
          x[p] = XC[0];
          y[p] = XC[1];
          z[p] = XC[2];
          u[p] = C_U(c,t);
          v[p] = C_V(c,t);
          w[p] = C_W(c,t);
            sumx += x[p];
            sumy += y[p];
            sumz += z[p];
          p += 1;
        }
      }
  end_c_loop(c,t);
}
sumx = sumx/p;
      /* Calculating average U velocity of the bubble */
      uvel = (sumx-sumx0)/CURRENT_TIMESTEP;
      sumy = sumy/p;
      /* Calculating average V velocity of the bubble */
      vvel = (sumy-sumy0)/CURRENT_TIMESTEP;
      sumz = sumz/p;
```

```
        /* Calculating average W velocity of the bubble */
        wvel = (sumz-sumz0)/CURRENT_TIMESTEP;
          fprintf(fout,"%d\n",p);
          /* Writing positions and velocities in file */
          for (n = 0; n < p; n++)
                {
                  fprintf(fout,"%15.13f %15.13f %15.13f %12.9f %12.9f %12.9f\n",
                  (x[n]-sumx),(y[n]-sumy),(z[n]-sumz),(u[n]-uvel),(v[n]-vvel),(w[n]-
wvel));
                 }

  sumx0 = sumx;
  sumy0 = sumy;
  sumz0 = sumz;
  fclose(fout); /* Closing file */

}
```

UDF 2: Dynamic Mesh Velocity

```
#include "udf.h"
FILE *fout1; /* A file to record the assigned dynamic velocity */
/* Getting average W velocity of the bubble from the UDF 1.  wvel is a global variable */
double wvel;
```

```
DEFINE_CG_MOTION(vel_comp, dt, vel, omega, time, dtime)
{
   fout1 = fopen("wvel.out","a"); /* File name assigned */
   Message ("WVEL =%f\n",wvel); /* Message displays on the screen during the run */
   vel[0] = wvel; /* Mesh velocity is assigned */
   fprintf(fout1,"%d %f\n",N_TIME,vel[0]); /* Records assigned mesh velocity in the file
*/
   fclose(fout1);
}
```

APPENDIX D

Some details related to the application of Eqn. (9.5) to the annular geometry of Figure (9.1) are provided in this appendix.

$$S_L = 2R_o\left[\pi - \cos^{-1}\left(\frac{h_L}{R_o} - 1\right)\right] + 2R_i\left[\pi - \cos^{-1}\left(\frac{h_L - \delta}{R_i} - 1\right)\right] \tag{B-1}$$

$$S_G = 2\pi(R_o + R_i) - S_L \tag{B-2}$$

$$S_I = 2R_o\left[1 - \left(\frac{h_L}{R_o} - 1\right)^2\right]^{\frac{1}{2}} - 2R_i\left[1 - \left(\frac{h_L - \delta}{R_i} - 1\right)^2\right]^{\frac{1}{2}} \tag{B-3}$$

$$\begin{aligned} A_G = {} & R_o^2\left\{\cos^{-1}\left(\frac{h_L}{R_o} - 1\right) - \left(\frac{h_L}{R_o} - 1\right)\sqrt{1 - \left(\frac{h_L}{R_o} - 1\right)^2}\right\} \\ & - R_i^2\left\{\cos^{-1}\left(\frac{h_L - \delta}{R_i} - 1\right) - \left(\frac{h_L - \delta}{R_i} - 1\right)\sqrt{1 - \left(\frac{h_L - \delta}{R_i} - 1\right)^2}\right\} \end{aligned} \tag{B-4}$$

$$\alpha = \frac{A_G}{\pi(R_o^2 - R_i^2)} \tag{B-5}$$

$$\frac{dA_L}{dh_L} = 2R_o\left[1 - \left(\frac{h_L}{R_o} - 1\right)^2\right]^{\frac{1}{2}} - 2R_i\left[1 - \left(\frac{h_L - \delta}{R_i} - 1\right)^2\right]^{\frac{1}{2}} \tag{B-6}$$

$$U_G = j_G/\alpha \tag{B-7}$$

$$U_L = j_L/(1-\alpha) \tag{B-8}$$

$$\tau_I = \tau_{WG} = C_{fG}\,\tfrac{1}{2}\rho_G U_G^2 \tag{B-9}$$

$$\tau_{WL} = C_{fL}\,\tfrac{1}{2}\rho_L U_L^2 \tag{B-10}$$

For phase k (k = L or G), $C_{fk} = C_k\,Re_k^{-n}$, where $C_k = 0.046$ and $n = 0.2$ for turbulent flow, and $C_k = 16$ and $n = 1$ for laminar flow. Re_k is defined based on the phase velocity U_k,

and the hydraulic diameter of the segment of the channel cross-section occupied by phase k. Laminar to turbulent flow transition was assumed to occur at $Re_k = 2200$.

BIBLIOGRAPHY

- Akbar, M.K., and Ghiaasiaan, S.M., "Modeling the Gas Absorption in a Spray Scrubber with Dissolving Reactive Particles", *Chem. Eng. Sci.,* 59(5), March 2004, 967-976.
- Akbar, M.K., Ghiaasiaan, S.M., and Karrila, S., "An Experimental Study of Interfacial Surface Area Concentration in a Short Column Subject to Paper Pulp-Water-Gas Three-phase Flow," *Chem. Eng. Sci.,* 59(5), March 2004, 1079-1086.
- Ghiaasiaan, S.M., Karrila, S., Xie, T., and Akbar, M.K., "Bubble Size Control to Improve Oxygen-Based Bleaching," Final Report, Georgia Institute of Technology, presented to US Department of Energy, 2004.
- Ghiaasiaan, S.M., and Akbar, M.K., "Modeling of Thin Film Evaporative Cooling," Final Report, Georgia Institute of Technology, presented to NASA Langley Research Center, September 2004.
- Akbar, M.K., Yan, J., and Ghiaasiaan, S.M., "Mechanism of Gas Absorption Enhancement in a Slurry Droplet Containing Reactive, Sparingly Soluble Micro Particles", *Int. J. Heat and Mass Transfer*, 46 (2003), 4561-4571.
- Akbar, M.K., and Ghiaasiaan, S.M., "Stability of stratified gas-liquid two-phase flow in a horizontal annular channels," *Experimental Thermal and Fluid Science*, 28 (2003) 17–21.
- Akbar, M.K., Plummer, D.A., and Ghiaasiaan, S.M., "On gas–liquid two-phase flow regimes in microchannels," *Int. J. Multiphase Flow*, 29 (2003), 855-865.
- Akbar, M.K., and Ghiaasiaan, S.M., "Radiation Heat Transfer and Soot Thermophoresis in Laminar Tube Flow," accepted, and soon to appear in *Numerical Heat Transfer.*
- Akbar, M.K., and Ghiaasiaan, S.M., "A CFD Model for Aerosol Transport in Rising Gas Bubbles," submitted to *Chem. Eng. Sci.*
- Akbar, M.K., and Ghiaasiaan, S.M., "Radiation Heat Transfer and Soot Thermophoresis in Laminar Tube Flow," 2004 ASME Heat Transfer/Fluids Engineering Summer Conference, Charlotte, North Carolina, July 11-15, 2004.
- Akbar, M.K., Chedester, R.C., and Ghiaasiaan, S.M., "Thermocapillary Effects in Heterogeneously-Formed Bubble s in Microsystems," presented in the 2002 ASME IMECE Conference, New Orleans, Louisiana, November 17-22, 2002.
- Akbar, M.K., Plummer, D.A., and. Ghiaasiaan, S.M., "Gas-Liquid Two-Phase Flow in Microchannels," presented in the 2002 ASME IMECE Conference, New Orleans, Louisiana New, November 17-22, 2002.
- Akbar, M.K., Sharif, M.A.R., and Bradt, R.C.,- "Particle Trajectory Calculation in Turbulent Flow Through a Zigzag Channel," presented in the 4th International Conference On Multiphase Flow; May 27 to June 1, New Orleans, Louisiana, 2001.

- Akbar, M.K., Sharif, M.A.R., and Bradt, R.C.,- "Effect of Forces on a Particle in a Straight Channel Turbulent Flow," presented in the 4th International Conference On Multiphase Flow; May 27 to June 1, New Orleans, Louisiana, 2001.

REFERENCES

Abdelmassih, A.H., Hooper, F.C., Nangia, S. (1972). Flow Effects on bubble Growth and Collapse in Surface Boiling, *Int. J. heat Mass Transfer*, 15, 115-125.

Akbar, M.K., Yan, J., Ghiaasiaan, S.M. (2003). Mechanism of gas absorption enhancement in a slurry droplet containing reactive, sparingly soluble micro particles. *Int. J. Heat Mass Transfer*, 46, 4561-4571.

Akita, K., Yoshida, F. (1974). Bubble size, interfacial area, and liquid-phase mass transfer coefficient in bubble columns. *Ind. Eng. Chem., Process Des. Develop*., 13 (1), 84-90.

Al-Hayes, R.A.M., Winterton, R.H.S. (1981). Bubble Diameter on Detachment in Flowing Liquids, *Int. J. Heat Mass Transfer*, 24, 223-230.

Al Taweel, A.M., Divakarla, R., Gomaa, H.G. (1984). Measurement of large gas-liquid interfacial areas. *Can. J. Chem. Eng*., 62, 73-77.

ANSYS 5.7 (2001). User's Guide.

Banerjee, S. (1979a). Flow Regimes and Modelling PART I, Stanford University Two-Phase Short Course, Sec. 2, pp. 1-43.

Banerjee, S. (1979b). Flow Regimes and Modelling PART II, Stanford University Two-Phase Short Course, Sec. 3.

Banerjee, S., Lahey, R.T. (1981). Advances in two-phase flow instrumentation. *Advances in Nuclear Science and Technology* (Edited by Lewins, J., and Becker, M.), 13, 227-414, Plenum Press, New York.

Barajas, A. M., Panton, R. L. (1993). The effect of contact angle on two-phase flow in capillary tubes. *Int. J. Multiphase Flow*, 19, 337-346.

Barnea, D., Luninski, Y., Taitel, Y. (1983). Flow in small diameter pipes. *Can. J. Chem. Eng*. 61, 617-620.

Barnea, D., Taitel, Y. (1993). Kelvin-Helmholtz stability criterion for stratified flow: viscous versus non-viscous (inviscid) approaches, *Int. J. Multiphase Flow* 19, 639-649.

Batchelor, G.K. (1956). On steady laminar flow with closed streamlines at large Reynolds number, *J. Fluid Mech*. 1, 177-190.

Ben-dor, G., Elperin, T., Krasovitov, B. (2000). Thermo and Diffusiophoretic Motion of Flame-Generated Particles in the Neighborhood of Burning Volatile and Non-Volatile Aerosols, *J. Aerosol Sci.*, 31, SUPPL 1, 11, S829-S830.

Benjamin, T.B. (1968). Gravity currents and related phenomena, *J. Fluid Mech*. 31, 209-248.

Bennington, C.P.J. (1996). Bleach Plant Operations, Equipment and Engineering: Mixing and Mixers, Pulp Bleaching: Principles and Practice, *Tappi Press*.

Bergles, A.E., Rohsenow, W. M. (1964). The Determination of forced Convection Surface Boiling Heat Transfer, *J. Heat Transfer*, Vol. C86, pp. 365-372.

Bibeau, E.L., Salcudean, M. (1994). A Study of Bubble Ebullition in forced Convective Subcooled Nucleate Boiling at Low Pressure, *Int. J. Heat Mass Transfer*, 37, 2245-2259.

Bird, R.B., Stewart, W.E., Lightfoot, E.N. (2002). *Transport Phenomena*, 2nd Ed., Wiley, New York.

Bjerle, I., Bengtsson, S., Färnkvist, K. (1972). Absorption of SO_2 in $CaCO_3$ slurry in a laminar jet absorber, *Chem. Eng. Sci.* 27 1853-1861.

Boyadzhiev, L., Elenkov, D., Kyuchukov, G. (1969). On Liquid-Liquid Mass Transfer Inside Drops in a Turbulent Flow Field. *Can. J. Chem. Eng*. 47, 42-44.

Brignell, A.S. (1975). Solute extraction from an internally circulating spherical liquid droplet, *Int. J. Heat Mass Transfer* 18, 61-68.

Brogren, C., Karlsson, H.T. (1997). Modeling the absorption of SO_2 in a spray scrubber using the penetration theory. *Chem. Eng. Sci*., 52, 3085-3099.

Brunson, R. J., Welleck, R. M. (1970). Mass Transfer within Oscillating Liquid Droplets. *Can. J. Chem. Eng.* 48,:267-274.

Calderbank, P.H., Korchinski, I.J.O. (1956). Circulation in liquid drops, *Chem. Eng. Sci*., 6, 65-78.

Calvo, M., Guntay, S., Ramsdale, S. A. (1991). Development and Validation of BUSCA Code: A Model to Assess the Aerosol and Fission Product Retention in a Water Pool. *J. Aerosol Sci*. 22(Suppl. 1), S765-S768.

Castillo, J.L., Mackowski, D.W., Rosner, D.E. (1990). Photophoretic modification of the transport of absorbing particles across combustion gas boundary layers, *Progress in Energy and Combustion Science*, v 16, n 4, p 253-260.

Chang, T.H., Chung, J.N. (1985). The effect of surfactants on the motion and transport mechanisms of of condensing droplet in a high Reynolds number flow. *AIChE J*., 37, 1149-1156.

Chaudhari, R., Ramachandian, P. (1980). Three Phase Slurry Reactors. *AIChE J* 26 (2), 117-201.

Chawla, T.C., Ishii, M. (1980) Two-Fluid Model of Two-Phase Flow in a Pin Bundle of a Nuclear Reactor, *Int. J. of Heat and Mass Transfer*, Vol. 23, pp. 991-1000.

Chedester, R.C. (2002). Transport Phenomena in Microchannels and Proton Exchange Membrane Assemblies in Fuel Cells, *MS Thesis*, Georgia Institute of Technology.

Chen, M., McLaughlin, J. B. (1995). A New Correlation for the Aerosol Deposition Rate in Vertical Ducts. *J. Colloid Interface Sci*. 169, 437-455.

Cipolla, J.W., Morse, T.F. (1987). Thermophoresis in an Absorbing Aerosol, *J Aerosol Sci.*, 18, 245-260.

Clift, R., Grace, J.R., Weber, M.E. (1978). *Bubbles, Drops, and Particles*, Academic Press, New York.

Coleman, J. W., Garimella, S. (1999). Characteristics of two-phase patterns in small diameter round and rectangular tubes. *Int. J. Heat Mass Transfer*, 42, 2869-2881.

Davis, E.J., Anderson, G.H. (1966). The Incipience of Nucleate Boiling in Forced Convection Flow, *AIChE J*., 12, pp. 774-780.

Damianides, C.A, Westwater, J.W. (1988). Two-phase flow patterns in a compact heat exchanger and in small tubes. In: Proc. Second UK National Conf. On Heat Transfer, Glasgow, 14-16 September. Mechanical Engineering Publications, London, pp. 1257-1268.

Danckwerts, P.V. (1955). Gas absorption accompanied by chemical reaction. *A.I.Ch.E.J.,* December, 456-463.

Danckwerts, P.V., Sharma, M.M. (1966). The absorption of carbon dioxide into solutions of alkalis and amines. *The Chemical Engineer*, 244-280.

Danckwerts, P.V. (1970). *Gas-Liquid Reactions*. McGraw-Hill Book Company, New York.

Dejesus, J.M. (1989). Measurement of Interfacial Area and Void Fraction for Two-Phase Flow in a Vertical Tube, *Master's Thesis*, University of Toronto.

Edwards, D.K., Denny, V.E., Mills, A.F. (1979). *Transfer Processes – An introduction to diffusion, convection, and radiation*, 2nd Ed., McGraw-Hill Book Company, New York.

Ekberg, N.P., Ghiaasiaan, S.M., Abdel-Khalik, S.I., Yoda, M., Jeter, S.M. (1999). Gas-liquid two-phase flow in narrow horizontal annuli, *Nucl. Eng. Design* 192, 59-80.

Elghobashi, S., Truesdell, G. C. (1992). Direct Simulation of Particle Dispersion in a Decaying Isotropic Turbulence. *J. Fluid Mech*. 242, 655-700.

Feng, J.Q. (1992). The Oscillations of a Bubble Moving in an Inviscid Fluid. *SIAM J. Appl. Math.* 52, 1-14.

Fluent Inc. (2003). User's Guide.

Friedlander, S.K., Fernandez De La Mora, J., Gokoglu, S.A. (1988). Diffusive leakage of small particles across the dust-free layer near a hot wall; *Journal of Colloid and Interface Science*, v 125, n 1, 351-355.

Friedlander, S.K. (2000). *Smoke, Dust, and Haze*, 2nd Ed., Oxford University Press, New York.

Fuchs, N. A. (1964). *The Mechanics of Aerosols*. Pergamon Press, Oxford.

Fukano, T., Kariyasaki, A. (1993). Characteristics of gas-liquid two-phase flow in a capillary. *Nucl. Eng. Design*, 141, 59-68.

Gaddis, E.S. (1972). The Effects of Liquid Motion Induced by Phase change and thermocapillary on the thermal Equilibrium of a Vapor bubble, *Int. J. Heat Mass Transfer*, 15, 2241-2250.

GAMBIT (2003). User's Guide.

Ghiaasiaan, S.M., Eghbali, D.A. (1994). Transient mass transfer of a trace species in an evaporating spherical droplet with internal circulation. *Int. J. Heat Mass Transfer*, 37, 2287-2295.

Ghiaasiaan, S. M., Wassel, A. T., Lin, C. S. (1993). STARRS-MMS Code: Evaluating Steam Generator Tube Ruptures. *Electric Power Research Institute Report EPRI TR-102623,* Palo Alto, CA.

Ghiaasiaan, S. M., Yao, G. F. (1995). A Theoretical Model for Deposition of Aerosols in Rising Spherical Bubbles with Internal Circulation. *Int. J. Multiphase Flow*. 21, 907-918.

Ghiaasiaan, S. M., Yao, G. F. (1997). A Theoretical Model for Deposition of Aerosols in Rising Spherical Bubbles due to Diffusion, Convection, and Inertia. *Aerosol Sci. Tech*. 26, 141-153.

Ghiaasiaan, S. M., Abdel-Khalik, S. I. (2001). Two-phase flow in microchannels. *Adv. Heat Transfer*, 34, 145-254.

Ghiaasiaan, S.M., Chedester, R.C. (2002). Boiling Incipience in Microchannels, *Int. J. of Heat Mass Transfer*, v 45, n 23, 4599-4606.

Ghiaasiaan, S.M., Laker, T.S. (2001). Turbulent Forced Convection in Microtubes. *Int. J. Heat Mass Transfer*, 44, 2777-2782.

Gomez, A., Rosner, D.E. (1993). Thermophoretic Effects on Particles in Counterflow Laminar Diffusion Flames; *Combustion Science and Technology*, v 89, n 5-6, p 335-362.

Greaves, M., Kobbacy, K.A.H. (1984). Measurement of bubble size distribution in turbulent gas-liquid dispersions. *Chem. Eng. Res. Des.*, 62, 3-12.

Hadamard, J. (1911). Mouvement permanent lent d'une sphere liquid et visqueuse dans un liquid visqueux. *Compt. Rend*, 152, 1735.

Han, C.V., Griffith, P. (1965). The Mechanism of Heat Transfer in Nucleate Pool Boiling – I. Bubble Initiation, Growth and Departure, *Int. J. Heat mass Transfer*, Vol 8, 887-904.

Handlos, A. E., Baron, T. (1957). Mass and Heat Transfer from Drops in Liquid-Liquid Extraction. *AIChE J*. 3, 127-136.

Hao, Y., Prosperetti, A. (2000). The Collapse of Vapor Bubbles in a Spatially Non-Uniform Flow, *Int. J. Heat Mass Transfer*, 43, pp. 3539-3550.

Harper, J.F., Moore, D.W. (1968). The motion of a spherical liquid drop at high Reynolds number. *J. Fluid Mech*., 32, 367-391.

Heald, C.C. (1988). *Cameron Hydraulic Data.* Seventh Ed., Ingersoll-Rand Co., New Jersey, USA.

Heinscheid, W., Schültz, W. (1984). Particle Formation, Transportation, and Removal in a Rapidly Expanding and Rising Bubble. *J. Aerosol Sci*. 15, 358-360.

Herranz, L. E., Peyrés, V., Polo, J., Escudero, M. J., Espigares, M. M., López-Jiménez, J. (1997). Experimental and Analytical Study of Pool Scrubbing Under Jet Induction Regime. *Nuclear Reactor Safety*. 120, 95-109.

Incropera, F.P., Dewitt, D.P. (2000). *Introduction to Heat and Mass Transfer*, John Wiley & Sons; 3rd edition.

Ishii, M. (1975) Thermo-fluid Dynamic Theory of Two-Phase Flow, Eyrolles, Paris, France.

Ishii, M., and Mishima, K. (1984). Two-Fluid Model and Hydrodynamic Constitutive Relations, *Nuclear Engineering and Design*, Vol., 82, pp. 107-126.

Jepsen, J.C. (1970). Mass Transfer in Two-Phase Horizontal Pipelines, AIChE J., Vol. 16, pp. 705-711.

Jiang, P., Carey, V.P. (Nov 11-16, 2001). Parallelized DSML Modeling of Transport Near Liquid-vapor Interfaces in a Micro Bubble Heat Pipe, *Proc. 2001 International Mechanical Engineering Conference and Exposition*, IMECE 201, HTD-24194, New York.

Johnson, A. I., Hamielec, A. E. (1960). Mass Transfer inside Drops. *AIChE J*. 6, 145-149.

Johnston, A.J. (1985). Transition from stratified to slug regime in countercurrent flow, *Int. J. Multiphase Flow* 11, 31-41.

Jonas, R., Schültz, W. (1988). Motion and Deposition of Particles in Expanding and Oscillating Gas Bubbles. *J. Aerosol Sci.* 19, 753-765.

Joseph, D.D. (1973). Dynamic Perturbations: The Higher Order Theory of Infinitesimal Water Waves. *Arch. Rat. Mech. Anal*. 51, 295-305.

Kao, Y.S., Kenning, D.B.R. (1972). Thermocapillary Flow Near a Hemispherical Bubble on a Heated Wall, *J. Fluid Mech*., 53, 715-735.

Kasturi, G. (1973). Mass Transfer in Two-Phase Co-Current Gas-Liquid Flow, Ph.D. Thesis, University of Salford.

Kasturi, G., Stepanek, J.B. (1974). Two-phase flow-III. Interfacial area in cocurrent gas-liquid flow. *Chem. Eng. Sci*., 29, 713-719.

Kataoka, I., Ishii, M., Serizawa, A. (1986). Local Formulation and Measurements of Interfacial Area Concetration in Two-Phase Flow, *Int. J. Multiphase Flow*, Vol. 12, No. 4, pp. 505-529.

Kennedy, I.M., Kollmann, W., Chen, J.Y. (1991). Predictions of Soot in Laminar Diffusion Flame, *AIAA J*., 29, 1452-1457.

Kiss, L.B., Söderlund, J., Niklasson, G.A., Granquist, C.G. (1999). New Approach to the origin of Lognormal Size Distribution of Nano-Particles, *Nanotechnology* 10, 25-28.

Kittelson, D.B., Ambs, J.L., Hadjkacem, H. (Feb 26-Mar 2, 1990) Particulate emissions from diesel engine. Influence of In-cylinder surface, *SAE Technical Paper Series, SAE International Congress and Exposition*, Detroit, MI, USA.

Kordyban, E.S., Ranov, T. (1970). Mechanism of slug formation in horizontal two-phase flow, *Trans. ASME, J. Basic Eng.* 92, 857-864.

Krishnan, V.S., Kowalski, J.E. (1984). Stratified-slug flow transition in a horizontal pipe containing a rod bundle, *AIChE Symp*. Ser. No. 236, Vol. 80, 282-289.

Kronig, R., Brink, J.C. (1950). On the theory of extraction from falling droplets. *Appl. Sci. Res*., A2, 142-154.

Laker, T. S., Ghiaasiaan, S. M. (2003). Monte-Carlo Simulation of Aerosol Transport in Rising Spherical Bubbles with Internal Circulation. *J. Aerosol Sci.* 35, 473-488.

Lamb, H. (1932). *Hydrodynamics*, 6th Ed., Cambridge University Press, Cambridge.

Lamb, H. (1945). *Hydrodynamics,* Dover Publications, New York.

Lancia, A., Musmarra, D., Pepe, F., Volpicelli, G. (1994). SO_2 absorption in a bubbling reactor using limestone suspensions. *Chem. Eng. Sci*., 49, 4523-4532.

Lawson, D. (1997). A closer look at Planck's Blackbody Equation, *Phys. Educ.* 32, 321-326.

Lee, J.S., Humphrey, J.A.C. (1986). Radiative-convective heat transfer in dilute particle-laden channel flows, *Physico Chemical Hydrodynamics*, 7, 5-6, 325-351.

Lee, R.C., Nydahl, J.E. (1989). Numerical Calculations of bubble Growth in Nucleate boiling from Inception through Departure, *J. Heat Transfer*, 111, pp. 474-479.

Levich, V.G. (1962). *Physicochemical Hydrodynamics*, Prentice-Hall, New York.

Levy, S. (1967). Forced Convection Subcooled Boiling: Prediction of Vapor Volumetric Fraction. *Int. J. Heat mass Transfer*, 10, pp. 951-965.

Lin, P.Y., Hanratty, T.J. (1986). Prediction of the initiation of slugs with linear stability criterion, *Int. J. Multiphase Flow* 12, 79-98.

Lindsay, J.D., Ghiaasiaan, S.M, Abdel-Khalik, S.I. (1995). Macroscopic flow structures in a bubbling paper pulp-water slurry. *Ind. Eng. Chem. Res*., 34, 3342-3354.

Lowe, D. C., Rezkallah, K. S. (1999). Flow regime identification in microgravity two-phase flow using void fraction signals. *Int. J. Multiphase Flow*, 25, 433-457.

Maa, R.A. (1967). Evaporation Coefficient of Liquids, *Ind. Eng. Chem. Fund*., vol. 6, pp. 504-518.

Mackowski, D.W. (1989). Photophoresis of aerosol particles in the free molecular and slip-flow regimes, *International Journal of Heat and Mass Transfer*, v 32, n 5, 843-854.

Marek, R., Straub, J. (2001). The Origin of Thermocapillary Convection in Subcooled Nucleate Pool Boiling, *Int. J. Heat Mass Transfer*, 44, 619-632.

Maricq, M.M., Harris, S.J., Szente, J.J. (Feb 1, 2003). Soot size distributions in rich premixed ethylene flames, *Combustion and Flame*, v 132, n 3, p 328-342.

Marsh, W.J., Mudawar, I. (1989). Predicting the Onset of Nucleate boiling in Wavy Free-Falling Turbulent Liquid Films, *Int. J. Heat Mass Transfer*, 32, pp. 361-378.

Mata, C., Pereyra, E., Trallero, J.L., Joseph, D.D. (2002). Stability of stratified gas-liquid flows, *Int. J. Multiphase Flow* 28, 1249-1268.

Mehra, A. (1996). Gas absorption in reactive slurries: particle dissolution near gas-liquid interface. *Chem. Eng. Sci*., 51, 461-477.

Miller, C.A., Scriven, L.E. (1968). The oscillations of a fluid droplet immersed in another fluid. *J. Fluid Mech*. 32 Part 3, 417-435.

Milne-Thompson, L.M. (1960). *Theoretical Hydrodynamics*, McMillan, New York.

Minitab Statistical Software (2000). *Minitab Inc*., Release 13 for Windows.

Mishima, K, Hibiki, T., Nishihara, H. (1995). Some characteristics of air-water two-phase flow in small diameter tubes. *Proc 2nd Int. Conf. Multiphase Flow*, Vol. 4, pp 39- 46, April 3-7, 1995, Tokyo, Japan.

Mishima, K., Hibiki, T. (1996). Some characteristics of air-water two-phase flow in small diameter vertical tubes. *Int. J. Multiphase Flow*, 22, 703-712.

Mishima, K., Ishii, M. (1980). Theoretical prediction of onset of horizontal slug flow, *J. Fluids Eng*. 102, 441-445.

Miyahara, S., Sagawa, N. (1996). Iodine mass transfer from Xenon-Iodine mixed gas bubble to liquid sodium pool. *J. Nuclear Sci. and Tech*. 33, 220-228.

Montes, F.J., Galon, M.A., Cerro, R.L. (1999). Mass Transfer from Oscillating Bubbles in Bioreactors. *Chem. Eng. Sci*. 54, 3127-3136.

Montes, F.J., Galon, M.A., Cerro, R.L. (2002). Comparison of Theoretical and Experimental Characteristics of Oscillating Bubbles. *Ind. Eng. Chem. Res*. 41, 6235-6245.

Muginstein, A., Fichman, M., Gutfinger, C. (2001). Gas absorption in a moving drop containing suspended solids. *Int. J. of Multiphase Flow*, 27, 1079-1094.

Neter, J., Kutner, M.H., Nachtsheim, C.J., Wasserman, W. (1996). *Applied Linear Statistical Models*. Fourth Ed., McGraw Hill.

Nijsing, R.A.T.O., Hendriksz, R.H., Kramers, H. (1959). Absorption of CO_2 in jets and falling films of electrolyte solutions, with and without chemical reaction. *Chem Eng. Sci.*, 10, 88-104.

Olander, D. R. (1966). The Handlos-Baron Drop Extraction Model. AIChE J. 12, 1018-1019.

Osamusali, S.I., Chang, J.S. (1988). Two phase flow regime transition in a horizontal pipe and annulus flow under gas-liquid two-phase flow, *ASME Fundamentals of Gas-Liquid Flows*, FED-Vol. 72, ASME, New York, 63-69.

Ounis, H., Ahmadi, G., McLaughlin, J. B. (1991). Dispersion and deposition of Brownian particles from point sources in a simulated turbulent channel flow. *J. Colloid Interface Sci.* 147, 233-250.

Owczarski, P. D., Postma, A. K., Schreck, R. I. (1985). Technical Bases and User's Manual for the Prototype SPARC—A Suppression Pool Aerosol Removal Code. U. S. Nuclear Regulatory Commission Report NUREG/CR-3317.

Pasiuk-Bronikowska, W., Rudzinski, K.J. (1991). Absorption of SO_2 into aqueous system, *Chem. Eng. Sci*. 46, 2281-2291.

Paterson, A.H.J., Kerekes, R.J. (1985). Fundamentals of Mixing in Pulp Suspensions: Measurement of Microscale Mixing in Chlorine. *J. of Pulp and Paper Science*, 11 (4), J108-J113.

Paterson, A.H.J., Kerekes, R.J. (1986). Fundamentals of Mixing in Pulp Suspensions: Measurement of Microscale Mixing in Mill Chlorination. *J. of Pulp and Paper Science*, 12 (3), J78-J83.

Peebles, F.N., Garber, H.J. (1953). Studies on the Motion of Gas Bubbles and Liquids. *Chem. Eng. Progr*. 40, 88-97.

Peng, X.F., Wang, B.X. (1993). Forced Convection and Flow Boiling Heat Transfer for Liquid Flowing through Microchannels, *Int. J. Heat Mass Transfer*, Vol. 36, 3421-3427.

Peng, X.F., Wang, B.X. (1994) Liquid Flow and heat Transfer in Microchannels with/without Phase Change. Heat Transfer, *Proc. 10th Int. Heat Transfer Conf.*, Vol. 5, pp. 159-177.

Peng, X.F., Hu, H.Y., Wang, B.X. (1994). Boiling Nucleation during Liquid Flow in Microchannels, *Int. J. Heat mass Transfer*, Vol. 41, pp. 101-106.

Peng, X.F., Liu, D., Lee, D.J., Yan, Y., Wang, B.X. (2000). Cluster Dynamics and Fictitious boiling in Microchannels, *Int. J. Heat Mass Transfer*, vol. 43, pp. 4259-4265.

Petzold, L.R., Hinmarsh, A.C. (1997). LSODA – Livermore Solver for Ordinary Differential Equations, with Automatic Method Switching for Stiff and Non-stiff Problems, Computing and Mathematics Research Division, l-316, Lawrence Livermore National Laboratory.

Pich, J., Schültz, W. (1991). On the Theory of Particle Deposition in Rising Gas Bubbles: The Absorption Minimum. *J. Aerosol Sci.* 22, 267-272.

Prosperetti, A. (1980). Free Oscillations of Drops and Bubbles: The Initial-Value Problem. *J. Fluid Mech*. 100, 333-347.

Puri, I.K. (1993). *Environmental Implications of Combustion Progresses*, CRC Press, Boca Raton, Florida.

Raabe, O.G. (1971). Particle Size Analysis Utilizing Grouped Data and the Log-Normal Distribution, *Aerosol Science*, Vol. 2, 289-303.

Ramachandran, P.A., Sharma, M.M. (1969). Absorption with fast reaction in a slurry containing sparingly soluble fine particles. *Chem. Eng. Sci.*, 24, 1681-1686.

Reichardt, H. (1951). Die Grudnlagen des Turbulent Warmeuberganges, *Arch. Ges. Warmetech*, 2, 129-142.

Reist, P.C. (1993). *Aerosol Science and Technology*, 2nd Ed., McGraw-Hill, Inc., New York.

Rewatkar, V.B., Bennington, C.P.J. (2000). Gas-Liquid Mass Transfer in Low- and Medium-Consistency Pulp Suspensions. *The Can. J. Chem. Eng*., 78 (6), 504-512.

Rezkallah, K. S. (1996). Weber number based flow-pattern maps for liquid-gas flows at microgravity. *Int. J. Multiphase Flow*, 22, 1265-1270.

Robin, Jr., T.T., Snyder, N.W. (1970). Bubble dynamics in Subcooled Nucleate boiling Based on the Mass Transfer Mechanism, *Int. J. Heat Mass Transfer*, 13, pp. 305-318.

Rogers, T.J., Salcudean, M., Abdullah, M., McLeod, Z., Poirier, D. (1987). The Onset of Significant Void in Up-flow Boiling of Water at Low Pressure and Velocity, *Int. J. Heat Mass Transfer*, 30, 2247-2260.

Sada, E., Kumazawa, H., Butt, M.A. (1977). Single gas absorption with reaction in a slurry containing fine particles. *Chem. Eng. Sci.*, 32, 1165-1170.

Sato, T., Matsumura, H. (1963). On the Conditions of Incipient Subcooled Boiling and forced Convection, *Bulletin Japan Soc. Mech. Eng*., 7, pp. 392-398.

Shaw, B.T., Dryer, F., Williams, F.A., Haggard, J.D. (1988). Sooting and Desorption in Spherical-Symmetrical Combustion of Decane Droplets in Air, *Acta Astronautica*, 17, 1195-1202.

Shilimkan, R.V. (1975). Mass Transfer in Co-Current Gas-Liquid Vertical Flows, Ph. D. Thesis, University of Salford.

Shima, A. (1970). The Natural Frequency of a Bubble Oscillating in a Viscous Compressible Liquid. *ASME J. Basic Eng*., Series D, 92, 555-562.

Siegel, R., Howell, J.R. (2002) *Thermal radiation heat transfer*, 4th Ed. Taylor & Francis, New York.

Serizawa, A., Feng, Z. P. (2001). Two-phase flow in microchannels. *Proc. 4th International Conf. Multiphase Flow*, May 27-June 1, 2001, New Orleans, LA, USA.

Serizawa, A., Kataoka, I., Michiyoshi, I. (1975). Turbulence structure of air-water bubbly flow – I. Measuring techniques. *Int. J. Multiphase Flow*, 2, 221-233.

Sirignano, W.A. (1999). Fluid Dynamics and Transport of Droplets and Sprays, Cambridge Neter, J., Kutner, M.H., Nachtsheim, C.J., Wasserman, W. (1996). *Applied Linear Statistical Models*. Fourth Ed., McGraw Hill.

Smook, G. A. (1990). Handbook of pulp & paper terminology, *Angus Wilde Publications Inc.*

Staub, F.W. (1968). The Void Fraction in Subcooled Boiling: Prediction of the Initial Point of Net Vapor Generation. *J. Heat Transfer*, 90, 151-157.

Straub, J., Betz, J, Marek, R. (1994). Enhancement of Heat Transfer by Thermocapillary Convection Around Bubbles – a Numerical Study, *Num. Heat Transfer: A*, 25, pp. 501-518.

Sudo, Y., Miyata, K., Ikawa, H., Kaminaga, M. (1986). Experimental Study of Incipient Nucleate boiling in narrow Vertical Rectangular Channel Simulating Subchannel of Upgraded JRR-3, J. Nucl. Sci. Technol., 23, pp. 73-82.

Suhre, B.R., Foster, D.E. (1992) In-Cylinder Soot Deposition Rates due to Thermophoresis in a Direct Injection Diesel Engine, *SAE Special Publications, n 931, Diesel Combustion, Emissions, and Exhaust Aftertreatment*, 35-48.

Suo, M., Griffith, P. (1964). Two-phase flow in capillary tubes. *J. Basic Eng.*, 86, 576-582.

Taitel, Y., Dukler, A.E. (1976). A model for predicting flow regime transitions in horizontal and near-horizontal gas-liquid flow, *AIChE J.*, 22, 47-55.

Talbot, L., Cheng, R.D., Scheffer, R.W., Willis, D.R. (1980) Thermophoresis of Particles in a Heated Boundary Layer, *J. Fluid Mech.*, 101, 737-758.

Tandon, P., Terrell, J.P., Fu, X., Rovelstad, A. (2003). Estimation of Particle Volume Fraction, Mass Fraction and Number Density in Thermophoresis Deposition Systems, *Int. J. Heat and Mass Transfer*. 46, 17, 8, 3201-3209.

Thakurta, D. G., Chen, M., McLaughlin, J. B., Kontomaris, K. (1998). Thermophoretic Deposition of Small Particles in a Direct Numerical Simulation of Turbulent Channel Flow. *Int. J. Heat Mass Transfer* 41, 4167-4182.

The Numerical Algorithm Group (2002). NAG Fortran Library Manual.

Tomida, T., Yusa, F., Okazaki, T. (1978). Effective Interfacial Area and Liquid-Side Mass Transfer Coeffiecient in the Upward Two-Phase Flow of Gas-Liquid Mixtures, *Chem. Eng. J.*, Vol. 16, pp 81-88.

Triplett, K. A., Ghiaasiaan, S. M., Adbel-Khalik, S. I., Sadowski, D. L. (1999). Gas-liquid two-phase flow in microchannels. Part I: Two-phase flow patterns. *Int. J. Multiphase Flow*, 25, 377-394.

Tsamopoulos, J.A., Brown, R.A. (1983). Nonlinear Oscillations of Inviscid Drops and Bubbles. *J. Fluid Mech.* 127, 519-537.

Uchida, S., Koide, K., Shindo, M. (1975). Gas absorption with fast reaction into slurry containing fine particles. *Chem. Eng. Sci*., 30, 644-646.

Uchida, S., Miyachi, M., Ariga, O. (1981). Penetration model of gas absorption into slurry accompanied by an instantaneous irreversible chemical reaction. *Can. J. Chem. Eng*., 59, 560-561.

Unal, H.C. (1976).Maximum Bubble Diameter, Maximum Bubble-growth Time and Bubble-growth Rate during the Subcooled Nucleate Flow Boiling of Water up to 17.7 MN/m^2. *Int. J. Heat Mass Transfer,* 19, pp. 643-649.

Vandervort, C.L., Bergles, A.E., Jensen, M.K. (1994).An Experimental Study of Critical Heat Flux in Very High Heat Flux Subcooled Boiling. *Int. J. Heat Mass Transfer*, 37 (Suppl. 1), 161-173.

Vedha-Nayagam, M., Mackowski, D.W. (12-13 October, 1992). Radiation Induced Thermophoretic Effects on Particle Concentration in a Laminar Tube Flow, *The Combustion Institute Fall Meeting*, San Francisco, CA.

Waldmann, L., Schmitt, K.H. (1966). Chapter VI. Thermophoresis and Diffusiophoresis of Aerosols, *Aerosol Science*, edited by C. N. Davies. Academic Press, New York, pp. 137–162.

Wallis, G.B., Dobson, J.E. (1973). Prediction of the initiation of slugs with linear stability criterion, *Int. J. Multiphase Flow* 1, 173-193.

Wassel, A. T., Mills, A. F., Bugby, D. C. (1985). Analysis of Radionuclide Retention in Water Pools. *Nucl. Eng. Design* 90, 87-104.

Watson, H.H. (1936). The Dust-Free Space Surrounding Hot Bodies, *Trans. Faraday Soc.*, 1073-1083.

Watson, A.P., Cormack, D.E., Charles, M.E. (1979). A Preliminary Study of Interfacial Areas in Vertical Cocurrent, Two-Phase Flow, *Can. J. Chem. Eng.*, Vol. 57, pp. 16-23.

Wen, C. S. (1996). *The Fundamentals of Aerosol Dynamics*. World Scientific, Singapore.

Yang, C. Y., Shieh, C. C. (2001). Flow pattern of air-water and two-phase R–134a in small circular tubes. *Int. J. Multiphase Flow*, 27, 1163 – 1177.

Yin, S.T., Abedlmessih, A.H. (1974). Prediction of Incipient Flow Boiling from a Uniformly Heated Surface, *AIChE Symp*. Series 164, pp. 236-243.

Yoa, S.J., Kim, S.S., Lee, J.S. (1990). Thermophoresis of Highly Absorbing Emitting Particulates in Laminar Tube Flow, *Int. J. Heat and Fluid Flow*, 11, 98-104.

Yuan, H., Oguz, H.N, A. Prosperetti (1999). Growth and Collapse of a Vapor Bubble in a Small Tube, *Int. J. Heat Mass Transfer*, 42, 3643-3657.

Zeng, L.Z., Klausner, J.F., Mei, R. (1993). A Unified Model for the Prediction of bubble Detachment Diameters in Boiling Systems – I. Pool Boiling, *Int. J. Heat Mass Transfer*, 36, pp. 2261-2270.

Zeng, L.Z., Klausner, J.F., Bernhard, D.M., Mei, R. (1993). A Unified Model for the Prediction of Bubble Detachment Diameters in boiling Systems – 11. Flow Boiling. *Int. J. Heat Mass Transfer*, 36, 2271-2279.

Zhao, B., Yang, Z., Johnston, M.V., Wang, H., Wexler, A.S., Balthasar, M., Kraft, M. (2003). Measurement and Numerical Simulation of Soot Particle Size Distribution Function in a Laminar Premixed Ethylene-Oxygen-Argon Flame, *Combustion and Flame,* 133, 173-188.

Zhao, L., Rezkallah, K. S. (1993). Gas-liquid flow patterns at microgravity conditions. *Int. J. Multiphase Flow*, 19, 751-763.

Zhao, T. S., Bi, Q. C. (2001). Co-current air-water two-phase flow patterns in vertical triangular microchannels. *Int. J. Multiphase Flow*, 27, 765 – 782.

Zuber, N., Findlay, J.A. (1965). Average Volumetric Concentration in Two-Phase Flow Systems, *J. of Heat Transfer*, Vol. 87, pp. 453-468.